1-1-2013

Oxide Semiconductors for Organic Opto-Electronic Devices

Ajaya Kanta Sigdel
University of Denver

OXIDE SEMICONDUCTORS FOR ORGANIC OPTO-ELECTRONIC DEVICES

A Dissertation

Presented to

the Faculty of Natural Sciences and Mathematics

University of Denver

In Partial Fulfillment

of the Requirements for the Degree

Doctor of Philosophy

---

by

Ajaya K. Sigdel

June 2013

Advisor: Professor Sean E. Shaheen

Author: Ajaya K. Sigdel
Title: Oxide Semiconductors for Organic Opto-electronic Devices
Advisor: Professor Sean E. Shaheen
Degree Date: June 2013

Abstract

Development of transparent oxide semiconductors (TOS) from Earth-abundant materials is of great interest for cost-effective thin film device applications, such as solar cells, light emitting diodes (LEDs), touch-sensitive displays, electronic paper, and transparent thin film transistors. The need of inexpensive or high performance electrode might be even greater for organic photovoltaic (OPV), with the goal to harvest renewable energy with inexpensive, lightweight, and cost competitive materials. The natural abundance of zinc and the wide bandgap ($\sim$3.3 eV) of its oxide make it an ideal candidate. In this dissertation, I have introduced various concepts on the modulations of various surface, interface and bulk opto-electronic properties of ZnO based semiconductor for charge transport, charge selectivity and optimal device performance. I have categorized transparent semiconductors into two sub groups depending upon their role in a device. Electrodes, usually 200 to 500 nm thick, optimized for good transparency and transporting the charges to the external circuit. Here, the electrical conductivity in parallel direction to thin film, i.e bulk conductivity is important. And contacts, usually 5 to 50 nm thick, are optimized in case of solar cells for providing charge selectivity and asymmetry to manipulate the built in field inside the device for charge separation and collection. Whereas in Organic LEDs (OLEDs), contacts provide optimum energy level alignment at organic oxide interface for improved charge injections.

For an optimal solar cell performance, transparent electrodes are designed with maximum transparency in the region of interest to maximize the light to pass through to the absorber layer for photo-generation, plus they are designed for minimum sheet resistance for efficient charge collection and transport. As such there is need for material with high conductivity and transparency. Doping ZnO with some common elements such as B, Al, Ga, In, Ge, Si, and F result in n-type doping with increase in carriers resulting in high conductivity electrode, with better or comparable opto-electronic properties compared to current industry-standard indium tin oxide (ITO). Furthermore, improvement in mobility due to improvement on crystallographic structure also provide alternative path for high conductivity ZnO TCOs.

Implementing these two aspects, various studies were done on gallium doped zinc oxide (GZO) transparent electrode, a very promising indium free electrode. The dynamics of the superimposed RF and DC power sputtering was utilized to improve the microstructure during the thin films growth, resulting in GZO electrode with conductivity greater than 4000 S/cm and transparency greater than $\sim 90\%$. Similarly, various studies on research and development of Indium Zinc Tin Oxide and Indium Zinc Oxide thin films which can be applied to flexible substrates for next generation solar cells application is presented. In these new TCO systems, understanding the role of crystallographic structure ranging from poly-crystalline to amorphous phase and the influence on the charge transport and optical transparency as well as important surface passivation and surface charge transport properties.

Implementation of these electrode based on ZnO on opto-electronics devices such as OLED and OPV is complicated due to chemical interaction over time with the organic layer or with ambient. The problem of inefficient charge collection/injection due to poor understanding of interface and/or bulk property of oxide electrode exists at several oxide-organic interfaces. The surface conductivity, the work function, the formation of dipoles and the band-bending at the interfacial sites can positively or negatively impact the device performance. Detailed characterization of the surface composition both before and after various chemicals treatment of various oxide electrode can therefore provide insight into optimization of device performance. Some of the work related to controlling the interfacial chemistry associated with charge transport of transparent electrodes are discussed. Thus, the role of various pre-treatment on poly-crystalline GZO electrode and amorphous indium zinc oxide (IZO) electrode is compared and contrasted. From the study, we have found that removal of defects and self passivating defects caused by accumulation of hydroxides in the surface of both poly-crystalline GZO and amorphous IZO, are critical for improving the surface conductivity and charge transport. Further insight on how these insulating and self-passivating defects cause charge accumulation and recombination in an device is discussed.

With recent rapid development of bulk-heterojunction organic photovoltaics active materials, devices employing ZnO and ZnO based electrode provide air stable and cost-competitive alternatives to traditional inorganic photovoltaics. The organic light emitting diodes (OLEDs) have already been commercialized, thus to follow in the footsteps of this technology, OPV devices need further improvement in power conversion efficiency and stable materials resulting in long device

lifetimes. Use of low work function metals such as Ca/Al in standard geometry do provide good electrode for electron collection, but serious problems using low work-function metal electrodes originates from the formation of non-conductive metal oxide due to oxidation resulting in rapid device failure. Hence, using low work-function, air stable, conductive metal oxides such as ZnO as electrons collecting electrode and high work-function, air stable metal such as silver for harvesting holes, has been on the rise. Devices with degenerately doped ZnO functioning as transparent conductive electrode, or as charge selective layer in a polymer/fullerene based heterojunction, present useful device structures for investigating the functional mechanisms within OPV devices and a possible pathway towards improved air-stable high efficiency devices. Furthermore, analysis of the physical properties of the ZnO layers with varying thickness, crystallographic structure, surface chemistry and grain size deposited via various techniques such as atomic layer deposition, sputtering and solution-processed ZnO with their respective OPV device performance is discussed. We find similarity and differences in electrode property for good charge injection in OLEDs and good charge collection in OPV devices very insightful in understanding physics behind device failures and successes. In general, self-passivating surface of amorphous TCOs IZO, ZTO and IZTO forms insulating layer that hinders the charge collection. Similarly, we find modulation of the carrier concentration and the mobility in electron transport layer, namely zinc oxide thin films, very important for optimizing device performance.

Acknowledgements

I started at the foothills of the Himalayas. This journey to the summit was possible with the help of many people. My superstar advisers Joseph Berry and Sean Shaheen are heartily acknowledged for providing me a map, showing me the trails, handing me ropes and ladders and oxygen tanks needed for the climb. My sincere gratitude to my thesis committee:- David Ginley, Dana Olson, Davor Balzar, Barry Zink and Julanna Gilbert for helping me define a single path. A special thanks to Paul Ndione, John Perkins, Thomas Gennett, Arrelaine Dameron, Maikel van Hest, Philip Parilla, Andriy Zakutayev, Jennifer Leisch, Matthew Reese, Scott Hammond, Jennifer Hoffman and various scientists and professors for sharing the vast knowledge to navigate cliffs and valleys. Thank you Erin Ratcliff for showing me the alternate gears used by chemist. A sincere gratitude to all fellow graduate students at NREL and DU for hiking along. Specially, I am thankful to Nicodemus Edwin Widjonarko for being there at various adventures Joe entrusted to us. Thank you Jamie Lomax and Azure Avery for inspiration and sharing your blueprint of humility and discipline needed in this journey. Thanks to Alex Nardes, Abby Johnson, Tula Paudel and various friends for reminding me to rest and recharge. Thank you dear sisters Aruna Sigdel and Bhawana Sigdel, mama Omkar Parajuli, sanomuma Durga Parajuli, sanobuba Ishwori Sharma and all the family members for support and motivation from the base camp. Most importantly, I am thankful for the moral compass and the illuminations provided by my mother Maiya Sigdel and my father late Surya Kanta Sigdel. Without their love, blessings and sacrifices, this journey was impossible and futile. I the invincible son dedicate this dissertation to the loving memory of my father, the sun.

Contents

Acknowledgements vi
List of Tables x
List of Figures xi

1 Introduction **1**
1.1 Renewable Energy 1
1.2 Flexible Thin Film Devices 2
1.3 Earth Abundant Semiconductor Material 5

2 Tools for Development of Oxide and Organic Semiconductors **8**
2.1 Simplified Architecture of OPV and OLEDs 10
2.2 Thin Film Deposition 12
2.2.1 Pulse Laser Deposition (PLD) 12
2.2.2 Plasma Sputtering 13
2.2.3 Atomic Layer Deposition 17
2.2.4 Solution Precursor Spin Cast 18
2.2.5 Evaporation 20
2.3 Thin Film Characterization 21
2.3.1 Structural 21
2.3.2 Electrical 25
2.3.3 Optical 26
2.4 ZnO Semiconductor Fundamentals 30
2.5 Organic Photovoltaic Device Physics 34
2.5.1 Current Density and Voltage Measurement 35
2.5.2 Light Management in a Device 38
2.5.3 Diode Ideality 39

3 Research and Development of Transparent Semiconductors **41**
3.1 Radio-Frequency Superimposed Direct Current Magnetron Sputtered Ga:ZnO Transparent Conducting Thin Films 43
3.1.1 Introduction 44
3.1.2 Experimental Details 46

3.1.3 Characterizations 47
3.1.4 Results and Discussion 48
3.1.5 Conclusions 64

4 Surface Studies of Transparent Semiconductors 66
4.1 Surface composition, Work function and Electrochemical Characteristics of Ga-doped ZnO (GZO) Semi-transparent Electrodes . . . 67
4.1.1 Introduction 68
4.1.2 Experimental Methods 71
4.1.3 XPS Studies of Different Ga:Zn Atomic Ratio Oxides 76
4.1.4 XPS Studies As-received and Pre-treated GZO Films 83
4.1.5 UPS Studies of As-received and Pre-treated GZO Films . . . 87
4.1.6 Electrochemical Activities of As-received and Pre-treated GZO Electrodes 96
4.1.7 Conclusions 101
4.2 Effect of Surface Pretreatment on Surface Passivation on Amorphous Indium Zinc Oxide (IZO) 103
4.2.1 Introduction 104
4.2.2 Experimental Methods 107
4.2.3 Optical and Structural Properties 108
4.2.4 XPS and UPS Studies As-received and Pre-treated IZO Films 110
4.2.5 Kelvin probe and Conductive AFM Studies of As-received and Pre-treated IZO Films 118
4.2.6 Electrochemical Reactivities of As-received and Pre-treated IZO Electrodes 119
4.2.7 Conclusions 122

5 Efficient Hole Injection in OLEDs using Zinc Tin Oxide (ZTO) 124
5.1 Introduction to Blue Phosphorescent OLEDs 126
5.2 Experimental 130
5.2.1 PLD Depositions 130
5.2.2 OLEDs Fabrication and Measurement 131
5.3 Results: ZTO Varying O_2 Partial Pressure and Substrate Temperature (Ts) 133
5.4 Results: ZTO and TCO (ITO, GZO) Heterostructure 135
5.5 Results: OLEDs Studies with ZTO 137
5.6 Conclusion 141

6 Impact of Oxide Property on Devices - BHJ OPV Devices 142
6.1 Various Zinc-Based TCOs with and without Electron Selective Layer in Inverted Organic Photovoltaics 144

6.1.1 Introduction . . . 144
6.1.2 Experimental . . . 146
6.1.3 Results and Discussion . . . 147
6.1.4 Conclusions . . . 154
6.2 Modulation of Mobility and Carrier Concentration in ZnO Electrode for Efficient Charge Collection in OPV . . . 156
6.2.1 Introduction . . . 157
6.2.2 Experimental . . . 160
6.2.3 Results and Discussion . . . 162
6.2.4 Conclusions . . . 168

7 Next Generation Tailored TCO : Indium Zinc Tin Oxide 170
7.1 Introduction . . . 171
7.2 Materials and Methods . . . 174
7.3 Results and Discussion . . . 176
7.4 OPV Device Study on Indium Zinc Tin Oxide Thin Film . . . 194
7.5 Conclusions . . . 194

8 Conclusions 196

Bibliography 203

Appendix A: Electrical Measurements 238

Appendix B: List of symbols and acronyms 244

Appendix C: List of publications 248

List of Tables

4.1 Binding energies (eV) for O 1s, Zn 2p and Ga 2p peaks in Figure 4.1.3. 80

4.2 Binding energy (eV) and atomic percentage of total O 1s fit ($\% = \frac{O1s_{peak}}{O1s_{Total}}$) for the different pretreatments of GZO electrodes and Ga to Zn atomic percentages. 86

4.3 Electrochemical response for $\mathrm{Me_{10}Fc}$. 97

4.4 Electrochemical response of chemisorbed $Fc(COOH)_2$. 98

4.5 Normal and angle resolved XPS for the O 1s core electrons of IZO exposed to different surface pretreatments showing relative binding energies and percentages for each fit component, as well as relative Zn:In and Zn:In:O ratios. 113

4.6 Electrochemical response of Me10Fc 121

4.7 Electrochemical response of $Fc(COOH)_2$. 121

5.1 O_2 and temperature variation study on ZTO ($\sim$375 nm) film on glass. 133

5.2 TCO (ITO or GZO) modified with various thickness ZTO. 135

5.3 OLED: TCO (ITO or GZO) modified with various thickness ZTO. . 139

6.1 Physical properties of TCO films with and without ZnO layer. 149

6.2 Photovoltaic parameters of devices with various TCOs 153

List of Figures

1.1 Lewis and Nocera, Proceedings of the National Academy of Science, Perspective, 2006. 2

1.2 Global photovoltaics by the numbers. 3

1.3 Research and development guiding principles for photovoltaics. . . . 4

1.4 OPV efficiency growth chart: Compiled by Karl Leo, IAPP Dresden. 4

1.5 The natural abundance of Zinc is higher compare to Indium. 6

2.1 A simplified diagram of OPV device. 10

2.2 Pulse Laser Deposition 12

2.3 Cross-sectional TEM image of GZO and IZO thin film deposited using PLD with 6 nm periodicity. 14

2.4 A systematic diagram of sputtering technique, and plasma glow during oxide deposition. 14

2.5 Ag nano structure array. 16

2.6 Spin coater for solution spin cast 18

2.7 X-ray diffraction to find the size and orientation of crystallite. Better crystallographic orientation help reduce grain boundary scattering mechanism. Dopants and other phase separated impurities can also be detected, which may hinder the charge transport 22

2.8 X-ray diffraction (2D raw image) of 21 nm and 49 nm ZnO film deposited via ALD. 23

2.9 In our setup, the transmission and the reflection measurements are done with the incidence angle at zero degree. 27

2.10 Undoped stoichiometric state (left) and degenerately doped with displaced Fermi level, due to increasing N called Burstein-Moss shift (right). 29

2.11 Systematic of OPV device with an inverted architecture. Here, holes are collected at the metal electrode, while electrons are collected at the transparent electrode. (TCO/ZnO/P3HT:PCBM/HTL/Ag) 35

2.12 Energy level diagram for TCO/ZnO/P3HT:PCBM/HTL/Ag device, before fermi level alignment. 36

2.13 An illustration of a J-V curve for a typical OPV device. 37

2.14 Electric field is continuous throughout the device. Photon absorption is discontinuous. 37

3.1 (a) Deposition rates and (b) Discharge voltage for different γ_{rfdc} from 0 to 1 and various P_{Tot} of 60, 80, 100 and 120 W respectively. By varying γ_{rfdc}, similar deposition rate can be achieved at varying P_{Tot}. 49

3.2 (a) XRD peaks for GZO films grown at P_{Tot} = 100 W with various γ_{rfdc} showing (002) peak characteristic of c-axis oriented zinc oxide with wurtzite structure. No Ga_2O_3 peaks are evident and inset showing 2D diffraction image files. (b) ZnO PDF (c) Ga_2O_3 PDF. . 51

3.3 XRD data on 44 data points for 2×2 inch GZO substrate. 52

3.4 (a) χ for P_{Tot} of 100 W at various γ_{rfdc} b) FWHM on χ for P_{Tot} of 100 W and 120 W at various γ_{rfdc}. Films grown with more RF component have small FWHM. 54

3.5 Hall data for various P_{Tot} and at varying γ_{rfdc}. Panels a, b and c respectively show σ, N and μ. Films grown with 50% or higher RF power portion have high μ. 55

3.6 RGA data showing σ vs measured O_2 partial pressure in the deposition chamber. 57

3.7 a) Total counts/thickness of the entire 002 peak b) σ vs FWHM χ c) μ vs FWHM χ for films grown at P_{Tot} of 100 W and 120 W at various γ_{rfdc}. Films with more structural order obtained with increased RF component, resulting in high σ and μ. 59

3.8 GZO film on a 2×2 inch substrate. 60

3.9 Transmittance and Reflectance data for P_{Tot} = 100 W. Films have ∼90% transparency in visible spectrum. Inset showing $(\alpha h\nu)^2$ vs $h\nu$ and E_{opt} (± 0.02 eV). 61

3.10 AFM image for P_{Tot} = 100 W: (a) γ_{rfdc} = 1 with S_{rms} = 1.8 nm (b) γ_{rfdc} = 0.5 with S_{rms} = 1.7 nm (c)γ_{rfdc} = 0 with S_{rms} = 2.2 nm. Films grown with 50% or higher RF power portion have low S_{rms}. . 63

3.11 Clear correlation is observed with improvements in μ and reduced S_{rms}. 63

4.1 XPS results for Ga 2p, Zn 2p, and O 1s core levels for four different Zn:Ga atomic ratio oxides (100% Zn, 95%Zn:5%Ga, 15%Zn:85%Ga, and 100% Ga; from top to bottom) deposited by sputtering from a single target, with XPS data shown for as received (—) and Ar sputtered (−−) pretreatments. The O 1s spectra have been labeled with the five different O 1s components discussed in the text: O_I (ZnO wurtzite lattice), O_{II} (defect in ZnO), O_{III} ($Zn(OH)_2$), O_{IV} (carbonaceous species such as CO, CO_2, CO_3^{2-} etc) and O_V Ga_2O_3, a species not detected in the GZO electrode (95%Zn:5% Ga). $ZnGa_2O_4$ species discussed in previous section of the text were not detected. 78

4.2 Normal (left-hand panel) and angle (right-hand panel) resolved XPS for the O 1s core electrons of GZO exposed to different surface pretreatments. Peak fits are discussed in the text and relative areas and binding energies are given in Table 4.2. 85

4.3 Ultraviolet photoemission spectroscopy (UPS) measurements of GZO electrodes exposed to different surface pretreatments, as labeled in panel iii. Panel i shows the high binding energy (low kinetic energy) edge of the secondary electrons, panel ii shows the valence structure of the different pretreatments, and panel iii gives the near-Fermi edge for each pretreatment. 90

4.4 Energy band diagrams based on UPS measurements of GZO electrodes following different surface pretreatments. Work function (ϕ) is calculated as the energy from the Fermi level (EF) to the vacuum level (E_{vac}). The band tail states (BT state) are representative of the near Fermi edge states ($\sim$ 2 eV below the EF) and the ionization potential from the valance band O_{2p} states (VBM_{O2p}) are fit to the O 2p edge of the GZO electrode ($\sim$ 3.5 to 4 eV below EF). 94

4.5 Change in work function ($\Delta\ \phi$) with respect to time for each of the different pretreatments, as measured by Kelvin probe, for GZO electrodes. Markers are spaced for clarity. 96

4.6 AFM images of the GZO electrodes post treatment (a) as received :1.8 $\pm$ 0.2 nm (b) O_2-plasma treated: 1.9 $\pm$ 0.2 nm, (c) base etched: 2.4 $\pm$ 0.2 nm and (d) acid etched: 3.0 $\pm$ 0.4 nm. 99

4.7 Transmission and Reflection of IZO 109

4.8 XRD spectrum of amorphous IZO (left) and poly-crystalline ITO (right) 110

4.9 Normal (left-hand panel) and angle (right-hand panel) resolved XPS for the O 1s core electrons of IZO exposed to different surface pretreatments. Peak fits are discussed in the text and relative areas and binding energies are given in Table 4.5 112

4.10 Schematic of the double layer for (a) the base etch and (b) the as received IZO electrode 115

4.11 Ultraviolet photoemission spectroscopy (UPS) measurements of IZO electrodes exposed to different surface pretreatments 116

4.12 Energy band diagrams based on UPS measurements of IZO electrodes following different surface pretreatments. Work function (ϕ) is calculated as the energy from the Fermi level (E_F) to the vacuum level (E_{vac}) 116

4.13 Work-function as a function of time for IZO electrodes with various surface treatment 119

4.14 Current voltage measurement done by Conductive AFM on IZO electrodes with various surface pretreatments. 120

4.15 Conductive AFM for as received and KOH etch IZO films at +2V and -2V bias. 120

5.1 Schematic of a simple two layer OLED device structure. 127

5.2 a) TCO materials (ITO and GZO) engineered for transparency and conductivity in concert with a deep work-function functional oxide interfacial layer (ZTO). Figure not drawn to scale. b) The barrier height between the HTL anode has to be matched energetically to HOMO of organic side. 128

5.3 (a) X-ray diffraction 2D detector image file and (b) Surface topography of ZTO film on glass. 134

5.4 Transmission and reflection of ITO with varying ZTO thickness. Some loss in transparency seen for thicker ZTO film. 137

5.5 Power efficiency as a function of brightness for blue OLEDs (Bare TCO or TCO with 10nm ZTO /TAPC(350) /TCTA(50) /mCP: 6% FIrpic(150) /PO15(500) /LiF /Al.) commercial ITO (black), ZTO/ITO (red) and ZTO/GZO (green). 138

5.6 A comparative study of N,N'diphenyl-N,N'-bis(1-naphthol) 1,1'-biphenyl-4,4'diamine (NPD)/tris (8-hydroxyquinolinolato) aluminum (Alq3) OLEDs fabricated on anodes of indium tin oxide (ITO) and gallium doped zinc oxide (GZO). 140

6.1 poly (3-hexylthiophene):[6,6]-phenyl C60 butyric acid methyl ester . 147

6.2 XRD measurements of (a)IZO, (b) GZO, (c) AZO, and (d) ITO. . . 149

6.3 Transmission and reflection spectra of ITO, IZO, GZO and AZO on glass. 150

6.4 Surface topography of (a) AZO and (b) AZO with ZnO layer. 151

6.5 J-V plots under light (a) and dark (b) of TCO/P3HT:PCBM/HTL/Ag and TCO/ZnO/P3HT:PCBM/Ag devices with ITO, IZO, GZO and AZO TCO bottom electrodes. . . . 152

6.6 a) Changes in series resistance of 48nm ZnO thin film b) Changes in ϕ (Kelvin probe) for various thickness ZnO with UV light λ = 248 nm and recovery. 163

6.7 a) Changes in dark JV device evolution with UV light λ = 248 nm, with exposure at T_0. (b) Changes in device performance in light (100 mW/cm^2 AM 1.5 G) during measurement. 164

6.8 a) Dark JV for devices with ZnO ETL with varying thickness (b) n-prime analysis for same sets of devices. Low ideality near V_{oc} yields good device performance. 165

6.9 Light JV for devices with ZnO ETL via sputtering with metallic target, Zn rich condition 166

6.10 Light JV for devices with ZnO ETL via sputtering with metallic target, O_2 rich condition 166

6.11 Diode ideality at V_{oc} as a function of (a) Mobility μ (with color code as N) (b) N (with color code as μ) 167

6.12 Diode ideality at V_{oc} as a function of μ/N 167

7.1 (XRD of films grown at ρ_{rf} = 3 W/cm^2 with varying deposition pressure (4.0 Pa, 2.0 Pa, 0.6 Pa) with T_s at a) 250 °C b) 150 °C c) 25 °C (d)/(e)/(f) showing PDF for In_2O_3 / ZnO/SnO_2. 177

7.2 AFM height image (left)and phase image (right) for samples grown at P = 4.0 Pa (a,b) 2.0 Pa (c,d) 0.6 Pa (e,f) at T_s = 250 °C and ρ_{rf} = 3 W/cm^2 constant. 179

7.3 (a) a cross-sectional TEM image for a-IZTO grown at 250 °C/2.5 W/cm^2 /0.6 Pa. (b) AFM of the same sample indicating phase separated domains. (c) and (d) TEM images of a-IZTO grown at 25 °C/2.5 W/cm^2 /0.6 Pa (e) EDX showing amorphous phase for room temperature film. 181

7.4 (a) σ (b) N, (c) μ as a function of T_s, for films grown at various ρ_{rf} and P of 4.0 Pa and 0.6 Pa. Films grown at high T_s = 250 °C have high σ due to increased number of carriers. 183

7.5 σ, N and μ as a function of P, for films grown at ρ_{rf} = 3 W/cm^2 and T_s =250 °C. Changes in structure dominates the electrical properties. 185

7.6 Transmittance (T) and Reflectance (R) for high conductivity c-IZTO and a-IZTO, and one at room temperature. Higher temperature deposition yields better transmittance, with $250\,^{\circ}\mathrm{C}$ film showing T $> 80\%$ in visible spectrum. Inset shows Tauc plot of $(\alpha h\nu)^2$ vs hν indicating increased optical gap as well for high temperature deposition film. 186

7.7 a, b shows ϕ and μ as a function of σ for films grown at $T_s = 250\,^{\circ}\mathrm{C}$, $150\,^{\circ}\mathrm{C}$ and $25\,^{\circ}\mathrm{C}$ respectively. 188

7.8 Height topography with corresponding C-AFM data of reference ITO sample(a,b), c-IZTO(c,d) and a-IZTO(e,f). Both c-IZTO and a-IZTO had similar work-function (ϕ), but very different heterogeneity in the surface. Panel (g, h) show JV data indicating the difference between white and dark pixel in the C-AFM data. 190

7.9 IZTO/P3HT:PCBM/Ca/Al devices on films shown in Figure 7.2 . . 193

7.10 IZTO/PEDOT:PSS/P3HT:PCBM/Ag devices on films shown in Figure 7.2 193

A-1 Resistivity Van der Pauw configuration 240

A-2 Van der Pauw configuration 241

Chapter 1

Introduction

1.1 Renewable Energy

Clean, renewable energy is in high demand, as traditional fuel resources are either limited in supply or have a very negative impact on our global health. With the rising population, now crossing 7 billion, we need to either consume less energy so that existing supply of energy is sufficient or we have to find better ways to produce more. The global consumption of energy is currently $\sim$15 TW, but only $\sim$0.3 TW of that is from renewable energy. It has been estimated that global demand for energy will rise to around 28 TW by 2050. (See Figure 1.1). "How are we going to produce twice as much energy?" has been the scientific as well as the social challenge we face today.

One way to get there is to harvest incident solar power into electricity. With about $\sim$86,000 terawatts of solar power striking the earth at any given moment, solar energy has enough capacity to meet a major portion of our future energy

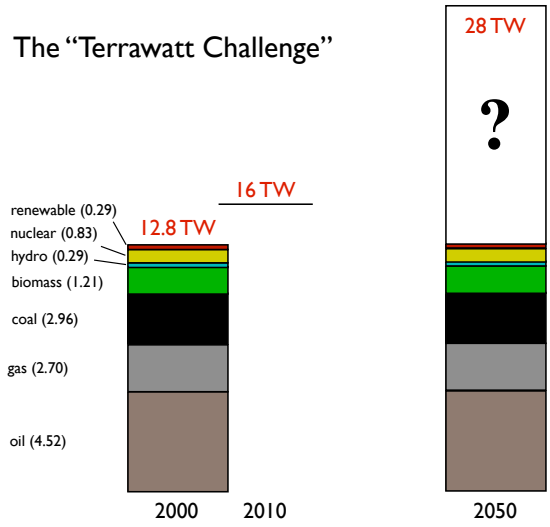

Figure 1.1: Lewis and Nocera, Proceedings of the National Academy of Science, Perspective, 2006.

needs. (1) Harvesting solar energy using solar panel is not a new concept, but the challenge lies in harvesting the energy in a relatively inexpensive manner, as well as developing the required infrastructure at a rate that is sustainable to our rising energy demands. Current estimates on total number of photovoltaic (PV) installed in the world is around 100 GW (Figure 1.2).

1.2 Flexible Thin Film Devices

Organic photovoltaics (OPV) are under consideration as we seek to manufacture the solar cell with similar efficacy as printing a newspaper. We need to produce solar panels at the same rate as we pave the roads. (2, 3) OPV for solar energy harvesting hold tremendous potential as an inexpensive renewable energy source due to their light weight, versatility in design of new absorber material and

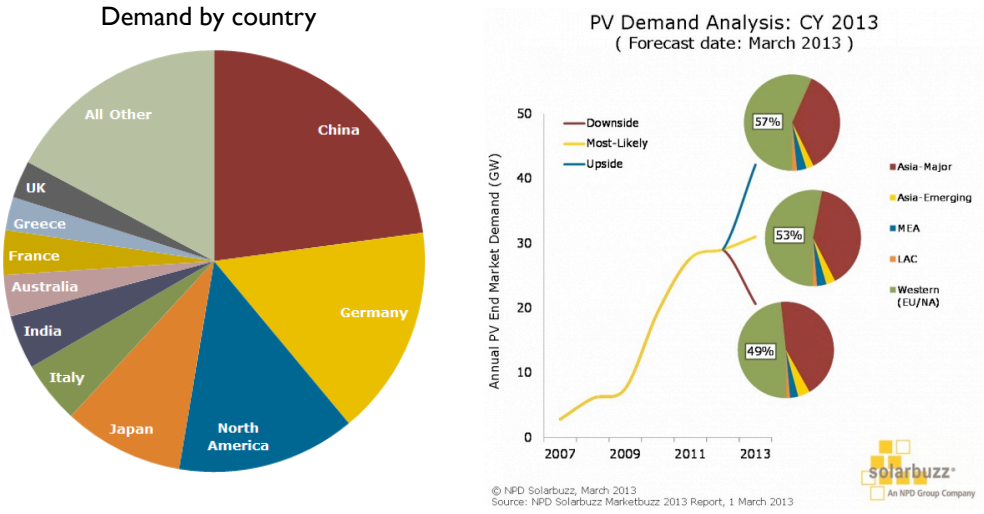

Figure 1.2: Global photovoltaics by the numbers.

ease of processing flexible large area devices. (4, 3, 5, 6) However, to compete effectively with other alternative solar energy, the efficiency of the OPV cells need to be further improved. (7)

How far are we at realizing that goal of printing the solar cell like a newspaper? Not that far, because we have made a tremendous progress in the last few years (Figure 1.4). OPV devices have reached $>10\%$ cell efficiency (η) mostly resulting from development of new photo-active materials. Further research is ongoing to increase overall device performance. In addition, one can highlight the fact that curved televisions on flexible substrates based on the organic light emitting diodes (OLEDs), thin-film cousins of OPV, where carbon-based materials convert electricity into light, have been commercialized (LG Electronics, 2013).

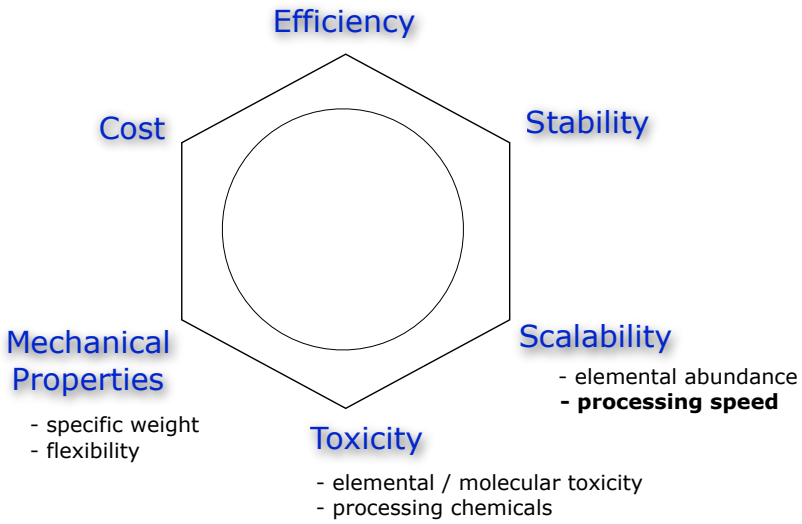

Figure 1.3: Research and development guiding principles for photovoltaics.

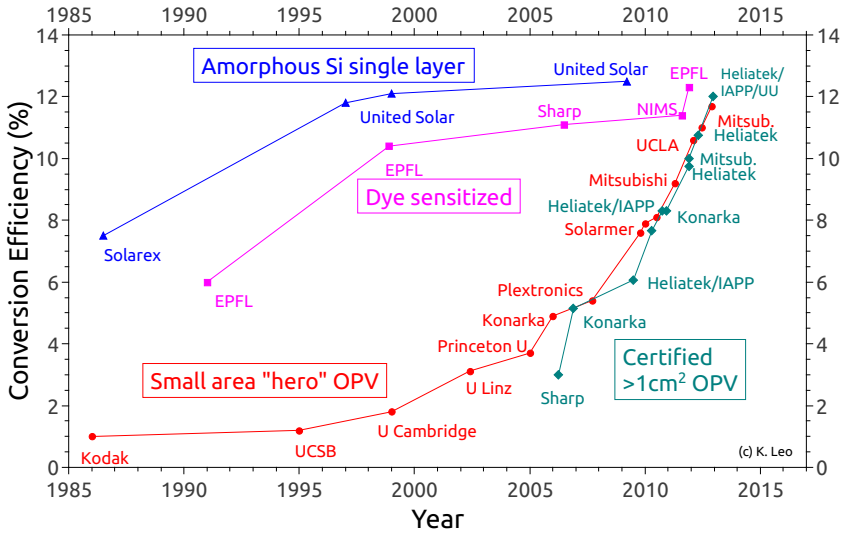

Figure 1.4: OPV efficiency growth chart: Compiled by Karl Leo, IAPP Dresden.

1.3 Earth Abundant Semiconductor Material

So what are the hurdles? Development of transparent oxide semiconductors (TOS) from Earth abundant materials is of great interest for device applications, such as solar cells, light emitting diodes, touch sensitive displays, electronic paper, and transparent thin film transistors so on. Lighting consumes 22% of the electricity used in the United States. Currently, indium tin oxide (ITO) is the most commonly used commercial material for optoelectronic TCO applications including OLEDs for displays, liquid crystal displays (LCDs), solar panels etc. (8, 9, 10) Typically material for these anode applications uses an In:Sn ratio of 10:1. It is known that ITO has interfacial charge transport problems and is chemically unstable in organic device applications. (11)

The research and development of low- or no indium content TCOs that will lead to a lower cost by reducing or eliminating the expense of indium, thereby decreasing optoelectronic device cost. One of the primary areas of research is based on the zinc based electrodes due to the high natural abundance, see Figure 1.5. In the figure, as shown by arrows, we find that zinc is three magnitudes of order more abundant compare to indium. (8, 9) As the demand for display technologies and other application grows, so will the demand for high performance TCOs.

Transparent conducting oxides (TCOs) are an important optoelectronic component of many photovoltaic (PV) technologies. (12) Even the existing silicon based solar cells can benefit from use of TCOs either by increasing the grid spacing and increasing the area of photocurrent collection, or due to improved light trapping in

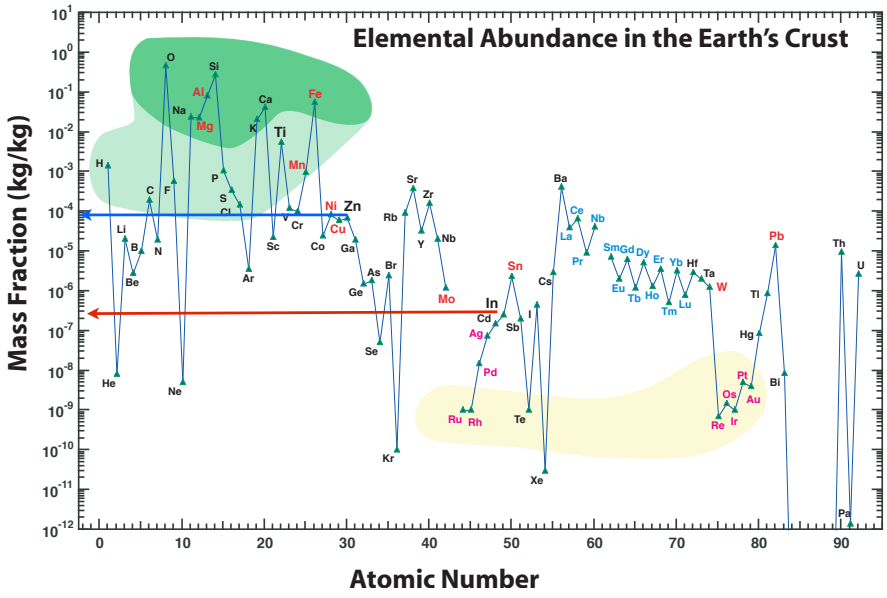

Figure 1.5: The natural abundance of Zinc is higher compare to Indium.

the device due to TCOs acting as an anti-reflection coating. (7) As such there is a need to develop stable, high conductivity TCOs at low cost from earth abundant materials to enable cost effective solar conversion technologies. (8, 9)

The need for inexpensive electrodes might be even greater for organic photovoltaics (OPV), with the goal to harvest renewable energy with inexpensive, lightweight, and cost competitive material. The natural abundance of zinc and the wide bandgap (∼3.3 eV) of its oxide make it an ideal candidate. With recent rapid development of bulk heterojunction organic photovoltaic active materials, devices employing ZnO and ZnO based electrodes provide air stable and cost competitive alternatives to traditional inorganic photovoltaics. The organic LEDs have already been commercialized, thus to follow the footsteps, OPV devices need further improvement in power conversion efficiency and stable materials

resulting in long device lifetimes. Use of low work function metals such as Ca/Al in standard geometry do provide good electrode for electron collection, where transparent electrode harvest holes, but bigger problem using low work function metal electrode is with formation of nonconductive metal oxide due to oxidation resulting in rapid device failure. (13) Hence, using low work function, air stable, conductive metal oxides such as ZnO as an electron collecting electrode and high work function, air stable metals or metal oxides such as silver for harvesting holes, has been on the rise. (7)

Understanding the charge transfer characteristics at the organic interface for both organic light emitting diodes (OLED) and organic photovoltaic (OPV) devices will be pivotal for the development of efficient devices. Moreover, there is a need for development of contact electrodes that are superior compared to indium tin oxide (ITO) with either improved carrier injection/extraction at the interface and/or greater mechanical/chemical stability for improved device performance.

Chapter 2

Tools for Development of Oxide and Organic Semiconductors

The research, development and application of semiconductors in opto-electronic devices involves a comprehensive understanding of semi-conductors, both individually and together in a stack in a device. (8, 9, 10, 7) The diodes in this study, both organic solar cells and organic LEDs are ensemble of oxide semi-conductors, metals, organic polymers and functional materials with varying bulk, surface or interface properties. An accurate characterization of these properties, especially the optical and the electrical properties of thin films and devices with nanoscale morphology has become increasingly important both for fundamental physics as well as industrial applications. (2, 3, 4, 3, 5, 6, 7, 14)

Some electrical measurements of the completed devices are relatively straight forward, but trying to co-relate those measurements to a basic physical property, especially the bulk and surface properties of the standalone layers, and once they

are stacked together in a device are much more challenging. (14) The challenge arises from the mere fact that the various layers in the device undergo changes in the property due to the thermal, the chemical, the mechanical interactions such as stress and strain when a subsequent layer is deposited on to it. Another challenge is due to the inter-dependence of various physical properties, making it very difficult to control one parameter or one variable at a time. For example if the thin film transitions from the amorphous phase to the crystalline phase, we find drastic changes in electrical and mechanical properties, and those changes in the electrical and the mechanical properties can further impact other physical properties such as optical properties. Thus, controlling and retaining the property of the layer, namely the variable in the experiment, during the deposition and during the fabrication of subsequent layers, and during post analysis of the device performance makes it both interesting to study as well as a challenging task.

In this chapter we introduce the tools that are used for depositing the various layers of solar cells and LEDs, followed by a study of various physical properties of the individual layers and the completed device. This chapter will thus provide some prospective on why certain methods are implemented and how we collect and analyze those data in order to relate the physical properties of materials at a basic science level and understand their functionality on completed devices. In the process of describing various tools and techniques I have used some of the figures, equations and graphs from various works we published previously.

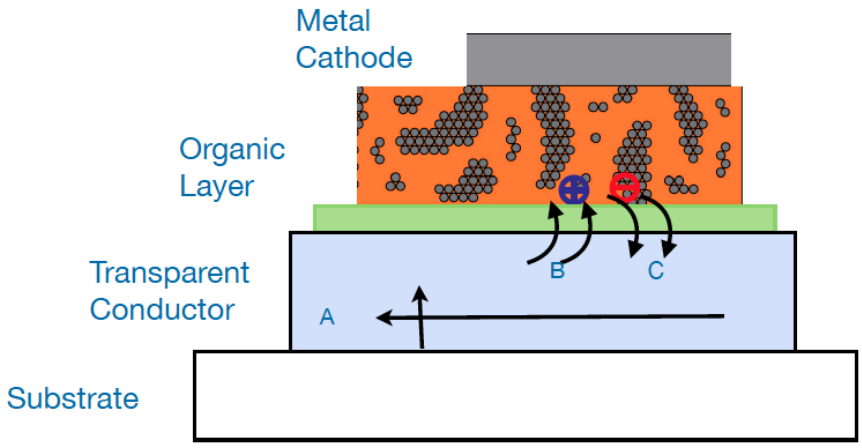

Figure 2.1: A simplified diagram of OPV device.

2.1 Simplified Architecture of OPV and OLEDs

Organic solar cells and organic LEDs are thin film devices consisting of various layers, whose thickness are in nanometer scale. A simplified diagram of the device is shown in Figure 2.1. In the device, oxide semiconductors and metals act as electrodes for charge transport, the organic polymer layer functions as light harvesting in OPV or light creation in OLED. A few other layers which we call functional layers are added for energy alignment and controlling the interfaces for efficient charge collection or injection. (15)

Most of our study focuses on understanding the bulk and surface properties of an oxide electrode towards developing high efficiency opto-electronics devices. We will primarily focus our discussions on the thin film characterization involving the transparent electrode. To further simplify the scope of this work, transparent

electrodes are divided into two sub groups depending upon their role in a device. The first sets are called the contact electrodes, usually 200 to 500 nm thick. These are optimized for transparency as well as transporting the charge to the external circuit. Here, the electrical conductivity in parallel direction, and optical property in perpendicular direction to the thin film is important, as shown by arrows marking A in Figure 2.1.

The other group are classified as selective contacts or interface modifier, usually 5 to 50 nm thick, optimized for providing charge selectivity (electrical property in perpendicular direction) and providing asymmetry/ built in field inside the solar for charge separation and collection or better charge injection in LED device. These selective contacts help collect or inject charges and transport in organic/oxide interface, or in perpendicular direction to the thin film as indicated by arrows labeled B and C in Figure 2.1. In particular, the work presented in this dissertation explores the modulations of various surface, interface and bulk opto-electronic properties of ZnO based semiconductor when used both as the contact electrode and as a selective contact to understand the role of these properties on on charge transport, charge selectivity and device performance. Accordingly, the physical properties and the characterization of ZnO based semi-conductor and devices employing them will be discussed.

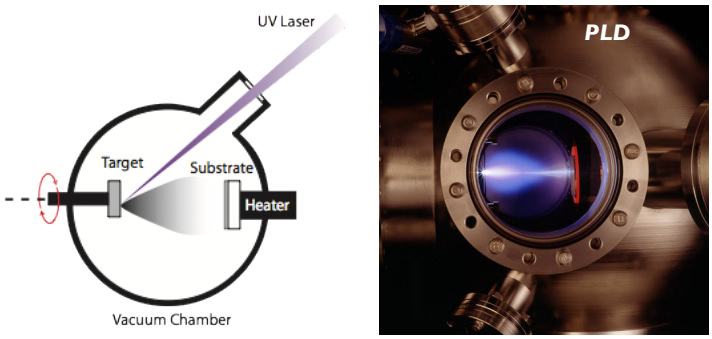

Figure 2.2: Pulse Laser Deposition

2.2 Thin Film Deposition

Physical properties of thin film are very dependent upon the tools or techniques used. During the deposition, various variables that can be varied systematically. In this section we will briefly discuss the methods employed to deposit the organic and metal oxide semiconductor films and highlight the merits and demerits of the technique used. (9, 8)

2.2.1 Pulse Laser Deposition (PLD)

The pulse laser deposition technique employs a high power, pulsed laser beam inside a vacuum chamber to ablate the material that is to be deposited, see Figure 2.2. Our system has λ = 248 nm KBr laser as the source and high purity stoichiometric oxide target (ZnO), or oxide alloys ($ZnSnO_3$,In_2O_3 :ZnO) as the material to be deposited. The ablated materials form a plasma plume with high energetic ions, and get deposited onto a heated substrate. (16) Thin film growth dynamics can be altered by changing variables such as rate, energy

or wavelength of laser pulse, the distance from the substrate and the target, the substrate type, the temperature of substrate, ion assist, and the partial pressure of the deposition chamber by introducing gas of ones choice such as O_2, N_2, H_2O. PLD has very good control over various aspects of film growth. It is known to retain the composition of target material and provide more flexibility in tuning the oxidation state of the film. Plus, it yield thin films with better adhesive strength and homogeneity. Thus, this is a preferred method of growing high quality thin films used in material exploration and optimization by various researcher. (8, 9)

Some of the recent work we have done in our group to optimize the p-type oxides such as CoNiO (17) or NiOx (18), to understand and improve hole collection in the electrodes for improving the performance of OPV devices, were done via PLD technique. For a given material, film thickness is primarily controlled by varying the partial pressure and the number of pulses. Under a nominal condition, 20 pulses of laser yield 1 nm of ZnO film over 1 sq inch area. Due to the firm control over the thickness of film, we have created thin film stacks, which we call digital alloying, such as one shown in Figure 2.3. Study on varying the electrical property of $ZnSnO_3$ material for understanding the charge injection in OLED devices were done using the PLD system and will be discussed in later chapters.

2.2.2 Plasma Sputtering

Various metal oxides in this study are deposited via the sputtering process, which is the industry standard for deposition of transparent oxides. The sputtering method involves the creation of a gas plasma with inert Argon as processing gas

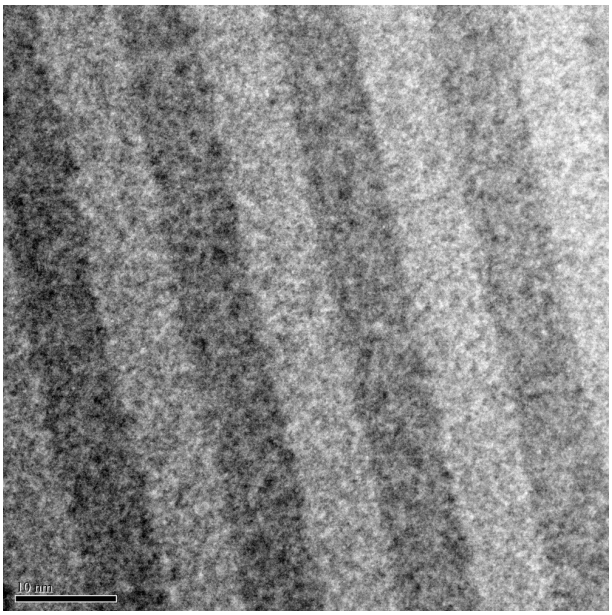

Figure 2.3: Cross-sectional TEM image of GZO and IZO thin film deposited using PLD with 6 nm periodicity.

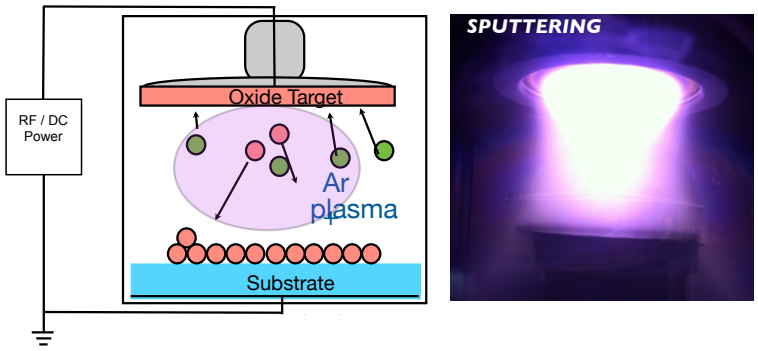

Figure 2.4: A systematic diagram of sputtering technique, and plasma glow during oxide deposition.

and by applying RF or DC voltage between a cathode and anode. The cathode consist of source material (Zn metal, ZnO or other mixed composition oxide) and the anode is the substrate (glass or TCO coated glass) as shown in the Figure 2.4. Source material is subjected to intense bombardment by ions. By momentum transfer, particles are ejected from the surface of the cathode and they diffuse away from it depositing a thin film onto a substrate. (16, 8, 9) Some of the critical parameters that can be controlled for good film growth using sputtering technique are: deposition time which controls the thickness, the substrate temperature (T_s), the RF or DC power applied to the target, the distance between substrate to target D_{ts}, the partial pressure of gas in the chamber such as O_2, Ar, N_2, H_2O. Film growth dynamics are controlled by three things: the manipulation of mean free path of the ions, the energy and number of ions that travel to the substrate, the energy available for ions to move around in the surface of film during growth provided by lattice of substrate, and the thermal energy of the substrate. The sputtering process provides a very good control over thickness and composition. Since the film growth occurs in a vacuum chamber, it is a highly reproducible technique with high film quality compare to some CVD techniques. Sputtering techniques has slightly worse control and quality compare to PLD, but it yields thin films with good enough electrical and optical property for various device application. (16)

Moreover, sputtering allows large scale production, hence it is heavily used by the industry for coating application. Incorporation of other metals such as Al, Ga or B onto a ZnO lattice is done via use of alloy targets. Some of the studies on TCOs such as GZO, IZO and IZTO involving optimization of sputtering parameters to obtain thin films with desired physical property for specific experiments are

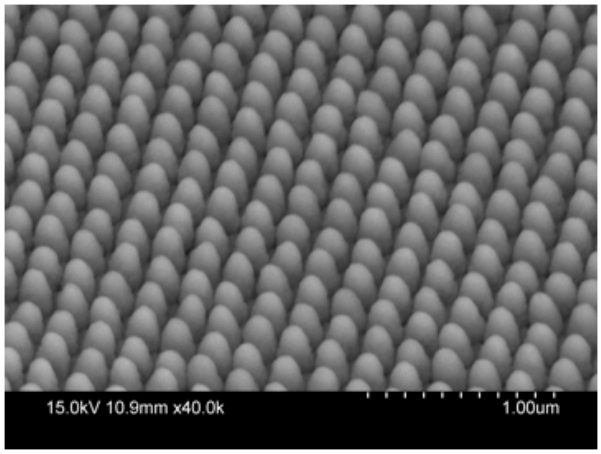

Figure 2.5: Ag nano structure array.

discussed in Chapter 3, 4 and 7 respectively. Similarly, the studies where the electrical property of ZnO, both mobility (μ) and carrier concentration (N) are varied using the sputtering parameters and their impact on efficient electron transport in OPV devices will also be provided in Chapter 6.

I have stayed away from discussion of p-type oxides to minimize the length of this dissertation. We have employed the sputtering method to develop and understand the role of p-type oxides such as NiOx (19) and Zn-Ni-Co-O (20) for improving OPV devices. Also, we have used sputtering for the development of nano-structured arrays, see Figure 2.5, for creating nanostructured silver, ITO or IZO electrode structures over large areas that are capable of producing high aspect ratio nanoscale structures with feature sizes below 100 nm and a large range of dimensional tunability. (21)

2.2.3 Atomic Layer Deposition

Atomic layer deposition involves sequential oxidation or decomposition of compounds on to a substrate, one layer at a time. The desired metals or ions travel to deposition surface as a compound, where decomposition occurs. The decomposition can be assisted by either plasma or thermal energy from the heated substrate. The deposition is done via one atomic layer at a time with each sequence in the deposition cycle as self-limiting. Thus the ALD technique has super accurate control over the film thickness. The process requires knowledge of chemistry for controlling the various aspects of film formation including defects, foreign contaminants, doping desired atoms and if done properly yields highly stochiometric films. This process is scaleable, and film morphology is dependent upon the nature of chemical reaction.

In one of the studies using ALD (22) we studied the incorporation of Al in ZnO by varying the stoichiometry, thus obtaining high quality TCO for use in OPV devices. The films Al_2O_3 :ZnO with 1:20 periodicity are found to exhibit the highest values of electrical conductivity (1.2×10^3 S/cm; more than six times higher than for neat ZnO films), while retaining a high optical transmission ($\geqslant$80 $\%$ in the visible region) and a low work function (4.0 eV). The studies of the electrical property of ZnO, both μ and N are varied for evaluation in OPV device, some subsection of ZnO films are deposited using atomic layer deposition, and details will be discussed in Chapter 6 as well. The rational behind choosing this method for depositing thin films is to provide an alternative deposition tool to validate the observations seen via sputtering and other deposition technique and vice versa. In

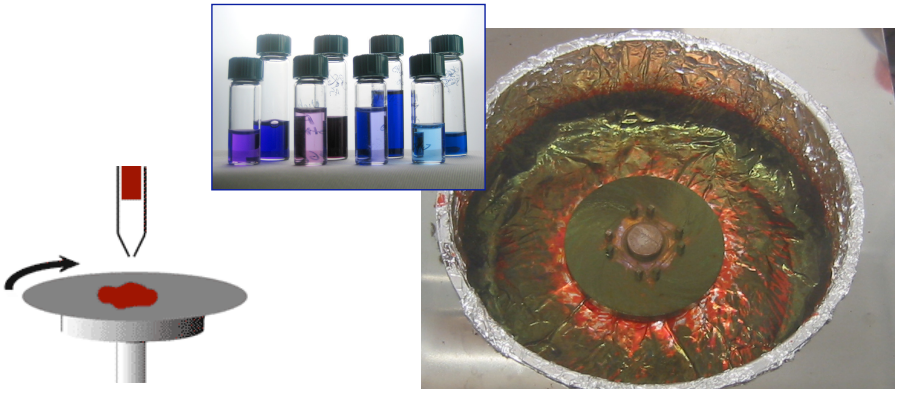

Figure 2.6: Spin coater for solution spin cast

this way, the trends observed in certain experiments would be deposition system independent and the co-relation can be extracted between the physical property of the film and the device made across the different film fabrication techniques.

2.2.4 Solution Precursor Spin Cast

In this study, solution processing is used for depositing both organic and oxide semi-conductors. Solution processing can be done via various techniques such as drop casting, spin-coating, doctor-blading, inkjet printing. We have primarily used spin-coating techniques for depositing organic layers, where excess amount of solution containing the semi-conducting material of interest, is placed on the substrate, which is then rotated in high speed in order to spread the fluid by centrifugal force, see Figure 2.6.

The uniform film obtained goes through further processing such as annealing at elevated temperature to either oxidize or remove the excess solvent. This method

is very fast, and easy to use with inexpensive deposition tools but the details of the highly-folded nanostructures in the film are largely dependent on the kinetics of phase-segregation and self-aggregation, solvent evaporation, and substrate influence. Atmospheric pressure solution routes provide an attractive alternative to conventional high-vacuum PVD techniques due to their ease of fabrication, scalability, and potential to lower device manufacturing costs. A lot of research has been dedicated to develop solution routes to TCO materials that are comparable to those of PVD materials. (16, 8, 9) In Chapter 6, we will discuss various OPV devices fabricated with organic films deposited via spin coating directly onto either on the TCO films or on TCO films covered with a ZnO electron transport layer deposited from a diethyl zinc solution precursor. The ZnO oxide films deposited via solution route provides alternative method for comparing the films deposited via techniques mentioned earlier.

We have done various other studies, not included in this dissertation, to understand the charge transfer properties of solution processed ZnO oxides. In one of the studies, we have evaluated solar cells with Cu_2O /ZnO junctions, with ZnO layer fabricated via various solution processing routes such as use of Diethylzinc (DEZ) or Zinc acetate (ZnAc) precursor, and electrodeposition. (23) Similarly, we have used solution processing method for surface modification of oxide electrodes for improving energy alignment and performance of OPV devices. Both NiOx (24, 25) and MoOx (26) thin films studies provided an avenue for understanding and improving hole collection in the electrodes for improving the performance of OPV devices.

2.2.5 Evaporation

In all our devices, we have used metal or metal oxide top electrode deposited via evaporation. Semi-conductor or metals of interests are evaporated in a vacuum, where evaporated particle travel directly to the substrate and condense back to a solid state thin layer. This method is suitable for large scale production. The thickness of the film is monitored using quartz crystal microbalance which measures the changes in mass per unit area as the change in frequency of a quartz crystal resonator. (16, 8, 9) Most of the OPV devices discussed in Chapter 6 consist of metal electrode that are deposited by thermal deposition of 100 nm Ag electrodes with an area of 11 mm^2 via a shadow mask at a base pressure of $\sim 3\times10^{-8}$ Torr.

Various OPV devices use low work function metals such as Ca/Al, which are primarily deposited via evaporation. In this standard geometry, Ca/Al with low workfunction provide energy alignment suitable for electron collection. The bigger problem of using low work-function metal electrode is with formation of non-conductive metal oxide due to oxidation resulting in poor charge collection and thus the rapid device failure.

Since these type of devices need to fabricated and evaluated in inert atmosphere, most of the work in this dissertation involves use of low work-function, air stable, conductive metal oxides such as ZnO as a electron collecting electrode and high work-function, air stable metals such as silver for harvesting holes. Note: Ag is self-limiting, and even if silver oxidizes, the resultant oxide is still semiconducting and helps improve the device performance. (13) Although oxidation of thin film

on most cases is undesirable, conversely, in one of the studies we have utilized the rate of oxidation of 100 nm evaporated Ca, to monitor the water ingress and to evaluate the small atmosphere chamber that allows optical and electrical device characterization of OPV and OLED devices outside a glovebox. (27)

2.3 Thin Film Characterization

The range of thin films we have studied in this work ranges from mono-layer which are sub < 1 nm to 500 nm. Changes in one physical property can have drastic influence on other physical properties and vice-versa. In this section we will discuss some direct and indirect measurement of physical properties pertinent for optoelectronic thin film devices.

2.3.1 Structural

As discussed earlier, we have thin films with varying structural properties. Some of the techniques we use to directly measure bulk structural properties such as microstructure, crystallinity, grain size of the crystallites are done via X-ray diffraction (XRD), or Transmission Electron Microscopy (TEM), while surface properties such as surface roughness are evaluated by Scanning Electron Microscopy (SEM) and Atomic Force Microscopy (AFM). Thickness measurement is done directly using Dektek/AFM, or indirectly via optical method such as variable angle spectroscopic ellipsometry, cross-sectional SEM and cross-sectional TEM. Mostly, we have used XRD to evaluate grain size, crystallographic orientation,

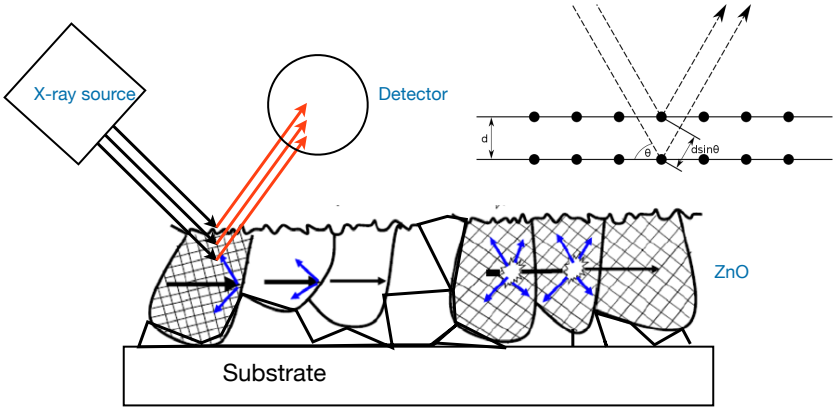

Figure 2.7: X-ray diffraction to find the size and orientation of crystallite. Better crystallographic orientation help reduce grain boundary scattering mechanism. Dopants and other phase separated impurities can also be detected, which may hinder the charge transport

strain, phases of oxide thin films. In Chapter 3 we will discuss in detail about the structural improvement of thin film, mainly the crystallographic orientation of gallium doped zinc oxide (GZO) thin films. Similarly, extensive characterization of structural property of other oxide semiconductors such as ZnO, IZO and IZTO thin films will be discussed in Chapters 4-7 as well. Brief discussion on XRD technique to measure ZnO film is as follows.

X-ray Diffraction

X-ray diffraction (XRD) is used to identify the specimen's crystalline phases and various other structural properties such as strain, epitaxy and the size and orientation of the crystallites. The X-ray diffraction system we have are a Bruker Discovery 08 with a large area detector, and a Rigaku Ultima IV X-ray diffractometer both using Cu-Kα radiation with λ = 1.54 Å. As seen in Figure 2.7, two

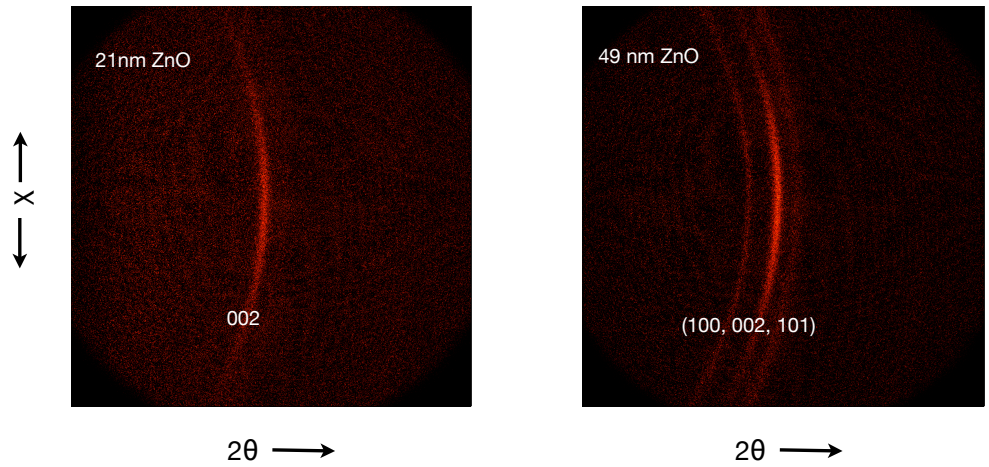

Figure 2.8: X-ray diffraction (2D raw image) of 21 nm and 49 nm ZnO film deposited via ALD.

beams with identical wavelength and phase approach a crystalline solid and are scattered off two different layers within it. The lower beam traverses an extra length of 2dsinθ, where, d is the spacing between atomic planes in the crystalline phase, and θ is the angle of incidence. Constructive interference occurs when this length is equal to an integer multiple of the wavelength of the radiation. Very strong intensities are obtained in the diffraction pattern when scattering waves satisfy the Bragg's law, see equation 2.3.1. By measuring the intensity of the diffracted X rays as a function of the diffraction angle 2θ and the specimen's orientation, one can determine the d-spacing.

Bragg's Law

$$n\lambda = 2dsin\theta \tag{2.3.1}$$

Most of the thin film TCOs we investigate are poly-crystalline with multiple phases present in the film. An example measurement on 21 nm and 49 nm ZnO

film deposited via ALD is shown in Figure 2.8. The 21 nm film has only (002) plane of wurtzite ZnO with the c-axis oriented perpendicular to the plane of the substrate, while (100, 002, 101) planes are seen for 49 nm film. Measurement can also be done on amorphous materials to determine atomic arrangements. Moreover, X-ray diffraction can identify the phase separated impurities which may hinder the charge transport. The average grain size is estimated using the Scherrer equation,

$$D = \frac{0.9\lambda}{\beta cos\theta} \tag{2.3.2}$$

where D is the average crystallite diameter, λ is the wavelength of Cu Kα radiation, β is FWHM of the (002) peak, in radians, and θ is equal to the Bragg angle. This formula is applied to XRD data taken for each sample and the calculations yield average grain size in a direction that is orthogonal to the plane of the film.

Structural information, especially the surface topography of organic or oxide semiconductor was obtained using Atomic force microscopy (AFM). In AFM, interatomic forces between the atoms on the surface and those on the tip cause the deflection of a micro-fabricated cantilever. By measuring the deflection, one can measure the force, and thus the distance between the surface and the tip. AFM is a versatile tool with varying modes providing various physical properties: Tapping mode (height topography, grains), Contact mode (height topography, lateral frictional force), Conductive mode (surface electronic heterogeneity), Kelvin probe mode (electrostatic distribution), Magnetic mode (magnetic domains). (8, 9) Some details of the measurement, such as conductive mode AFM will be discussed in chapter pertaining to the study of TCO surfaces. Further structural information can

be obtained via some other techniques such as angle-dependent near-edge X-ray absorption fine structure (NEXAFS) spectroscopy and polarization modulation infrared reflection absorption spectroscopy (PM-IRRAS). We have employed some of these techniques in conjunction with density functional theory (DFT) to determine the molecular orientations of a model phenylphosphonic acid on TCOs. (28) Here, the dipolar phosphonic acids form a self-assembled monolayer (SAMs) at the interface between organic semiconductors and transparent conductive oxides modifying interface properties such as work function and wettability at the critical interface. (24) We will briefly discuss the role of dipoles and their impact on charge transport behavior in Chapter 6.

2.3.2 Electrical

Conductivity - Ohm's law

$$J = \sigma E \tag{2.3.3}$$

where J is the current density and E is the electric field. Conductivity (σ) is related to μ and N by following formula.

$$\sigma = N \times q \times \mu = \frac{1}{R_s \times t} \tag{2.3.4}$$

For a thin film, conductivity can also be calculated using sheet resistance (R_s) of the thin film measured by four point probe, and thickness (t) of the film by various other techniques. Measurement of fundamental properties of materials such as the type and the concentration of electric charge carriers are important for a broad range of semiconducting devices. Various transparent electrodes in our study have

utilized the hall measurement system as we focus on developing the novel oxide materials with the goal of achieving simultaneous high optical transparency and high electrical conductivity. Hall measurement done in room temperature provides μ, N, and carrier type of a semi-conductor. Measurement of the μ_H using Hall setup is explained in Appendix A. The temperature dependent hall measurement can provide further details such as identification of the dominant mechanism for electron scattering such as the ionized impurities scattering and the grain boundary scattering.

Although the hall measurement is versatile, it is very hard measure low-mobility materials such as some intrinsic oxides or organic semiconductors. Similarly, the hall measurement is not reliable for magnetic materials such as NiOx, NiCoOx, that we employ in the OPV devices as HTL layers due to the small magnetic field (0.3 T) available in our commercially available hall measurement system. In those stances, we use alternative method via Seebeck measurement to measure the low-mobility and the magnetic material.

2.3.3 Optical

Transmission and reflection measurement

Optical properties of thin film, transmission (T) and reflection (R) are measured over the range of 250 nm to 2000 nm or higher using a fiber optical measurements. Light of varying wavelength from the source: Deuterium arc lamp (UV), Tungsten lamp (visible) and quartz tungsten halogen lamp (IR) are focussed into an optical

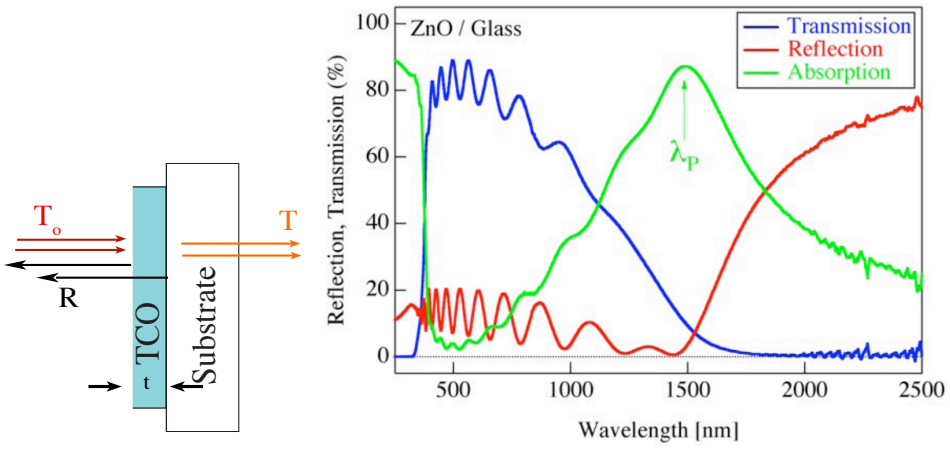

Figure 2.9: In our setup, the transmission and the reflection measurements are done with the incidence angle at zero degree.

fiber, then to a small spot in film and collected in another fiber that feeds onto Ocean Optics CCD array spectrometers. Measuring transmission and reflection measurement are critical for either optimizing the transparency of the oxide, or improving the light management in in device applications. Also it allows us to calculate the plasma wavelength and optical gap. An example T, R measurement for ZnO thin film is shown in Figure 2.9. The film has high transparency in visible range, the range of interest for solar cells and LEDs. A better measure of transparency is absorption (A), which can be estimated from the transmission and reflection measurement.

$$A(\lambda) = 1 - T(\lambda) - R(\lambda) \tag{2.3.5}$$

$$T = \frac{(1-R)^2 e^{-\alpha t}}{1 - R^2 e^{-2\alpha t}} \tag{2.3.6}$$

Here, t is the thickness, and the absorption coefficient (α) is defined as $\alpha = \frac{4\pi k}{\lambda}$, where k is the imaginary part of the complex refractive index and λ is the wave-

length. If αt is large or R is small, the equation simplifies to

$$\alpha = \frac{-ln(\frac{T}{(1-R)^2})}{t} \tag{2.3.7}$$

Note: in a transparent thin film, first and second reflections are very hard to separate experimentally, thus the measured r is 2R.

Optical Gap Calculations

The photons with energy higher than the bandgap of the semiconductor are absorbed. As seen in Figure 2.9 where transmission goes to zero for $\lambda < 380$ nm due to the onset of optically induced electronic transitions. For a direct bandgap material (or indirect bandgap material at thin film limit), the absorbance measurement above can provide optical gap ($E_{optical}$) using the Tauc equation. (29) The relationship between the $E_{optical}$ and α is

$$\alpha = \frac{e^2(2m_r)^{\frac{3}{2}}}{Nch^2m_e^*}(h\nu - E_{optical})^{\frac{1}{2}} \tag{2.3.8}$$

where m_r is the reduced carrier mass, h is Plank's constant, and ν is the photon frequency. (30) The x-intercept obtained by plotting α^2 vs hν, and fitting the linear portion to a line is the optical bandgap.

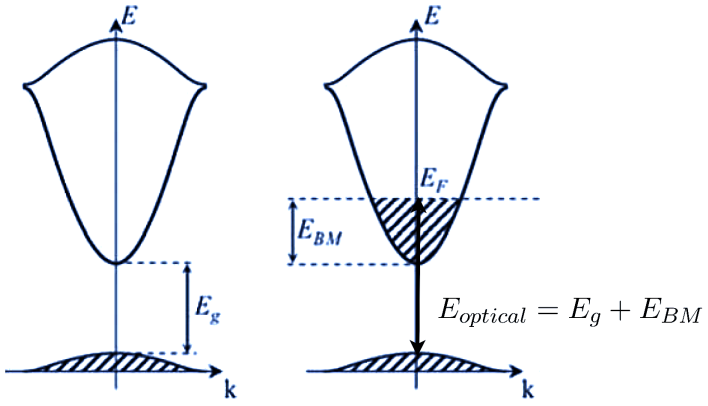

Figure 2.10: Undoped stoichiometric state (left) and degenerately doped with displaced Fermi level, due to increasing N called Burstein-Moss shift (right).

Plasma Frequency and Burstein-Moss Shift

In a semiconductor, the free electrons in conduction band can coherently oscillate and resonate at a frequency (ω_{plasma}) as a whole in response to an incident wave. (30, 31)

$$\omega_{plasma}^2 = \frac{Ne^2}{m_e^* \epsilon_0 \epsilon_\infty} \tag{2.3.9}$$

where, N is carrier concentration, e is the electron charge, m^* is effective mass, ϵ_0 is permittivity of free space, and ϵ_∞ is high frequency permittivity. Now, plugging in $\lambda = \frac{2\pi c}{\omega}$, we get the relation,

$$\lambda_p^2 = \frac{4\pi^2 c^2 m_e^* \epsilon_0 \epsilon_\infty}{Ne^2} \tag{2.3.10}$$

where, c is the speed of light. This shows that $\lambda_p \propto \mathrm{N}^{-1/2}$. Thus by measuring optical property λ_p, shown in Figure 2.9, we can also estimate the carrier concentration of the thin film.

Similarly, when conduction band is filled with carriers, and the fermi level is above the conduction band edge, during optical transition the electrons have to jump from valance band to the top of the conduction band, rather than the bottom of the conduction band. (30) This effective increase in bandgap due to carriers is the Burstein-Moss shift E_{BM} shown in Figure 2.10.

$$E_{optical} = E_g + E_{BM} \tag{2.3.11}$$

where, E_g is the fundamental bandgap of the material and E_{BM} is defined as,

$$\Delta E_{BM} = \frac{(\hbar)^2}{2m^*}(3\pi^2 N)^{\frac{2}{3}} \tag{2.3.12}$$

where $\hbar$ is the reduced Planks constant $\frac{h}{2\pi}$and m^* is the effective electron mass.

2.4 ZnO Semiconductor Fundamentals

Zinc oxide (ZnO) discussed in this study are mostly n-type semiconductor with an ideal structure of hexagonal wurtzite. Zinc oxide and doped n-type zinc oxides have recently been studied as transparent conductive oxide (TCO) materials for organic electronic devices designed to replace indium tin oxide (ITO) contacts. (8, 9) The natural abundance of zinc and the wide bandgap ($\sim$3.3 eV) (32) of its oxide make it an ideal candidate for applications requiring a transparent conductive oxide. Zinc oxide as a typical compound semiconductor can be made conductive both by intrinsic dopants (defects) as well as by extrinsic ones (foreign atoms). (33, 34, 35) Perfect stoichiometric ZnO at temperature where k_bT is less than the

bandgap energy, is insulating due to the lack of charge carriers. Highly resistive intrinsic ZnO single crystals have been shown with very low carrier concentration in the order of 10^{13} /cm^3. ZnO thin films in our study are produced in processes that permit film formation far away from thermodynamic equilibrium, thus these films contain defects resulting from a displacement and/or removal of lattice atoms. These intrinsic defects have been linked to an increase in conductivity in the undoped oxide. (36, 37, 9). The lattice defects oxygen vacancies or zinc atoms on interstitial lattice sites can create these intrinsic donors, with the later established recently as the dominant donor. (38, 39, 9)

In both sputtering and PLD, the oxygen partial pressure and deposition rates can be carefully adjusted so as to get ZnO thin films with varying zinc to oxygen ratios. This tuning of the stoichiometry is also possible for various other metal oxides as well. Thus, depending upon the deposition condition, films can be either zinc rich or oxygen rich, which has significant impact on optical and electrical properties. Zinc metal rich films have poor transparency but relatively high conductivity and the oxygen vacancy is more likely the dominant defect present. While oxygen rich ZnO films have good transparency but they have poor electrical properties due to compensation of carrier with both zinc vacancies or oxygen interstitials present in the materials. Quantitate measurements of zinc to oxygen ratio in materials are difficult. However, various techniques such as X-ray photoelectron spectroscopy (XPS), Photoluminescence (PL), have been used to estimate the relative composition and/or track changes in stoichiometry with deposition conditions. The measurement of the electrical properties and optical properties in conjunction with deposition conditions do provide us the perhaps the most useful estimates on stoi-

chiometry and defects present in the thin film. The use of substitutional dopants can further increases the overall conductivity of zinc oxides by significantly increasing carrier density, with gallium-doped ZnO having the highest conductivity over other group III ZnO dopants. Specifically, it is known that group III dopants can be substituted into the zinc lattice sites, giving up an additional electron which causes the Fermi level to move towards the conduction band of zinc oxide, as assumed by the classic extrinsic doping mechanism: (9)

$$\mathrm{M_2O_3} \longleftrightarrow 2M_{Zn} + 2e^- + 2O_O + \frac{1}{2}\mathrm{O_2} \tag{2.4.1}$$

The highest reported conductivities ($\sim$ 12,000 S/cm) for Group III doped ZnO are for gallium-doped ZnO (GZO). (9) The higher conductivity of GZO films relative to other Group-III doped zinc oxides has been partially attributed to the atomic and ionic radii matching of Ga and Ga^{3+} to that of Zn and Zn^{2+} (when compared to the radii of Al and Al3+) and should result in minimal distortion of the ZnO lattice. (40) Furthermore, the higher electronegativity of Ga over Al suggests that GZO should have a higher stability to oxidation over aluminum-doped zinc oxide (AZO) counterparts, (41) which is confirmed by the improved stability of GZO versus AZO when exposed to moisture. (42, 43) The studies of oxide materials presented throughout this dissertation implicitly use film fabrication techniques discussed in the introduction to controllably and systematically tune the defect in the films with the goal of manipulating the bulk and near surface properties of the oxide films. For example the study presented in Chapter 6 implicitly involves modulating the defects and thus the electrical property N and μ in the ZnO films, with the goal of understanding the impact of properties on the charge recombination and the charge

selectivity in OPV devices. While the work in Chapter 3, bulk physical properties of GZO are optimized via modulation of defects and incorporation of Ga in ZnO lattice by manipulating the deposition conditions. We discuss in these studies the mechanism to minimize the negative ions during film growth, which can form electron killing defects. Other aspects including more in-depth discussions on role of defects at the surface of GZO thin film due to various foreign contaminants and surface treatment and their impact on surface properties of TCOs are discussed in Chapter 4.

Various other oxide semiconductors explored in this dissertation utilize the knowledge of defects and associated structure/property engineering in order to obtain thin film with the desired physical property. Even in amorphous TCOs, which will be discussed in details later : IZO in Chapter 4, ZTO in Chapter 5 and IZTO in Chapter 7, despite lack of long range ordering, the carrier generation and various other physical properties are still dictated by the same basic materials physics and chemistry although traditional definition of defects and dopants are not as clearly applicable. These amorphous TCOs also follow the same general trend where metal rich films exhibit poor transparency, while varying the oxygen partial pressure during deposition result in many orders of magnitude variation in the electrical conductivity (σ). Chapters 4, 6 and 7 will provide details on how device performances are impacted by surface passivation, surface heterogeneity, surface conductivity and various physical properties of TCOs that originate from these microscopic variations.

2.5 Organic Photovoltaic Device Physics

As shown in Figure 2.11, solar cell consist of various layers and each with different functions. In brief, an incoming light is absorbed in polymer (P3HT) and it creates an exciton. Unlike various inorganic absorber layer, in many inorganic solids the excitons are very tightly bound and do not split spontaneously. The electrostatic field or the built in field available from the difference in the work functions of the electrodes is not sufficient to split an exciton. Thus, the excitons must diffuse to donor-acceptor interface (P3HT:PCBM), where due to the electric field at the heterojunction, exciton dissociation can efficiently occur. The length the excitons travel before they recombine is called the exciton diffusion length and is on the order of only 10 nm in the P3HT:PCBM system. (10) Thus, only the 10 nm material closest to an acceptor-donor interface contribute to the photocurrent. A lot of research has been focused on understanding and engineering the morphology of the bulk-heterojunction (BHJ). The thickness of BHJ is in hundreds of nm to minimize transport losses and still maintain a good optical path. (2, 44)

Once the charge separation occurs at the junction, the electric field provided by the contacts drive the free electrons and holes towards respective electrodes.. Figure 2.12 shows the representative energy level diagram for TCO/ZnO/P3HT:PCBM/HTL/Ag device, before fermi level alignment. The energy level requirements in OPV are constantly changing due to the development of high efficiency new photo-active materials. This has resulted in the need for optimized contact electrodes with good energy level alignment, so as to obtain maximum performance out of the solar cell. Various work done in this dissertation are

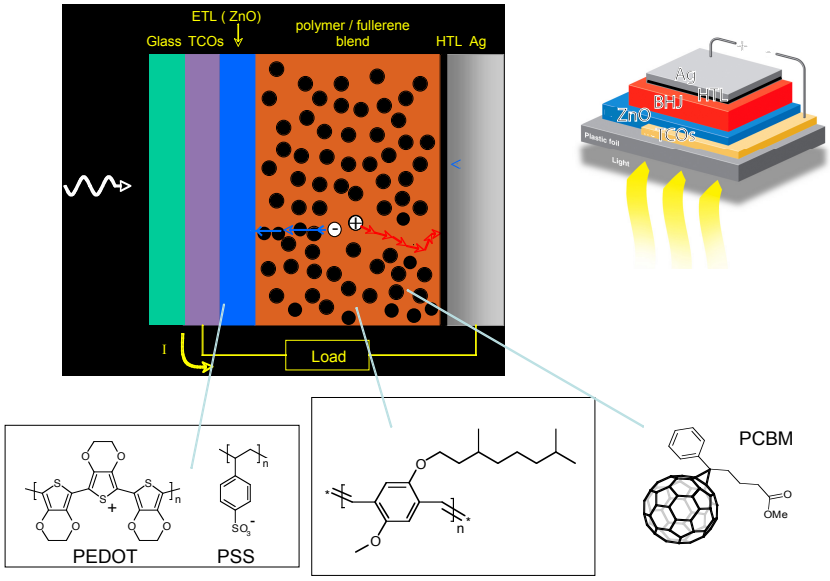

Figure 2.11: Systematic of OPV device with an inverted architecture. Here, holes are collected at the metal electrode, while electrons are collected at the transparent electrode. (TCO/ZnO/P3HT:PCBM/HTL/Ag)

concentrated on engineering various transparent contacts for efficient transport and collection/injection of free charges. More details of the working principle of OPV are nicely described in the book " The physics of solar cells, by Jenny Nelson" (10) and various other papers. (6, 45, 5, 3)

2.5.1 Current Density and Voltage Measurement

The current density-voltage (J-V) characteristics of the devices both in the dark and under standard solar simulation (100 mW/cm^2 AM 1.5G, corrected for spectral mismatch) provide us an operational measure of the solar cell. A typical J-V curve for a solar cell device is shown in Figure 2.13. From the J-V data obtained from a solar cell, one can determine the power-conversion efficiency of converting light

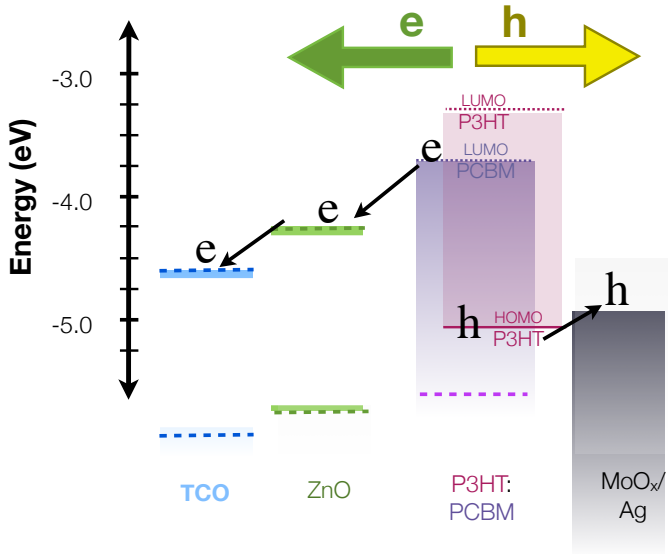

Figure 2.12: Energy level diagram for TCO/ZnO/P3HT:PCBM/HTL/Ag device, before fermi level alignment.

into electricity. The efficiency is given by $\eta = \frac{P_{MaxOut}}{P_{In}}$, where P_{In} is the incident power, and P_{MaxOut} is the maximum output power of the cell. On the light curve, the point where voltage is zero, is the short circuit current (J_{sc}), and the point where current density if zero is called the open circuit voltage (V_{oc}). In the figure, the diode ideality factor, or the Fill Factor (FF) is the ratio of maximum power output to the product of V_{oc} andJ_{sc}. For an ideal diode with sharp turn on in JV, the FF is 100%. Overall, efficiency (η) of the device is maximized by improving these three parameters: FF, V_{oc} andJ_{sc}. (10)

$$\eta = \frac{P_{MaxOut}}{P_{In}} = \frac{V_{oc} \times J_{sc} \times FF}{P_{In}} \tag{2.5.1}$$

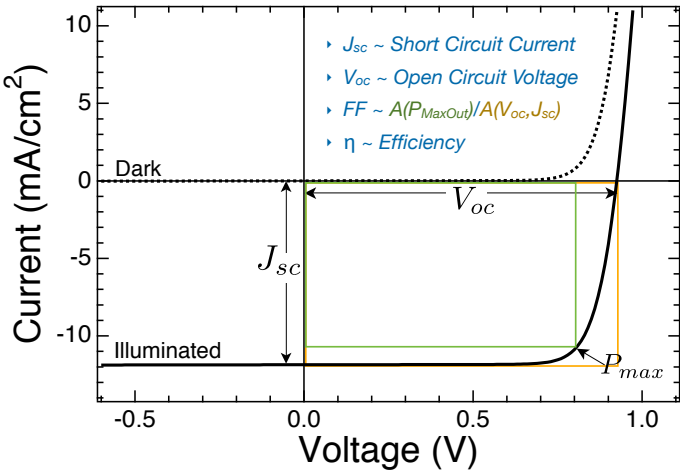

Figure 2.13: An illustration of a J-V curve for a typical OPV device.

where,V_{oc} is the open circuit voltage, J_{sc} is the short circuit current, and $FF = \dfrac{Area(P_{MaxOut})}{Area(V_{oc}, J_{sc})}$ is the fill factor.

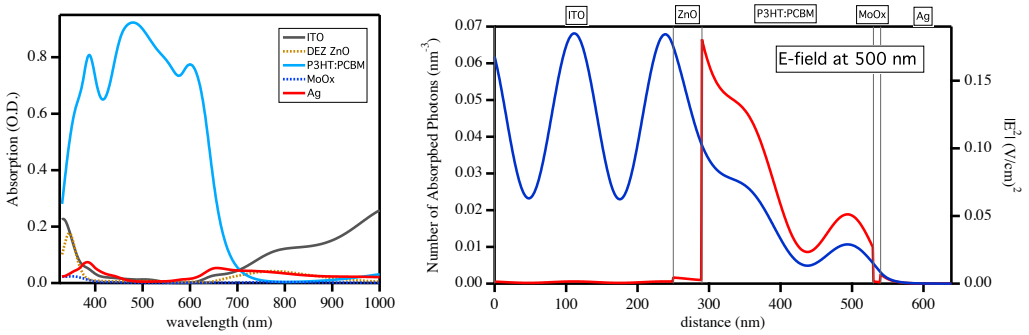

Figure 2.14: Electric field is continuous throughout the device. Photon absorption is discontinuous.

2.5.2 Light Management in a Device

The bulk of the work in this dissertation is focused on maximizing the transparency of the oxide electrodes (TCOs) in order to obtain efficient devices. In thin film devices, the light management is critical in improving the performance. A typical OPV device with an inverted architecture is shown in Figure 2.11. Here we require both TCOs and ETL layers to have maximum transparency so that most of the incident light passes through oxide electrodes in order for maximum photons to reach the active layer. The reflection back from the metal contact can also enhance the light absorption. Or in some cases, the back electrode can be replaced with an another transparent electrode, making it a semi-transparent device. (10, 4, 3, 5, 6) A calculation based on transfer-matrix method is used to optimize the various layer thickness in order to obtain the maximum photon absorption at the active layer. Absorption profiles of various layers as a function of wavelength are shown in (Figure 2.14). Also shown in Figure 2.14 is an example electric field distribution and photon absorption at λ = 500 nm for an inverted OPV device (ITO/ZnO/P3HT:PCBM/MoOx/Ag). The electric field is continuous throughout the device following Maxwell's equation. The photon absorption is discontinuous as layers have different absorption coefficients. Once the optimum condition for maximum absorption at the BHJ is obtained via the modeling, it is realized experimentally. The absorption profile of various layers, and the incident solar irradiation are not constant and vary with the wavelength. The relationship between J_{sc} in a device and the photon flux is given by,

$$J_{sc} = q \int_0^\infty QE(\lambda) b_s(\lambda) \mathrm{d}\lambda \tag{2.5.2}$$

where, b_s (λ) is incident photon flux, and QE (λ) is the quantum efficiency of the device. The QE is dependent upon various other factors, but it is usually limited by the fraction of incident light absorbed. There are various other considerations to maximize the QE, but few we seek are done via maximizing the transparency of TCO so that more light reaches the active layer and light engineering so that the maximum light absorption occurs at the BHJ. A semiconductor with a given band-gap (E_g) will only absorb photons with energy greater than E_g, so the absorber polymer or absorber layer semiconductor has a low band-gap so as to maximize J_{sc}. Similarly, there is a limit for maximum V_{OC}, which is always less than E_g/q. After factoring various losses, the maximum efficiency of a solar cell, i.e Shockley and Queisser limit (46) is given by

$$\eta = \frac{\int_{E_g}^{\infty} b_s(\lambda)\mathrm{d}\lambda}{\int_{0}^{\infty} \lambda b_s(\lambda)\mathrm{d}\lambda} \tag{2.5.3}$$

For a single junction solar cell, with optimal bandgap of E_g = 1.4 eV, the theoretical limit on η = 33%. Currently, the highest performing OPV devices have efficiencies $\eta \sim 12\%$, with lots of rooms for improvements.

2.5.3 Diode Ideality

Solar cells are photo-diodes. The ideality factor is another metric that is useful and is derived from the slope of the dark-JV curve. Unusually high ideality factor from a device indicates that either there are significant sources of recombination taking place inside the device and/or that the recombination is changing in

magnitude as a function of the operational condition of the device. An ideal diode equation in the dark is defined as,

$$I = I_o(exp(\frac{qV}{nkT}) - 1) \tag{2.5.4}$$

where I is the current through the diode, V is the voltage across the diode, I_o is the dark saturation current, n is the ideality factor and T is the temperature in Kelvin. And q - Elementary charge (1.602 x 10^{-19} C) and k - Boltzmann constant (8.617 x 10^{-5} eV/K). Ignoring -1 in the limit V $>$ 100mV, the equation reduces to

$$I = I_o exp(\frac{qV}{nkT}) \tag{2.5.5}$$

Now, taking the natural log of both sides of the equation gives:

$$ln(I) = ln(I_o) + \frac{q}{nkT}V \tag{2.5.6}$$

This equation is in the form of y = mx + C, which is the equation of a line. Thus, plotting y = ln (I), and x = V, we can get the slope m = $\frac{q}{nkT}$, and C = ln (I_o). In Chapter 6, calculation of the ideality factor (n) from the above equation at T = 300 K will be denoted by n'. The ideality factor (n) varies with the bias voltage. We are usually interested at the value of n near V_{oc} so as to minimize the recombination in the device, and improve the efficiency. Note: At high forward voltages in a dark-IV curve, the series resistance dominates and the device is operating in injection, this causes a large increase in the ideality factor. So in this limit, the interpretation that the diode ideality factor provides the metrics of recombination is not as clear.

Chapter 3

Research and Development of Transparent Semiconductors

This chapter presents the study on the development of transparent electrode, gallium doped zinc oxide (GZO). This chapter contains the optimization of the bulk physical property of GZO electrode, while the next few chapters contain the studies of the surface of the electrode followed by surface modification and applications in OLED and OPV devices.

Development of a contact electrode, high conductivity gallium doped zinc oxide (GZO), was done in various phases: development from small scale to large scale, followed by device applications in both organic LEDs and OPV, finally studies on charge transport in surfaces/interface. Initial study of material exploration and optimization of various compositional parameter for application in OLEDs was done previously in our group using pulse laser deposition. (47) From small scale 1×1 sq. inch area to larger scale deposition 2×2 sq. inch, the initial study resulted

in development of GZO deposited using RF sputtering technique, industrially standard for depositing thin film, was published on *Thin Solid Films*, Gorrie et al, title "Effect of deposition distance and temperature on electrical, optical and structural properties of radio-frequency magnetron-sputtered gallium-doped zinc oxide. (48) Further work included deposition in larger area and application in OLED devices, which was published on *SPIE proceeding*, D Matson et al, title: "Development of large area transparent conducting oxides from a combinatorial lead for organic solid state lighting". (49)

To keep the length of this dissertation reasonably short, in this chapter we will discuss only the latest study on GZO thin films where the dynamics of the superimposed RF and DC power is manipulated to improve the microstructure of the film. Next chapter contains the surface study on optimized electrode from this chapter. The study in this chapter contains key physical insights on improving the gallium-doped zinc oxide transparent conducting thin film, as an indium-free electrode, and using an industry scalable stuttering technique. Films with conductivity $\sim$ 4000 S/cm and transparency $\sim$90%, at good deposition rates were obtained from Earth-abundant material. These results and approach presented in the paper is very important for community involved in device applications such as solar cells, light emitting diodes, transparent thin film transistors and other technologies employing transparent conducting oxides.

This text was written in 2011 and published in *Journal of Applied Physics* titled "Radio-Frequency Superimposed Direct Current Magnetron Sputtered Ga:ZnO Transparent Conducting Thin Films" by Ajaya K. Sigdel, Paul F Ndione, John D.

Perkins, Thomas Gennett, Maikel F.A.M. van Hest, Sean E. Shaheen, David S. Ginley and Joseph J. Berry. [DOI:10.1063/1.4709753] In order to provide clarity and completeness, this version has extra data, figures and discussions that was not included in the original published paper.

3.1 Radio-Frequency Superimposed Direct Current Magnetron Sputtered Ga:ZnO Transparent Conducting Thin Films

Abstract: The utilization of radio-frequency (RF) superimposed direct-current (DC) magnetron sputtering deposition on the properties of gallium doped ZnO (GZO) based transparent conducting oxides (TCOs) has been examined. The GZO films were deposited using 76.2 mm diameter $ZnO:Ga_2O_3$ (5 at % Ga vs. Zn) ceramic oxide target on heated non-alkaline glass substrates by varying total power from 60 W to 120 W in steps of 20 W and at various power ratios of RF to DC changing from 0 to 1 in steps of 0.25. The GZO thin films grown with pure DC, mixed RF and DC, and pure RF resulted in conductivities of 2200 $\pm$ 200 S/cm, 3920 $\pm$ 600 S/cm, and 3610 $\pm$ 400 S/cm respectively. X-ray diffraction showed all films have wurtzite ZnO structure with the c-axis oriented perpendicular to the substrate. The films grown with increasing RF portion of the total power resulted in the improvement of crystallographic texture with smaller full-width half maximum in chi χ and broadening of optical gap with increased carrier concentration via more efficient doping. Independent of the total sputtering power, all films grown

with 50% or higher RF power portion resulted in high mobility ($\sim$ 28 $\pm$ cm^2/Vs), consistent with observed improvements in crystallographic texture. All films showed optical transmittance of $\sim$90% in the visible range.

3.1.1 Introduction

Development of high conductivity transparent conducting oxides (TCOs) at low cost from Earth-abundant materials is of great interest for cost-effective thin film device applications, such as solar cells, (50, 51) light emitting diodes, (52, 47, 53) touch-sensitive displays, electronic paper, and transparent thin film transistors. (54, 55) TCOs based on Group III elements such as B, Al, Ga doped into zinc oxide (BZO, AZO, GZO) have been studied extensively as an alternative to indium tin oxide (ITO). (56, 57) Historically, aluminum has been the most common dopant however in contrast gallium with its atomic radius similar to zinc allows substitutional doping in the ZnO wurtzite lattice with minimal strain. In addition, gallium is less reactive and less mobile compare to Al and therefore less prone to phase separation and oxidation during film growth. (58, 59, 9)

A variety of techniques for GZO deposition have been reported in the literature, including pulsed laser deposition (PLD), (60, 61) plasma enhanced metal-organic chemical vapor deposition, (62) spray pyrolysis, (63) direct-current (DC) magnetron sputter deposition (64) and radio-frequency (RF)-magnetron sputter deposition. (65, 66) Conductivities greater than 12,000 S/cm have been reported for epitaxial GZO materials fabricated by PLD on quartz substrates. (67) In comparison, polycrystalline GZO deposited using industrially scalable

sputtering technique exhibits typical conductivities in the range of 2500-3500 S/cm for films deposited on glass or other amorphous substrates. This considerable difference in conductivity between the polycrystalline and epitaxial thin films is due in part to grain boundary scattering. (68, 69)

In this study, the impact on conductivity and structural properties of GZO films deposited using superimposition of RF and DC magnetron sputter deposition is examined. Previous studies on ITO and AZO have shown the approach of an RF + DC power results in films with high mobility and better micro structure albeit at an average of both deposition rates. (70, 71, 72, 73, 74, 75) This RF + DC technique takes advantage of both power sources by combining the higher energy provided by RF and larger area uniformity provided by DC to modulate the ion density during the film deposition.

Accordingly, we have analyzed GZO films grown by systematically varying total power

$$P_{Tot} = P_{RF} + P_{DC} \tag{3.1.1}$$

and at various power ratios of RF to DC,

$$\gamma_{rfdc} = \frac{P_{RF}}{P_{RF} + P_{DC}} \tag{3.1.2}$$

for each total power have been analyzed. The films have optical transmittance $\sim$ 90% in the visible range and conductivity >2000 S/cm, with the highest conductivity exceeding 4000 S/cm. Improvement in crystallographic texture with smaller full-width half maximum in χ and broadening of optical gap with increased

carrier concentration in accordance to Burstein-Moss theory are observed for films with increasing RF portion of the total power. Independent of P_{Tot}, all films grown with γ_{rfdc} >0.5 have improved mobility, which is attributed to improved crystallographic texture. We also observe a distinct change in the doping efficiency of the films with varying γ_{rfdc}.

3.1.2 Experimental Details

Thin Films Fabrication

Films of Ga-doped zinc oxide (GZO) were deposited using a 99.99% pure, 76.2 mm diameter ZnO:Ga_2O_3 (5 at% Ga vs. Zn) ceramic oxide target (Cerac, Inc.) on 50.8 mm x 50.8 mm Corning Eagle 2000 glass substrates. All films were deposited using RF magnetron sputtering at 13.56 MHz (Dressler Cesar RF power generator) superimposed onto DC magnetron sputtering (Ad-vance Energy DC Pinnacle Plus) with a conventional magnetron sputtering source (Onyx 2 MagII, Angstrom Sciences, Inc). The experimental arrangement for this approach from Advanced Energy Inc. is described in detail elsewhere. (70) We have previously reported the optimized conditions for RF sputtered GZO. (48)

For all depositions in this work, pure argon (>99.999%) was used as sputtering gas, the substrate to the target distance was 68.5 mm, the substrate temperature was 250 °C and the deposition pressure was kept at 0.60 Pa. P_{Tot} was varied from 60 W to 120 W with steps of 20 W, and γ_{rfdc} was varied from 0 to 1 with steps of 0.25.The chamber base pressure prior to backfilling with argon was less

than 1.3×10^{-4} Pa. Water and oxygen partial pressure during the deposition were monitored using a MKS quadrupole residual gas analyzer mass spectrometer (RGA). The partial pressure of oxygen and water content in the deposition chamber has been known to control the equilibrium of defects on the surface creating oxygen vacancies, thus influencing the number of carriers in ZnO based TCOs. (48, 76, 77, 78)

Considerable efforts were taken to keep the O_2 and H_2O partial pressure $<0.1\%$ of total chamber pressure with $<10\%$ variation among various depositions. The system was equilibrated with a 10 minute burn-in period before the films were deposited onto the substrate. The deposition time was varied in order to achieve films with similar thickness ($\sim$ 500 $\pm$ 100 nm) such that the effect of the variation in crystal structure due to thickness effect is minimized. (9, 76)After the deposition, the substrates were allowed to cool to <100 $^{\circ}$C before being removed from the chamber to minimize oxidation of the thin film surface.

3.1.3 Characterizations

Conductivity of the films were calculated by method of measuring the thickness with a Sloan Technologies Dektak profilometer and a J. A. Woollam M-2000 spectroscopic ellipsometer, and the sheet resistance via a linear four-point probe method. A Hall measurement system (Accent HL5500PC) was used to obtain carrier concentration, mobility and also to confirm the conductivity values obtained with the four-point probe measurements. Hall measurement data was taken using van der Pauw configuration at room temperature in a magnetic field of 0.1 T.

Structural assessments via x-ray diffraction (XRD) at the center of the films were done using a Bruker Discovery D8 with a Hi-Star area detector. Atomic force scanning probe microscopy (AFM) em-ployed an Asylum Research MFP-3D in tapping mode with tip radius <15 nm (Tap300DLC) to obtain RMS surface roughness (S_{rms}) of our film. Optical properties of the films were obtained using two coupled Ocean Optics spectrometers to measure transmittance and reflectance over the range of 330-1000 nm. All optical transmission (T) data shown were normalized to the glass substrate, and the reflectance (R) measured and corrected using a reference front surface aluminum mirror.

In general, the data shown here reflect an average value obtained from a minimum of 2 depositions. Error bars represent the variation resulting from multiple films from nominally identical depositions. For higher conductivity films, a large set of more than five samples obtained from independent depositions were used to validate the results and extract the reported experimental error estimate.

3.1.4 Results and Discussion

Figure $3.1a$ shows the deposition rate (r_{dep}) as a function of P_{Tot} and γ_{rfdc} for the various GZO films in this study. High r_{dep} = 0.97 nm/s is measured for P_{Tot} = 120 W and γ_{rfdc} = 0 and slow r_{dep} = 0.3 nm/s is measured for P_{Tot} = 60 W and γ_{rfdc} = 1. As expected, an increase in total power results in increase in the deposition rates. Furthermore, consistent with earlier studies on RF+DC, it can be seen that the r_{dep} decreases almost linearly with increasing γ_{rfdc} at a constant total power. (74, 76, 77) Utilizing the dynamics of RF superimposed DC conditions,

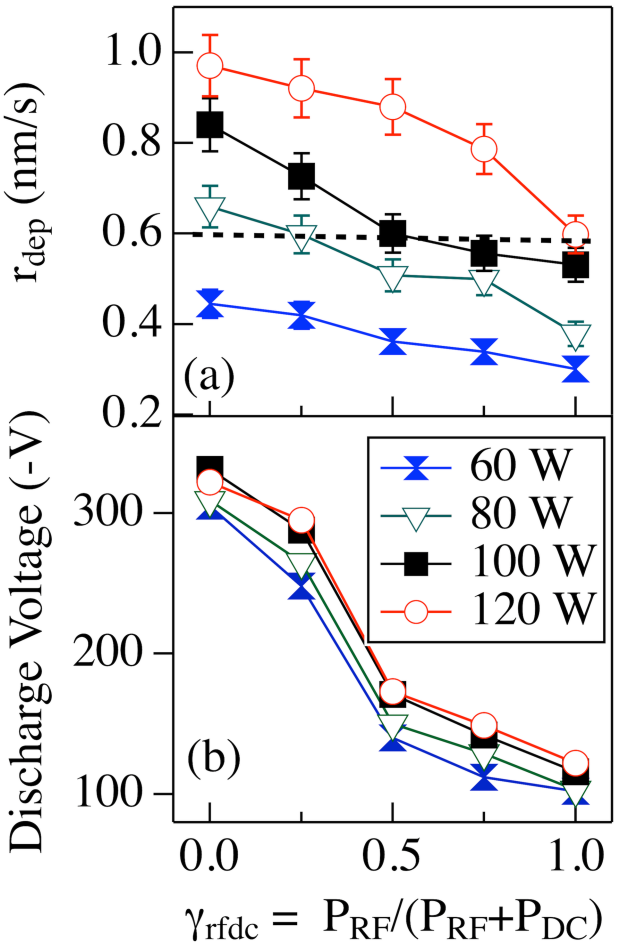

Figure 3.1: (a) Deposition rates and (b) Discharge voltage for different γ_{rfdc} from 0 to 1 and various P_{Tot} of 60, 80, 100 and 120 W respectively. By varying γ_{rfdc}, similar deposition rate can be achieved at varying P_{Tot}.

similar deposition rate can be achieved at varying P_{Tot}. For example, the dotted line in figure 1 indicating 80 W at γ_{rfdc} = 0.25, 100 W at γ_{rfdc} =0.5 and 120 W at γ_{rfdc}= 1, all have similar deposition rates around 0.6 nm/s.

Figure 3.1(b) shows variation of the discharge voltage from -315 V to -110 V, over a range of γ_{rfdc} = 0 to 1 respectively. The variation in γ_{rfdc} has a larger impact on the discharge voltage, compare to variation in P_{Tot}. This large impact of γ_{rfdc}on discharge voltage is expected since ionization mechanisms of RF and DC magnetron sputtering are different. DC sputtering uses high voltage to maintain the discharge by secondary electron emission at the target surface due to ion bombardment. On the other hand, in RF sputtering, ionization is achieved by the oscillating electrons in the plasma, which results in lower discharge voltage. (74, 79)

Variation in growth rate and the dynamics of RF superimposed DC plays a key role in modulating structural properties of GZO thin films. Figure 3.2(a) shows integrated XRD patterns for GZO samples grown at P_{Tot} of 100 W with varying γ_{rfdc}. These XRD patterns are obtained from a 2D detector image file, by integrating over the χ direction. The detector images are shown in the inset for γ_{rfdc} = 0 and 1, where x-axis is the standard 2θ, the y-axis is the χ and the color code representing the logarithm of x-ray intensity in counts. All the XRD measurement analyzed are from the center of the film, with very high uniformity from center to edge, see Figure 3.3.

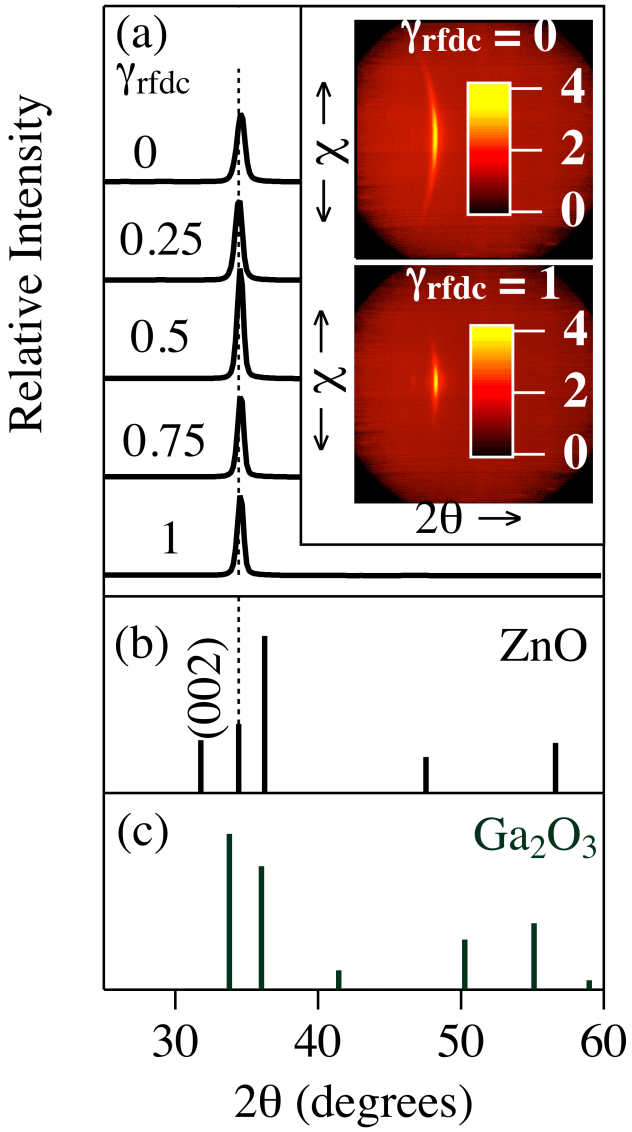

Figure 3.2: (a) XRD peaks for GZO films grown at P_{Tot} = 100 W with various γ_{rfdc} showing (002) peak characteristic of c-axis oriented zinc oxide with wurtzite structure. No Ga_2O_3 peaks are evident and inset showing 2D diffraction image files. (b) ZnO PDF (c) Ga_2O_3 PDF.

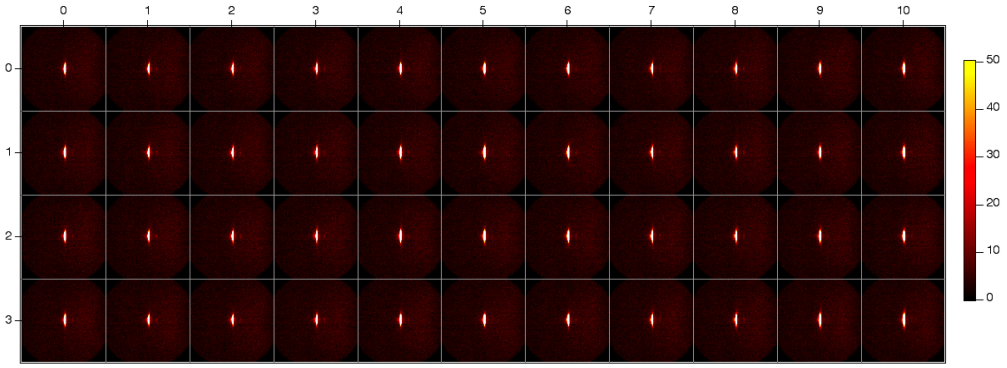

Figure 3.3: XRD data on 44 data points for 2×2 inch GZO substrate.

Figure 3.2(b) and 3.2(c) show the powder diffraction file (PDF) peak locations for ZnO and Ga_2O_3 respectively obtained from the International Centre for Diffraction Data (INT- 361451, INT-060503). All five films show peaks at 2θ = 34.35 attributed to the (002) plane of wurtzite ZnO with the c-axis oriented perpendicular to the plane of the substrate. No other peaks are observed in the XRD patterns. Similar observations are seen for other films grown with varying P_{Tot}. This indicates Ga is substitutionally doped in the ZnO wurtzite lattice with no evidence of a separate Ga_2O_3 phase. Furthermore, we find variation in the compact bright region in the raw image, indicating various spreads in χ, due to a range of (002) orientations.

To further analyze this spread, the (002) peaks are integrated in the 2θ direction and plotted vs χ as shown in Figure 3.4(a). This technique is analogous to a rocking curve except that the effective rocking angle is χ instead of ω. A highly textured film will show a small spread in χ, whereas a randomly oriented polycrystalline film will display a nearly constant intensity in χ. As shown in Figure 3.4(a), increasing the

RF component of power results in an increase in relative intensity, and a decrease in spread in χ, indicating the improvement in crystallographic texture (orientation).

To further quantify this spread, the full-width half maximum (FWHM) in χ is measured. Improvement in orientation resulting in lower angle between grain boundaries will produce small FWHM in χ. Figure 3.4(b) shows FWHM in χ for films grown at P_{Tot} of 120 W and 100 W for various γ_{rfdc}. We see a systematic decrease in FWHM value, from 8 degrees for P_{Tot} = 100W and γ_{rfdc} = 0 down to 4 degrees for P_{Tot} = 100 W and γ_{rfdc} = 1. The films grown at pure DC (γ_{rfdc} = 0) are consistently poorer in crystallographic texture compared to films grown at pure RF (γ_{rfdc} = 1). Overall, the films grown at $\gamma_{rfdc} > 0.5$ have lower FWHM in χ and thus improved crystallinity.

This is consistent with earlier studies where films grown at $\gamma_{rfdc} > 0.5$ had lower mechanical stress due to improvement in crystallinity. (80, 76) Furthermore this improvement in structure is coincident with the reduction in the discharge voltage as γ_{rfdc} is increased. Previous studies have shown that smaller discharge voltage decreases the bombardment of various types of energetic negative ions, which can have adverse effect on the film growth. (80) Since there is interplay between the structural and electronic properties, more detail about the impact of the structural properties will be given after the discussion of the electronic properties.

The conductivity (σ), carrier concentration (N) and mobility (μ) for various films in this study obtained from Hall measurement are shown in Figure 3.5. The trend illustrates that the conductivity σ increases with the increase of RF power

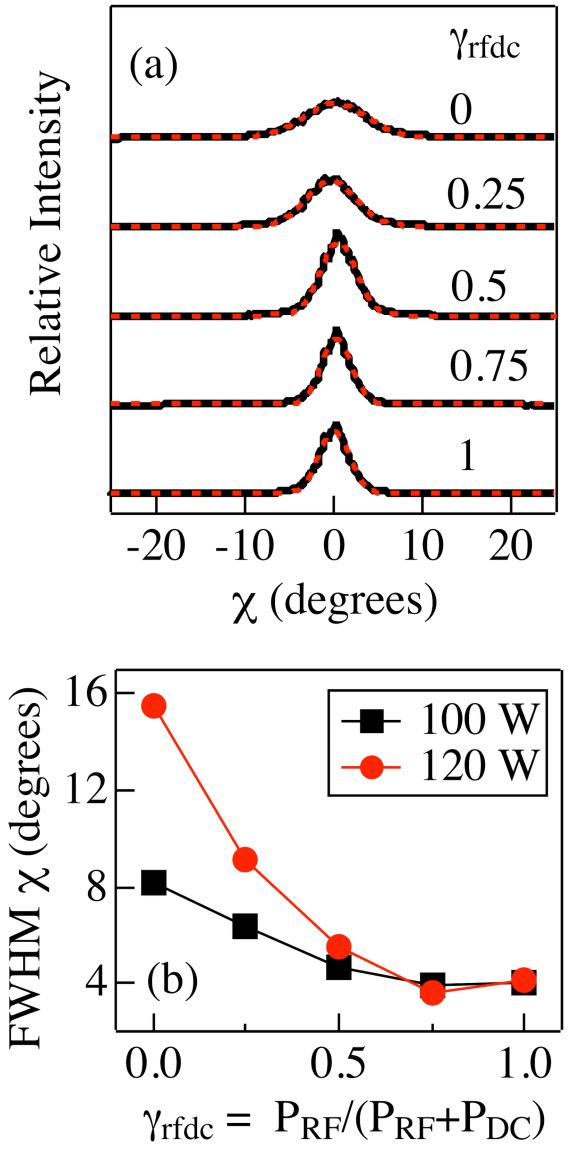

Figure 3.4: (a) χ for P_{Tot} of 100 W at various γ_{rfdc} b) FWHM on χ for P_{Tot} of 100 W and 120 W at various γ_{rfdc}. Films grown with more RF component have small FWHM.

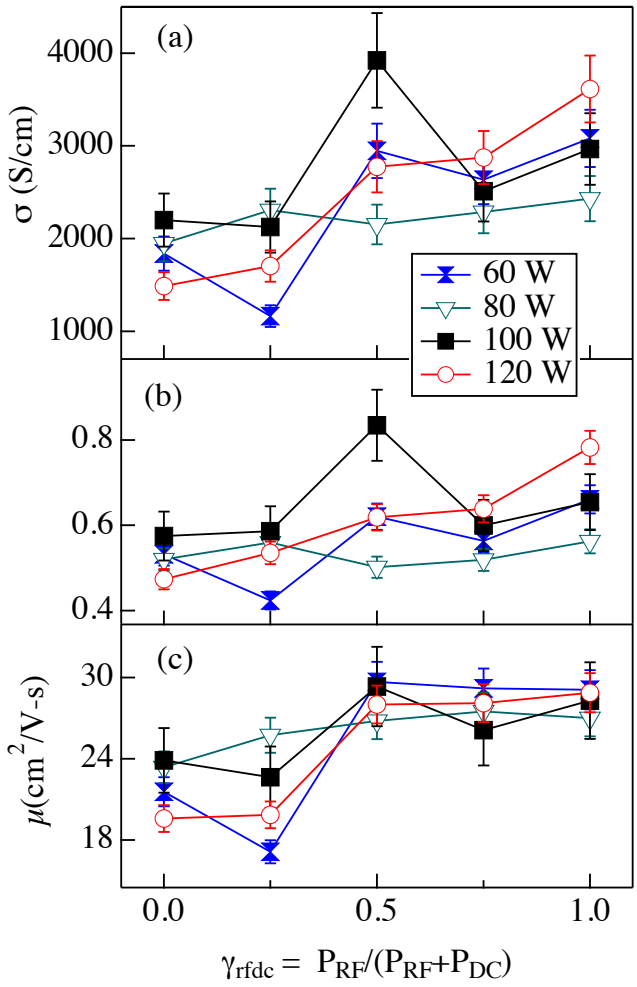

Figure 3.5: Hall data for various P_{Tot} and at varying γ_{rfdc}. Panels a, b and c respectively show σ, N and μ. Films grown with 50% or higher RF power portion have high μ.

component. Figure 3.5(a) shows that GZO films grown at P_{Tot} = 120 W have increasing σ with increasing RF component with maximum σ (3610 $\pm$ 400 S/cm) at γ_{rfdc} = 1. However, the GZO films grown at P_{Tot} = 100 W have maximum σ (3920 S/cm $\pm$ 600) at γ_{rfdc} = 0.5. Similarly films grown at P_{Tot} of 80 W and 60 W have peak σ at γ_{rfdc} = 0.25 and 0.5 respectively. Thus for γ_{rfdc} = 0, 0.25 and 0.5, highest conductivities are obtained at P_{Tot} of 100 W, whereas for $\gamma_{rfdc} > 0.5$ highest conductivities are obtained at P_{Tot} of 120 W. The maximum in conductivity is consistent with the highest deposition rate that does not negatively impact the materials microstructure and resulting doping efficiency. (81, 48, 74)

Films grown at P_{Tot} = 100 W, γ_{rfdc} = 0.5 have the highest σ in this study, and have the better crystallographic texture as well. This is consistent with studies on indium doped zinc oxide using similar technique and showing the highest conductivity films deposited at 50% RF component. (74) On top of the good electrical and structural properties, the films deposited with a mixed power approach have better deposition rates compare to RF sputtering. This can provide a minimal deposition time for technological applications where a high conductivity TCO and low sheet resistance is desirable.

Figure 3.5(b) shows a clear trend in the carrier concentration with N ranging from 4.2 $\times 10^{20}$ /cm^3 to 7.8 $\times 10^{20}$ /cm^3. Carrier concentration increases with the inclusion of RF power. For pure RF (γ_{rfdc} = 1), the highest N of 7.8 $\times 10^{20}$/cm^3 is obtained at P_{Tot} of 120 W. Similarly, at γ_{rfdc} = 0.5, the high N of 8.3 $\times 10^{20}$/cm^3 is obtained at P_{Tot} of 100 W. This carrier concentration corresponds to a doping efficiency of 40%, whereas for pure DC (γ_{rfdc} = 0), N = 5.7 $\times 10^{20}$/cm^3 is obtained

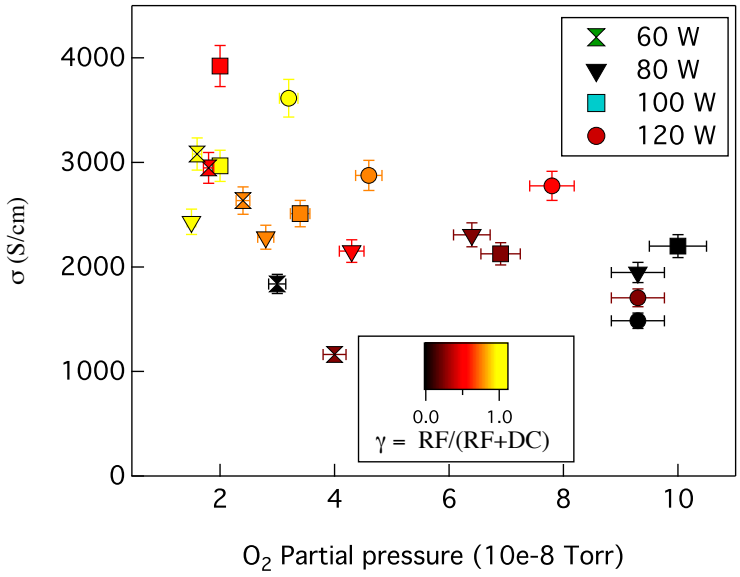

Figure 3.6: RGA data showing σ vs measured O_2 partial pressure in the deposition chamber.

at P_{Tot} of 100 W, with doping efficiency of 35%. Film conductivities are directly correlated with crystallographic quality, number of carriers and doping efficiencies. This result is consistent with our previous work and suggests the importance of the microstructure properties in governing the films electronic properties. (48)

Variation in μ as a function of P_{Tot} and γ_{rfdc} is shown in Figure 3.5(c). Figures shows μ increases from less than 24 cm^2/Vs at γ_{rfdc} = 0 to average of 28 cm^2/Vs for $\gamma_{rfdc} > 0.5$ for all P_{Tot} values. This corresponds to an increase in μ of $\sim$ 20 %. The highest μ measured in this study is $\sim$ 29.7 cm^2/Vs for films grown at γ_{rfdc} of 0.5 and P_{Tot} of 60 W. This high mobility value is comparable to mobility value of 30.1 cm^2/Vs obtained by Park et. al. for GZO films deposited on quartz substrate using pulsed-laser deposition. (67)

No significant correlations between measured partial pressure of O_2 and H_2O level during deposition with the number of carriers in our GZO films were found, see Figure 3.6. The residual O_2 and H_2O partial pressure during deposition may be below the threshold of influence. We therefore attribute these trends in μ and N, and thus the conductivity to differences in the microstructure of the films resulting from the dynamics of the sputtering process produced by both RF and DC power components.

The improvement in the electronic properties of GZO films due to improvement in the structure quality is further illustrated in Figure 3.7. Figure 3.7(a) shows σ as a function of integrated peak area normalized to thickness for GZO deposited at various γ_{rfdc} and at P_{Tot} of 100 W and 120 W, obtained first by integrating across 2θ to get the χ distribution shown in Fig 3.4 and then integrating these curves in χ. From the graph, we find a direct correlation between σ and counts/thickness with the most intense XRD signal seen for the highest conductivity film deposited at P_{Tot} = 100W and γ_{rfdc} = 0.5. The figure also highlights the improvement in conductivity due to structural improvement as well as due to the improvement in the doping efficiency for higher γ_{rfdc} ratio. Similarly, Figure 5 (b) and (c), show σ and μ respectively as a function of FWHM in χ. Figure 3.7(b) shows films with $\sigma > 2000$ S/cm having < 8 degrees FWHM in χ. Consistent with this, Figure 3.7(c) shows films with μ values >25 cm^2/Vs having < 5 degrees FWHM in χ. This indicates the films with $\gamma_{rfdc} > 0.5$ have higher mobilities that are strongly correlated with improved structural quality and enhanced doping efficiency in the films.

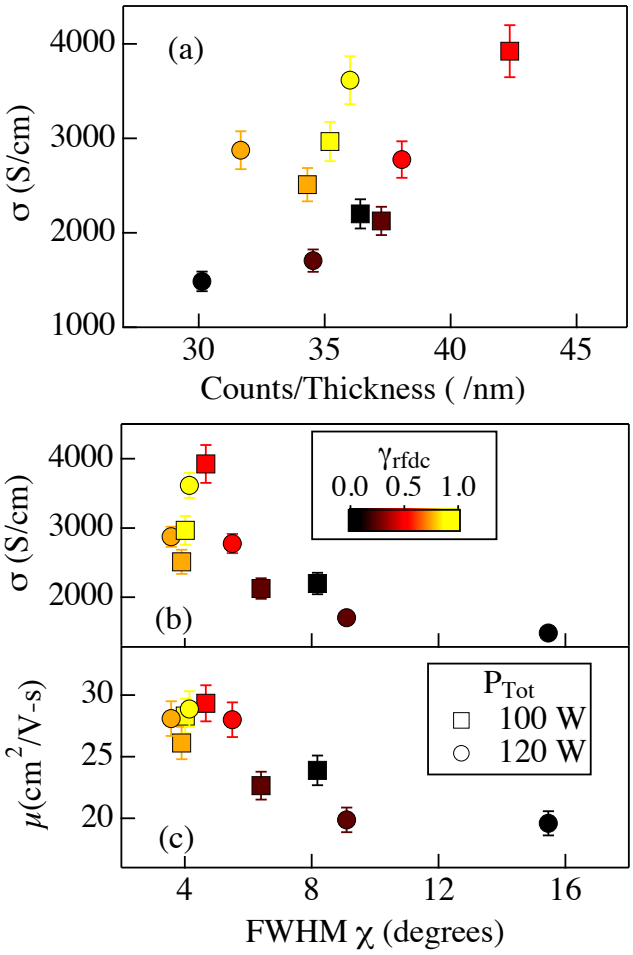

Figure 3.7: a) Total counts/thickness of the entire 002 peak b) σ vs FWHM χ c) μ vs FWHM χ for films grown at P_{Tot} of 100 W and 120 W at various γ_{rfdc}. Films with more structural order obtained with increased RF component, resulting in high σ and μ.

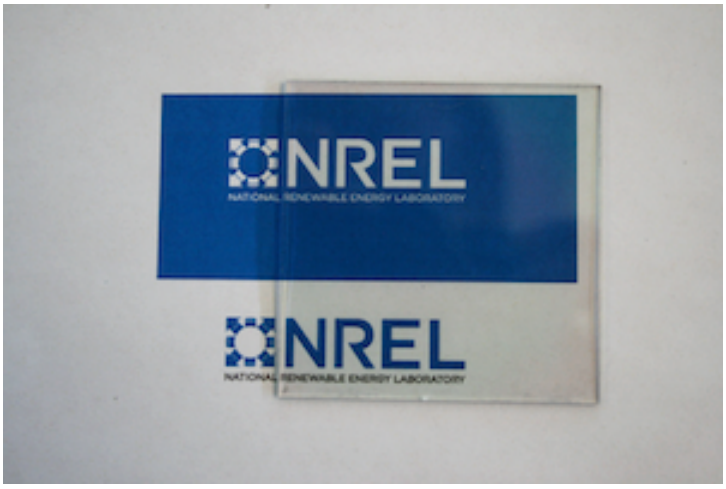

Figure 3.8: GZO film on a 2×2 inch substrate.

GZO film on a 2×2 inch substrate is shown in Figure 3.8. The optical spectra for transmittance (T) normalized to the glass substrate and the reflectance (R) relative to a standard Al mirror for samples grown at P_{Tot} of 100 W are show in Figure 3.9. T $\sim$ 90% in visible spectrum are seen for all samples. Similarly, the average reflectances of the samples are around 10%. We calculated the absorptance = 100 -T_{air} - R, where T_{air} = 0.92T. All the GZO films have absorptance values consistently $<$5% in the visible spectrum. We find increased free carrier absorption in $>$900 nm range for film with high carrier concentration. We do not find any systematic reduction in T in the visible range associated with metal rich film. This indicates that even though the films are grown in pure argon, there is enough oxygen available from the oxide target for near stoichiometric crystal growth, which results in highly transparent films. Moreover, index of refraction at wavelength of 500 nm for all GZO films are around 1.9, consistent with the existing literature.

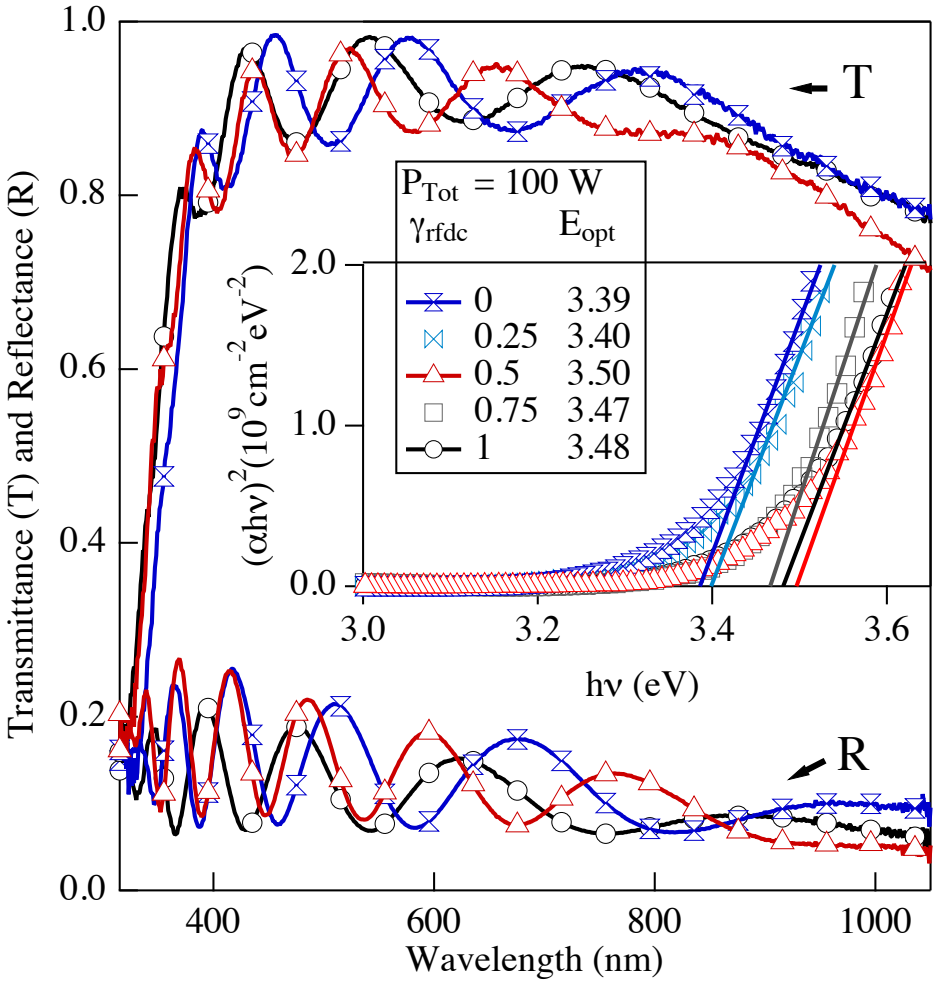

Figure 3.9: Transmittance and Reflectance data for P_{Tot} = 100 W. Films have ∼90% transparency in visible spectrum. Inset showing $(\alpha h\nu)^2$ vs $h\nu$ and E_{opt} ($\pm$ 0.02 eV).

The inset in Figure 3.9 shows a Tauc plot of $(\alpha h\nu)^2$ vs $h\nu$ for GZO samples grown at P_{Tot} of 100 W with varying γ_{rfdc}. We have extrapolated the linear portion of this plot for $\alpha > 1x10^4$ /cm to find the effective optical gap (E_{opt}). There is an increase in optical gap with the increase in RF component i.e the P_{Tot} 100 W, films for γ_{rfdc} = 0, 0.5 and 1 have E_{opt} of 3.39 $\pm$ 0.02, 3.50 $\pm$ 0.02 and 3.48 $\pm$ 0.02 eV respectively. This trend of a slight increase $\sim$ 0.1 eV, in E_{opt} with increasing RF component, is confirmed by spectroscopic ellipsometry measurement as well. This shift of E_{opt} is due in part to the Burstein-Moss shift (ΔE), associated with the increase in number of carriers given by the equation

$$\Delta E_{BM} = \frac{(\hbar)^2}{2m^*}(3\pi^2 N)^{\frac{2}{3}} \tag{3.1.3}$$

where $\hbar$ is the reduced Planks constant $\frac{h}{2\pi}$ and m^* is the effective electron mass. Taking m^* as 0.3 and increase in N = 2.0 x $10^{20}/cm^3$ from Figure 3.5(b). The ΔE is estimated to be around 0.09 eV, consistent with the observed shift in E_{opt}. We note that while these changes in optical gap are consistent with the Burstein-Moss shift, some changes in structural property could be at play as well.

In thin films, measured surface structural properties can sometimes provide further insights on the bulk structural property such as grain size and orientation. AFM data showing surface features for GZO samples grown at P_{Tot} of 100 W with varying γ_{rfdc} are shown in Figure 3.10. Panel a, b, c show surface topography for the films grown at γ_{rfdc} = 1, γ_{rfdc} = 0.5 and γ_{rfdc} = 0. Root mean square surface roughness (S_{rms}) of the films are 1.8 $\pm$ 0.1 nm, 1.7 $\pm$ 0.1 nm, 2.2 $\pm$ 0.1 nm and respectively. Similar surface morphologies with slight variations in

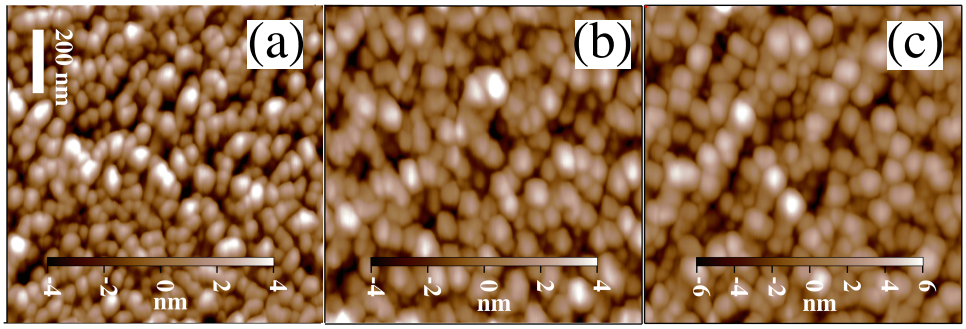

Figure 3.10: AFM image for P_{Tot} = 100 W: (a) γ_{rfdc} = 1 with S_{rms} = 1.8 nm (b) γ_{rfdc} = 0.5 with S_{rms} = 1.7 nm (c)γ_{rfdc} = 0 with S_{rms} = 2.2 nm. Films grown with 50% or higher RF power portion have low S_{rms}.

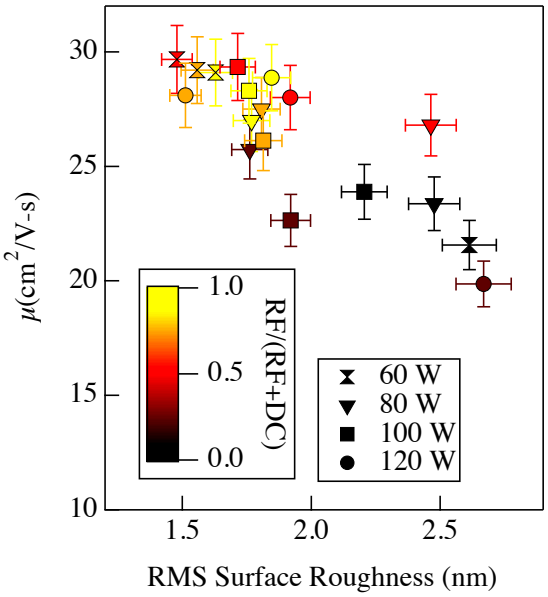

Figure 3.11: Clear correlation is observed with improvements in μ and reduced S_{rms}.

S_{rms} are obtained for films grown at various growth conditions. The smoothest film grown at P_{Tot} = 60 W, γ_{rfdc} = 0.5 with S_{rms} = 1.5$\pm$ 0.1 nm has the highest mobility 29.7 cm^2/Vs. Although, high mobility samples grown at $\gamma_{rfdc} > 0.5$ with μ above 26 cm^2/Vs do not have statistically significant differences in the S_{rms}, a clear correlation is observed with improvements in μ and reduced S_{rms} as shown in Figure 3.11. This indicates a weak correlation of the surface S_{rms} consistent with our earlier assessment of improvement in crystallographic texture due the dynamics of RF superimposed DC yielding high mobility films.

3.1.5 Conclusions

GZO films are deposited on heated glass substrates using RF superimposed with DC magnetron sputtering with varying both the RF and the DC power ratios and the total power applied to ZnO:Ga_2O_3 (5 at% Ga vs. Zn) ceramic oxide target. All the films have optical transmittance $\sim$90% in the visible range and XRD indicates that all films have wurtzite ZnO structure with the c-axis oriented perpendicular to the substrate. We find that by varying the RF portion of the total power it is possible to optimize the microstructure of the GZO films as evident in both the change in crystal structure, doping efficiency and overall film conductivity. Specifically, improvement in crystallographic texture (smaller FWHM in χ) for films grown with increased RF portion of the total power are observed, consistent with changes in surface morphology as measured by AFM. We also find that all films grown with 50% or more RF power component result in high-mobility ($\sim$ 28 $\pm$ 1 cm^2/Vs) films, with observed improvements in crystallographic quality. Commensurate with these changes, we also observe that films grown with increased

RF portion of the total power have broader optical gap due to a Burstein-Moss shift resulting from the increase in carrier concentration and improved doping efficiency. Thus, the RF-superimposed-DC approach allows deposition of films with good structural, electrical and optical properties by manipulation of the microstructure of the films. This approach permits the benefits of high film quality provided by RF power and higher deposition rate provided by DC power.

Acknowledgements: Materials development including oxide deposition and characterization equipment was provided by the U.S. Department of Energy under Contract No. DOE-AC36-08GO28308 with the National Renewable Energy Laboratory. Support for deposition, characterization and analysis work was provided as part of the Center for Interface Science: Solar-Electric Materials (CIS:SEM), an Energy Frontier Research Center Funded by the U.S. Department of Energy, Office of Basic Sciences, under Award Number DE-SC0001084

Chapter 4

Surface Studies of Transparent Semiconductors

In the previous chapter, our discussion involved understanding and improving the bulk physical properties of transparent electrode GZO. The bulk properties of thin films are important, but in a thin film device surface properties of the individual layers dominate the charge transfer. This chapter will focus on understanding the surface of electrodes. The role of various pre-treatments on poly-crystalline GZO electrode and amorphous indium zinc oxide (IZO) electrode and how they impact the surface conductivity, passivation and other physical properties will be discussed. Some of the text related to GZO pretreatment study mentioned here has already been published: "Surface composition, Work function and Electrochemical Characteristics of Gallium-doped Zinc Oxide (GZO) Semi-transparent Electrodes. Erin L. Ratcliff, **Ajaya K. Sigdel**, Mariola R. Macech, Kenneth Nebesny, Paul A. Lee, David S. Ginley, Neal R. Armstrong, Joseph J. Berry, **Thin Solid Films, 520(17), 56525663 (2012)** DOI: 10.1016/j.tsf.2012.04.038.

4.1 Surface composition, Work function and Electrochemical Characteristics of Ga-doped ZnO (GZO) Semi-transparent Electrodes

Abstract: Gallium-doped zinc oxide (GZO) possesses the electric conductivity, thermal stability, and earth abundance to be a promising transparent conductive oxide replacement for indium tin oxide electrodes in a number of molecular electronic devices, including organic solar cells and organic light emitting diodes. The surface chemistry of GZO is complex and dominated by the hydrolysis chemistry of ZnO, which influences the work function via charge transfer and band bending caused by adsorbates. A comprehensive characterization of the surface chemical composition and electrochemical properties of GZO electrodes is presented, using both solution and surface adsorbed redox probe molecules.

The GZO surface is characterized using monochromatic X-ray photoelectron spectroscopy and ultraviolet photoelectron spectroscopy after the following pretreatments: (i) hydriodic acid etch, (ii) potassium hydroxide etch, (iii) RF oxygen plasma etching, and (iv) high-vacuum argon-ion sputtering. The O 1s spectra for the GZO electrodes have contributions from the stoichiometric oxide lattice, defects within the lattice, hydroxylated species, and carbonaceous impurities, with relative near-surface compositions varying with pretreatment. Solution etching procedures result in an increase of the work function and ionization potential of the GZO electrode, but yield different near surface Zn:Ga atomic ratios, which significantly influence charge transfer rates for a chemisorbed probe molecule.

The near surface chemical composition is shown to be the dominant factor in controlling surface work function and significantly influences the rate of electron transfer to both solution and tethered probe molecules.

4.1.1 Introduction

Zinc oxide and doped n-type zinc oxides have recently been studied as transparent conductive oxide (TCO) materials for organic electronic devices designed to replace indium tin oxide (ITO) contacts. The natural abundance of zinc and the wide bandgap ($\sim$ 3.3 eV) (32) of its oxide make it an ideal candidate for applications requiring a transparent conductive oxide. Zinc oxide (ZnO) is typically thought of as an n-type semiconductor with an ideal structure of hexagonal wurtzite. Intrinsic ZnO is insulating due to the lack of charge carriers, but can contain defects resulting from a displacement and/or removal of lattice atoms; these intrinsic defects have been linked to an increase in conductivity in the undoped oxide. (36, 37, 9)

The use of substitutional dopants further increases the overall conductivity of zinc oxides by significantly increasing carrier density, with gallium-doped ZnO having the highest conductivity over other group III ZnO dopants. Specifically, it is known that group III dopants can be substituted into the zinc lattice sites, giving up an additional electron which causes the Fermi level to move towards the conduction band of zinc oxide, as assumed by the classic extrinsic doping mechanism: (9)

$$\mathrm{M_2O_3} \longleftrightarrow 2M_{Zn} + 2e^- + 2O_O + \frac{1}{2}\mathrm{O_2} \tag{4.1.1}$$

The highest reported conductivities for Group III doped ZnO are for gallium-doped ZnO (GZO). (9) The higher conductivity of GZO films relative to other Group-III doped zinc oxides has been partially attributed to the atomic and ionic radii matching of Ga and Ga^{3+} to that of Zn and Zn^{2+} (when compared to the radii of Al and Al^{3+}) and should result in minimal distortion of the ZnO lattice. (40) Furthermore, the higher electronegativity of Ga over Al suggests that GZO should have a higher stability to oxidation over aluminum-doped zinc oxide (AZO) counterparts, (41) which is confirmed by the improved stability of GZO versus AZO when exposed to moisture. (42, 43)

Recent reports indicate that GZO has a higher conductivity than traditional ITO thin films, with conductivities as high as $8.12 \times 10^{-5}\Omega$ cm, accompanied by excellent optical transparency $> 80\%$ in the visible, making GZO particularly appealing for TCO applications. (82, 83, 84) The potential of improved electrical, optical, and environmental stability of ZnO-based TCO electrodes has motivated the experimental demonstration of GZO electrodes as replacement TCOs for thin film and dye sensitized solar cells, (12, 85) liquid crystal displays, (86, 87) thin film transistors, (88) organic photovoltaics, (89, 90, 91, 92) and organic light emitting diodes. (47) These technological demonstrations indicate GZO is a relevant TCO material which can be produced using a variety of processing technologies including magnetron sputtering, (93) spray pyrolysis, (94) pulsed laser deposition, (67) ion plating, (95) and sol-gel deposition techniques. (96, 97)

Currently, the majority of research on GZO has focused on the bulk properties including optical transparency and conductivity. Here we present studies focused

instead on the surface characteristics of GZO in an effort to understand composition and its impact on electronic properties at interfaces relevant to the application of GZO in a range of optoelectronic device technologies. The surface composition and structure of TCOs has been shown to affect key parameters that impact the performance of contacts such as work function. One device technology in which work function along with electrochemically determined charge transfer rates, appear to be of critical importance is in organic photovoltaics (OPV). (98, 99, 100, 101)

Although similar device design considerations are relevant to other optoelectronic devices, the role of the contact in OPV systems is particularly concern to the overall device performance. (102, 103, 104, 105, 106, 107, 15) It is known that various surface pre-treatments can significantly alter the surface composition of metal oxides, resulting in changes in photovoltaic device performance. (100, 101, 103) For ZnO and doped ZnO, the surface chemistry is complex because zinc oxides are among the most easily hydrolyzed metal oxides, forming $Zn(OH)_2$ and related oxy-hydroxides. (108) Furthermore, the hydrolysis products of zinc oxides have a higher solubility than indium and tin oxides, which suggests that understanding and control of the surface chemistry will be critical to optimizing the use of the materials as TCOs, especially in OPV technologies. (101, 109, 110) Multiple research groups have shown that high surface conductivity results from the accumulation of hydroxides on ZnO surfaces, (111, 112, 113) associated with the formation of a shallow electron donor state and an increase in carrier concentration in the space-charge layer via the reaction: (36, 114)

$$H + O^{2-} \longrightarrow OH^{-} + e^{-} \tag{4.1.2}$$

Exposure of ZnO to different gases (H_2, CO, O_2, and CO_2) have also been demonstrated to change surface conductivity and work function over time due to charge transfer and band-bending at the interfacial sites. (115) Detailed characterization of the surface composition both before and after various surface pre-treatments can therefore provide insight into the impact of doped ZnO in the formation of organic/oxide heterojunctions that must be optimized in organic optoelectronic applications and suggest possible routes to controlling the interfacial chemistry associated with charge transport.

Surface treatments of the GZO and the impact on the surface properties are studied using X-ray photoelectron spectroscopy (XPS) and correlated directly with observed changes in work function measured by ultraviolet photoelectron spectroscopy (UPS). Surface compositions of the GZO electrodes are correlated with changes in electrochemical charge transfer rates. These experiments are compared with recently understood pre-treatment results on commercially available ITO electrodes to provide direct technological comparison and relevance. (100, 101, 103)

4.1.2 Experimental Methods

Substrate Fabrication

Although there are multiple techniques to deposit GZO thin films, all those examined here were deposited via sputtering onto either 50.8 mm $\times$ 50.8 mm Corning Eagle 2000 glass substrates for the conductive samples or gold-coated

glass substrates for the resistive reference samples from targets (a), (c), and (d) described below. Greater than 99.99% pure single composition ceramic oxide sputter targets (Cerac Inc) were used with molar ratios of (a) ZnO 100%, (b) ZnO 97.5% : Ga_2O_3 2.5%, (c) ZnO 67%: Ga_2O_3 33%, and (d) Ga_2O_3 100% and thicknesses ranging from 300 to 500 nm. The GZO film with composition (b) is the TCO under study for electrode and photovoltaic applications. The TCO sputtering depositions with target (b) employ superimposed RF at 13.56 MHz (Dressler Cerac RF power generator) and DC magnetron sputtering (Advance energy DC pinnacle plus) with a conventional magnetron sputtering source (Angstrom Sciences, Inc) in pure argon (>99.999%) atmosphere. These deposition parameters were optimized to obtain a TCO with conductivity of $\sim$ 4500 S/cm and optical transparency of $\sim$ 90% in the visible wavelength region. (116, 117)

The films with composition (a), (c), and (d) were selected to be used as binding energy position and peak shape references in XPS studies, and were deposited using pure RF source with the same nominal conditions. Films prepared from targets (b) and (c) had atomic ratios of $\sim$ 95:5 and $\sim$ 15:85 Zn:Ga respectively, as verified by XPS. The results from target (c) are significantly different than from the expected atomic ratio of the target (50%Zn:50%Ga atomic ratio). A previous report from Yan et al. proposes a surface depletion mechanism for Zn, using the same composition target as (c), yielding a Ga:Zn ratio of 2.5. (118)

Substrates were oriented parallel to the plane of the target and centered with the race-track. The films were deposited at a substrate temperature of 250 °C, with a substrate to target distance of 68.5 mm, total power density of $\sim$ 2.2 W/cm^2, an

argon flow into the chamber of 20 sccm, and a total deposition pressure of 0.60 Pa. (119) To facilitate a good thermal contact, the substrates were attached with silver paint to the stainless steel heater block and the temperature on the front surface of the substrate was measured in-situ with a physically grounded, unshielded, k-type thermocouple to allow accurate temperature measurements during the deposition. Typically, a temperature rise of approximately 25 $^{\circ}$C is observed over the course of a deposition. The chamber base pressure prior to backfilling with argon was less than $<1.3\times10^{-4}$ Pa. Each deposition began with a 10-minute burn-in period during which the system was allowed to reach a steady-state condition before the film deposition was started. After deposition, the substrates were allowed to cool in vacuum for until the sample surface temperature was below 100 $^{\circ}$C before removal to ambient, in order to minimize strain due to a thermal gradient.

Surface Pretreatments.

Prior to use, GZO electrodes were cut from the center of the substrate, to size, and cleaned in detergent (diluted Triton X-100) followed by rinsing with deionized water. The electrodes were then successively sonicated in acetone for 10 minutes and isopropanol for 5 minutes, followed by drying in a nitrogen stream. This is referred to as the as received pretreatment in the text. Other pretreatments, described below, were performed in addition to the as received pretreatment. Electrodes pretreated with the HI etch were briefly etched using a 57% aqueous hydriodic acid solution (Aldrich) for approximately 2 seconds, followed by rinsing with purified water ($>$18 MΩ resistivity and $<$8 ppb organic content), obtained using a Waters Milli-Q UV Plus purification system (Millipore Corp) water and

drying in a nitrogen stream. The KOH etch pretreatment etched the electrodes with 6M aqueous potassium hydroxide solution (Aldrich) for 15 seconds, followed by rinsing with filtered water and drying in a stream of nitrogen. The O_2 plasma treatment was accomplished by placing as received GZO electrodes into an oxygen plasma cleaner (Harrick) for 10 minutes at 60 W power dissipation and a pressure of 40.0 Pa (300 mTorr). Argon-ion sputtering was done at $\sim 2.0\times10^{-5}$ Pa (1.5×10^{-7} Torr) for approximately 5 minutes with an acceleration voltage of 2.0 kV and a sample current of 1.5 μA, which was sufficient time for there to be no detectable C(1s) peak in angle resolved XPS. These samples are referred to as Ar sputtered; any shadowing effects from a possible increased roughness were not considered.

XPS/UPS.

XPS studies were performed with a Kratos Axis Ultra X-ray photoelectron spectrometer with a monochromatic Al Kα source at 1486.6 eV and a He(I) excitation source (21.2 eV) for UPS measurements. In the UPS experiments, a 9.00 V bias was applied to the sample to further enhance the collection of the lowest kinetic energy electrons. A separate UPS spectrum was measured for a sputter-etched, atomically clean gold sample before characterization of the GZO electrodes to ensure accurate values for the low and high kinetic edges relative to the Fermi edge. For XPS results, the biding energy calibration of the spectra is corrected using the procedure outlined by Powell, using the Au $4f_{7/2}$and Cu $2p_{3/2}$ lines, with linearity corrected using the Cu L3VV line. (120) Prior to each pretreatment, the work function and XPS peaks were measured for the as received

electrodes, in order to ensure that there were no inconsistencies between pieces of GZO that could be misinterpreted to be due to the pretreatments. In each case, the as received GZO showed the same results as reported within the manuscript, both for XPS and UPS measurements, within the allotted ± 0.1 eV error.

Kelvin Probe Measurements

Work function (Φ) measurements were made on using a Kelvin probe system (KP technology) using a gold (Au) probe in air. Work functions measured in mV was converted into eV using reference measurement done on gold (Au) and aluminum (Al) with Au (Φ) = -5.1 eV and Al(Φ)= -4.1 eV, respectively. Initial measurements were performed within 1 minute of surface treatment. The instrument has detection limit of $\sim$ 0.01 eV but there are larger errors associated with sample variations and time for measurement. The solid lines in the graph represent data points, which were recorded every 7 sec interval and markers are spaced (few minutes) for clarity.

Electrochemistry

For the electrochemical studies, decamethylferrocenium/decamethylferrocene ($Me_{10}Fc^{+/0}$), ferrocene dicarboxylic acid ($Fc(COOH)_2$), and tetrabutylammonium hexafluorophosphate (TBAHFP) were purchased from Aldrich and used without further purification. Commercial ITO electrodes were purchased from Colorado Concept Coating, LLC, with a sheet resistance of $\sim$ 15 Ω/sq and a film thickness of $\sim$ 100 nm. The ITO was cut into 1 inch squares and cleaned in detergent

(diluted Triton X-10) followed by successive sonication in 50:50 ethanol/DI water and pure ethanol. GZO electrodes were cleaned according to the pre-treatments previously described and then immediately either (i) placed in an electrochemical cell for cyclic voltammetry measurements with 1mM $Me_{10}Fc^{+/0}$ or (ii) placed in a solution for adsorption of $Fc(COOH)_2$. Adsorption of $Fc(COOH)_2$ onto the GZO and ITO electrodes was achieved by soaking the electrodes in a 1mM solution of $Fc(COOH)_2$ in pure ethanol for 1 hour and then rinsing with acetonitrile. (121) All electrochemical studies used a standard three electrode set-up with a CH1030A potentiostat (CH Instruments, Inc., Austin, TX) in 0.1 M TBAHFP in acetonitrile. The GZO or ITO working electrode, with an area of 0.1 cm^2, was placed directly across from a counter electrode of a gold foil (area = 0.76 cm^2), versus a Ag+ (0.01 M $AgNO_3$, 0.1 M TBAHFP, acetonitrile)/Ag reference electrode (Bioanalytical Systems). Charge transfer rates are reported for 100 mV/s scan rate.

Atomic Force Microscopy (AFM) Measurements

An Asylum Research Molecular Force Probe (MFP-3D) Atomic Force Microscopy (AFM) was used to determine surface morphology in tapping mode with tip radius $<$12nm, k = 40 N/m, f = 300kHz (Budget Sensors Inc Tap300DLC tip).

4.1.3 XPS Studies of Different Ga:Zn Atomic Ratio Oxides

Previous (XPS) studies of ZnO, (122) and GZO, (88) have shown at least three unique components in the O 1s core level spectra: a wurtzite lattice component

(O_I); a defect component (O_{II}); [1] and contamination that can be attributed to a multiple monolayer coverage of hydroxide, present as a component in the O 1s core level located at 1.3 - 2 eV higher binding energy than the lattice oxygen (O_{III}). There is also indication for significant contribution from surface carbonaceous species such as CO, CO_2, CO_3^{2-}, or $ZnCO_2^-$ (O_{IV}) that can be correlated with high binding energy components in the C 1s level spectra. (125, 122, 88, 9)

Despite these results, there is still much debate surrounding the defect structure of ZnO and its effect on carrier concentration and work function.The presence of Ga in non-substituted octahedral sites (126) has also been detected with support for both $ZnGa_2O_4$ (126, 127) and Ga_2O_3 domains, (128, 129, 130) suspected to lie at the grain boundaries. This is a result of the solubility limit of Ga substitution into the zinc lattice sites in ZnO, which is suggested to be as low as 2.32 wt%. (131, 127)

A series of sputter deposited oxides with different Zn:Ga ratios, in addition to the ZnO 97.5% : Ga_2O_3 2.5% ratio typical of high conductivity GZO for TCO applications, were used to evaluate the O 1s core spectra, as measured by XPS. This study is insightful in determining to what degree the O 1s contributions are ZnO-like or if the surface chemistry is changed more dramatically with increasing Ga content. Argon sputtering was used to remove the carbon contamination from the as received oxides (O_{IV}).

[1] There is some debate with regards to the origin of the defect component (O_{II}). Aside from defect components of the wurtzite ZnO lattice, it may be possibly related to plasmons, as reported for Sb-doped SnO_2 and ITO, and may also be associated with the energy loss processes due to the relaxation of the density of states near the Fermi edge, also suggested for ITO. (123, 124)

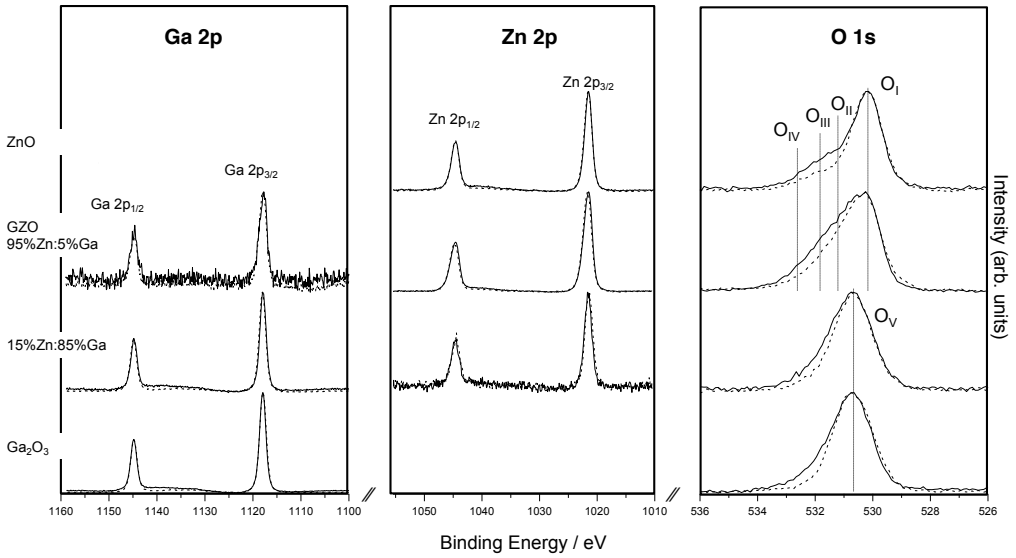

Figure 4.1: XPS results for Ga 2p, Zn 2p, and O 1s core levels for four different Zn:Ga atomic ratio oxides (100% Zn, 95%Zn:5%Ga, 15%Zn:85%Ga, and 100% Ga; from top to bottom) deposited by sputtering from a single target, with XPS data shown for as received (—) and Ar sputtered ($--$) pretreatments. The O 1s spectra have been labeled with the five different O 1s components discussed in the text: O_I (ZnO wurtzite lattice), O_{II} (defect in ZnO), O_{III} ($Zn(OH)_2$), O_{IV} (carbonaceous species such as CO, CO_2, $CO_3{}^{2-}$ etc) and O_V Ga_2O_3, a species not detected in the GZO electrode (95%Zn:5% Ga). $ZnGa_2O_4$ species discussed in previous section of the text were not detected.

Figure 4.1.3 gives the XPS results for Ga 2p, Zn 2p, and O 1s core levels for the four different oxide films of differing Zn:Ga atomic ratios (100% Zn, 95%Zn:5%Ga, 15%Zn:85%Ga, and 100% Ga) each deposited by sputtering from a single fixed composition target, with XPS data shown for as received and Ar sputtered oxides (dashed lines). The 15%:85% Zn:Ga oxide film was used to evaluate whether there were any surface effects detectable by XPS upon the inclusion of Ga_2O_3 and/or ZnGa2O4 within the grain boundaries, as detected by relative binding energies between the Zn 2p, Ga 2p, and O 1s peaks, given in Table 4.1. For all of the oxide films in Figure 4.1.3, the Zn 2p and Ga 2p peaks show no change in peak shape with changing Zn-to-Ga ratio or with Ar sputtering. However, there is a subtle shift in the binding energy difference between Ga $2p_{3/2}$ and Zn $2p_{3/2}$ for different Zn:Ga ratios, as shown in Table 4.1.

For the pure ZnO and Ga_2O_3 oxides, the difference between the Ga $2p_{3/2}$ and Zn $2p_{3/2}$ is 96.5 eV, which is also measured for the 15%Zn:85%Ga atomic ratio oxide film. However, because the relative binding energy difference is reported for two separate oxides (Zn $2p_{3/2}$ from ZnO and Ga $2p_{3/2}$ from Ga_2O_3) as opposed to a single oxide, the expected error is greater than 0.1 eV in this case. For the 95%Zn:5%Ga atomic ratio oxide, the binding energy difference between the Ga $2p_{3/2}$ and Zn $2p_{3/2}$ is only 96.3 ($\pm$ 0.1) eV. Similar differences in binding energy between the Ga $2p_{3/2}$ and Zn $2p_{3/2}$ peaks have been previously reported for bulk ceZnGa2O4 prepared by sintering mixtures of ZnO and Ga_2O_3, for which the pure stoichiometric oxide powders an energy separation of $\sim$ 96.7 eV was found, while the $ZnGa_2O_4$ compound had a binding energy difference of 96.3 eV. (132)

Table 4.1: Binding energies (eV) for O 1s, Zn 2p and Ga 2p peaks in Figure 4.1.3.

As received						
Species	$Zn2p_{3/2}$ (eV)	O1s (eV)	$Ga2p_{3/2}$ (eV)	$Zn2p_{3/2}$- O1s (eV)	$Ga2p_{3/2}$- O1s(eV)	$\Delta 2p_{3/2}$(eV)
ZnO	1021.8	530.2[a]	N/A	491.6	N/A	N/A
		531.2[b]		490.6		
		532.0[c]		489.8		
		532.9[d]		488.9		
95%Zn:5%Ga	1021.8	530.3[a]	1118.1	491.5	587.8	96.3
		531.2[b]		490.6	586.9	
		532.0[c]		489.8	586.1	
		532.9[d]		488.9	585.2	
15%Zn:85%Ga	1021.7	530.8	1118.3	490.9	587.5	96.6
Ga_2O_3	N/A	530.7	1118.3	N/A	587.6	96.5*
Ar Sputtered						
Species	$Zn2p_{3/2}$ (eV)	O1s (eV)	$Ga2p_{3/2}$ (eV)	$Zn2p_{3/2}$- O1s (eV)	$Ga2p_{3/2}$- O1s (eV)	$\Delta 2p_{3/2}$(eV)
ZnO	1021.8	530.4[a]	N/A	491.4	N/A	N/A
		531.5[b]		490.3		
		532.2[c]		489.6		
95%Zn:5%Ga	1022.0	530.4a	1118.3	491.6	587.9	96.3
		531.4[b]		490.6	586.9	
		532.2[c]		489.8	586.1	
15%Zn:85%Ga	1021.8	530.9	1118.3	490.9	587.4	96.5
Ga_2O_3	N/A	530.9	1118.3	N/A	587.4	96.5m*

Δ $2p_{3/2}$ = $Ga2p_{3/2}$-$Zn2p_{3/2}$ a) Denotes the contribution from the ZnO wurtzite lattice. b) Oxygen assumed to be adjacent to defect sites ZnO discussed in the text. c) Due to $Zn(OH)_2$ (see text). d) Results from carbonaceous components on the surface. m* Calculated by using the $Zn2p_{3/2}$ peak for pure ZnO and the $Ga2p_{3/2}$ peak for pure Ga_2O_3.

The results presented in Figure 4.1.3 and Table 1 suggest it is unlikely that a significant segregation of the Ga_2O_3 occurs within the domains for the 95%Zn:5%Ga atomic ratio oxide film. This indicates that at this 5%Ga ratio and for the RF-DC sputtered films, the Ga atoms are substitutionally replacing the Zn atoms within the wurtzite lattice, as determined within the sensitivity of the XPS measurement technique.

Unlike the metal 2p peaks, there are more significant peak shape differences in O 1s core levels that coincide with changes in Zn:Ga ratios. There is also a general decrease in peak width for Ar sputtered materials, where some surface carbon contamination species have been removed. This suggests that photoemission from the O 1s core level is extremely sensitive to local Zn:Ga ratios and surface state environments, while core metallic peaks (Zn 2p and Ga 2p) are only minimally influenced by changing metal ratios. As the Ga concentration increases within the film, the O 1s peaks shift to higher binding energy, resulting in a decrease in the Zn $2p_{3/2}$-O1s and Ga $2p_{3/2}$-O 1s binding energies. The O 1s peaks also broaden into a more asymmetric line shape, indicating an increasing degree of disorder within the material. Ga_2O_3 is known to be polymorphic, similar to Al_2O_3. (133) The β-form is the most prevalent crystalline phase, (134) which is monotropic and known to be thermodynamically stable at all temperatures, appearing in both monoclinic and orthorhombic systems. (135) There is little evidence within the XPS data for the formation of alternative oxides (such as GaO), but unlike ZnO, there is also no suggestion of hydrates (Ga_2O_3:xH_2O), hydroxyls, or defect species.

In Figure 4.1.3, the different oxygen surface species are most dramatic for the high zinc content oxides, as shown in the multi-component shoulders of the O 1s peaks. For pure ZnO, aside from the prominent peak at $\sim$ 530.2 eV (O_I), there is a clear shoulder at $\sim$ 532.0 eV binding energy for the O 1s, which is associated with the presence of $Zn(OH)_2$ surface states, O_{III}. This O 1s relative binding energy (with respect to the O^{2-} ions for the wurtzite lattice component O_I) has also been suggested for peroxides for transition metals. (136) However, given the rigorous treatment required for the formation of ZnO_2, (137) we eliminate the possibility for significant contributions from a zinc peroxide species. While this ZnO substrate has no extrinsic substitutional dopant (i.e. Ga), we do expect the ZnO to have a number of carriers generated by intrinsic defects. Binding energy shifts are hence smaller than what would be predicted for a more stoichiometric ZnO when compared with the extrinsically doped ZnO.

For the 95%Zn:5%Ga atomic ratio oxide film, the O 1s peak is also broad, indicating the presence of a significant amount of defect states within the film and requiring a peak at 531.2 eV (O_{II}) in addition to the O_I and O_{III} peaks; this peak is also present to a lesser degree in the pure ZnO. It has been previously suggested that the inclusion of extrinsic doping of ZnO with Group XIII elements can result in the formation of zinc vacancies or the oxidation of the dopant metal to its corresponding oxide (Ga_2O_3), resulting in electron traps. (138, 139, 9) The O_{II} peak in ZnO and low Ga content ZnO suggests that its presence is not attributed to the formation of Ga_2O_3 domains within the film consistent with the conclusions from the analysis of the metal 2p peaks (Ga $2p_{3/2}$ Zn $2p_{3/2}$). Furthermore, high Ga content oxide films have more prominent O 1s peak at a binding energy of 530.9 eV (O_V),

which is neither associated with the defect O_{II} peak nor the ZnO O_I peak. The O 1s core spectra and the resultant $Ga2p_{3/2}$ - $Zn2p_{3/2}$ binding energy differences all indicate that the defects created within the GZO films are inherent to ZnO and possibly are associated with oxygen interstitials or zinc vacancies within the film. It may be possible that with the inclusion of the Ga at low donor concentrations, the oxide has a lowered formation enthalpy for intrinsic acceptors. This would result in an increase in zinc vacancies and oxygen interstitials (37, 140) and an increase in the contribution of O_{II} to the overall O 1s line shape compared to the pure ZnO film.

The results above indicate there is a four-component model that can be used to describe the O 1s spectrum for the GZO electrodes. The defect component (O_{II}) is not considered to be directly related to the formation of Ga_2O_3 domains within the film, but is attributed to deviations from the ZnO lattice (O_I). There are also contributions from hydroxyls chemisorbed to the surface of all of the presented ZnO-based films (O_{III}) and contributions from carbon contamination species (O_{IV}). Using this fit, we can correlate the relative coverages of surface components on the GZO electrodes exposed to various pre-treatments with changes in work function and electrochemical charge transfer kinetics.

4.1.4 XPS Studies As-received and Pre-treated GZO Films

In order to evaluate the influence of the near surface composition of GZO electrodes on work function and electron charge transfer rates, various pre-treatments were used to change the local surface coverage of hydroxyls/hydrates and carbonaceous surface components (CO, CO_2, etc.) adsorbed at the electrode

surface. We have focused these studies on the 95%Zn:5%Ga atomic ratio films because the lower Ga content GZO films were found to be best suited as TCOs for OPV and OLED applications. (47, 18)

Ar−ion sputtering is well known to remove carbonaceous impurities, and in the case of some oxides, can also remove hydroxyl groups within ultra-high vacuum. O_2 plasma treatment is a popular surface treatment for oxides; by bombarding the surface with O^- atoms, oxygen vacancies (V_O) may be populated and surface adsorbates removed. An acid (HI) and base (KOH) etch were used to locally control the hydroxyl coverage, and Ga/Zn ratios at the surface. ZnO undergoes dissolution in acidic solutions and hydroxylation under basic conditions; it has been suggested that Ga_2O_3 undergoes dissolution under high pH conditions. (108)

Figure 4.1.4 gives the XPS results for the O 1s peaks for the GZO films following each pretreatment, with the left-hand panel showing the normal take off angle XPS results and the right-hand panel showing more surface sensitive XPS results at a 60^0 take off angle. Peak fitting was used to evaluate the ratio of the lattice oxide to hydroxide on the surface, which was found to vary with pretreatment conditions. All of the peaks were fit with the same model developed for ZnO above, with the minimum number of components (70% Gaussian, 30% Lorentzian) to provide a reasonable agreement between the experimental data and the resulting fit. Binding energy and peak full width half maximum values were constrained and only the heights of the different components were allowed to vary. Parameters for O 1s core fits are given in Table 4.2 along with Zn:Ga atomic percentage ratios measured for the areas of the Ga $2p_{3/2}$ and Zn$2p_{3/2}$ peaks.

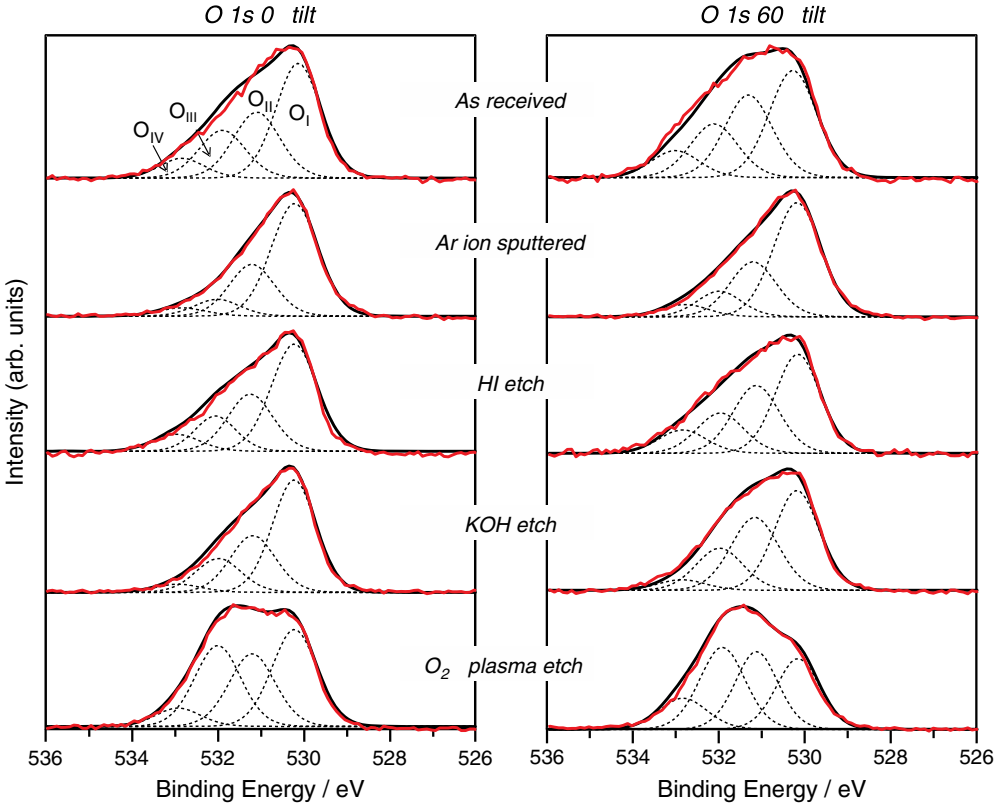

Figure 4.2: Normal (left-hand panel) and angle (right-hand panel) resolved XPS for the O 1s core electrons of GZO exposed to different surface pretreatments. Peak fits are discussed in the text and relative areas and binding energies are given in Table 4.2.

Table 4.2: Binding energy (eV) and atomic percentage of total O 1s fit (% = $\frac{O1s_{peak}}{O1s_{Total}}$) for the different pretreatments of GZO electrodes and Ga to Zn atomic percentages.

Normal XPS

Pretreatment	As received		Ar sputtered		HI etch		KOH etch		O_2plasma	
	eV	%	eV	%	eV	%	eV	%	eV	%
O 1s I	530.2	45.5	530.3	60.1	530.3	50.6	530.3	52.1	530.3	35.7
O 1s II	531.2	27.0	531.3	26.8	531.3	26.4	531.3	27.5	531.3	27.2
O 1s III	532.0	19.6	532.1	8.7	532.1	14.9	532.1	16.4	532.1	30.3
O 1s IV	532.9	7.9	532.9	4.5	533.0	8.1	533.0	4.0	533.0	6.8
Ga:Zn ratio	4.8:95.2		5.6:94.4		6.7:93.3		4.3:95.7		5.0:95.0	

Angle resolved XPS

Pretreatment	As received		Ar sputtered		HI etch		KOH etch		O_2plasma	
	eV	%	eV	%	eV	%	eV	%	eV	%
O 1s I	530.4	39.4	530.3	55.9	530.2	41.8	530.3	42.8	530.2	26.5
O 1s II	531.4	30.6	531.3	26.4	531.2	29.8	531.3	33.5	531.2	28.6
O 1s III	532.2	19.9	532.1	11.8	532.0	17.8	532.1	19.0	532.0	32.1
O 1s IV	533.1	10.0	532.9	5.9	532.96	10.6	533.0	4.8	532.9	12.7
Ga:Zn ratio	4.6:95.4		5.7:94.3		6.5:93.5		2.2:97.8		4.0:96.0	

For all pretreatments, the difference in binding energy between the Ga2p$_{3/2}$ and Zn2p$_{3/2}$ peaks was 96.3 ($\pm$ 0.1 eV). The Ar-ion sputtering treatment resulted in the lowest hydroxylated species coverage (O_{III}) but still had residual carbon species left on the surface (O_{IV}). The hydroxyl coverages for the as received, KOH etch, and HI etch were all comparable, within the error of the fit, while the O_2 plasma treatment had the highest O_{III} and O_{IV} peak percentage contributions, indicating these films have the highest coverages of surface adsorbates. As expected, the HI etch treatment changed the Zn:Ga ratio by etching away some of the Zn surface species. Conversely, the KOH etch increased the local surface concentration of Zn atoms relative to the Ga species in comparison to the as received electrode. As summarized above, the differences in these surface species can directly impact surface conductivities and work functions of the material. The role of the surface adsorbate species and metal atomic compositions on work function and charge transfer rates will be discussed below.

4.1.5 UPS Studies of As-received and Pre-treated GZO Films

A very important surface property for the incorporation of TCOs in organic photovoltaics is the work function of the TCO prior to subsequent formation of the oxide/organic interface. By controlling the work function of the TCO, one can locally control thermionic emission and Schottky barrier formation for non-ohmic contacts (Metal-Insulator-Metal model) and the extent of charge transfer between the oxide and the organic layer (Integer charge transfer model). (102, 141, 142, 143) In the case of non-Fermi level pinning (non-ohmic contacts), the work function difference of the contacting electrodes can limit the open-circuit

voltage realized in an organic photovoltaic device. (102, 144) For oxides, changes in the bulk crystal structure that are propagated to the surface can yield changes in work function. The inclusion of Group XIII metals in ZnO results in a decreased work function (movement of the Fermi level toward the conduction band edge) due to the donation of excess electrons not required for bonding. However, the movement of the Fermi energy results in a lowering of the defect formation enthalpy and an increase in the local defect concentration. (9) In the case of GZO, self-compensation mechanisms can result in the formation of intrinsic acceptors, thus limiting the doping of the GZO electrodes. (9, 145, 146) But doping can also be limited by the oxidation of the dopant metal to its corresponding oxide, resulting in electron trap sites. (147, 9) Therefore, controlled doping of the oxide results in an increase in carrier density and in the case of GZO, a lowering of the work function. In contrast, increased doping beyond the solubility limit of the dopant results in electron trapping and a net decrease in overall conductivity. (9)

For oxides, the work function is extremely sensitive to the surface states of the oxide. Differences in adsorbates, surface reconstructions, and point defect densities can all result in changes in the surface work function of the oxide. (36) It is well known that local changes in concentration and orientation of dipoles in the near surface region can impact the effective work function of the material. (148) Surface dipoles can result from numerous factors including: charge transfer, mirror forces, rearrangement of the electron cloud at the surface, strong chemical interactions, interfacial states, and permanent dipoles, as detailed by a recent review by Ishii et. al. (148)

Detailed studies on the chemisorption of small gas molecules onto polar (0001) and (0001) and non-polar (1010) (1010) single crystal ZnO surfaces reveal that there are influential changes in work function depending on the dipole of the adsorbate. (115) For example, O_2 interacts weakly with all of the surfaces at temperatures between 300 and 650 K, with chemisorption occurring via charge transfer at the surface and the formation of adsorbed O^{2-}. (149, 36)

This results in an upwards shift in the local vacuum level and an increase in effective work function. However, coverages are low ($\sim 2.5\times10^{-4}$ monolayers) and O_2 chemisorption has been attributed predominantly to defect sites (oxygen vacancies). (36) CO was found to adsorb onto surface Zn atoms (as determined from the comparable heat of adsorption for CO on both ZnO (0001) and (0001) crystal faces) and increases the observed work function by $\sim$ 0.2-0.3 eV. (150, 36)

The changes in photoemission spectra were attributed to the formation of both CO_2 at the oxygen vacancy sites and surface carbonate species CO_3j^{2-}, with the same species detected for CO_2 adsorption on ZnO (0001). (150) However, work function was shown to increase by $\sim$ 0.8 eV for CO_2 adsorption but only 0.2 eV for CO adsorption. (150, 36) Adsorption of water is assumed to occur via its O atom at an on-top site above the Zn surface atoms and shows distinct changes to valence band O 2p structure for both polar surfaces of ZnO single crystals measured by UPS. (151) Adsorbed water is expected to dissociate to a hydroxyl with the other H bonding to the surface O ion as the H+ species. (36) The driving force for water dissociation is the stabilization of the surface O ions by the adsorbate relative to the clean surface. (36) Therefore, by combining both work function information from

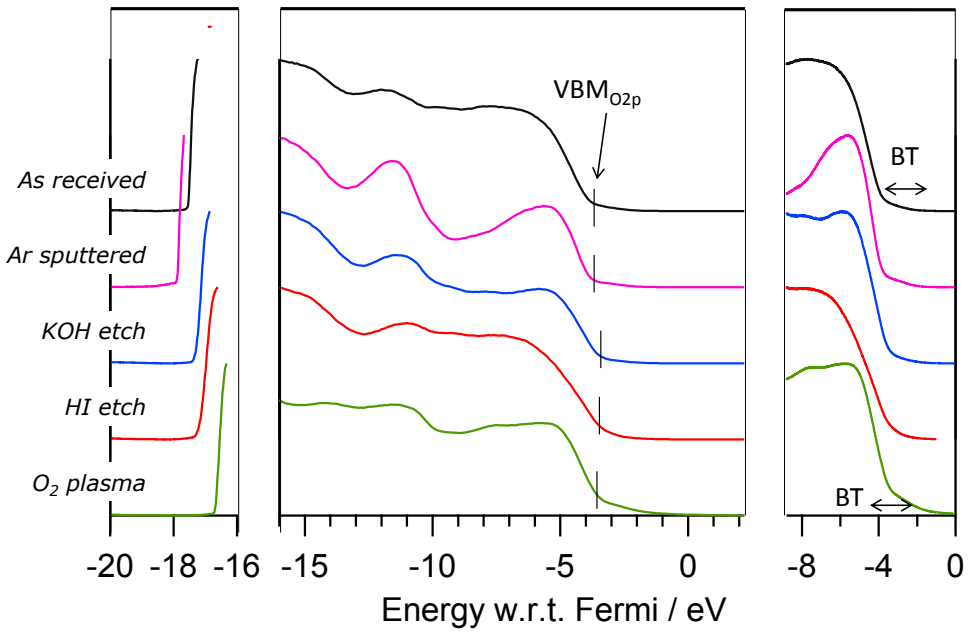

Figure 4.3: Ultraviolet photoemission spectroscopy (UPS) measurements of GZO electrodes exposed to different surface pretreatments, as labeled in panel iii. Panel i shows the high binding energy (low kinetic energy) edge of the secondary electrons, panel ii shows the valence structure of the different pretreatments, and panel iii gives the near-Fermi edge for each pretreatment.

UPS with normal and angle resolved XPS measurements, we can develop a clearer understanding of the role of surface and bulk defect states on the changes in work function of the material.

Figure 4.1.5 shows the UPS results for the as received GZO films, as well as films exposed to the four different pretreatments: Ar-ion sputtering, O_2 plasma, HI etch, and KOH etch; data is plotted as binding energy with respect to (w.r.t.) the Fermi level. Figure 4.1.5 shows the corresponding energy band diagram for each of the different GZO electrodes. The different ZnO pretreatments result in unique valence band profiles, as demonstrated in the center panel of Figure 4.1.5.

The large peak at approximately 10 to 11 eV below the Fermi is associated with the filled Zn 3d band, while the valence band appears at binding energies between 4 to 8 eV. The lower binding energy (3-5 eV) is attributed to the non-bonding O 2p orbitals while bonding combinations from O 2p and Zn 4s orbitals appear at slightly higher binding energies (5 to 8 eV). (36)

ZnO has been well characterized using UPS, with evidence for differences in emission associated with different crystallographic surfaces and adsorbates. (115) The shifts in the binding energies of the valence structure correlate with changes in the ionization potential. There are two key regions that will be discussed: the first, closest to both the Fermi level and the vacuum level (E_{vac}) are referred to as interband or band tail states (BT). The BT states are low density of states that extend from the valence band into the gap of the TCO and result from disorder in the system, and measured at $\sim$ 3 to 4 eV below the vacuum level (E_{vac}). The second feature is the deeper state ionization potential and is associated with the valence band maximum, as defined by the oxygen 2p of the ZnO valence band (VBM_{O2p}) at $\sim$ 7 eV below E_{vac}.

The work function (ϕ) of the GZO is measured as the energetic difference between the Fermi level (E_F) and E_{vac}. For the as received GZO, the O 2p valence structure is rather broad, spanning more than 5 eV, with little distinction between bonding and non-bonding regions. Ar sputtering appears to reduce the oxide slightly, lowering both its BT states and work function while narrowing both the Zn 3d and O 2p bands and shifting both bands to a lower binding energy by just under 2 eV (closer to the Fermi level) compared to the as received GZO. The

prominence of the Zn 3d and O 2p suggests a more homogenous oxide surface, with an energetically narrower distribution of states, with the removal of carbon contributions and a decrease in surface hydroxyls consistent with the XPS data.

A similar effect of peak narrowing and movement of the valence bands to lower binding energies is also seen following the KOH etch, but to a lesser degree than for the Ar sputtered films. For the KOH etch, however, the Zn 3d is shifted to an even lower binding energy than the Ar sputtered surface, while the O 2p valence band remains in a comparable position. This is again consistent with the XPS results shown in Figure 4.1.4. However, this base etch also yields a subtle increase in the work function and ionization potential relative to the as received GZO electrode.

By comparing the Ar sputtered and KOH surface treatments there is clear evidence of a significant change in the surface dipole. The UPS data following HI etch has a similar broad O 2p peak to the as received GZO, but has a Zn 3d peak at approximately 11 eV below the Fermi level. The XPS data in Figure 4.1.4 shows a slightly higher surface concentration of O 1s surface species (O_{III} and O_{IV}), which yields a slightly higher surface dipole and thus, only a subtle increase in both work function and BT states compared to the KOH etched film.

The O_2 plasma treatment appears to oxidize the GZO electrode and showed the largest shift in work function and ionization potential. The UPS measurements indicate a more prevalent contribution from bonding O 2p and Zn 4s orbitals, while the Zn 3d peak has a subtle shift to lower binding energy, comparable to the Ar sputtered film. From XPS, we see that the O_2 plasma treatment dramatically

changes the GZO surface, increasing both the hydroxyl (O $1s_{III}$) and carbon (O $1s_{IV}$) contamination peaks. This should result in an increase in work function and ionization potential, as verified by UPS and summarized in Figure 4.1.5. The increase in surface contamination is most likely due to the enhanced reactivity of the electrode upon removal from the O_2 plasma cleaner followed by brief exposure to ambient conditions. Future work will focus on evaluation of the effects of O_2 plasma treatment on the GZO electrode with and without ambient exposure.

From Figure 4.1.5, there is a general decrease in work function for all the GZO electrodes compared to ZnO, which has a reported work function ranging from 4.4 to 4.6 eV for clean single crystals. (112) This is expected from the doping strategy for Group XIII elements in ZnO. The substitution of Ga into Zn sites within the wurtzite crystal structure further n-dopes the ZnO, raising the Fermi level closer to the conduction band. However, like the ZnO counterpart, the work function of GZO is extremely sensitive to surface defects and adsorbates. From the XPS results in Figure 4.1.4, O_2 plasma treated GZO has the greatest coverage of hydroxyls and carbonaceous surface components.

All these surface contaminants have been reported to increase the work function for ZnO through surface dipole effects, (36) resulting in the highest work function (ϕ $\sim$4.5 eV). Ar-ion sputtered films have the least coverage of surface species, and as a result, has the lowest work function at $\sim$ 3.3 eV. One may expect that by locally increasing the Ga concentration through the use of an acid etch, the effective work function may increase due to an increase in the higher work function insulating material. However, there is little difference in the work function of $\sim$

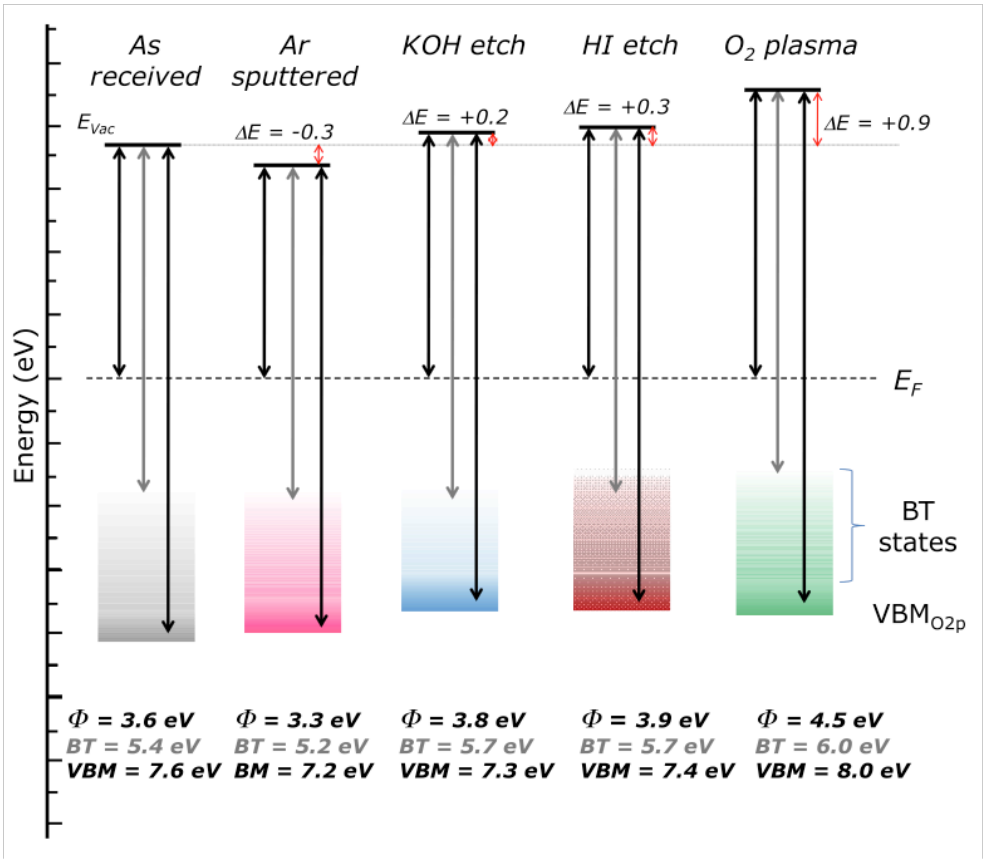

Figure 4.4: Energy band diagrams based on UPS measurements of GZO electrodes following different surface pretreatments. Work function (ϕ) is calculated as the energy from the Fermi level (EF) to the vacuum level (E_{vac}). The band tail states (BT state) are representative of the near Fermi edge states ($\sim$ 2 eV below the EF) and the ionization potential from the valance band O_{2p} states (VBM_{O2p}) are fit to the O 2p edge of the GZO electrode ($\sim$ 3.5 to 4 eV below EF).

6.5% Ga to 93.5% Zn surface following HI etch (ϕ ~3.9 eV) compared to the ~ 2.2% Ga to 97.8% Zn surface following KOH etch (ϕ ~3.8 eV), while both the acid and base etched surfaces have similar coverages of O $1s_{III}$and O $1s_{IV}$ peaks. The results above indicate a clear correlation in the effective work function of the electrode with the coverages of surface components and may play a critical role in charge transfer rates for organic photovoltaics.

This suggests that in order to effectively incorporate GZO electrodes in organic photovoltaics, there is a need to control the surface composition of the electrode as well as tune bulk properties. The stabilities of the work functions with regard to pretreatments were also evaluated by Kelvin probe to measure the change in work function of the electrode with respect to time. Figure 4.1.5 gives the change in work function with time, as recorded every seven seconds; the $\Delta\phi$ is referenced with respect to the initial time measurement. From the plots in Figure 4.1.5, it is clear that all pretreatments are not equal with respect to time. The O_2-plasma treatment shows a sharp decrease in work function ($\Delta\phi$ ~ -0.2) within the first 1×10^3 seconds (15 minutes), indicating a high reactivity of the surface with ambient species. The acid etch was found to be the most stable with respect to time, with little change in the work function with respect to time.

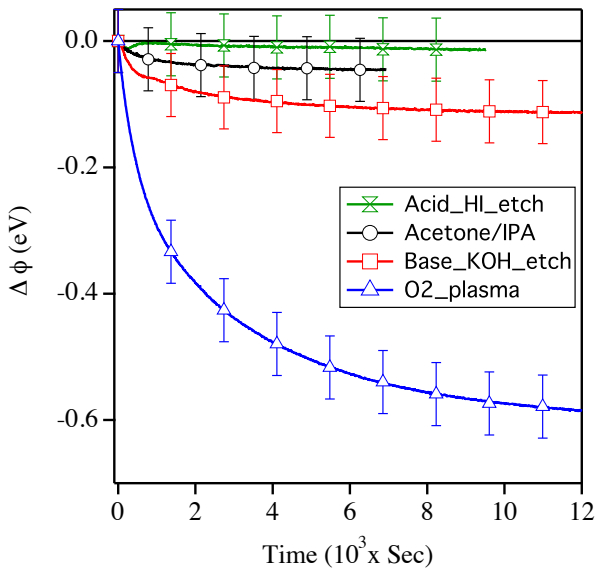

Figure 4.5: Change in work function ($\Delta\ \phi$) with respect to time for each of the different pretreatments, as measured by Kelvin probe, for GZO electrodes. Markers are spaced for clarity.

4.1.6 Electrochemical Activities of As-received and Pre-treated GZO Electrodes

The electrochemical reactivity of adsorbed probe molecules on TCO surfaces can be used to understand further how changes in near-surface composition can impact electrical properties, and charge transfer rates at an organic/oxide heterojunction which may be relevant for OPV devices. (101) Tables 4.3 and 4.4 present the results for electrochemical charge transfer rate measurements for the different pretreatments, using the redox probe $Me_{10}Fc^{+/0}$ which undergoes simple, outer-sphere one-electron oxidation/reduction (Table 4.3), and a chemisorbed redox probe $Fc(COOH)_2$ (Table 4.4).Also given in Tables 4.3 and 4.4 are the cyclic voltammogram peak separation used to estimate the charge transfer rates

Table 4.3: Electrochemical response for $\mathrm{Me_{10}Fc}$.

Electrode	Δ Ep (mV)	$k_{s,apparent}$ (cm/s) x 10^3	Relative OH conc.*
As received	140 ($\pm$ 4)	3.7 ($\pm$ 0.2)	19.9
HI etch	190 ($\pm$ 6)	2.1 ($\pm$ 0.2)	17.8
KOH etch	190 ($\pm$ 8)	2.1 ($\pm$ 0.3)	19.0
O_2 plasma	$>$800	N/A	32.1
ITO (as received)	120 ($\pm$3)	5.3 ($\pm$0.3)	N/A
Gold	102 ($\pm$2)	8.1 ($\pm$0.5)	N/A

* O1 speak III /O (1s)Total in Figure 4.1.4 and Table 4.2.

($k_{apparent}$), the surface coverages achieved for adsorbed Fc(COOH)$_2$ on GZO, and the relative hydroxyl coverages and metal ratios estimated from XPS for the different pretreatments. For both sets of redox probes, charge transfer rates for as received ITO electrodes are included for comparison.

The influence of pretreatments on ITO electrodes has been summarized elsewhere. (101, 103, 100) All voltammetric measurements were collected at 100 mV/s in 0.1 M TBAHFP in acetonitrile. Me10Fc$+/0$ was chosen as a redox probe to study charge transfer reactions at the GZO electrode surfaces because it has been found to be a superior redox probe in studying solvent effects on the thermodynamics of charge transfer rates. (152) Electron transfer rates were estimated using the Nicholson method, (153) with a diffusion coefficient for $Me_{10}Fc^{+/0}$ of 1.8$\times$ 10^{-5} cm^2/s (154) in 1 mM $Me_{10}Fc^{+/0}$ and 0.1 M TBAHFP in acetonitrile at a scan rate of 100 mV/s. Figure 5, all pretreatments for the GZO electrodes have lower current densities (Appendix) and slower rates of electron transfer ($k_{apparent}$, cm/s) than ITO for $Me_{10}Fc^{+/0}$, as indicated by the larger peak separations (Ep).

Table 4.4: Electrochemical response of chemisorbed $Fc(COOH)_2$.

Treatment	Δ Ep (mV)	Γx10^{-10} (mols/cm^2)	Redox potential (V vs Ag/Ag+)	e^- transfer rate (/s)	Relative OH conc.*
ITO	168±8	2.7 ± 0.3	0.39	0.42±0.04	-
As received	176±4	2.7 ± 0.4	0.36	0.38±0.01	19.9
O_2 plasma	144±4	3.0 ± 0.4	0.34	0.55±0.02	32.1
HI etch	197±2	3.1 ± 0.2	0.40	0.30±0.01	17.8
KOH etch	155±5	3.5 ± 0.2	0.46	0.48±0.03	19.0

*O1 $s_{peakIII}$/O (1s)$_{Total}$ in Figure 4.1.4 and Table 4.2

It is interesting to note that by changing the local surface concentration of Zn:Ga with the KOH etch (increase the zinc concentration) and the HI etch (increases the gallium concentration), there is little difference in charge transfer rates. From Table 4.3, the outer sphere charge transfer rates correlate loosely with the relative hydroxyl and carbonaceous concentration on the surface; the higher the concentration of hydroxyls and carbonaceous species (O_{III} and O_{IV}), the less the probe molecule is able to interact with the electrode. This is due to the large steric hindrance of the methyl groups on the ferrocene molecule and the solvent sphere surrounding the probe molecule, which minimize the degree of interaction with the electrode, reducing charge transfer rates. Hydroxide coverages for as received ITO electrodes have been previously reported to be $\sim 25\%$. (101) The correlation with surface species coverage and the lack of impact with Zn:Ga ratio changes suggests that the surface species have a more blocking role on the rate of charge transfer and that the Zn:Ga ratio is less important for an outer sphere electron transfer reactions.

AFM measurements for each of the pretreated electrodes show no statistical difference in roughness between the as received, base-etched, and O_2-plasma treated electrodes (RMS$\sim$ 2 nm) is shown in Figure 4.6. There was a slightly larger

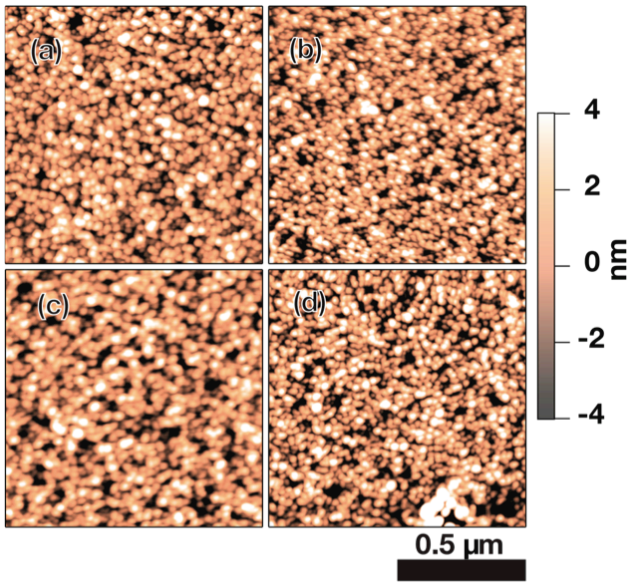

Figure 4.6: AFM images of the GZO electrodes post treatment (a) as received :1.8 $\pm$ 0.2 nm (b) O_2-plasma treated: 1.9 $\pm$ 0.2 nm, (c) base etched: 2.4 $\pm$ 0.2 nm and (d) acid etched: 3.0 $\pm$ 0.4 nm.

surface roughness for the acid-etched electrode (RMS$\sim$ 3 nm). An enhancement in roughness is expected to increase the overall surface area of the electrode, resulting in an increase in overall current density. No statistically different current density was observed, suggesting that the subtle increase in roughness is not impacting the performance of the electrode. Therefore, it is concluded that the pretreatments, as described, do not significantly alter the surface morphologies. For ITO electrodes, it has previously been shown that chemisorbed ferrocenes can be used to probe the changes in electrochemical activity of the surfaces as a function of pretreatment, which show dependence on the surface composition of the ITO film. (155)

Surface composition influences both the coverages and electron transfer rates, but a more systematic study with respect to surface hydroxyls suggests little

correlation between hydroxyl surface coverage and charge transfer rates (101) and a more direct correlation with the local concentration of Sn sites. (100) Table 4.4 gives the corresponding coverages and charge transfer rates ($k_{apparent}$, s-1) for tethered $Fc(COOH)_2$ monolayers on GZO electrodes with respect to different pretreatments and for a commercial ITO electrode at a scan rate of 100 mV/s in 0.1 M TBAHFP in acetonitrile (cyclic voltammograms given in the Appendix). All coverages are less than a single monolayer, with a close packed monolayer having a coverage of $\sim 4\times10^{-10}$ mol/cm^2. (121) Electron transfer rates were calculated using the Laviron method, (156) with redox potentials measured at the midpoint of the cyclic voltammogram.

In the case of a tethered carboxylic acid, coverages are greater than the ITO commercial electrode and appear to be independent of relative hydroxyl coverages on the surface of the electrode. Charge transfer rates are also independent of both hydroxyl and monolayer coverages, with the highest rate of charge transfer being for the O_2 plasma treated GZO electrode. Increasing the local surface concentration of gallium (by HI etch) yields comparable monolayer coverages to other pretreatments, but has the lowest rate of electron transfer. This suggests the gallium sites are acting to reduce the rate of charge transfer at the surface.Increasing the zinc oxide and zinc hydroxide concentrations at the surface shows an increase in charge transfer rates (in the following order, from lowest to highest: HI etched, to as received, and to KOH etched). The increase in charge transfer rates suggests that the zinc sites have a prominent role in charge transfer rates at the surface.

The results of the studies of tethered electrochemical redox probes suggest that in order for GZO electrodes to be a viable alternative to ITO electrodes without the use of additional charge transport layers, a direct interaction with the GZO surface is required for subsequent organic layers, most likely through bonding. We suspect that the carboxylic acid from the $Fc(COOH)_2$ slowly etches the hydrolyzed zinc oxide species at the near surface region and thereby increases the fractional area that is truly electroactive; an analogous phenomenon has been proposed for ITO electrodes. (157) Thus, we see an enhanced rate of electron transfer from the inner sphere, tethered redox probe molecule $Fc(COOH)_2$ when compared to the charge transfer rates for the solution outer sphere redox probe $\mathrm{Me}_{10}\mathrm{Fc} + /0$.

4.1.7 Conclusions

From this work, we observe generally that the electronic charge transfer properties of GZO are not radically different from ITO materials, but that the role of the surface states for ZnO based TCOs is vital for understanding the charge transfer rates that are relevant to organic device systems. This appears to be of particular importance in organic photovoltaics, in which efficient charge transfer is critical for device performance. This work demonstrates that inclusion of a substitutional dopant, Ga, to form a GZO electrode, results in a complex surface chemistry different from the already rich chemistry of ZnO generated by, lattice defects, as well as products resulting from reaction with ambient surroundings, all of which can be manipulated through different surface pretreatments. The products, derived from hydrolysis and carbonaceous species that dominate changes in surface work function of the GZO electrode, can be altered, potentially in

advantageous ways, to influence energetic barrier-controlled charge transfer rates in organic photovoltaics. Specifically through manipulation of the surface dipole generated by the local electron cloud of the substrate and adsorbates, the work functions for the GZO electrode can be varied from as low as 3.3 eV for Ar-ion sputtered electrodes and as high as 4.5 eV for O_2 plasma etched surfaces. The coverage of hydroxyls at the surface of the GZO electrodes is demonstrated to be directly linked to a reduction of the measured outer sphere charge transfer rates, where by systematically increasing hydroxyl surface coverage, charge transfer rates are found to decrease. In contrast, for inner sphere, tethered species, charge transfer rates were found to be independent of the hydroxyl surface coverage but well correlated to changes in the surface Zn:Ga ratios, suggesting that for a GZO electrode in a device such as an OPV, lower Ga surface content may be more favorable. Despite, these clear results the underling mechanism and hence routes to manipulate these properties remains unclear: the hydroxyls may be acting purely as an electron blocking layer to a probe molecule undergoing outer sphere electron transfer, or the induced dipole at the surface may result in a local change in electric field directly at the electrode surface which alters the rates of electron transfer.

Future work will focus on the systematic modification of the GZO electrode surface with different linkage groups in a further effort to understand the role of surface states on the charge transfer rates of GZO electrodes for organic optoelectronic applications through observed changes in wettability, redox activity and surface work function upon modification.

4.2 Effect of Surface Pretreatment on Surface Passivation on Amorphous Indium Zinc Oxide (IZO)

Abstract: Indium Zinc Oxide (IZO) electrodes show promise as replacement transparent conductive oxides (TCOs) for indium tin oxide (ITO) electrodes due to more resilient mechanical properties, amorphous phase with lack of grain boundaries providing superior water vapor transmission rate and high mobilities (μ), and deposition in room temperature allowing it to be incorporated in flexible substrates. The incorporation of amorphous IZO thin film into devices have not been straightforward due to complex surface chemistry of In_2O_3/ZnO and the surface conductivity and work function are variable due to charge transfer and band bending caused by adsorbates. In order to fully understand the role of these electrodes for organic photovoltaic applications, it is necessary to understand the near-surface composition correlated with the electrical and electrochemical properties of IZO electrodes after various pretreatment conditions. IZO films with Zn:In atomic ratios of (20:80 ZnO:In_2O_3) were prepared by magnetron RF superimposed DC sputtering. The surface is characterized using monochromatic X-ray photoelectron spectroscopy (XPS) and ultraviolet photoelectron spectroscopy (UPS) with respect to the following surface pretreatments: i) KOH etch, ii)RF oxygen plasma etching, iii) UV ozone and iv) high-vacuum argon-ion sputtering. Elemental peak fitting was used to evaluate the ratio of the stoichiometric oxides to hydroxides on the surface, which was found to vary depending on the pretreatment conditions. KOH etching, O_2plasma and UV ozone increase the work function and ionization potential of the IZO elec-

trode by $\sim$ 0.1 to 0.3 eV, but result in different near surface compositions of the metal atoms. Where as high-vacuum argon-ion sputtering resulted in lower work function and ionization potential. Small variations in atomic In:Zn ratios are found to have little impact on the work function of the electrode, but significantly influence inner sphere charge transfer rates. KOH etch yielded the surface with similar In:Zn ratio as the bulk, and had least amount of carbonaceous impurities as well. It had the highest rate of electron transfer rate as measured by cyclic voltammetry, and low turn on voltage and ohmic contact measured by conductive AFM.

4.2.1 Introduction

Currently, most of the solar cell devices employ poly-crystalline ITO as transparent electrode. (158) Poly-crystalline TCOs such as ITO, AZO, GZO, FTO have good conductivity (σ) due to large number of carriers. However, amorphous oxides with lack of grain boundaries have demonstrated superior water vapor transmission rate (159) and high mobilities (μ) compare to poly-crystalline oxides, which can be a critical factor for some device application. (160) Plus, amorphous TCOs such as IZO, IGZO (161) have more resilient mechanical properties, and can be deposited at room temperature thus making them attractive for incorporation into flexible electronics. (162, 163, 164) These applications as well as others in which a flexible form factor is desirable have already generated a considerable amount of effort on amorphous InZnO, ZnSnO and related material systems by our research group as well as others. (165, 166, 167)

Organic Photovoltaic Devices (OPV) show a great promise in solving our rising energy demands due to the potential for low material cost, lightweight with high

flexibility, (168) and have been shown to be compatible for roll to roll processing. (169) OPV devices using low work function metals such as Ca/Al in standard geometry do provide good electrode for electron collection, but bigger problem using low work-function metal electrode is with formation of non-conductive metal oxide due to oxidation resulting in rapid device failure. (13, 170) Recently, using low work-function, air stable, conductive metal oxides such as ZnO, (170) TiO_2, ZTO (167), in combination with other TCOs and standalone AZO (22), IZO (171) as an electron collecting electrode has been on the rise. (172, 173) One of the key hurdle in increasing overall device performance is poor charge collection at the oxide/inorganic interface.

Amorphous phase IZO has good transparency ($>90\%$) and conductivity $\sim$ 3000 S/cm, (174) shallow work-function (4.2 eV to 4.6 eV) and can be deposited at room temperature on flexible substrates, (74, 175) thus making it a good candidate in organic photovoltaics (OPVs) for electrode to provide matching energy alignment of interest. With mobilities $>$100 cm^2/Vs, amorphous IZO has been incorporated very well in thin film transistors (176, 177) as well as various other solar cells. (178) Amorphous IZO thin film can be fabricated in room temperature, and allows better option of incorporating it in flexible substrates for organic photovoltaic (OPV) devices, but only handful of studies are reported with IZO as transparent electrode in OPV. This lack in enthusiasm on IZO incorporation in OPV device study may be due to poor understanding of TCO/organic interface.

Majority of research on OPV with standard architecture, despite various problems, (179) still employ acidic PEDOT:PSS as hole transport layer, which

unfortunately is incompatible with IZO or ZnO based TCOs. That problem may be mitigated with use of various oxide semiconductors (NiOx (25, 180), MoOx (26), CoZnO (20), CoNiO (17)) function as hole transport layer. Since these oxide layers for surface modification have to be ultra thin, depositing them in ITO with poor electrical heterogeneity with surface roughness rms $>$ 3 nm has been tricky (100). IZO or amorphous TCOs in general may be a better alternative with smooth rms roughness ($\sim$ 0.2 nm).

A lot of research has been focused on optimizing IZO especially the bulk properties including electronic and optical properties. Good electrical property, especially the high electron mobility in IZO, amorphous TCOs in general, is thought to arise from the direct spatial overlap of the large spherical s-orbitals which make the conduction band. (163, 181) In TFTs, amorphous TCOs are known to have higher contact resistance. (182, 183) Amorphous materials are harder to model using DFT hence, and further research may be needed to fully understand some of these theories.

Earlier work on ITO (100) and GZO (184) have shown the role of surface composition as a key parameters that impacts the performance of contacts such as work function. Here, we have focused on studies focused on similar surface characterization of IZO, in an effort to understand the interface of amorphous TCO which is relevant to the application of IZO in a range of opto-electronic technologies. The incorporation of amorphous IZO into OPV devices has not been straight forward due to complex surface chemistry of In_2O_3/ZnO. In order to fully understand the role of these electrodes for organic photovoltaic applications, in this

work we have studied the near-surface composition correlated with the electrical and electrochemical properties of IZO electrodes after various pretreatment conditions. The surface is characterized using monochromatic X-ray photoelectron spectroscopy (XPS) and ultraviolet photoelectron spectroscopy (UPS) with respect to the following surface pretreatments: KOH etch, RF oxygen plasma etching, UV ozone and high-vacuum argon-ion sputtering. In this study, IZO surface has been characterized both before and after various surface pre-treatments. We find the impact of pretreatment and changes in interfacial chemistry critical in improving the electrochemical charge transport.

4.2.2 Experimental Methods

Oxide Deposition

Four-inch diameter In_2O_3-ZnO (80:20 wt%) ceramic sputtering targets was used to deposit thin films by mixed RF and DC magnetron co-sputtering for a fixed time of 10 minutes. A total power of 150 W with ratios of 50% RF to 50%DC was employed. (73, 74, 116) The films were sputtered in 4.5 mTorr total pressure of mixed argon and 0.5% oxygen. A MKS mass flow controller maintained gas flow of argon at 14.4 sccm and allowed for various O_2 flow rates($\sim$ 0.02 sccm) in order to maintain 0.5% ratio of O_2/ (O_2+Ar). Two-inch by two-inch Corning Eagle 2000 glass was used for the substrate in all depositions. Prior to deposition, the substrate glass was cleaned in detergent (diluted Triton X-100) followed by ringing with deionized water. Sonicated in acetone for 5 min and isopropanol for 5 min, followed by drying in nitrogen stream. Finally, substrates were cleaned in

a Novascan PSD-UVT ozone decontamination system for five minutes at $120\,^{\circ}\mathrm{C}$. The chamber was pumped down with a rough vacuum and turbo vacuum to base pressures of 10^{-7} Torr to 10^{-6} Torr prior to depositions. All depositions were done at ambient temperature. Process Eye Professional MKS Easy View software was used to monitor the amount of argon, oxygen, atomic oxygen, and water in the chamber during depositions.

Thin film measurement

Thin film characterization has been described previously in previous sections. (116, 184) Similarly, conductive AFM (C-AFM) measurement was done using Asylum Research MFP-3D system with Orca mode using Pt/Cr coated tip with tip radius $<$15nm, k = 2 N/m, ω = 70 kHz (Olympus AC240TS Electric) at 100mV bias. The C-AFM system has a current detection limit of 1 pA to 20 nA. The tip (+ bias) to sample surface (ground) was 100mV. Optical properties of the films were obtained using two coupled Ocean Optics spectrometers to measure transmittance and reflectance over the range of 330-1000 nm.

Surface Pretreatments, *XPS/UPS* and *Electrochemistry*: See previous section.

4.2.3 Optical and Structural Properties

The IZO substrates under study are $\sim$ 400 nm thick. The films had conductivity (σ) = 2500 $\pm$ 200 S/cm, carrier concentration (N) = 3.5 $\times$ 10^{20} /cm^3 and mobility(μ) = 42 cm^2/Vs. We did not find any significant differences in bulk electrical properties due to surface treatment. Transmission normalized to glass

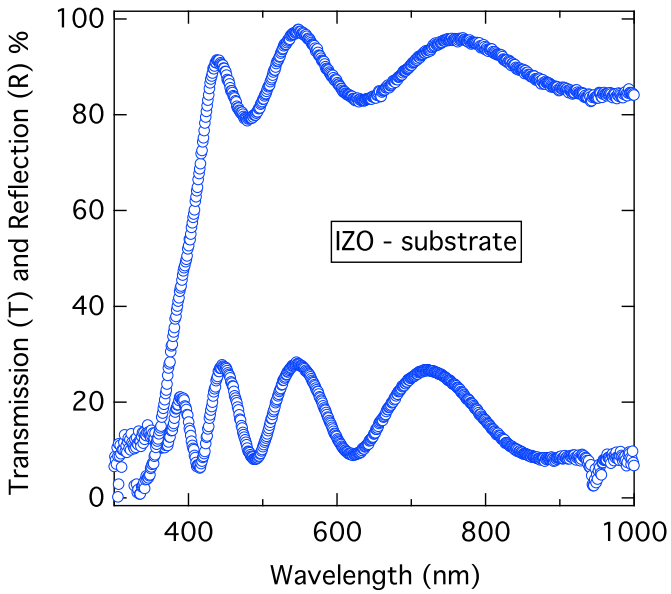

Figure 4.7: Transmission and Reflection of IZO

substrate and reflection measured and corrected for front Al mirror for as received sample is shown in Figure 4.7. The IZO film had good transparency $\sim 90\%$ in visible and $\sim 10\%$ reflectance. Figure 4.8 shows 2D detector images of IZO thin film on left and ITO thin film on right. In the image, x-axis is the standard 2θ, the y-axis is the χ and the color code represents the x-ray intensity.Polycrystalline ITO XRD is shown as a reference, where various sharp diffraction peak lines can be seen. The IZO thin films have broad amorphous hump, indicating largely amorphous phase. No In_2O_3 or ZnO diffraction peaks are absorbed.

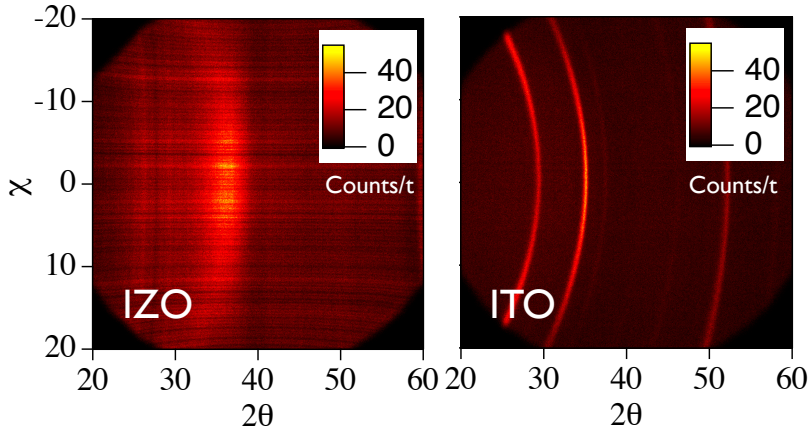

Figure 4.8: XRD spectrum of amorphous IZO (left) and poly-crystalline ITO (right)

4.2.4 XPS and UPS Studies As-received and Pre-treated IZO Films

The surface chemistry of the amorphous IZO electrode with respect to different pretreatments was characterized using XPS. Figure 4.9 gives the O 1s core level spectrum for the four different pretreatments for high tilt angle (60°); the less surface sensitive normal tilt angle XPS is given in the SI section. The O 1s spectrum for each pretreatment was fit to a four component model. The lowest binding energy component, O_I, is associated with stoichiometric indium oxide (In_2O_3). O_{II} is accredited to local defects at the surface typically ascribed to oxygen vacancies. These oxygen vacancies act as donor states, contributing electrons to the conduction band. O_{III} is assigned to surface hydroxyls associated with either $In(OH)_3$ or InOOH species and O_{IV} is due to carbonaceous species or surface water physisorbed to the surface. Table 4.5 provides the relative binding energies and percentages for each fit component, as well as relative Zn:In and Zn:In:O ratios.

From Figure 4.10, it is evident that the pretreatments produce unique surface features. The as received electrode has the highest concentration of oxygen vacancy defects (O_{II}) and hydroxyls (O_{III}) at the surface, relative to the In_2O_3 peak (O_I). Treating the electrode with a base etch produces the most stoichiometric surface, with the highest contribution from the In_2O_3 peak (O_I), implying that at high pH, there is a kinetic barrier to the hydrolysis products of the oxide. There is also an increase in the surface concentration of Zn to In upon base treatment; the increased presence of Zn at the surface may be influencing the local hydration energy. In fact, the hydrolysis constant (K_{H_2O}) for Zn^{2+} is larger than for In3+, where K_{H_2O} is defined as the equilibrium constant for the reaction of a metal cation (M^{2n+}) with water:

$$M^{2n+} + H_2O \Leftrightarrow M(OH)^{(2n-1)+} + H^+ \tag{4.2.1}$$

This is due in part to the larger ionic radius of indium (see C.F. Baes and R. E. Mesmer: The Hydrolyis of Cations 1976 and page 45-47 of Chemical Dissolution of Oxides). Etching the IZO surface with either an ozone or an O_2-plasma treatment results in an increase in the relative stoichiometric to defect ration (O_I to O_{II}) while also increasing the local hydroxyl coverage. Both of these pretreatments bombard the surface with highly reactive oxygen, so it is not surprising that defect components are reduced. The increase in surface hydroxyls is predicted to be due to the reaction of the new surface with ambient surroundings.

Previous reports on the surface chemistry of transparent conductive oxides have determined that electrochemical charge transfer rates are directly dependent upon the local surface chemistry. For a given redox couple, the oxide extracts electrons

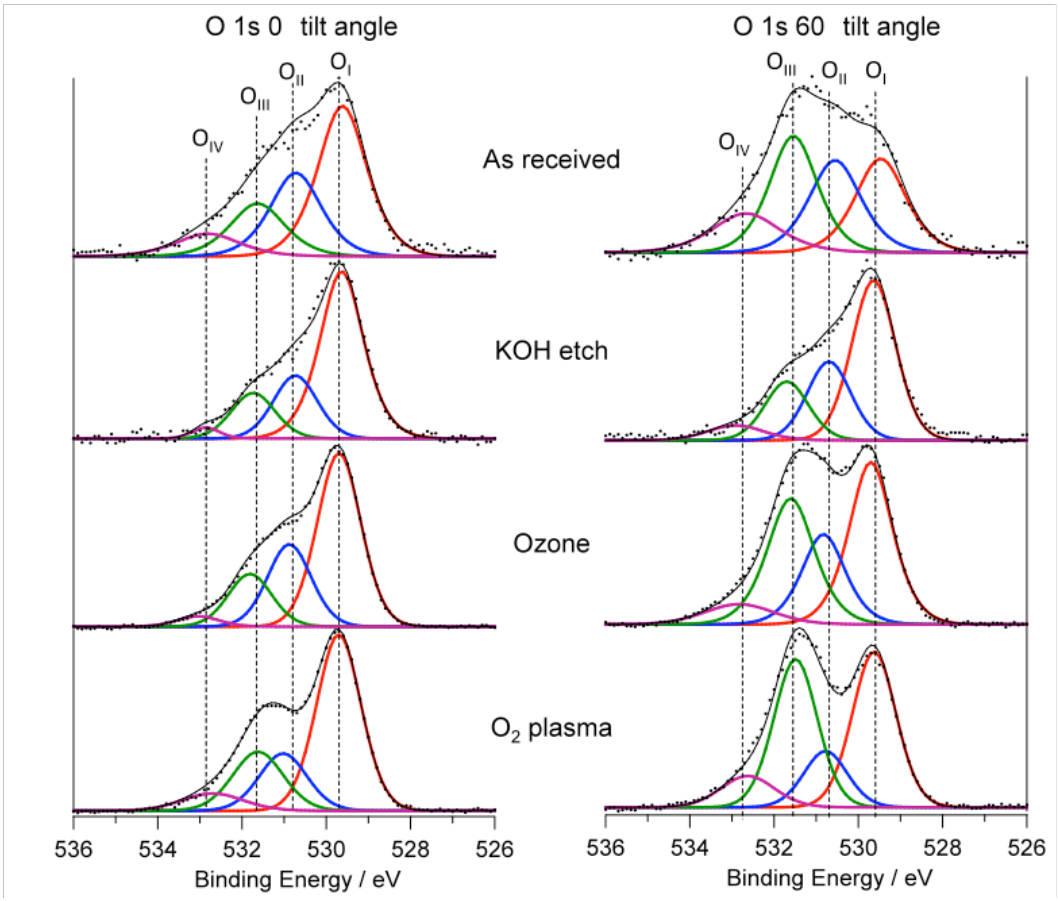

Figure 4.9: Normal (left-hand panel) and angle (right-hand panel) resolved XPS for the O 1s core electrons of IZO exposed to different surface pretreatments. Peak fits are discussed in the text and relative areas and binding energies are given in Table 4.5

Table 4.5: Normal and angle resolved XPS for the O 1s core electrons of IZO exposed to different surface pretreatments showing relative binding energies and percentages for each fit component, as well as relative Zn:In and Zn:In:O ratios.

Normal XPS

	As received		KOH etch		Ozone		O_2 plasma etch	
O 1s component	eV	%	eV	%	eV	%	eV	%
In_2O_3 (O_I)	529.6	46.2	529.6	60.1	529.7	54.4	529.7	53.6
Defect (O_{II})	530.7	26.7	530.7	21.8	530.9	25.9	531.0	18.7
Hydroxyl (O_{III})	531.6	18.1	531.7	15.8	531.8	16.5	531.6	20.4
Carbon/Water (O_{IV})	532.8	9.1	532.8	2.4	533.1	3.2	532.7	7.3
Zn:In ratio	17.4:82.6		17.7:82.3		18.7:81.3		18.3:81.7	
Zn:In:O ratio	4.1:19.7:76.2		5.4:25.0:69.7		5.3:23.0:71.7		5.0:22.2:72.8	

Angle resolved XPS

	As received		KOH etch		Ozone		O_2 plasma etch	
O 1s component	eV	%	eV	%	eV	%	eV	%
In_2O_3 (O_I)	529.5	26.8	529.6	50.7	529.7	38.6	529.6	39.1
Defect (O_{II})	530.6	27.0	530.7	24.8	530.8	21.5	530.8	14.1
Hydroxyl (O_{III})	531.6	31.5	531.7	18.5	531.6	32.5	531.5	37.1
Carbon/Water (O_{IV})	532.7	14.8	532.9	6.0	532.8	7.3	532.6	9.7
Zn:In ratio	9.3:90.7		15.8:84.2		12.9:87.1		10.3:89.7	
Zn:In:O ratio	2.0:19.8:78.2		4.6:24.4:71.0		3.1:21.1:75.8		2.5:22.0:75.4	

from the HOMO level of the probe molecule (oxidation) in the increasing forward bias direction and injects electrons into the empty state in the reverse bias direction (reduction). Changes in the local surface chemistry of the oxide can alter the local kinetic rate of charge transfer. Solution phase electrochemistry was used as a simple model and starting point for the much more complex interfacial electron transfer between the oxide and the organic in an organic photovoltaic. Table 2 gives the peak separation, and electron transfer rates for the different pretreatments for a solution phase redox probe decamethyl ferrocene. The results can be directly correlated with the surface species of the electrode given in the XPS results give in Figure 4.9.

As the near-surface concentration of the hydroxyls and carbonaceous species decreases, the electron transfer rate is increased. Specifically, the as received electrode, which has the highest relative concentration of hydroxyls (O_{III}) and carbonaceous species (O_{IV}), has an immeasurable charge transfer rate, due to a very large peak to peak separation. Conversely, the base etched electrode was shown to have the lowest relative concentration of hydroxyls and carbonaceous species and highest rate of electron transfer to the solution redox probe. In oxide chemistry, hydrolysis products are commonly less compact than the stoichiometric oxides. Furthermore, hydroxyls are capable of participating in extensive hydrogen bonding; the presence of hydroxyls on the surface often propagates into extensive double layers.

This implies that the surface of the as received electrode has the largest double layer, which is essentially impenetrable to the redox probe while the double layer

of the base-etched electrode is assumed to be the thinnest. A schematic of the proposed double layer is given in Figure 4.10 for each of the different pretreated electrodes.

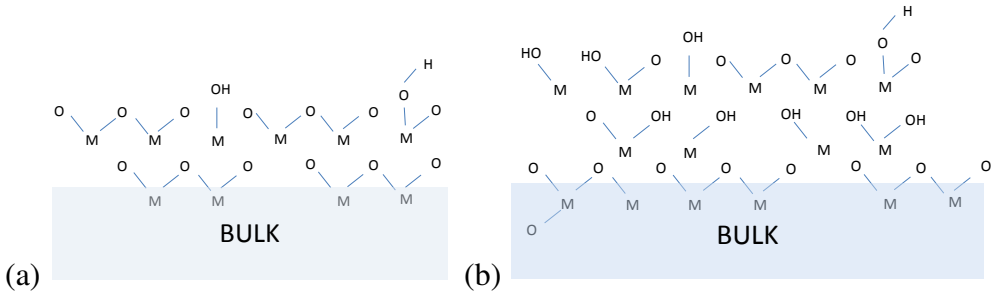

Figure 4.10: Schematic of the double layer for (a) the base etch and (b) the as received IZO electrode

In OPVs, the charge transfer rate at the interface between a TCO and the photoactive layer can be related to the tunneling barrier or boundary layer, which is dependent on the difference in electric potential (work function) of the two materials. The thickness of the boundary layer, or the width of the electric field, is dependent upon both the dielectric constant of the materials and the density of donors at the surface. Therefore, local perturbations in the surface chemistry of the TCO are expected to act as local donors or acceptors and affect the rectification of the interface. Furthermore, the effective width of the double layer in the electrochemical experiment is expected to be related to the effective boundary layer thickness.

We first evaluated the change in ϕ and ionization potential of the TCO with the four different surface pretreatments and an in situ Ar^+ sputtered sample, void of

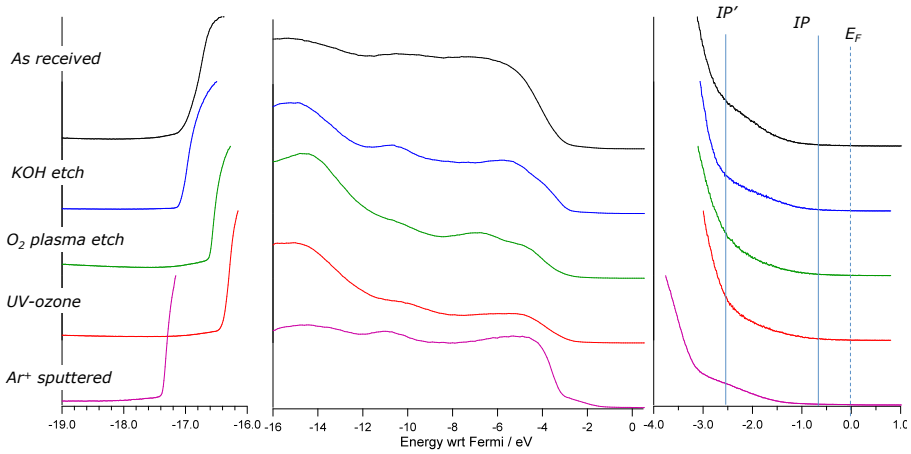

Figure 4.11: Ultraviolet photoemission spectroscopy (UPS) measurements of IZO electrodes exposed to different surface pretreatments

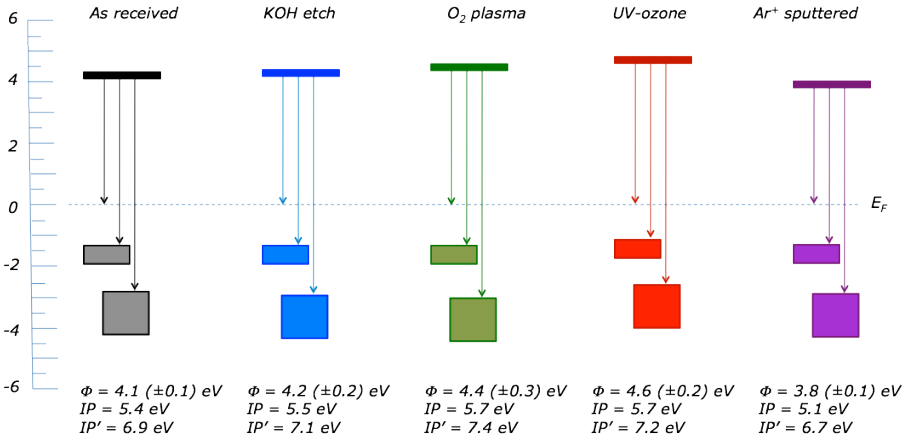

Figure 4.12: Energy band diagrams based on UPS measurements of IZO electrodes following different surface pretreatments. Work function (ϕ) is calculated as the energy from the Fermi level (E_F) to the vacuum level (E_{vac})

hydroxyls and adventitious carbon (XPS of Ar^+ sputtered IZO is not presented). Figure 4.11 shows the resultant UPS spectra, with the high binding energy showing local vacuum level shifts (panel i) and the low binding energy line shape relevant to valence band structure (panels ii and iii). In panel ii, contributions from can be detected from the O_{2p} (4-7 eV below the Fermi), the In 5d ($\sim$ 15 eV below the Fermi). Surface Zn 3d line shapes ($\sim$ 10 - 12 eV below the Fermi level) are also observed, with the feature most prominent for the base etched sample, which was found to have the highest near-surface concentration of Zn relative to In.

Consistent with amorphous materials, there is an extension of density of states beyond the O_{2p} edge into the band gap (4-7 eV below the Fermi level, panel iii). The width of this density of states varies with surface pretreatment, indicative of changes in the near-surface composition discussed in the XPS section. For example, the as received sample, which had the highest relative concentration of oxygen vacancies (O_{II}) has the largest fraction of tailing states within the gap while the base etch, having the lowest relative fraction of defects, has the the smallest fraction of mid gap states. This is consistent with self-compensation mechanisms for intrinsic doping of oxides; increasing the donor concentration near the conduction band lowers the enthalpy of formation for acceptor states near the valence band. Figure 4.12 gives the inferred energy level diagrams from the UPS spectra in Figure 4.11.

4.2.5 Kelvin probe and Conductive AFM Studies of As-received and Pre-treated IZO Films

The changes in work function($\Delta\phi$) with respect to time for each of the different pretreatment, as measured by kelvin probe, for IZO electrode is shown in Figure 4.13. The markers are spaced for clarity. From the graph, we find $>$1 eV increase in ϕ for O_2 plasma initially and it decays over time. Similar increase in ϕ and subsequent decay has been seen in other oxide semiconductor systems, such as n-type MoOx, (26) and p-type NiOx (25). Interestingly, O_2 plasma treated IZO surface, when treated further with acetone, IPA followed by N_2 dry, had very stable ϕ. Similarly, UV Ozone film showed similar initial increase $>$ 0.5 eV. Where as the KOH etch sample showed slight decrease 0.1 eV in ϕ over time. Ar sputtering data is not available.

Current voltage measurement done via conductive AFM for various surface treated IZO films is shown in Figure 4.14. Measurement setup is also shown in Figure 4.14. In this setup, the bulk resistance of the thin film is assumed negligible due to geometric factor of the setup and very low resistance of the film. As received IZO have very high turn on voltage $>$1.8 V. O_2 plasma followed by UV ozone treatment had turn on voltage 1 V $\pm$ 0.5 and 0.5 $\pm$ 0.2 V respectively. Finally, KOH etch etch yielded the least contact resistance with almost an ohmic behavior. Full current map of 2 μ sq area obtained from Conductive AFM for as received and KOH etch IZO films at +2V and -2V bias is shown in Figure 4.15. Here, white pixel indicates higher current flow via the tip. We find KOH etch has better CAFM data in both +2V and -2V bias. This matches with our earlier assessment that KOH

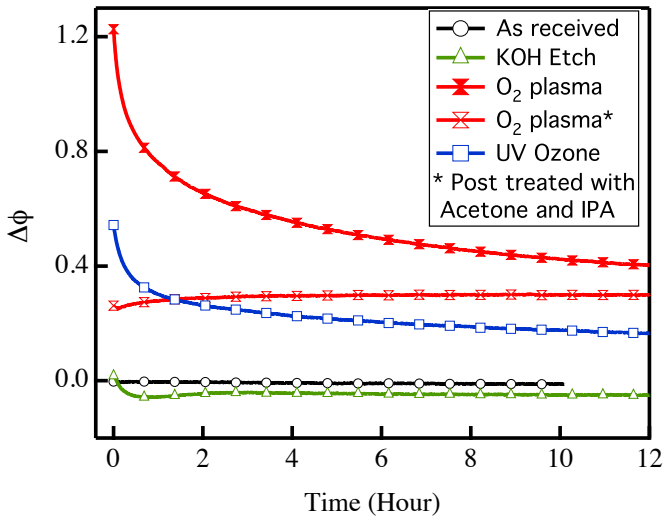

Figure 4.13: Work-function as a function of time for IZO electrodes with various surface treatment

etch yields surface with composition similar to the bulk composition, with least amount of carbonaceous impurities, with good electrical transport.

4.2.6 Electrochemical Reactivities of As-received and Pre-treated IZO Electrodes

Electrochemical reactivities of as -received and pre-treated IZO electrodes study was discussed extensively for GZO electrode in previous section. Here, Tables 4.6 and 4.7 present the results for electrochemical charge transfer rate measurements for the different pretreatments, using the redox probe Me10Fc+/0 which undergoes simple, outer-sphere one-electron oxidation/reduction (Table 4.6), and a chemisorbed redox probe $Fc(COOH)_2$ (Table 4.7). Also given in Tables 4.6 and 4.7 are the cyclic voltammogram peak separation used to estimate the charge

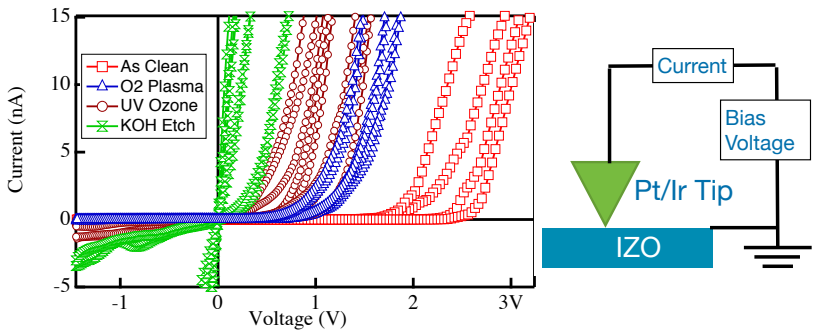

Figure 4.14: Current voltage measurement done by Conductive AFM on IZO electrodes with various surface pretreatments.

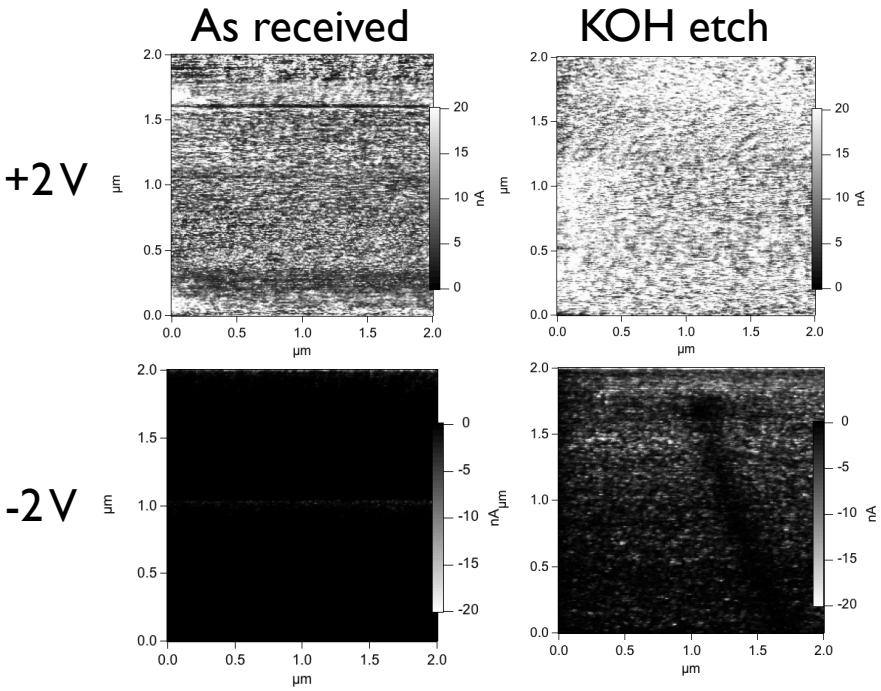

Figure 4.15: Conductive AFM for as received and KOH etch IZO films at +2V and -2V bias.

Table 4.6: Electrochemical response of Me10Fc

Electrode	Δ Ep (mV)	Redox potential (V vs Ag/Ag+)	Electron transfer rate ($K_{s,apparent}$(cm/s)$\times 10^3$
As received	N/A*		
O_2 plasma	169 ($\pm$ 1)	0.40 ($\pm$ 0.01)	0.77 ($\pm$ 0.01)
KOH	89 ($\pm$ 1)	0.42 ($\pm$ 0.01)	3.9 ($\pm$ 0.1)
ozone	157 ($\pm$ 1)	0.41 ($\pm$ 0.01)	0.91 ($\pm$ 0.02)
ITO control	100 ($\pm$ 1)	0.42 ($\pm$ 0.01)	2.8 ($\pm$ 0.1)

$*$- oxidation peak was not clear

Table 4.7: Electrochemical response of $Fc(COOH)_2$.

Treatment	Δ Ep (mV)	Γx10^{-10} (mols/cm^2)	Redox potential (V vs Ag/Ag+)	e^- transfer rate ($/s$)
As received	162 ± 1	1.7 ± 0.4	0.38 ± 0.01	0.44 ± 0.04
O_2 plasma	176 ± 6	1.7 ± 0.1	0.36 ± 0.01	0.38 ± 0.02
KOH	128 ± 2	2.7 ± 0.9	0.43 ± 0.02	0.67 ± 0.02
ozone	95 ± 2	2.8 ± 0.3	0.39 ± 0.02	1.06 ± 0.03

transfer rates ($k_{apparent}$), the surface coverages achieved for adsorbed $Fc(COOH)_2$ on GZO. The data shows that KOH yields good outer-sphere electron transfer rate $\sim$ 3.9 cm/s compare to other treatment and even better than ITO control $\sim$ 2.8 cm/s. This is consistent with other measurements discussed previously showing KOH etch results in good surface with least amount of carbonaceous species. The study on electrochemical reactivity of adsorbed probe molecules on TCO surfaces suggests that changes in near-surface composition can impact electrical properties, and charge transfer rates at an organic/oxide heterojunction which may be relevant for OPV devices. (101)

4.2.7 Conclusions

With the recent advances in flexible electronics, amorphous Indium Zinc Oxide (IZO) transparent electrodes with good bulk physical properties such as resilient mechanical properties, super smooth with amorphous phase with lack of grain boundaries providing superior water vapor transmission rate and high mobilities (μ), and deposition in room temperature allowing it to be incorporated in plastic substrates show great promises as replacement transparent conductive oxides (TCOs) for indium tin oxide (ITO) electrodes. However, the incorporation of amorphous IZO thin film into devices have not been straightforward due to complex surface chemistry of In_2O_3/ZnO and due to varying surface passivation and changes in work function due to charge transfer and band bending caused by adsorbates. In this work, we have looked into understanding the surface transport properties which are critical for thin film device application. From this work, we observe that surface pretreatment can modify and in some cases improve the surface electrical properties of IZO thin film. The surface of a-IZO seems to be prone to surface passivation and formation of defects readily, much more different than poly-crystalline GZO or ITO counterpart, possibly hindering the charge transport at the surface. So appropriate selection of surface pretreatment, such as KOH etch in our case can yield the surface with least amount of carbonaceous species, while retaining the indium to zinc ratio of the bulk, yielding the surface with good electrical transport. Thus, the knowledge gain here can provide further understanding and possibly better application of amorphous TCOs in organic opto-electronics device applications.

Acknowledgements: Materials development including oxide deposition and characterization equipment was provided by the U.S. Department of Energy under Contract No. DOE-AC36-08GO28308 with the National Renewable Energy Laboratory. Support for characterization and analysis work was provided as part of the Center for Interface Science: Solar-Electric Materials (CIS:SEM), an Energy Frontier Research Center Funded by the U.S. Department of Energy, Office of Basic Sciences, under Award Number DE-SC0001084

Chapter 5

Efficient Hole Injection in OLEDs using Zinc Tin Oxide (ZTO)

Understanding the charge transfer characteristics at the oxide/organic interface will be pivotal for the development and improvement of both organic light emitting diodes (OLEDs) and organic photovoltaic (OPV) devices. As discussed in the introduction, we consume more than 20% of our energy resources for lighting. This chapter presents study on the research and the development of deep work-function zinc tin oxide (ZTO) interfacial layer electrode ($\sim$ 5.2 eV) for improving hole injection and the performance of blue OLEDs.

As discussed in previous Chapter 4, surface property such as ϕ varying with time due to impurities and changes in metal to oxide stoichiometry at the surface, impacting the electric properties of oxide semiconductors. In this study we are seeking bit more stable material and more reproducible method to provide the tunability in ϕ needed for good energy alignment for efficient device performance.

Some of the results presented in this chapter were part of ROI in 2009. A related study, which is partly discussed in this text, on OLED devices employing large area GZO electrode was published on *SPIE proceeding*, D Matson et al, title: "Development of large area transparent conducting oxides from a combinatorial lead for organic solid state lighting." (49, 53) Also, the subsequent studies presented in Chapter 7 on IZTO materials can be credited to some of the results found on this chapter.

In this study heterostructured electrodes were created by pairing TCO materials (ITO and GZO) engineered for transparency and conductivity in concert with a deep work-function functional oxide interfacial layer (ZTO) optimized for charge injection and stability with organic active-layers. Initial optimization of optical and electrical property of ZTO films were done by depositing film on glass, with changing O_2 partial pressure and substrate temperature (Ts) in a PLD system. Both ITO and GZO were modified by depositing varying thickness (5 to 20 nm) of ZTO. The heterostructured electrode, TCOs with ZTO interfacial layer, has the bulk opto-electronic property of the TCO such as transparency, conductivity with surface properties dominated by the interfacial layer namely the work-function of the ZTO functional oxide. Both ITO $\sim$4.8 eV and GZO $\sim$4.6 eV showed increase in ϕ up to 5.4 eV with ZTO interfacial film. Blue OLEDs were fabricated with ITO or GZO (400 nm)/ZTO /TAPC(35nm)/TCTA(5 nm)/mCP:6$\%$FIrpic(15 nm)/PO15(50 nm)/LiF (1nm) /Al (100 nm) architecture with varying ZTO thickness. The best performing device with 10 nm ZTO on ITO, which exhibited an operational voltage of 4.23 $\pm$ 0.01 V, an external quantum efficiency of 16$\%$, and a power efficiency of 32 lm/W at 800 Cd/m^2. The modified TCO yielded blue OLEDs with power

efficiency at high brightness superior to that achieved using commercial ITO. Similarly, ZTO on GZO, an indium free electrode, resulted in comparable performance to a ITO standard. This demonstrates that the interfacial modification is a viable technique to provide optimal anode performance, including conductivity, charge injection, stability and ultimately the power conversion efficiency in organic light-emitting devices (OLEDs).

5.1 Introduction to Blue Phosphorescent OLEDs

A schematic cross section of an OLED is shown in Figure 5.1. In this basic structure, which is common to standard bottom-emitting OLEDs, charges (electrons or holes) are injected from the cathode or anode into the electron or hole transport layer (ETL/HTL), respectively. The electrons in the lowest unoccupied molecular orbital (LUMO) of the ETL and holes in the highest occupied molecular orbital (HOMO) of the HTL to form excitons in the emissive layer, where the excitons recombine in the emitter to produce photons. Phosphorescent molecular dopants are of particular interest because of their potential to reach internal quantum efficiencies of nearly 100%. This efficiency results from spin-orbit coupling in these systems, which facilitates radiative recombination in the dopant. Although the efficiency of the emission process is high, the overall power efficiency of the OLED is limited by the electronic properties within each layer, as well as at each interface.

Currently, indium tin oxide (ITO) is the most commonly used commercial material for optoelectronic TCO applications including OLEDs for displays, liquid crystal displays (LCDs), solar panels etc. OLEDs employing alternative anodes

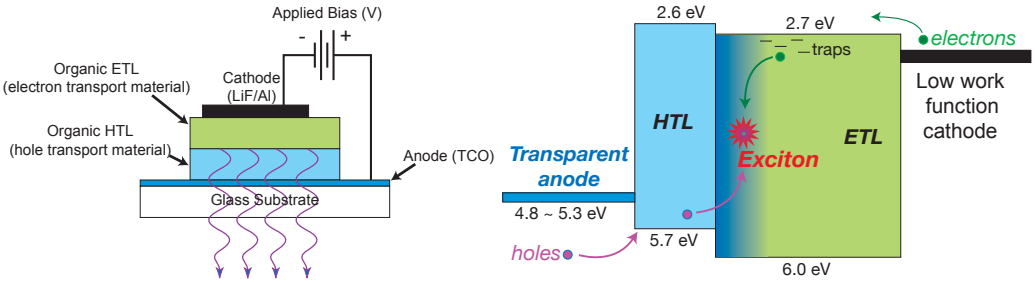

Figure 5.1: Schematic of a simple two layer OLED device structure.

such as indium zinc oxide (IZO) and substitutionally doped zinc oxide variants have been reported in the literature. (185, 186) In addition, amorphous TCOs, which are more stable and have higher quality in terms of optical and surface roughness than traditional materials such as indium tin oxide (ITO), are sought so that they could be incorporated in flexible devices. However, because of historic precedence and commercial availability, ITO remains the dominant TCO for OLED device studies targeting new organic light emitting materials. One of the primary factor for choosing zinc based electrode as an alternative to ITO, is high natural abundance of zinc, see figure 1.5. Lighting consumes 22% of the electricity used in the United States.

Typically material for these anode applications uses an In:Sn ratio of 10:1. It is known that ITO has interfacial charge transport problems and is chemically unstable in organic device applications. (11) Despite its ubiquity, ITO and other indium containing TCOs are less than ideal anodes for high-efficiency, low-cost organic solid state lighting (OSSL). Specific shortcomings of ITO include its increased cost because of the high price of indium, a fixed work function of ≈ 4.7 eV, and the mobile indium ions, which have been demonstrated to migrate into the

active material in devices adversely affecting performance. The instability in the electrode surface chemistry can also adversely affect injection efficiency and device lifetime. Currently, one of the remaining challenge in realizing efficient white OLEDs is the development of stable, high-efficiency, long-lived blue OLEDs. Of particular interest is the deep HOMO of the HTL to achieve efficient hole injection at the anode and low device operating voltages, the anode must be well matched energetically to the HTL. The general approach is analogous to the use of organic hole or electron injection layers to match the HOMO or LUMO of the organic side of the organic-inorganic interface to facilitate efficient charge transfer and minimize interfacial resistance.

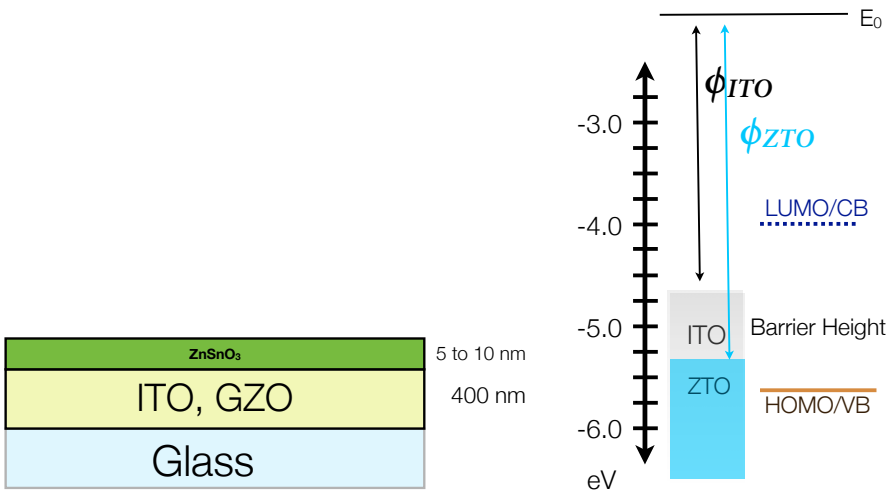

Figure 5.2: a) TCO materials (ITO and GZO) engineered for transparency and conductivity in concert with a deep work-function functional oxide interfacial layer (ZTO). Figure not drawn to scale. b) The barrier height between the HTL anode has to be matched energetically to HOMO of organic side.

Some modification of the ITO work function is possible via surface treatments such as O_2 and CF_4 plasma treatments resulting in modest enhancement of current injection. (187) These types of simple surface modifications are often metastable and do not provide the desired level of control or change in work function to truly optimize the TCO/organic interface. The surface morphology of ITO is also less than ideal for OLED devices with asperities (spikes) on the ITO surface, commonly resulting in failure via electrical shorting. (188) The combination of these deficiencies make the pursuit of more appropriate TCO systems critical for bottom-emitting OSSL to be a viable technology.

In this study heterostructured electrodes were created by pairing TCO materials (ITO and GZO) engineered for transparency and conductivity in concert with a deep work-function functional oxide interfacial layer (ZTO) optimized for charge injection and stability with organic overlayers, see Figure 5.2. Studies using this type of approach to band engineering have been demonstrated some time ago at the HTL and ETL anode/cathode interface by Choulis et al. in phosphorescent based OLEDs using a TFB layer. (189) The use of engineered organic hole injection layers (HILs) or tuned HTLs to match the work function of commercial ITO has been one approach, with companies such as Plextronics demonstrating the ability to alter the work function of organic HTL to improve device efficiency.

The work we intend to pursue in this study transitions this organic approach pioneered by Dr. Franky So and others from the organic/organic interfaces in the active region of the devices to the organic/TCO contacting interface. (190, 191) Thus, using heterostructure of TCOs and functional material, we seek to optimize

all of the necessary properties of the interface between the active layer in the OLED and the contact to maximize light output (i.e. TCO transparency), charge injection, and stability. The multicomponent system formed by separating the interface and bulk properties of the electrode using multilayer structures can be easier to optimized compare to single-component electrode, thus allowing for higher performance devices.

(Note: OPV device study discussed in next chapters and some previous OLED device study, (49) show that work function (ϕ) optimization, while important, is not a sufficient condition to guarantee good charge collection (OPV) or injection (OLED), as the interfacial chemistry may dominate the charge transfer process.)

5.2 Experimental

5.2.1 PLD Depositions

The ZTO samples were deposited on glass substrate or TCOs by PLD. ITO was obtained commercially (Colorado Concepts Coating Inc), and GZO was fabricated using RF sputtering with recipes described in previous chapters. (119, 116) The PLD system used has a base pressure of $<$1.0 x10^{-6} torr and employs a KrF laser operating at 242 nm. The substrate to target distance was held constant at $\sim$ 4 cm. The target material consist of 99.9$\%$ pure $ZnSnO_3$ oxide target. (Target Materials Inc) For these experiments, a pulse energy of 300 mJ was used to deliver an energy density to the target of approximately 0.76 J/cm^2 after optical losses.

The substrate temperature and chamber atmosphere were varied between 25 to 400°C. The partial pressure of oxygen P_{O_2}, was varied from 3.0 x10^{-3} torr to 5.6x10^{-2} torr respectively, by varying the flow rate of 99.999% O_2 gas that was introduced into the chamber using MKS mass flow controllers. The starting point for various deposition parameters which were optimized further for this material system and experiment, were obtained from previous study on OLED with GZO films of differing Ga composition done using the same PLD setup. (47)

Characterization: See previous chapters on GZO. (119, 116)

5.2.2 OLEDs Fabrication and Measurement

OLED studies were completed in collaboration with Pacific Northwest National Laboratory (PNNL). Details about fabrication tools and measurement on devices can be found elsewhere. (53, 49, 192) In short, TCO substrates (GZO films or reference commercial ITO, both on glass) were cleaned by sonication in a sequential series of solvents, including a dilute Tergitol solution, de-ionized water, trichloroethane, acetone, and 2-propanol. The substrates were then dried with flowing nitrogen. As a final cleaning step before device fabrication, the substrates were treated with UV ozone (UVO-Cleaner, Jelight Co., Inc.) at 15 mW/cm^2 for 15 min. The substrates were then loaded into a nitrogen glove box ($<$ 1 ppm H_2O, $<$ 1.5 ppm O_2) coupled to a multichamber vacuum deposition system. Organic layers were sequentially deposited onto the oxide-coated substrates by thermal evaporation from tantalum boats in a high vacuum chamber with a base pressure below 3×10^{-7} Torr. Cathodes were defined by thermally depositing a 1 nm thick

layer of LiF immediately followed by a 100 nm thick layer of Al through a shadow mask with 1 mm diameter circular openings. A quartz crystal oscillator was used to monitor the thicknesses of the films, which were calibrated ex situ using ellipsometry. The deposited stack of oxide, organic and metal layers is depicted as ITO or GZO / ZTO /35 nm 1,1-bis [(di-4- tolylamino) phenyl] cyclohexane (TAPC)/ 5 nm 4,4',4"- tris (carbazol-9-yl) triphenylamine (TCTA)/ 15 nm 1,3-bis (9-carbazolyl) benzene (mCP): 6 % iridium (III) bis [(4,6-difluorophenyl) -pyridinato - N,$C^{2'}$] picolinate (FIrpic) /50 nm 2,8-bis (diphenylphosphoryl) dibenzothiophene (PO15) /1nm LiF /100 nm Al.

Here the TAPC and TCTA constitute the hole-transport layer (HTL). The emissive layer (EML) is composed of host mCP doped with a blue phosphor FIrpic. The hole blocking/electron-transporting layer is comprised of PO15. Optical and electrical characteristics of the devices were determined in air, with electrical contact made via a tungsten probe tip on the TCO anode and a 0.002 in. diameter gold wire directly probing the Al cathode. Current-voltage characteristics were measured with an Agilent Technologies 4155B semiconductor parameter analyzer. The light output was detected using a 1 cm^2 Si photodetector placed behind the OLED, and the device brightness was directly measured using a Newport multifunction optical meter. No corrections were made for light wave guided in the organic thin films or the substrate.

Table 5.1: O_2 and temperature variation study on ZTO ($\sim$375 nm) film on glass.

P (torr)	O_2(sccm)	Ts	ϕ (eV)	(Ω/sq)
5.60×10^{-2}	254	23	$*$	$*$
2.80×10^{-2}	174	25	4.6	$5.7 \times 10^{+4}$
1.40×10^{-2}	105	27	4.5	$1.3 \times 10^{+7}$
1.00×10^{-2}	80	25	$*$	$*$
7.00×10^{-3}	57	30	4.5	$7.5 \times 10^{+5}$
3.00×10^{-3}	26	24	$*$	$*$
1.60×10^{-2}	118	150	4.9	$6.8 \times 10^{+4}$
1.60×10^{-2}	118	300	5.3	$7.4 \times 10^{+2}$
2.80×10^{-2}	174	300	5.3	$2.5 \times 10^{+6}$
1.40×10^{-2}	106	33	4.9	$1.8 \times 10^{+7}$
1.40×10^{-2}	106	150	4.6	$1.3 \times 10^{+4}$
1.40×10^{-2}	106	300	5.2	$3.5 \times 10^{+2}$
1.40×10^{-2}	106	450	5.3	$1.5 \times 10^{+3}$

$*$ To resistive to measure.

5.3 Results: ZTO Varying O_2 Partial Pressure and Substrate Temperature (Ts)

Zinc Tin Oxide ($ZnSnO_3$) is an n-type oxide with higher or deeper work function compare to ITO. Table 5.2.2 shows various ZTO thin films with ϕ ranging from 4.5 eV to 5.3 eV. (Note: Kelvin probe measurement may not be accurate for high resistivity samples). The data shows that work function is tunable. At room temperature, changing oxygen flow and deposition pressure displayed a change of more than 4 order of magnitude in the sheet resistance for similar thickness films, see table 5.2.2.

Films grown at excess O_2 or low O_2 resulted in very resistive samples. Thermal energy was required for carrier generation in the film, as we find increasing the

substrate temperature resulted in films with higher σ or lower resistivity. The sample with lowest sheet resistance of $\approx$ 350 Ω/sq (σ = 77 S/cm) was obtained at PLD deposition condition as follow: Laser pulse energy= 300 mJ, rate= 5 Hz, O_2 pressure= 1.40 $\times$ 10^{-2} torr, oxygen flow = 106 sccm and substrate temperature = 300 °C. All the ZTO films on glass substrate were largely amorphous with $S_{rms} <$ 1 nm as measured by XRD and AFM shown in Figure 5.3.

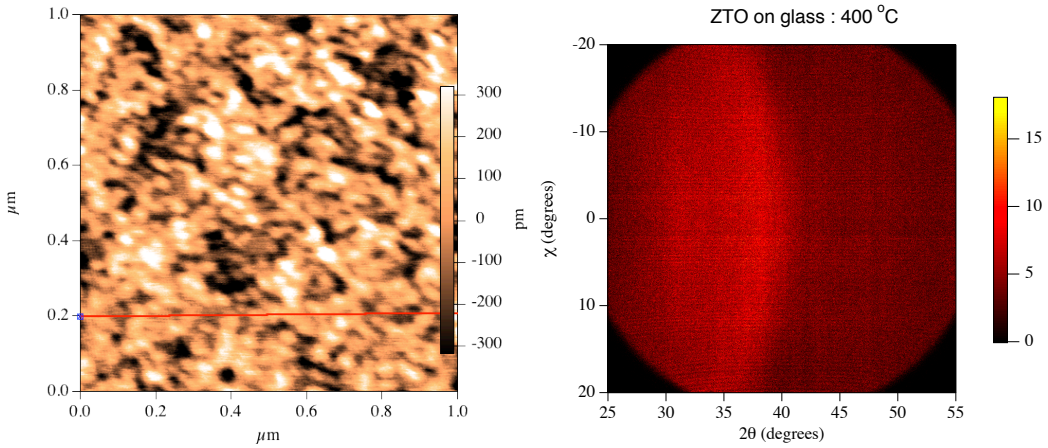

Figure 5.3: (a) X-ray diffraction 2D detector image file and (b) Surface topography of ZTO film on glass.

Amorphous TCOs, which are more stable and have higher quality in terms of optical and surface roughness than traditional materials such as indium tin oxide (ITO), are sought so that they could be incorporated in flexible devices. ZTO films with best conductivity of σ = 77 S/cm, also has ϕ = 5.2 eV, but it is not good enough for standalone TCO applications requiring threshold electrical conductivity of σ = 1000 S/cm, with reasonable optical transparency. In comparison, Ga doped ZnO deposited via PLD can have σ as high as 12,000 S/cm. (67)

Table 5.2: TCO (ITO or GZO) modified with various thickness ZTO.

t (nm)	ϕ (eV)	ITO	+ZTO(Ω/sq)	S_{rms}(nm)
0	4.80	13.50		>2
5	5.22	13.94	12.01	1.82
10	5.18	15.20	12.17	1.89
15	5.19	12.76	11.36	2.14
20	5.30	13.11	11.75	1.74

t (nm)	ϕ (eV)	GZO	+ZTO(Ω/sq)	S_{rms}(nm)
10	5.42	3.50	3.59	2.45
15	5.36	3.47	3.39	1.95
20	5.30	3.41	3.27	1.94

Deposition: 300 mJ, 5hz, O_2 pressure = 1.40×10^{-2} torr, T_s = 300 °C.

5.4 Results: ZTO and TCO (ITO, GZO) Heterostructure

It was not possible to obtain the ZTO films with low sheet resistance or $\sigma >$ 1000 S/cm. [One of the motivation for studying IZTO, which has higher electrical conductivity discussed in Chapter 7] Instead ZTO with varying thickness (5 to 20 nm) were deposited on top of already conductive TCOs such as ITO and GZO. In this way, the multicomponent system can be formed allowing to separate the interface and bulk properties of the electrode using multilayer structures. The ZTO interface layer films were deposited at the same condition that resulted in high conductivity film in Table 5.2.2.

The physical properties (ϕ, sheet resistance, surface roughness) of various thickness of ZTO on top of both ITO and GZO is shown in Table 5.2. The data

in Table 5.2 shows that the composite structure has slightly lower sheet resistance after ZTO modification. This is expected due to lowering of sheet resistance as electrical conductivity of two films are added in parallel. Moreover, both ITO and GZO films undergo annealing at 300 °C during ZTO film deposition. Vacuum annealing is known to improve the electrical property of various TCOs. (9) Moreover, ITO $\sim$ 4.8 eV and GZO $\sim$ 4.6 eV films showed increase in ϕ up to 5.4 eV with ZTO interfacial film on top. Note: the ϕ via kelvin probe is susceptible to variation in measured standard and lots of other factor but measurement accuracy usually improvs when conductive TCO provides the efficient electrical ground.

Surface morphologies obtained using AFM showed slight variations in S_{rms} for films grown with varying ZTO thickness, see last column of Table 5.2. We find loose trend of decrease in S_{rms} for increasing ZTO thickness. ZTO film is amorphous and results in a flattening of the surface of the ITO or GZO substrate.

The optical spectra for transmittance (T) normalized to the glass substrate and the reflectance (R) relative to a standard Al mirror for ITO films modified with various thickness ZTO are shown in Figure 5.4. T $\sim$ 90% in visible spectrum are seen for all samples. Similarly, the average reflectances of the samples are around 10%. We find some, very small systematic reduction in transparency with increasing ZTO thickness in the visible range.

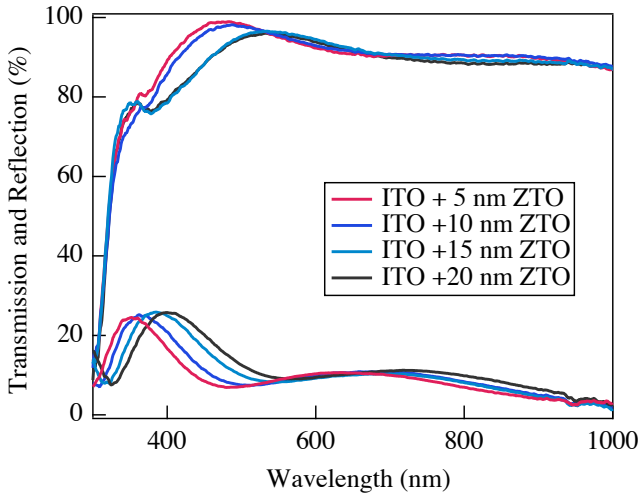

Figure 5.4: Transmission and reflection of ITO with varying ZTO thickness. Some loss in transparency seen for thicker ZTO film.

5.5 Results: OLEDs Studies with ZTO

The device study on the heterostructured electrode, TCOs with varying thickness ZTO interfacial layer, which has bulk opto-electronic property (both transparency, conductivity) of the TCO and interfacial properties namely the work-function of functional oxide ZTO are shown in Table 5.3. The performance EQE and Lm/W measured at 13 mA/cm^2 or at 800 Cd/m^2 of both ZTO/ITO and ZTO/GZO combination had maximum at around 10 nm of interfacial ZTO layer. The observed ϕ at 20 nm or 5 nm ZTO modification are higher than at 10 nm, but do not result in higher performance. The poor performance at 5 nm ZTO modification could be associated with non conformal coverage. While the poor performance at 20 nm ZTO modification is associated with increase in series resistance of the device, as ZTO has poor bulk electrical property.

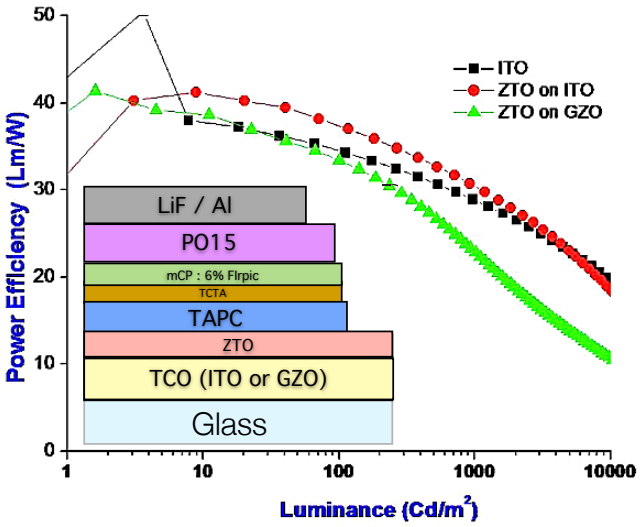

Figure 5.5: Power efficiency as a function of brightness for blue OLEDs (Bare TCO or TCO with 10nm ZTO /TAPC(350) /TCTA(50) /mCP: 6% FIrpic(150) /PO15(500) /LiF /Al.) commercial ITO (black), ZTO/ITO (red) and ZTO/GZO (green).

Thus the data in Table 5.3 show the validity of this approach using zinc tin oxide (ZTO) in combination with various TCOs, including ITO. As shown in Figure 5.5, improved performance for the ZTO/ITO system compared to commercial ITO was observed. These results are very promising however, ultimate device performance and stability as well as electrode tunability and scalability remain unknown.

Similarly, we find that the performance of GZO/ZTO, which had slightly higher ϕ compare to ITO/ZTO counterpart, do not yield an efficient devices. This matches with our previous assessment where we find that the macroscopic work function does not uniquely determine charge injection efficiency. That work was illustrated in a comparative study of N,N'diphenyl-N,N'-bis(1-naphthol)1,1'-biphenyl-4,4'diamine (NPD)/tris (8-hydroxyquinolinolato) aluminum (Alq3)

Table 5.3: OLED: TCO (ITO or GZO) modified with various thickness ZTO.

t (nm)	ϕ (eV)	ITO (Ω/sq)	+ZTO (Ω/sq)	S_{rms} (nm)	V (Volts)	EQE %	lm/W lm/W
						At 13 mA/cm^2	
0	4.80	13.50		>2	5.18 ±.38	13.50±1.36	21.93±2.36
5	5.22	13.94	12.01	1.82	5.07 ±.17	11.12 ±2.16	18.34 ±3.33
10	5.18	15.20	12.17	1.89	5.16±.07	14.59±.50	23.71±.94
15	5.19	12.76	11.36	2.12	6.62 ±1.61	11.79 ±1.49	15.84 ±4.76
20	5.30	13.11	11.75	1.74	4.16 ±.11	0.17 ±.02	0.36 ±.05
						At 800 Cd/m^2	
0	4.8	13.5		>2	4.26±.08	14.61±1.51	28.79±3.26
5	5.22	13.94	12.01	1.82	4.33 ±.11	11.97 ±2.41	23.24 ±4.89
10	5.18	15.20	12.17	1.89	4.23±.01	16.07±.63	31.89±1.33
15	5.19	12.76	11.36	2.14	4.97 ±.69	12.80 ±1.72	22.05 ±4.75
20	5.30	13.11	11.75	1.74	7.14 ±.37	1.20 ±.06	1.41 ±.14

t (nm)	ϕ (eV)	GZO (Ω/sq)	+ZTO (Ω/sq)	S_{rms} (nm)	V (Volts)	EQE %	lm/W lm/W
						At 13 mA/cm^2	
10	5.42	3.50	3.59	2.45	7.55±.21	11.79±.94	13.10±1.17
15	5.36	3.47	3.39	1.95	7.71±.58	10.86±1.09	11.87±1.50
20	5.30	3.41	3.27	1.94	7.52±.39	9.94±.57	11.09±.52
						At 800 Cd/m^2	
10	5.42	3.50	3.59	2.45	5.15±.19	13.31±1.06	21.72±2.30
15	5.36	3.47	3.39	1.95	5.53±.59	12.59±2.29	19.14±2.99
20	5.30	3.41	3.27	1.94	5.44±.28	10.78±.90	16.62±.85

Device: ITO/TAPC(350)/TCTA(50)/mCP:6%FIrpic(150)/PO15(500)/LiF/Al
PLD deposition parameters for ZTO films: Energy = 300 mJ, rate = 5 Hz, O_2 partial pressure = 1.40$\times$ 10^{02} torr, T_s = 300 °C.

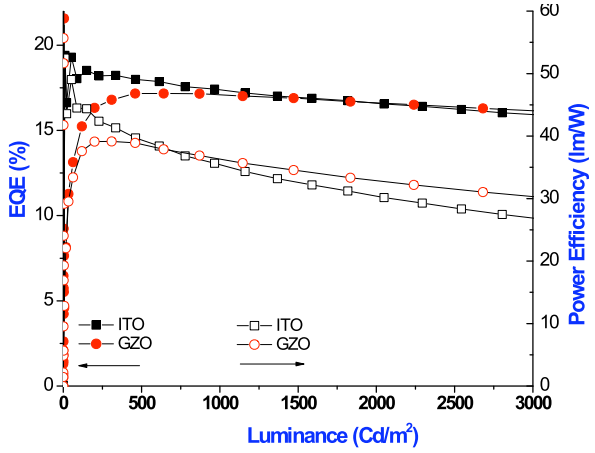

Figure 5.6: A comparative study of N,N'diphenyl-N,N'-bis(1-naphthol) 1,1'-biphenyl-4,4'diamine (NPD)/tris (8-hydroxyquinolinolato) aluminum (Alq3) OLEDs fabricated on anodes of indium tin oxide (ITO) and gallium doped zinc oxide (GZO).

OLEDs fabricated on anodes of indium tin oxide (ITO) and gallium doped zinc oxide (GZO). (47, 49) The measured work function of ITO was found to be 4.7 eV, whereas GZO was measured at 4.6 eV. While the 100 meV lower work function of the GZO should have impaired the hole injection efficiency into the NPD, the operating voltage of the GZO samples was slightly lower. With an operating voltage for a fixed current density of 10 mA/cm^2, the ITO samples were measured at 8.1 V compared to 6.9 V for the best GZO doping levels. These results indicate that the interfacial chemistry may be dominating the charge injection process.

5.6 Conclusion

In this study heterostructured electrodes were created by pairing TCO materials (ITO and GZO) engineered for transparency and conductivity in concert with a deep work-function functional oxide interfacial layer (ZTO) optimized for charge injection and stability with organic overlayers. The heterostructured electrode, TCOs with ZTO interfacial layer, has bulk opto-electronic property such as transparency, conductivity of the TCO and interfacial properties namely the work-function of functional oxide ZTO. Both ITO $\sim$ 4.8 eV and GZO $\sim$ 4.6 eV showed increase in ϕ up to $\sim$ 5.4 eV with ZTO interfacial film on top. The respective blue OLEDs were fabricated with ITO or GZO (400 nm) /ZTO /TAPC (35nm) /TCTA (5 nm) /mCP:6$\%$FIrpic (15 nm) /PO15 (50 nm) /LiF (1nm) /Al (100 nm) architecture with varying ZTO thickness. The modified TCOs with better energy alignment between oxide fermi level and HOMO of organics yielded blue OLEDs with power efficiency at high brightness superior to that achieved using commercial ITO. Similarly, ZTO/GZO combination, indium free electrode yielded comparable performance to ITO standard. Thus the interfacial modification is a viable technique to provide optimal anode performance, including conductivity, charge injection, stability and ultimately power conversion efficiency in organic light-emitting devices (OLEDs).

Chapter 6

Impact of Oxide Property on Devices - BHJ OPV Devices

The knowledge of oxide structure, morphology, band positions, various bulk and surface physical properties discussed in earlier chapters will be discussed in this chapter as it pertains to application in OPV devices. Historically, development of transparent electrodes for PV devices was focused on maximizing the conductivity and transparency. However, other design criteria have taken precedence, since interface modification of these electrodes either chemically or by deposition of thin layer of oxides, polymers or molecules have shown to yield improved contacts for specific device architectures. This chapter presents study on mostly n-type semiconductors based on ZnO oxide for investigating the functional mechanisms within OPV devices and a possible pathway towards air-stable high efficiency devices. Various studies on ZnO based TCOs such as GZO, AZO, IZO, IZTO are functioning either as the stand alone electrode or as an electron transport layer in a polymer/fullerene based heterojunction will be discussed.

The organic BHJ architectures based on photo-active polymers combined in an intimate blend with fullerene based acceptors has demonstrate internal quantum efficiencies approaching unity. However, in these devices as the BHJ has no net macroscopic electric field the contacts must be judiciously chosen to enable charge collection. In the standard architecture holes are collected thought the transparent contact facilitated by a deep work function hole transport layer such as PEDOT:PSS, MoOx or NiOx, while electrons are collected through a low work function metal cathode such as Ca/Al, which is one of the primary sources of device degradation in ambient conditions. By swapping the polarity of these devices via selection of different anode and cathode components to create what is commonly referred to as an inverted device architecture, in which the flow of carrier is reversed by choosing a low work function oxide electron transport layer (ETL) such as (TiO2) or more commonly ZnO paired with a deeper work function metal anode such as Ag. This inversion results in a device which has been demonstrated as air stable for thousands of hours buy several research groups. However, despite the potential appeal of the inverted organic solar cell there remains aspect of the device performance which can be improved and who's physical origins remain unclear.

6.1 Various Zinc-Based TCOs with and without Electron Selective Layer in Inverted Organic Photovoltaics

Abstract : A study of organic photovoltaics (OPVs) demonstrating the ability to use a ZnO electron transport layer (ETL) to improve the devices fabricated on a variety of zinc-based transparent conducting oxides (TCOs) electrodes: gallium-doped zinc oxide, aluminum-doped zinc oxide, and amorphous indium zinc oxide, is presented. All investigated TCOs exhibit ideal bulk optoelectronic properties for OPV applications. A large contrast in OPV device performance with and without the ZnO ETL are observed, demonstrating the critical role of interfacial layers to improve device performance. This also demonstrates that an appropriate choice of ETL permits efficient device performance independent of the underlying electrode properties, thus enabling the application of low-cost alternative electrodes for OPV applications.

6.1.1 Introduction

Organic photovoltaics (OPV) are an attractive technology that offers the potential for a low cost alternative to commercial PVs due in part to low temperature, high throughput, roll-to-roll manufacturing. (3, 193) Currently the most widely used transparent conductive oxide (TCO) electrode in OPV is tin-doped indium oxide (ITO), due to its high optical transparency, electrical conductivity and availability. (194) However, ITO has a number of drawbacks: high cost due to scarcity of indium, and performance constraints imposed in flexible and/or low

temperature processing desirable for OPV. To circumvent these problems a variety of alternative TCOs and metal grid transparent contacts have been demonstrated in OPV systems. (195, 196, 197) Despite the numerous demonstrations, a clear study of the critical role of the contact layer and its influence on device performance across different electrode material is absent.

In this work, we report on a comparison study of several TCO materials including gallium-doped ZnO (GZO), aluminum-doped ZnO (AZO), and amorphous indium zinc oxide (IZO) in OPV devices. TCOs based on the wide band gap semiconductor zinc oxide (ZnO) are attractive alternative materials that can possibly function as electrodes in OPVs with properties more suited with OPV technology. ZnO is abundant and inexpensive, and while it is relatively resistive trivalent n-type dopants can be incorporated into its wurtzite lattice to drastically improve the conductivity while still maintaining high transparency in the visible spectrum. (9)

We investigate the influence of the TCOs and the role of an ZnO electron transport layer (ETL) on the optoelectronic and device performance characteristics of inverted OPV cells. The TCO materials chosen possess attractive features besides high transparency and conductivity such as being earth abundant ($< 5\%$) in GZO (119, 116) and AZO (22) or, in the case of IZO, low-temperature processing compatibility for flexible PV applications despite still containing a significant fraction of indium (87% In_2O_3 and 13% ZnO by weight). (198) It is found that, when paired with a suitable ZnO-based ETL, that the excellent optoelectronic properties of these TCOs lead to high performance OPV devices equivalent to

those with ITO electrodes. In the absence of the ETL, however, the differences in surface properties of the TCO materials results in dramatically different OPV performance.

6.1.2 Experimental

All TCOs in this study were magnetron sputtered on glass substrates (Corning Eagle 2000). Details of the instrumentation, set up and deposition procedure is discussed previously : GZO (119, 116), IZO (198), AZO (Arkama Inc) and ITO (Thin Film Device). For optical, electrical, structural characterization as well as OPV devices fabrication, the TCO films were patterned by photolithography, cleaned by sonication in acetone and isopropanol, followed by a 20-minute ultraviolet-ozone (UV-O_3) treatment prior to use. Optical transmission was measured with an Ocean Optics spectrometer, sheet resistance measurements with a four-point probe and Keithley 2000 multimeter, work function measurements in air on a KP Technologies Kelvin probe with gold and aluminum reference standards, and X-ray diffraction (XRD) measurements with a Bruker Discovery 08 with a Hi-Star area detector.

For the organic active layer, bulk heterojuction (BHJ) of poly (3-hexylthiophene) :[6,6]-phenyl C60 butyric acid methyl ester (P3HT:PC60BM shown in Figure 6.1) films were deposited from 1:1 P3HT:PC60BM by weight dichlorobenzene solutions according to previous reports. (23, 199) The P3HT:PC60BM films were deposited either directly on the TCO films or on TCO films covered with a ZnO electron transport layer deposited from a diethyl

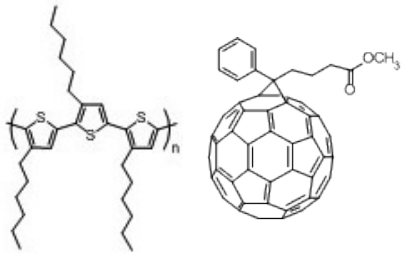

P3HT [C60]PCBM

Figure 6.1: poly (3-hexylthiophene):[6,6]-phenyl C60 butyric acid methyl ester

zinc solution according to a previous report.(13) On top of the BHJ films, a hole transport layer (HTL) film of Plexcore OC XA-1871ł was deposited in air followed by annealing at $110\,^{\circ}\mathrm{C}$ for 10 minutes in a N_2 -filled glove box. The PV devices were completed by thermal deposition of 100 nm Ag electrodes with an area of 11 mm^2 via a shadow mask at a base pressure of $\sim 3\times10^{-8}$ Torr. As a reference, a similar OPV device with commercially available patterned ITO on glass (Thin Film Devices) is used. Current-Voltage measurements of PV devices under a 100 mW/cm^2 illumination intensity (supplied by a tungsten halogen lamp and monitored with Hamamatsu Si photodiodes equipped with a KG5 filters) were carried out with a Keithley 236 source-measuring unit in an N_2 atmosphere. A 5.1 mm^2 aperture was used during testing to ensure consistent and accurate illuminated device areas.

6.1.3 Results and Discussion

The structural properties of ITO, IZO, GZO and AZO characterized by XRD are shown in Figure 6.2. Two-dimensional XRD plots show that IZO is largely

amorphous with distinct diffraction peak, rather a broad hump (Figure 6.2a), ITO and AZO are polycrystalline with sharp diffraction patterns (Figure 6.2c and 6.2d), while GZO is highly oriented with a very defined diffraction spot (Figure 6.2b). The detail analysis of XRD patterns and how it relates to crystallographic structure and orientation was discussed extensively in previous chapters. The role of the TCO structure and composition on OPV devices has not been widely investigated and the large differences observed between these TCOs can be useful in gaining a greater understanding of their importance on device performance, if any.

In this comparison study, the thicknesses of the TCO films were optimized to obtain films with similar optical transparencies since differences in light transmission are known to lead to changes in charge carrier generation in OPV devices and influence the open circuit voltage (V_{OC}), short circuit current (J_{SC}) and fill factor (FF). (200) All TCO films exhibit $> 80\%$ optical transmission throughout nearly the entire visible and near IR regions comparable to ITO (Figure 6.3). The electrical transport properties of IZO, GZO, and AZO were also observed to be comparable to that of ITO. Some variation in sheet resistance is due to difference in electrical conductivity (σ) of the films which is intrinsic material property. The sheet resistance (R_{sheet}) of IZO, GZO, and AZO are listed in Table 6.1 and are observed to be slightly larger than that of ITO. These differences, in part, can be attributed to thickness differences between films and in practice can be altered to reduce their R_{sheet} and obtained closer values to ITO, with corresponding changes in transmission characteristics.

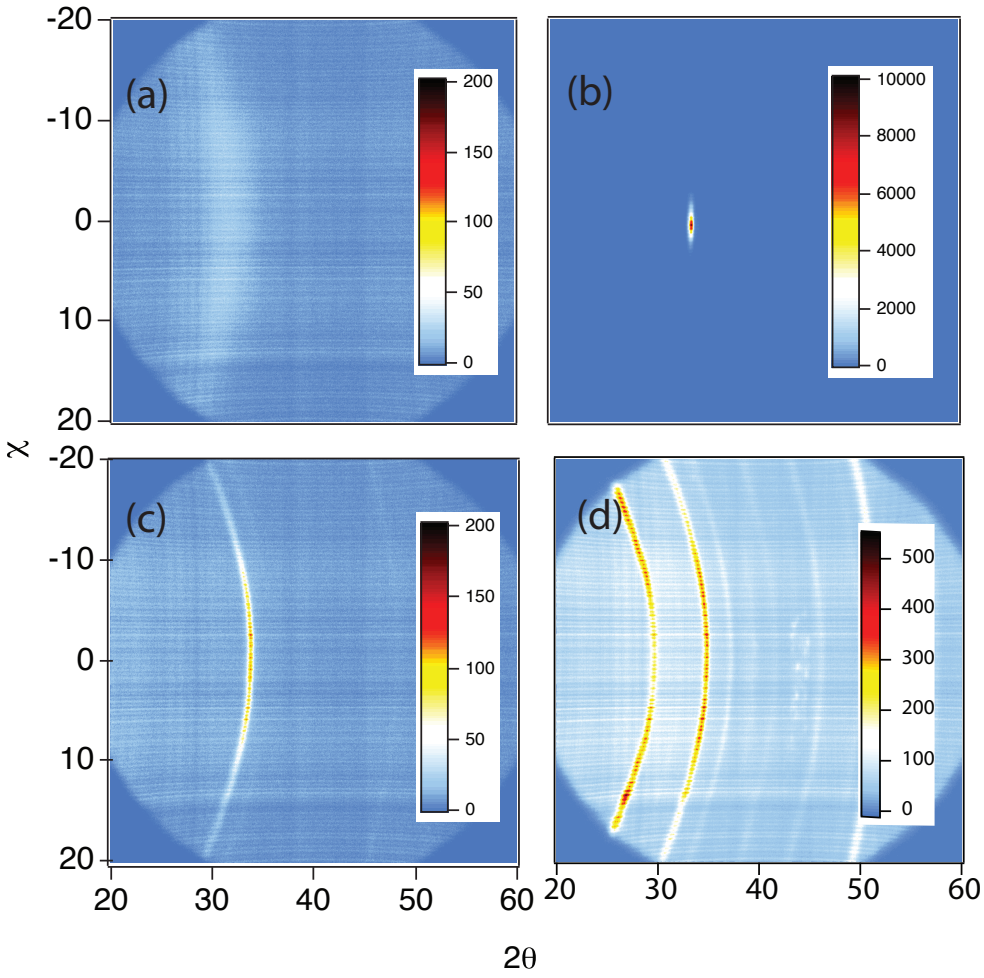

Figure 6.2: XRD measurements of (a)IZO, (b) GZO, (c) AZO, and (d) ITO.

Table 6.1: Physical properties of TCO films with and without ZnO layer.

	No ZnO			with ZnO	
	R_{sheet} (Ω/sq)	ϕ (eV±0.1)	ϕ_{UV-O_3} (eV±0.1)	S_{rms} (nm)	S_{rms} (nm)
AZO	26.3±1.9	4.4	5.1	3.65±0.24	1.83±0.13
GZO	15.2±1.6	4.4	5.2	3.48±0.17	1.79±0.08
IZO	12.3±0.9	4.5	5.1	0.24±0.02	2.15±0.17
ITO	9.8±0.5	4.9	5.1	2.10±0.22	1.15±0.13
Glass			< 0.2	1.74±0.15	

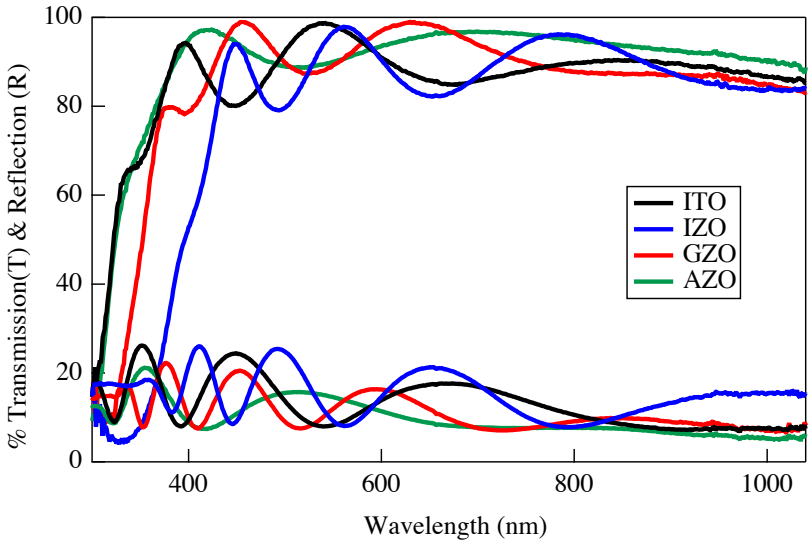

Figure 6.3: Transmission and reflection spectra of ITO, IZO, GZO and AZO on glass.

The work function (ϕ) of IZO, GZO, and AZO (Table 6.1) were also found to be comparable to ITO after UV-O_3 treatment ($\sim$ 4.9 eV). However, prior to the UV-O_3 treatment the work function of IZO, GZO, and AZO ($\sim$ 4.2 eV) were observed to be significantly lower than that of ITO (4.7 eV) and closer to the value of intrinsic ZnO films (4.2 eV). (9) A UV-O_3 treatment is believed to increase the work function of ITO (or other TCOs) by removing organic surface contaminates and increasing oxygen content of the surface. (201, 184)

A similar phenomenon may be occurring in these ZnO-based TCO films. Also in Table 6.1, surface roughness S_{rms} of TCOs, and with ZnO on top is shown. These S_{rms} values were obtained from AFM surface topography measurement, with example AZO and AZO with ZnO on top shown in Figure 6.4a and 6.4b respectively. From the figure and table, we find that effect of depositing ZnO on

top of TCOs result in decrease in S_{rms} for ITO, AZO and GZO. However, there is increase in IZO S_{rms} after ZnO modification. All the TCOs with ZnO on top had similar surface topography features like shown in Figure 6.4 b, suggesting that final surface roughness after ZnO ETL layer is independent of underneath substrate. This normalization of surface roughness could be a key reason why all the TCOs with ZnO on top had similar PV performance as discussed below. The hole transport layer oxides such as NiOx, MoOx are $<$10 nm thick so they tend to take the surface roughness of the underneath substrate, while PEDOT:PSS organic HTL are thicker ($\sim$ 40 nm) and yield flatter surfaces. (26, 18). Although not shown here, we do expect ZnO modification to result in similar chemical interaction and similar charge transfer to occur at organic/oxide interface.

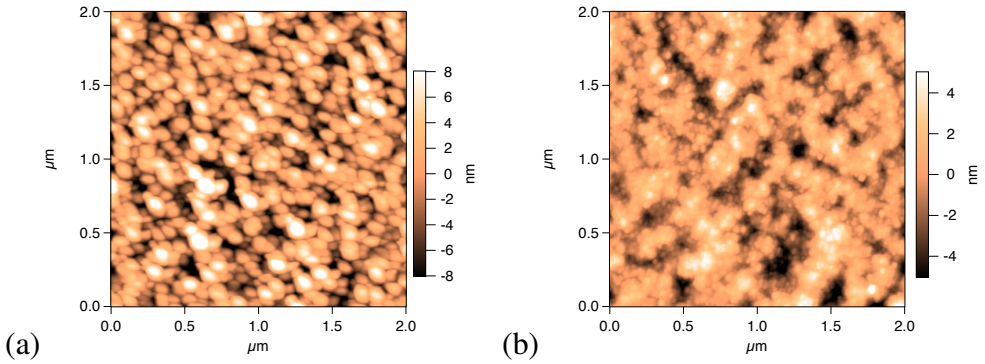

Figure 6.4: Surface topography of (a) AZO and (b) AZO with ZnO layer.

To evaluate the performance of OPV devices on untreated IZO, AZO, and GZO electrodes, P3HT:PC60BM BHJ devices with an inverted architecture were fabricated. (202, 171) The J-V data from the TCO/P3HT:PC60BM/HTL/Ag devices are shown in Figure 6.5a. We observe large differences in J-V characteristics between devices that are believed to arise from the differences in the

TCO electronic, structural, and surface properties. All devices exhibit poor PV behavior with low fill factors ($< 40\%$). Poor diode behavior is also observed in dark J-V measurements with poor rectification ratios of < 150 at ± 1V (Figure 6.5 b). The poor PV behavior observed is contrary to the excellent PV behavior previously reported in IZO devices. (171) This discrepancy is possibly due to and an indication of a strong dependence of the device performance on the TCO properties in devices with a similar architecture.

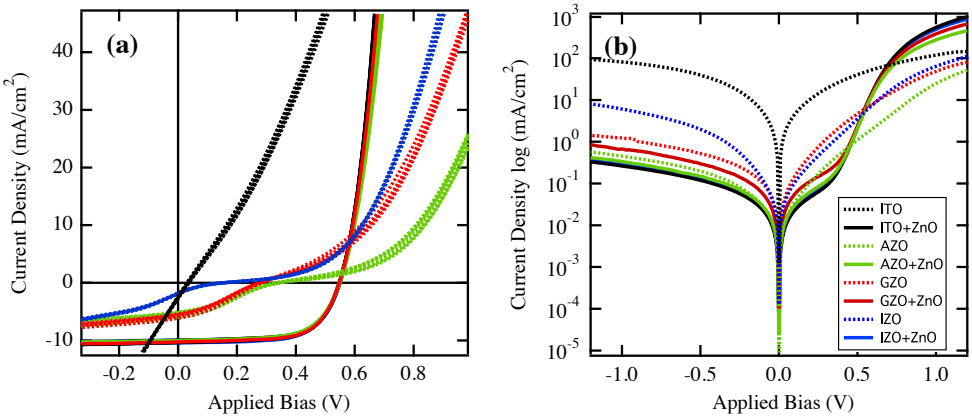

Figure 6.5: J-V plots under light (a) and dark (b) of TCO/P3HT:PCBM/HTL/Ag and TCO/ZnO/P3HT:PCBM/Ag devices with ITO, IZO, GZO and AZO TCO bottom electrodes.

The low fill factors and poor PV behavior in bare TCO devices arise predominately from the presence of double diodes (s-kinks) that are indicative of recombination at this contact in the devices. (203, 107, 204) A possible cause for significant recombination in the devices under investigation is poor electron collection properties of the TCOs such as energetic barriers, poor charge selectivity, and/or generation of weak built-in electric fields. Undesirable vertical phase segregation in the BHJ layer can also lead to poor device performance in part due to charge accumu-

Table 6.2: Photovoltaic parameters of devices with various TCOs

	R_{series} (Ω)	V_{oc} (mV)	J_{sc} (mA/cm^2)	FF (%)	PCE (%)
ITO	22.1±0.7	548±1	10.2	64.4±0.1	3.50
IZO	24.5±1.2	549±1	10.2	64.7±0.3	3.50
GZO	18.6±3.0	541±5	10.3	61.6±2.8	3.33
AZO	48.0±1.5	545±2	10.1	62.8±0.5	3.35

Note: Standard deviations in $J_{sc} < 0.2$ mA/cm^2 and PCE $< 0.1\%$.

lation and increase recombination. (44) Determining the exact origin for the J-V behavior observed is not within the scope of this work. However, as demonstrated in the following section, the disappearance of the double diode behavior when the TCO contact properties are decoupled from the BHJ layers point to the TCO/BHJ interface as a critical aspect in device performance.

OPV devices commonly utilized ETL and HTL layers between the electrodes and BHJ in an attempt to improve device performance. (102) Figure 6.5a and 6.5b also show the light and dark J-V plots of TCO/ZnO/P3HT:PC60BM/HTL/Ag devices in which a thin high resistivity (100 nm film has sheet resistance $>$ 1×10^8 Ω/sq) ZnO film was deposited as an ETL between the TCO and BHJ. Solution processed ZnO is commonly used as an ETL in inverted OPV devices due to a combination of relatively low carrier concentration ($\sim 10^{17}$cm^{-3}) (68), high electron mobility, and favorable conduction and valance band positions (4.2 eV and 7.4 eV respectively). (9) This results in a contact with a work function well suited for electron collection and a deep valence band position for hole blocking. A dramatic improvement in PV behavior is observed by the insertion of a ZnO ETL in all devices measured (Figure 6.5) with minor differences in PV performance

between devices (Table 6.2) and much improved rectification in the dark diodes ($\sim 1.1\times10^3$ at ±1 V). The nearly identical J_{SC} of $\sim$ 10.2 mA/cm^2 in all devices is consistent with the efforts to fabricate TCO films with similar optical transmissions as discussed above.

However, the differences in R_{sheet} obtained are believed to result in slightly lower fill factors ($\sim 62\%$ versus $\sim 64\%$) and higher series resistance ($\sim 48\ \Omega$ versus $\sim 22\ \Omega$) particularly in AZO devices (Table 6.1) due to their higher R_{sheet} values (26.3$\pm$019 Ω/sq versus 9.8$\pm$0.5 Ω/sq). Overall, similar and high PCEs ($> 3.3\%$) are measured in IZO, GZO, and AZO devices comparable to similarly fabricated ITO devices (PCE $\sim 3.5\%$) and those previously reported by others. (170, 205, 206)

This is despite differences in optoelectronic, structural, and contact properties of the TCOs. The great improvement in these devices emphasizes the importance of an ETL or interfacial contact layer to assist in the decoupling of the TCO contact properties from the device performances. This therefore permits the optimization of the performance in OPV devices, where the TCO electrode has electronic and/or structural/surface properties that inhibit efficient electrical contact to the photoactive layer.

6.1.4 Conclusions

In summary, we have demonstrated that sputtered IZO, GZO, and AZO films can be fabricated with attractive optoelectronic properties and function as excellent TCO electrodes in OPV devices when employing a solution processed ZnO ETL.

This control of the interfacial electronics using the ZnO ETL demonstrates the ability to effectively decouple the interface and surface properties of the TCOs from the organic active layer. This approach and demonstration of the equivalent device performance between these alternative TCOs, with comparable optoelectronic properties to ITO, demonstrate that their ability to function effectively as alternative OPV electrodes is largely dictated by the ETL contact layer. This demonstration provides a template for the use of electrodes with attractive features such as low precious element content or improved mechanical properties.

Acknowledgements: This work was done in collaboration with following authors: A.K.Sigdel, A. Garcia, M. L. Machala, P. F. Ndione, N. E. Widjonarko, M. T. Lloyd, D. S. Ginley, D. C. Olson and J. J. Berry. This work was support by the U.S. Department of Energy under Contract No. DOE-AC36-08GO28308 with the National Renewable Energy Laboratory DOE SETP program through the National Center for Photovoltaics for oxide materials development and materials for device fabrication. Work function, optical studies and device analysis were supported as part of the Center for Interface Science: Solar Electric Materials, an Energy Frontier Research Center funded by the U.S. Department of Energy, Office of Science, Office of Basic Energy Sciences, under Award Number DE-SC0001084. M. L. Machala received support from the DOE Office of Sciences Science Undergraduate Laboratory Internship Program.

6.2 Modulation of Mobility and Carrier Concentration in ZnO Electrode for Efficient Charge Collection in OPV

Abstract: The role of ZnO as a selective interlayer for organic photovoltaic systems has long been recognized. Here we present a detailed study of the role of the physical properties the thin ZnO layers on the performance of inverted architecture bulk heterojunction organic photovoltaics. Specifically we have employed the flexibility of ZnO system to modulate the mobility μ and the carrier concentration N to alter the performance of the device. This data provides a experimental foundation for the the design rules needed for optimizing the ETL (and HTL) contact with the organic active layer materials. ZnO films were prepared via sputtering with varying oxygen partial pressure during film growth in order to obtain the films with μ ranging from $\sim$ 0.3 to $\sim$ 30 cm^2/Vs and N ranging from $\sim 1\times 10^{16}$ to $\sim 1\times 10^{21}$ $/cm^3$. These layers are integrated with both p3HT:PCBM and (data not shown: PCDTBT:PCBM) absorbers. We present an analysis of the resulting devices as a function of the physical properties of the ZnO layers. We find that variations in performance are primarily controlled by electronic properties of the ZnO layer. Both mobility and N are interlinked, and can vary with photo-doping. Thus, we found diode ideality factor (n) obtained via dark JV measurement and comparing with μ/N a good indicator for evaluating the performance of solar cells. From our analysis, we find maximizing the μ and minimizing N required for ETL performance.

6.2.1 Introduction

Use of low work function metals such as Ca/Al in standard geometry do provide good electrode for electron collection, but bigger problem using low work-function metal electrode is with formation of non-conductive metal oxide due to oxidation resulting in rapid device failure. (13, 170, 173) Hence, using low work-function, air stable, conductive metal oxides such as ZnO as a electron collecting electrode has been on the rise.

Various reports on ZnO thin film deposited via techniques such as atomic layer deposition, sputtering and solution-processed ZnO has been shown to perform as electron transport layer(ETL) layer in literature. (202, 13, 170, 173) But variation in performance, along with a variety of other issues such as formation of double diode in the absence of UV-light, can cause problems in the resulting devices. (179, 207, 208, 202) Since, ZnO thin film deposited via different technique have vastly different bulk and surface physical properties, including the structure, morphology and related electronic properties. (209, 210, 39, 9)

Here we present a systematic study in which the key electronic properties (e.g. μ and N) of ZnO are systematically manipulated to determine to what extent these properties are responsible for the sigmoidal or double-diode phenomena and hence the performance of the devices are missing. Maximizing the conductivity via increase in both μ and N, while maintaining a good optical transparency is critical to maximize the TCO Figure of merit. The increase in bulk conductivity helps in charge transport in parallel to the thin film to minimize the series resistance

in typical device architectures. In ZnO based TCO systems, higher mobility film can be obtained by improving the microstructure, and improved crystallographic texture, (116) where as addition of dopants such as Al, B, Ga or intrinsic defects such as oxygen vacancies generated in the deposition process increases the carrier concentration. Similar techniques for optimization of electrical conductivity in TCOs, can be applied to modulate the physical properties of the ETL layers. However the requirements for the ETL is distinct from the typical TCO function and therefore the TOC figures of merit (17), specifically the ETL layers need to have charge transport and tailored selectivity in direction perpendicular to the plane of thin film or at the oxide/organic interface.

In standard architecture devices, employing oxide semi-conductor MoOx,VoOx, NiOx as hole transport layers, due to poor conductivity or due to poor optical properties, selective contacts are made very thin. (19, 26, 211, 212) But in inverted devices, where oxide semi-conductor does electron collection, ZnO with $E_g > 3.2$ eV, has good optical properties, and electrical properties which are tunable as a function of deposition resulting in less variation thickness variation once above a threshold value have very small impact on device performance. i.e loss in J_{sc} by employing thicker film, or impact in Rs is minimum. Due to columnar growth, differences in microstructure and the influence of substrate, variation in thickness results in changes in both structural and electronic property of the thin film. (9) Previous studies on ZnO thin film grown with varying thickness via ALD, Cheun et al has shown that critical thickness of 10 nm is required to obtain a good working device. (202) The study also showed that ZnO films ranging from 10 nm to 100 nm resulted in similar device performances.As stated above, the problem of in-efficient

charge collection due to poor understanding of interface and/or bulk property of oxide electrode exists at several other oxide-organic interfaces as well. Transparent metal oxides such as titanium dioxide (TiO_2) (102), Indium Zinc Oxide (IZO) (171) and few others seem to suffer the similar fate with limited success. But, immense literature on ZnO (9), plus the stability of devices in air (170) allows us to systematically probe the problem with various scientific tools. (213) The use hall voltage measurement technique to accurately measure mobility and carrier concentration in ZnO allows us, in contrast to NiO and NiCoOx HTL systems where these measurements are obscured due to complex magnetic properties of the materials, to pin-pointing influence of basic physical property of this oxide system on charge transport in the resulting devices. Moreover while the interfacial physics and chemistry likely result in variations dependent on the details of the organic/oxide interface the larger charge transport issues explored here provide insight into device physics and requirements of other charge collecting electrode.

In this work, ZnO films with varying mobility and carrier concentration were prepared via sputtering with varying oxygen partial pressure during film growth in order to obtain the films with μ ranging from $\sim$ 0.3 to $\sim$ 30 cm^2/Vs and N ranging from $\sim 1\times 10^{16}$ to $\sim 1\times 10^{21}$ $/cm^3$. We examined the physical properties of the ZnO layers and correlate their performance in inverted OPV geometry ITO/ZnO/P3HT:PCBM/PEDOT:PSS/Ag devices. We find improvement in device performance can be achieved by maximizing the mobility and minimizing the number of carriers ($\sim 10^{18}$ to $\sim 10^{16}$ $/cm^3$) in ZnO electron transport layer, with preferable energy level alignment with the organic counterpart. The results from the sputtered films were then compared to various techniques such as atomic layer

deposition and commonly used solution-processed ZnO, providing addition insight on the impact of the films micro structure on the device performance.

6.2.2 Experimental

ZnO films of varying opto-electronic properties were prepared in one of three ways: Sputtering, Solution Spin Cast, Atomic Layer Deposition

Sputtering: ZnO was deposited via sputtering depositions with 2 inch diameter 99.99% ZnO ceramic target or 99.99% Zn metal target using DC magnetron sputtering (Advance energy DC pinnacle plus) with a conventional magnetron sputtering source (Angstrom Sciences, Inc.). Partial pressure of oxygen in the deposition chamber was varied with respect to Argon ($>$ 99.999%) in order to yield ZnO films with varying physical properties.

Solution Spin Cast: Diethyl zinc decomposition (DEZ): 1 part dilute diethyl zinc (15% in toluene) was added to 2 parts tetrahydrofuran (THF) and the solution was spin-coated onto the ITO substrates (4000 rpm, 60 seconds). Films were left to dry at room temperature in air for 15 minutes, then annealed at $120\,^{\circ}\mathrm{C}$ for 10 minutes. These were rinsed in DI water and ethanol and dried on a hot plate at $120\,^{\circ}\mathrm{C}$ for 5 minutes.

Atomic Layer Deposition: See reference (22). *Thin Film Characterization*: Described in previous chapters.

Device Fabrication: Prepatterned ITO covered glass substrates were cleaned by sonication in acetone and isopropyl alcohol for 5-10 minutes each and rinsed with a stream of nitrogen. Substrates were cleaned of organic material using an oxygen plasma device for 5 minutes at a power of 150 watts (Technics). ZnO interlayer was deposited via various techniques described before. A 1:1 by weight solution of P3HT (Rieke Metals Inc.) and PCBM (Nano-C) in anhydrous dichlorobenzene (1 mL for every 40 mg of material, Aldrich) was allowed to stir overnight at $80\,^{\circ}\mathrm{C}$. The test and control substrates were placed in a nitrogen glove box ($<$5 ppm O_2, $<$5 ppm H_2O) and spin cast with the solution at a spin rate of 600 RPM.

Substrates were placed in a covered Petri dish while still wet and left to slow dry in the glove box for 90 minutes (reference). Oxygen plasma treatment of the active layer was performed at a power of 45 watts for 0.2 min. After plasma treatment, substrates were immediately spin cast with two layers of PEDOT:PSS (Clevios PVP Al 4083) at a rate of 4000 RPM in air and annealed at $120\,^{\circ}\mathrm{C}$ for 10 minutes. Samples underwent thermal evaporation through a shadow mask with 100 nm silver at a rate of 2 $\mathring{A}$/s in an Angstrom Engineering metal evaporator at a pressure of 10^{-7} torr, yielding a device area of 0.11 cm^2.

Device measurement and characterization: Samples were characterized for J-V behavior using light emitted from a tungsten halogen lamp (ELH) with a system controlled with a LabVIEW interface. Efficiencies were calculated by the following equation:

$$\eta = \frac{FF \times V_{OC} \times J_{SC}}{LI} \tag{6.2.1}$$

where FF is fill factor, VOC is open circuit voltage, JSC is short circuit current, and LI is light intensity. Two silicon photodiodes equipped with a KG5 filter (Hamamatsu) were used to determine a light intensity of 100 mW/cm^2 and a spectral mismatch factor of 1.0. A 420 nm cutoff filter was used for elimination of light emanating from the bulb in the UV range. Samples were light-soaked with UV light for 3 minutes and 15 minutes under the tungsten halogen lamp and for 30 seconds under an XT10 xenon solar simulator.

6.2.3 Results and Discussion

ZnO electrical properties changes due to photo-doping. Figure 6.6a shows the changes in series resistance of the ZnO thin film in the presence of UV light and in recovery. Figure 6.6b shows the changes in work-function (ϕ) in with UV-light and off. Some of this work-function changes can be attributed to changes in fermi level as more carrier are present in film with changes in surface defects resulting in Burstein Moss shift. Figure 6.7c, showing changes in Dark JV with initial UV dosing and finally changes device performance is seen in Figure 6.7d. Several reports have shown that device performance changes/ improves with light soaking, which can be hard to pinpoint if various physical properties of ZnO film are changing simultaneously. (202) In order to understand if μ and N had any effect on diode performance, proper way would be to first understand the diode characteristics in dark, where one would expect both μ and N be constant.

The ZnO thin film deposited via different technique have vastly different properties, especially the structure, morphology and electronic properties. Analysis

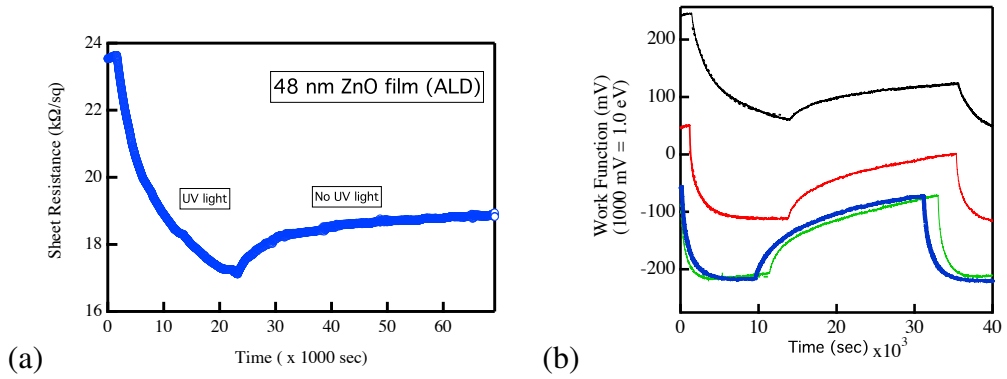

Figure 6.6: a) Changes in series resistance of 48nm ZnO thin film b) Changes in ϕ (Kelvin probe) for various thickness ZnO with UV light λ = 248 nm and recovery.

of the physical properties of the ZnO layers with their respective OPV device performance can be crucial for understanding the design rules needed for designing the good ETL or any charge selective electrode in OPV device. Primarily, the energy level mostly the band gap and fermi level are dependent on material property and can vary vastly within the same thin film. Due to limitation of our hall measurement system, or poor electronic property of thin ZnO film, we could only measure μ and N of films above 10 nm. There were some variation in μ and N of the film with increasing thickness. The μ varied from 5 cm^2/Vs for 10 nm film to 20 cm^2/Vs for 50 nm ZnO film. Changes in thickness had less effect on N, with various films around N of $\sim 6\times 10^{19}$ /cm^3.

It was necessary to establish in this device architecture, a good PV device which has good efficiency in light also has a low ideality factor or good diode characteristics in dark. This was the basis for rest of the study where μ and N can be varied to understand its impact on device performance. Figure 6.8a shows the thickness study on ZnO, with the known electrical properties. We found a good

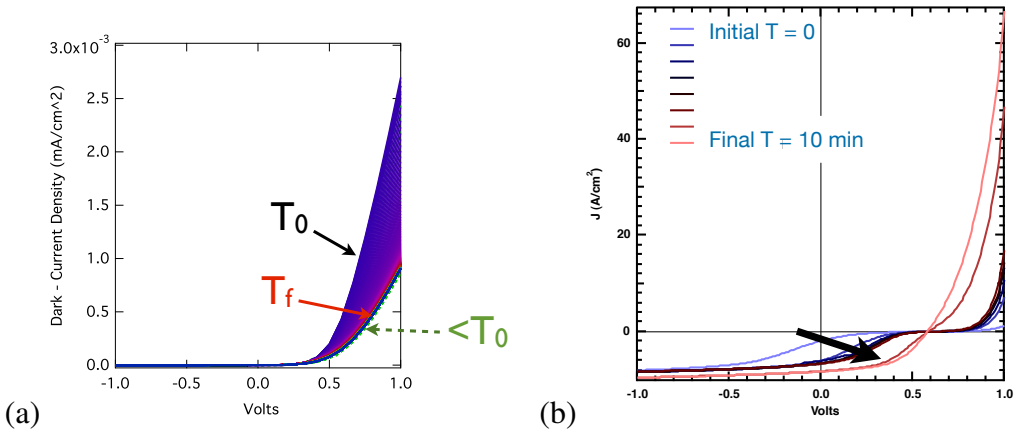

Figure 6.7: a) Changes in dark JV device evolution with UV light λ = 248 nm, with exposure at T_0. (b) Changes in device performance in light (100 mW/cm^2 AM 1.5 G) during measurement.

working devices, also had good diode characteristics as measured in dark, and matches with the existing literature. (202) Especially devices with good FF and η had a lower diode ideality factor n'. The analysis also indicated that smaller number near Voc (Figure 6.8b. So due to measurement convenience, as well as to compare the devices with solution processed ZnO as ETL layer standard, we have fixed the thickness of our ZnO thin film around 40 nm, above the critical thickness.

Accordingly, we have systematically varied oxygen partial pressure during film growth, and obtained films with varying μ and N. The physical properties of the ZnO layers with their respective OPV device performance, mainly the ideality factor derived from dark JV was analyzed. From the Figure 6.11, we see variations in performance are primarily controlled by electronic properties of the ZnO layer. In Figure 6.11a, we do not see clear correlation between μ and n. Some systematic trend were absorbed for devices with changes in N, as seen in Figure 6.11b. We find

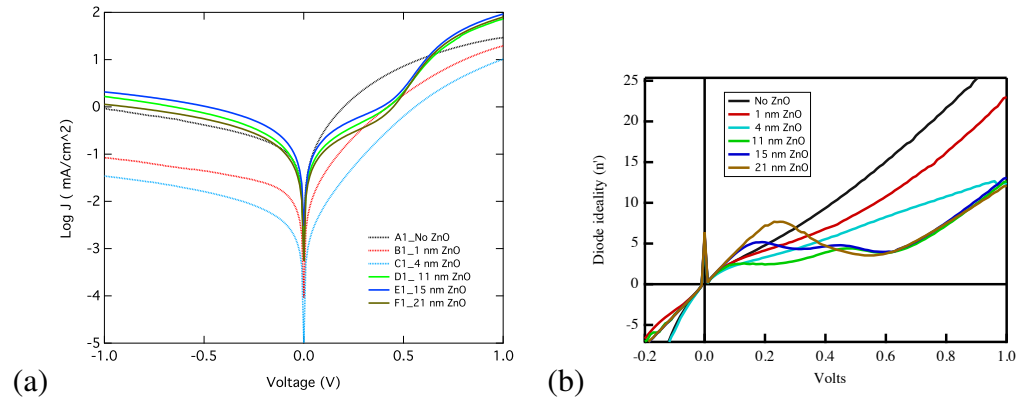

Figure 6.8: a) Dark JV for devices with ZnO ETL with varying thickness (b) n-prime analysis for same sets of devices. Low ideality near V_{oc} yields good device performance.

diode ideality increases with increasing N, especially beyond 10^{19} /cm^3 devices were marred with massive recombination and hence the high diode ideality.

Some representative Light JV curves for both Zn metal rich condition and O_2 rich conditions are shown in Figure 6.9 and Figure6.9 respectively. Thus, explained earlier that depending upon the deposition condition, films can be either zinc rich or oxygen rich, which has significant impact on optical and electrical properties. Zinc metal rich films have poor transparency but relatively high conductivity and the oxygen vacancy is more likely the dominant defect present. Due to poor transparency in this condition, loss in J_{sc} is observed in as shown in Figure 6.9. While on the other end, oxygen rich ZnO films have good transparency but they have poor electrical properties due to compensation of carrier with both zinc vacancies or oxygen interstitials present in the materials. As seen in Figure6.9, formation of a double diode, and poor performance is observed at this condition.

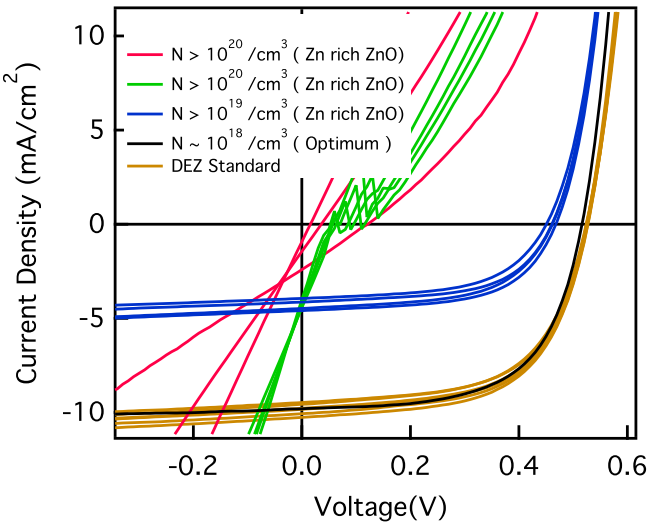

Figure 6.9: Light JV for devices with ZnO ETL via sputtering with metallic target, Zn rich condition

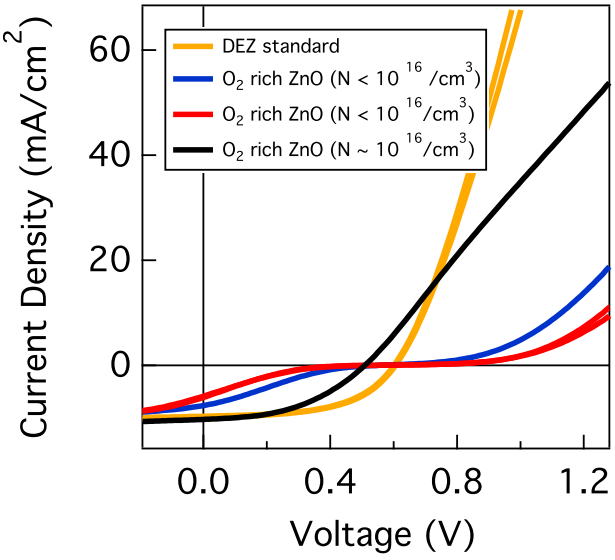

Figure 6.10: Light JV for devices with ZnO ETL via sputtering with metallic target, O_2 rich condition

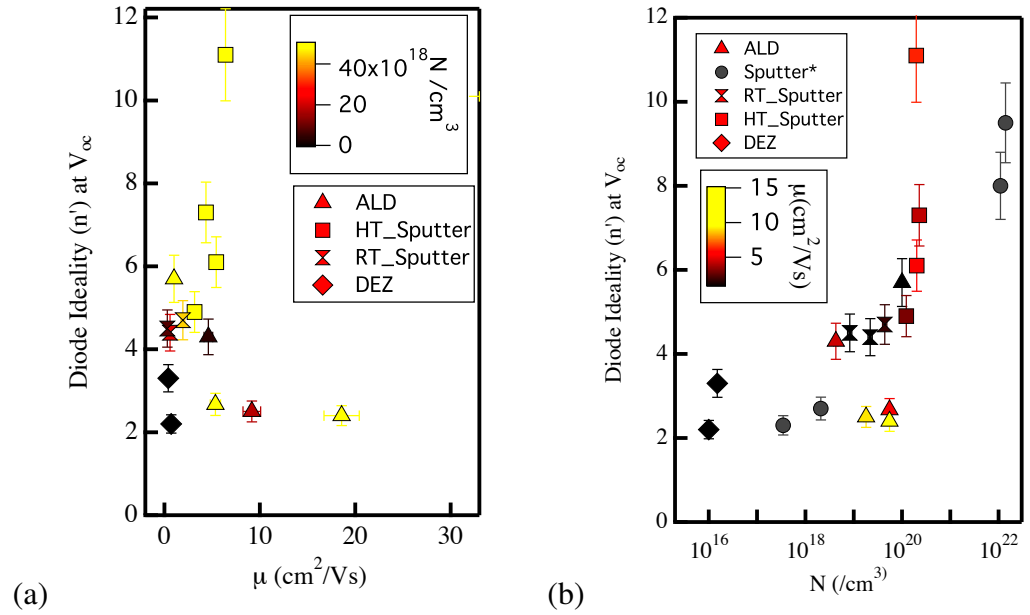

Figure 6.11: Diode ideality at V_{oc} as a function of (a) Mobility μ (with color code as N) (b) N (with color code as μ)

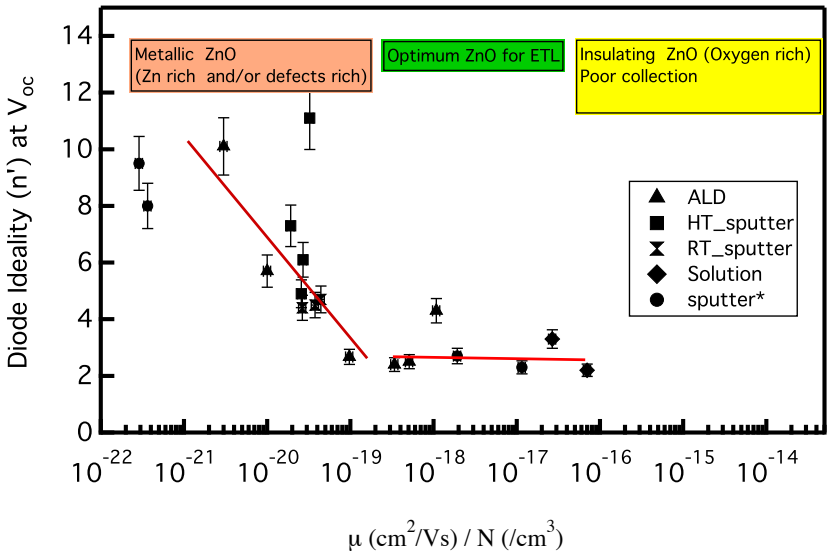

Figure 6.12: Diode ideality at V_{oc} as a function of μ/N

In a thin film both μ and N are interlinked physical parameters, as it is very hard to modulate one without changing the other. A diode ideality factor (n) obtained via dark JV measurement and comparing with μ/N (see Figure 6.12) a good indicator for evaluating the performance of solar cells. From the Figure 6.12 we find the range of μ/N = $\sim 1\times 10^{-16}$ to $\sim 1\times 10^{-19}$ result in good ETL performance. Mainly, we find maximizing the μ and minimizing N up to $\sim 1\times 10^{17}$ /cm^3 required for ETL performance.

6.2.4 Conclusions

The role of optoelectronic and structural properties of undoped and degenerately doped ZnO thin on the performance of inverted architecture bulk heterojunction organic phovoltaics as an selective contact has been examined. The flexibility of ZnO system allowed us to modulate various opto-electronic property mainly mobility μ and the carrier concentration N to examine optimizing the ETL (and HTL) contact layers. Analysis of the physical properties of the ZnO layers with their respective OPV device performance is discussed. Variations in performance are primarily controlled by electronic properties of the ZnO layer. Both mobility and N are interlinked, and can vary with photodoping. Thus, we found diode ideality factor (n) obtained via dark JV measurement and comparing with μ/N a good indicator for evaluating the performance of solar cells. Thus for good working device, along with appropriate energy level matching, ETL performance is further contingent upon maximizing the μ and minimizing the N.

Acknowledgements: Materials development including oxide deposition and characterization equipment was provided by the U.S. Department of Energy under Contract No. DOE-AC36-08GO28308 with the National Renewable Energy Laboratory. Support for characterization and analysis work was provided as part of the Center for Interface Science: Solar-Electric Materials (CIS:SEM), an Energy Frontier Research Center Funded by the U.S. Department of Energy, Office of Basic Sciences, under Award Number DE-SC0001084.

Chapter 7

Next Generation Tailored TCO : Indium Zinc Tin Oxide

Use of amorphous ZTO interfacial transport layer for hole injection in OLED instigated a study so see if energy level matching using ZTO allows for efficient hole collection in standard architecture OPV devices. While the increase in work function of the ZTO compare to ITO should have facilitated the hole collection efficiency in OPV devices, the resulting JV curve showed almost no photocurrent. We wanted to understand why a-ZTO failed so badly. Was it due to amorphous nature of the material with very different electronic property or is it something to do with some interfacial chemistry that dominates the charge transport? We wanted a similar system that would have deeper workfunction and could potentially exist in both crystalline and amorphous phases. In addition it had to have better chemical stability compare to ITO and ZTO. The quaternary oxide system, Indium Zinc Tin Oxide (IZTO), served that purpose. This material system in crystalline phase is used by OLED community for similar motivation as ZTO we discussed in previous

chapter. In this chapter we look into if IZTO films with same composition can exist in either amorphous or crystalline phase with deep(high) work function and low sheet resistance or $\sigma > 1000$ S/cm so that we could potentially utilize them in device applications. This system also allows for fixed compositional comparison on a TCO system to investigate effect of charge transport (hole collection in this case) as a function of crystallinity. This work is complementary to the other work we have done to on low work-function IZO (not included here, manuscript in preparation) where we investigate electron collection as a function of crystallinity.

The following section is based on TCO research and development aspects. Some IZTO based OPV device relevant data are also discussed at the end.

7.1 Introduction

Crystalline and amorphous transparent conducting oxides (TCOs) based on indium, zinc and tin are of general interest in a range of optoelectronic systems such as transparent thin film transistors (55, 214, 215) light emitting diodes (47) photovoltaics (170) and other emerging technologies. Crystalline TCOs such as ITO, AZO, GZO, FTO can have better conductivity (σ) compare to amorphous TCOs. However, amorphous TCOs such as IZO, IGZO have more resilient mechanical properties, and low surface roughness making them attractive for incorporation into flexible electronics. (175, 163) Also amorphous oxides with lack of grain boundaries have demonstrated superior reduced water vapor transmission rates and high mobilities (μ) compared to poly-crystalline TCOs, a critical factor

for some device application. (216, 159, 217) These possible applications in which a flexible form factor is desirable have already generated a considerable amount of effort on amorphous InZnO, ZnSnO and related material systems. (174, 177, 218)

Compared to the industry standard ITO based TCOs, IZTO materials have deeper work-function ranging from 5.0 eV to 6.1 eV. (219, 220, 221, 222) The deeper work function, is of particular interest in organic light emitting diodes (OLEDs) for an efficient hole injection (223, 224) while other technologies, such as organic photovoltaics (OPVs) and other thin photovoltaic PV technologies, have similar although slightly different considerations that make deep work function electrode to provide matching energy alignment of interest. (225, 19, 15)

Recent research efforts on IZTO were driven by the OLED communities focus on doping crystalline ITO with small amount of ZnO to make a deep work-function crystalline IZTO (c-IZTO) films. (226) Reports on amorphous IZTO (a-IZTO) films have shown that on flexible substrate, such as polyethylene terephthalate (PET), good mechanical durability is exhibited as compared to ITO. (227, 228, 72, 229) A variety of techniques for IZTO deposition have been reported in the literature with indium content as low as 40% to as high as 90%. Some of the techniques actively being researched include magnetron RF and DC sputtering (219, 230, 231) and various solution processing routes. (232, 233)

TCOs based on the IZTO ternary compound with the ability to remain conductive in either the crystalline or amorphous phase from a fixed composition oxide target via magnetron sputtering is significant for many potential applications.

Recently, using a fixed composition target of $In_{0.5}Zn_{0.25}Sn_{0.25}O_x$, which is known to exists in single phase in subsolidious phase space, (234, 235, 236) Cleva W Ow-Yang et al reported amorphous IZTO films deposited via a DC sputtering process with σ as high as 1250 S/cm. (231) However the ability to tune or control the properties was not investigated.

In this paper, we demonstrate the structural tunability of the sputtered films from this target composition can range from poly-crystalline to amorphous IZTO films by control of the RF sputter deposition parameters. The substrate temperature (T_s) in conjunction with both process gas pressure (Ps) and RF power density (ρ_{rf}) are critical in controlling crystallinity, conductivity (σ) and work function (ϕ). The films deposited at higher temperature of $250\,^{\circ}\mathrm{C}$ have more efficient carrier generation resulting in high conductivity films, but amorphous films (mixed phase) deposited at high temperature suffered some degree of phase segregation. Higher temperature deposited films show increase in optical gap due to a Burstein-Moss shift resulting from the increase in carrier concentration. Highest σ to date for this composition poly-crystalline and amorphous films were 2260 $\pm$ 30 S/cm and 1470 $\pm$ 20 S/cm respectively. The c-IZTO films have lower $\mu \sim 30$ cm^2/Vs and higher number of carriers, where as a-IZTO films have larger $\mu \sim 38$ cm^2/Vs with low number of carriers. Films have work-function ranging from 5.2 $\pm$0.1 eV to 5.6 $\pm$0.1 eV as measured by kelvin probe. For c-IZTO, increase in electron carrier concentration resulted in decrease in work-function, where as a-IZTO follows the opposite trend. Further examination of surface using c-AFM showed poor electrical transport for a-IZTO.

7.2 Materials and Methods

Films were deposited on 50.8 mm $\times$ 50.8 mm Corning Eagle 2000 glass substrate using RF magnetron sputtering source at 13.56 MHz (Dressler Cesar RF power generator Angstrom Sciences, Inc) with pure argon ($>$99.999$\%$) as the sputtering process gas. The sputter source was 50.8 mm diameter Zn:In:Sn ceramic oxide target (99.99$\%$ pure, Cerac Inc) with a atomic ratio of 1:2:1. The substrate to the target distance, which has been shown to influence the electrical properties of TCO was maintained at 64 mm for all depositions. The experimental details of substrate preparation, mounting procedures and temperature measurements during deposition were described previously. (48, 116) The deposition chamber had base pressure of $<1.3\times10^{-4}$ Pa and for all depositions, the substrate was baked at $250\,^{\circ}\mathrm{C}$ for 0.5 hours prior to deposition, and equilibrated to desired deposition temperature. For each deposition the plasma was allowed 10 minutes of a burn-in period to equilibrate. All the films were grown for 25 minutes resulting in films with thickness range of 400 $\pm$ 150 nm. The films grown at elevated temperatures were cooled down to $<100\,^{\circ}\mathrm{C}$ in the evacuated deposition chamber before removal in order to minimize oxidation and thermal stress due to rapid cooling of the films.

Structural analysis employed X-ray diffraction (XRD) patterns using a Bruker Discovery 08 with a large area detector, and on a Rigaku Ultima IV X-ray diffractometer both using Cu-Kα radiation with λ = 1.54 $\mathring{A}$. An Asylum Research Molecular Force Probe (MFP-3D) Atomic Force Microscopy (AFM) was used to determine surface morphology in tapping mode with tip radius $<$12 nm, k = 40 N/m, ω = 300 kHz (Budget Sensors Inc Tap300DLC tip). Transmission

electron microscopy (TEM) cross-section samples were prepared using a FEI Nova 200 focused ion beam workstation. The thinned TEM cross-section samples were examined at 300 kV in a FEI Tecnai 30 high resolution TEM fitted with a super-twin objective lens capable of a TEM point resolution of 0.20 nm.

The conductivity for the films was calculated using the approach of measuring the thickness (a Sloan Technologies Dektak profilometer and a J. A. Woollam M-2000 spectroscopic ellipsometer) and then the sheet resistance with a four-point probe.. A Hall measurement system (Accent HL5500PC) was used to obtain carrier concentration, mobility and also to confirm the conductivity values obtained with the four-point probe measurements. Hall data was taken using a van der Pauw configuration at room temperature in a magnetic field of 0.3 T. Work-function (ϕ) of oxygen plasma cleaned sample was measured using a kelvin probe system (KP technology) using a gold (Au) probe. Work-function measured in mV was converted into eV using reference measurement done on gold (Au) and aluminum (Al) with Au(ϕ) = 4.8 eV and Al(ϕ) = 4.1 eV respectively.

Optical properties of the films were obtained using two coupled Ocean Optics spectrometers to measure transmittance and reflectance over the range of 330-1000 nm. All optical transmission (T) data shown were normalized to the glass substrate and the reflectance (R).

7.3 Results and Discussion

Through experimental design, i.e., deposition conditions in RF sputtering system, we are able to control the structure of the resultant thin films to be either a-IZTO or c-IZTO. Specifically we have found that the three controlled variables, P, ρ_s, T_s, all influence the kinetics of film growth in different ways. Discussion of each individual variable as it relates to structural variation in IZTO films is as follows.

The substrate temperature (T_s) has a prominent effect on the crystallinity of the resultant IZTO films. The XRD patterns of films grown at various ρ_{rf}, P and T_s = $250\,^{\circ}\mathrm{C}$, $150\,^{\circ}\mathrm{C}$ and $25\,^{\circ}\mathrm{C}$ are shown in Figure 7.1a, Figure 7.1b, and Figure 7.1c respectively. These XRD patterns are obtained from 2D detector image file, by integrating over the χ direction, and normalized to both the thickness of the films and time. The films grown at T_s of $150\,^{\circ}\mathrm{C}$ and $250\,^{\circ}\mathrm{C}$ have sharp XRD peaks, indicative of the presence of a crystalline phase. Moreover, films grown at different P and ρ_{rf} show variation in normalized counts, indicating difference in degree of crystallinity. Whereas all films grown at T_s = $25\,^{\circ}\mathrm{C}$, Figure 7.1c, for all P and ρ_{rf} are largely amorphous as indicated by broad hump in XRD spectra.

Upon closer inspection of the XRD peaks seen for crystalline films in Figure 7.1a and Figure 7.1b the peaks with with 2θ values of 30.5, 35, 51 are attributed to the (222), (400) and (440) planes of the bixbyite In_2O_3 structure, as identified by the International Center for Diffraction Data PDF# 06-0416 shown in Figure 7.1d. Since the XRD peaks in c-IZTO films match only with In_2O_3, but not with

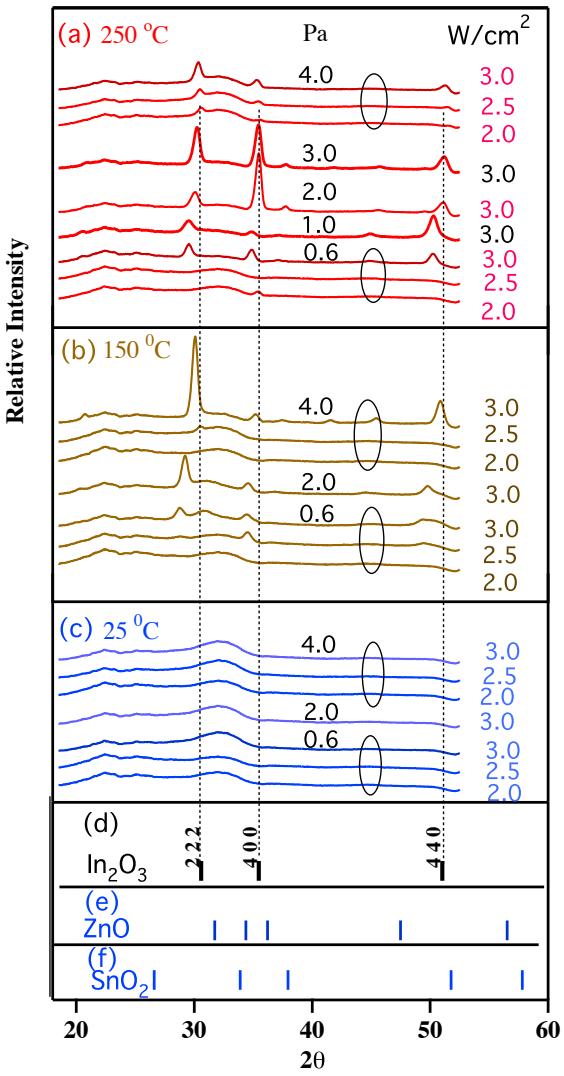

Figure 7.1: (XRD of films grown at ρ_{rf} = 3 W/cm^2 with varying deposition pressure (4.0 Pa, 2.0 Pa, 0.6 Pa) with T_s at a) 250 °C b) 150 °C c) 25 °C (d)/(e)/(f) showing PDF for In_2O_3 / ZnO/SnO_2.

any ZnO or SnO_2 PDF lines (Figure 7.1e and Figure 7.1f), this indicates the crystalline portion of the films have the In_2O_3 bixbyite lattice. Thus the growth temperature is critical in modulating the structure, since the films grown at higher T_s show presence of a crystalline, a mixed or an amorphous phase, whereas room temperature deposition only yielded the amorphous phase.

In contrast to T_s the effect of deposition pressure (P) has a more subtle impact on modulating crystallinity in the IZTO films. XRD peaks of films grown at T_s = $250\,^{\circ}\mathrm{C}$, ρ_{rf} = 3 W/cm^2 as a function of P as seen in Figure 7.1a. The varying normalized intensity indicates changes in degree of poly-crystallinity in both XRD and AFM data. The XRD data in Figure 7.1a shows a gradual increase from 0.35, 0.58 to 0.60 in full width half maximum, FWHM, which is related to the crystallite sizes in the 222 peak values for samples grown at 4.0 Pa, 2.0 Pa and 0.6 Pa respectively. Plus, the gradual decrease in normalized peak intensity for the films grown at lower pressure suggests shorter correlation lengths and lower crystal fraction.

These XRD results probing the bulk structural properties are consistent with surface morphology investigated by the AFM, Figure 7.2. The height and phase images shown in Figure 7.2a and 7.2b respectively are for the sample grown at P = 4.0 Pa, T_s = $250\,^{\circ}\mathrm{C}$ and ρ_{rf} = 3 W/cm^2. The phase image highlighting the grain boundaries indicates the film has small grains as seen from the surface. Similarly, Figure 7.2c and Figure 7.2d show film grown at P = 2.0 Pa, T_s = $250\,^{\circ}\mathrm{C}$ and ρ_{rf} = 3 W/cm^2 and this film shows much clear grain boundary in phase image and bigger crystallites as seen from the surface. The film grown at P = 0.6 Pa, T_s = $250\,^{\circ}\mathrm{C}$ and

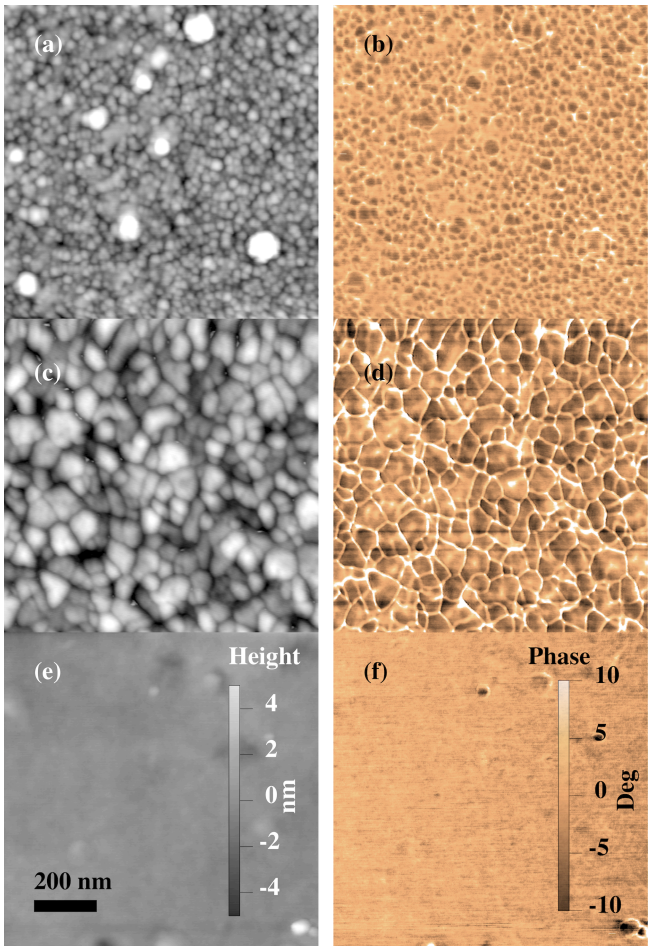

Figure 7.2: AFM height image (left)and phase image (right) for samples grown at P = 4.0 Pa (a,b) 2.0 Pa (c,d) 0.6 Pa (e,f) at T_s = 250 °C and ρ_{rf} = 3 W/cm^2 constant.

ρ_{rf} = 3 W/cm^2 is shown in Figure 7.2e and Figure 7.2f. These films show reduced peak intensity in XRD, and no grain boundaries as measured in AFM. Overall the IZTO films root mean square surface roughnesses ranges from 1.5 nm- 2 nm for crystalline films to as low as 0.2 nm for amorphous films.

Similar observations are seen for other films grown at $150\,^{\circ}\mathrm{C}$ with the films grown 4.0 Pa showing signs of grain formation, whereas no grains are seen for 0.6 Pa. Since all films grown at T$_s$ = $25\,^{\circ}\mathrm{C}$ are amorphous, no such observation about change in grain sizes are seen. The films grown at varying ρ_{rf} result in modulating IZTO film crystallinity as well. At high T$_s$ of $250\,^{\circ}\mathrm{C}$, a decrease in ρ_{rf} from 3.0 W/cm^2 to 2.5 W/cm^2 to 2.0 W/cm^2 results in films with smaller crystal fractions, or largely amorphous depending upon other deposition conditions, Figure 7.2. For films grown at P = 0.6 Pa, T = $250\,^{\circ}\mathrm{C}$, a small crystalline fraction as indicated by XRD is obtained at ρ_{rf} = 3.0 W/cm^2, but at lower ρ_{rf} no XRD peak is observed indicating a largely amorphous phase. Similarly, at P = 4.0 Pa, T$_s$ = $250\,^{\circ}\mathrm{C}$, decreasing ρ_{rf} from 3 W/cm^2 to 2 W/cm^2 result in In_2O_3 peaks in the XRD becoming less pronounced at lower ρ_{rf} as seen in Figure 7.2.

AFM surface topographies on these films indicate the films grown at lower power density have smaller RMS roughness. The films grown at T$_s$ = $250\,^{\circ}\mathrm{C}$, P = 4.0 Pa and at various ρ_{rf} of 2.0 W/cm^2, 2.5 W/cm^2 and 3.0 W/cm^2 have RMS surface roughness 0.6 nm, 0.7 nm and 1.0 nm respectively. Thus, changes in ρ_{rf} while keeping the other two variables, T$_s$ and P constant, results in a change in grain sizes and/or surface roughness in c-IZTO films. However, the variation of ρ_{rf} alone has only a modest effect on modulating the crystallinity as compared to T$_s$

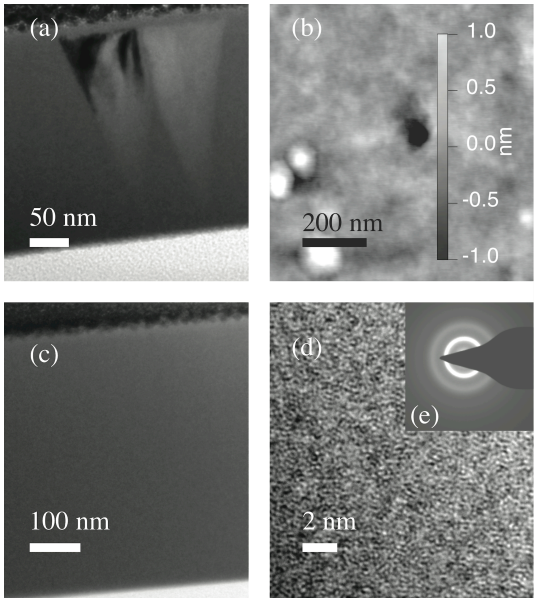

Figure 7.3: (a) a cross-sectional TEM image for a-IZTO grown at $250\,^{\circ}\mathrm{C}$/2.5 W/cm^2 /0.6 Pa. (b) AFM of the same sample indicating phase separated domains. (c) and (d) TEM images of a-IZTO grown at $25\,^{\circ}\mathrm{C}$/2.5 W/cm^2 /0.6 Pa (e) EDX showing amorphous phase for room temperature film.

and P. The energy available to the ions appears, unsurprisingly as the key factor at modulating structure. High temperature $>\ 150\,^{\circ}\mathrm{C}$, high ρ_{rf} >2.5 W/cm^2 and P > 10mT result in c-IZTO films.Whereas lower deposition temperature along with low ρ_{rf} is necessary to obtain a-IZTO films. It is, however, possible to obtain a-IZTO at higher temperature of $150\,^{\circ}\mathrm{C}$ and $250\,^{\circ}\mathrm{C}$ at $\rho_{rf} <$ 2.5 W/cm^2 or low P = 0.6 Pa.

The cross-sectional TEM image and AFM image respectively are shown in Figure 7.3a and Figure 7.3b respectively for a-IZTO grown at T$_s$ = $250\,^{\circ}\mathrm{C}$, ρ_{rf} = 2.5 W/cm^2 and P= 0.6 Pa. These a-IZTO films grown at high temperature suffer some degree of phase separation. The c-TEM image in Figure 7.3a shows triangular phase separated columns originating from base of the film and increasing

in width. This notion of phase-separated domains is further corroborated by the AFM image of these films, showing circular rings indicating phase separated crystalline domains with indication of grain boundaries in a largely amorphous film. Loose estimations of these phase-separated domain makes them about 5-10% of total film volume.

The cross-sectional TEM images with different magnification for a-IZTO grown at T_s = 32 °Care shown in Figure 7.3c and Figure 7.3d with a corresponding diffraction ring pattern shown in Figure 7.3e. All films grown at room temperature show no such phase-separated domains in both TEM and AFM.

Structural variations especially amorphous to crystalline transition in IZTO films controlled by variable deposition parameters have direct impact on electrical properties of the films. The conductivity (σ), carrier concentration (N) and mobility (μ) respectively are shown in Figure 7.4a, 7.4b and 7.4c for IZTO films grown at ρ_{rf} = 2 W/cm^2, 2.5 W/cm^2 and 3 W/cm^2 (color intensity) at varying P = 0.6 Pa and 4.0 Pa (symbols) plotted as a function of varying T_s = 250 °C, 150 °C and 25 °C. IZTO films grown at 25 °C and 150 °C, irrespective of other variables had σ of 100 S/cm to 900 S/cm. Whereas films grown at higher temperature of 250 °C have conductivities >1000 S/cm. The films grown at 250 °C have twice as many carriers compared to those grown at 150 °C and 25 °C.

The trend highlights an increase in carrier concentration via efficient carrier generation primarily responsible for the increase in σ. These results suggest that thermal energy is critical for efficient carrier generation and highly conductive

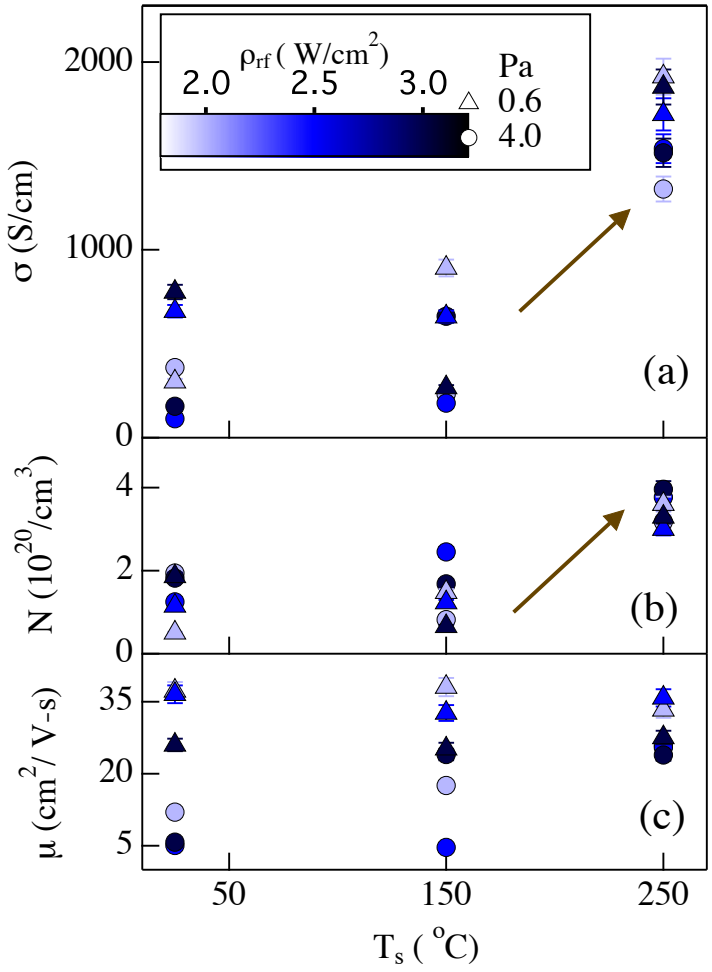

Figure 7.4: (a) σ (b) N, (c) μ as a function of T_s, for films grown at various ρ_{rf} and P of 4.0 Pa and 0.6 Pa. Films grown at high T_s = 250 °C have high σ due to increased number of carriers.

IZTO films. Unfortunately, there does not appear to be a clear trend in mobility as a function of deposition temperature, Figure 7.4c, however, it is apparent that films which are largely amorphous and deposited at low temperature/pressure, have higher mobility compare to mixed phase or poly-crystalline ones. Since crystalline TCOs are limited by grain boundary scattering, we expect similar mechanisms in the polycrystalline c-IZTO films to be responsible for the lower μ compared to a-IZTO films.

The films with the best electrical properties are produced from deposition conditions of ρ_{rf} = 2.0 W/cm^2, P = 0.6 Pa and T$_s$ = $250\,^{\circ}\mathrm{C}$ resulting in σ = 1920 S/cm, N = 3.6 $\times$ 10^{20} /cm^3 and μ = 33 cm^2/Vs, as shown in Figure 7.4. The highest conductivity for an a-IZTO film in our study is deposited at ρ_{rf} = 2.5 W/cm^2, P = 0.6 Pa and T$_s$ = $250\,^{\circ}\mathrm{C}$with a σ = 1720 S/cm, N = 3 $\times$10^{20} /cm^3, μ = 35.8 cm^2/Vs. The maximum μ of 38 cm^2/Vs is observed in an a-IZTO sample grown at 0.6 Pa, 3 W/cm^2, $150\,^{\circ}\mathrm{C}$ values well matched with the literature values for DC sputtered a-IZTO films. (231)

The electrical properties of films grown with varying deposition pressure and T$_s$ = $250\,^{\circ}\mathrm{C}$ and ρ_{rf} = 3 W/cm^2 as illustrated in Figure 7.2 are shown in Figure 7.5. The film grown at 2.0 Pa has σ = 2200 $\pm$ 100 S/cm, the highest conductivity for c-IZTO film in our study. This film has N = 4.9 $\times$10^{20} /cm^3, μ = 30 cm^2/Vs. Both μ and N decrease when pressure increases from P = 2.0 Pa to P = 4.0 Pa, hence the reduced σ. Films grown below 1.0 Pa suffer losses in N, but increase in μ, resulting in overall decrease in σ. This trend in electrical property correlates nicely with underlying structural property. The films grown at T$_s$ = $250\,^{\circ}\mathrm{C}$, ρ_{rf} =

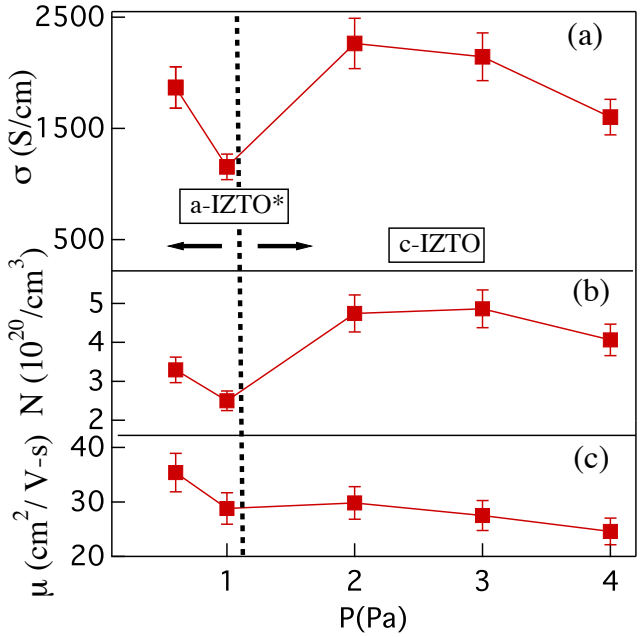

Figure 7.5: σ, N and μ as a function of P, for films grown at ρ_{rf} = 3 W/cm^2 and T$_s$ =250 °C. Changes in structure dominates the electrical properties.

3 W/cm^2 and P $>$ 1.0 Pa, have varying normalized intensity, as well as FWHM in XRD spectrum, indicating changes in crystalline nature and grain sizes. The films with biggest grain sizes yielded highest mobility, as one would expect from grain boundary scattering in polycrystalline films. Similarly, the films grown at lower deposition pressure $<$ 1.0 Pa are largely amorphous, show no presence of crystalline phase hence better mobility. The film at 0.6 Pa has the highest μ of 35 cm^2/Vs in this Figure 7.5c. This increase in mobility with drop of carriers, for the films grown at T$_s$ = 250 °C and P $<$ 1.0 Pa is related to structural changes as films transition from high poly-crystallinity into films with less measurable crystal component to mostly amorphous structure as previously described (Figure 7.1 and 7.2).

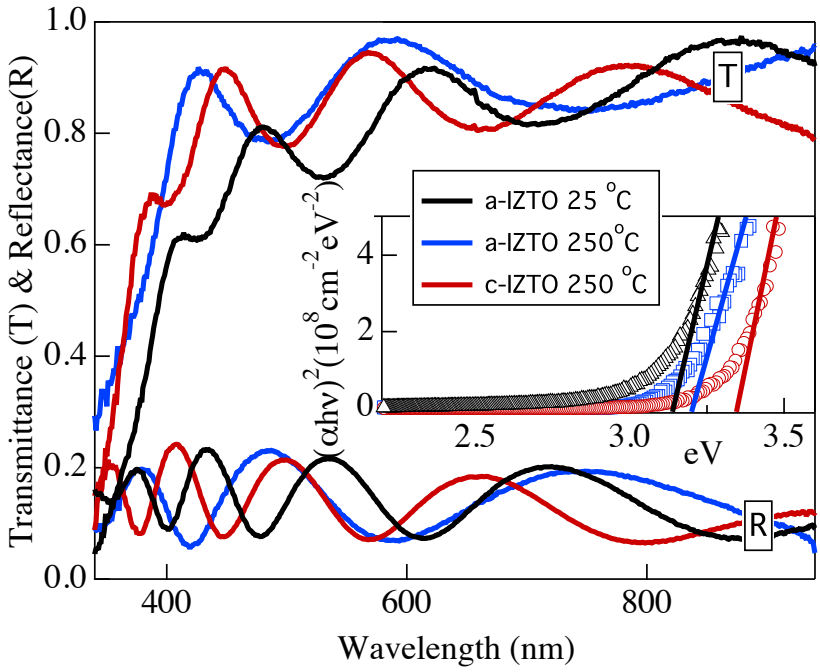

Figure 7.6: Transmittance (T) and Reflectance (R) for high conductivity c-IZTO and a-IZTO, and one at room temperature. Higher temperature deposition yields better transmittance, with $250\,^{\circ}\mathrm{C}$ film showing $\mathrm{T} > 80\%$ in visible spectrum. Inset shows Tauc plot of $(\alpha \mathrm{h}\nu)^2$ vs $\mathrm{h}\nu$ indicating increased optical gap as well for high temperature deposition film.

The transmittance (T) normalized to the glass substrate and the reflectance (R) relative to a standard Al mirror for high conductivity crystalline and amorphous films and room temperature deposition film are shown in Figure 7.6. Overall the trend is that IZTO the films grown at higher temperature of $250\,^{\circ}\mathrm{C}$, show T $> 80\%$ in visible spectrum. Whereas films grown at lower temperature have T $< 80\%$. The average reflectance of the samples are around 15%. All films with thickness $<$ 200 nm, have better transmittance $\sim 90\%$, consistent with the literature. (231)

The absorption spectrum for each sample calculated from the transmittance and reflectance data using

$$T = (1 - R)e^{-\alpha \times d} \tag{7.3.1}$$

where α represents the absorption and d the thickness. All the films grown at higher temperature of $250\,^{\circ}\mathrm{C}$ had lower α in 2.5 eV to 3.1 eV range compare to films deposited at $25\,^{\circ}\mathrm{C}$ and $150\,^{\circ}\mathrm{C}$. The inset in Figure 7.6 shows Tauc plot of $(\alpha \mathrm{h}\nu)^2$ vs hν for IZTO films. The linear portion of the resulting plot for $\alpha > 1{\times}10^4$ /cm was extrapolated to find the effective optical gap (E_{opt}). There is an increase $\sim$ 0.2 eV in optical gap for both amorphous and poly-crystalline films deposited at higher temperature. This trend of a slight increase of $\sim$ 0.2 eV, in E_{opt} with increasing deposition temperature is confirmed by spectroscopic ellipsometry measurement. This shift of E_{opt} is due in part due to the Burstein-Moss shift (ΔE), associated with the increase in number of carriers given by the equation

$$\Delta E_{BM} = \frac{(\hbar)^2}{2m^*}(3\pi^2 N)^{\frac{2}{3}} \tag{7.3.2}$$

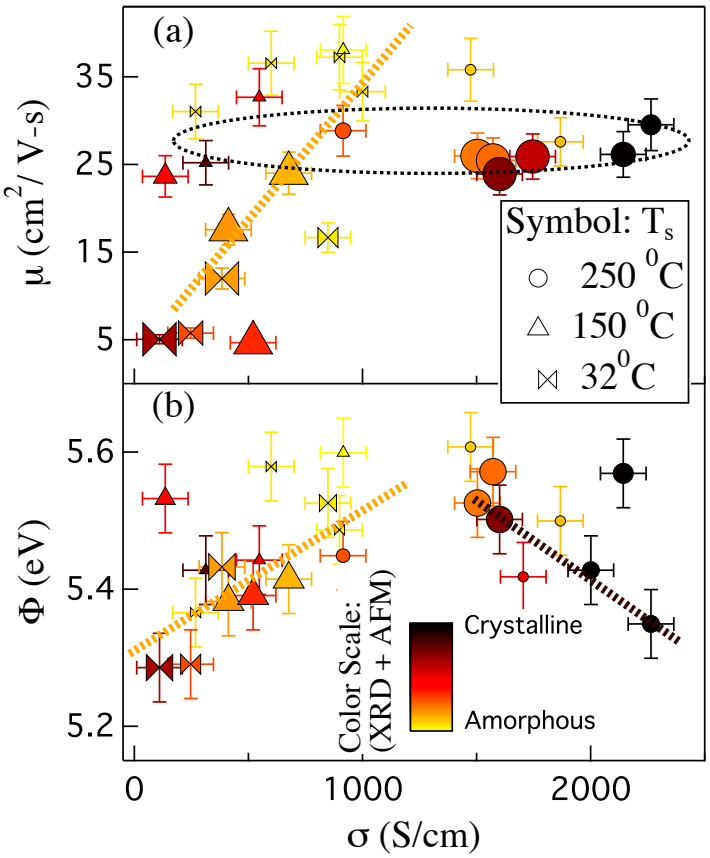

Figure 7.7: a, b shows ϕ and μ as a function of σ for films grown at T_s = 250 °C, 150 °C and 25 °C respectively.

where $\hbar$ is the reduced Planks constant $\frac{h}{2\pi}$and m^* is the effective electron mass. Using equation 7.3.2, taking m^* as 0.3 and the increase in N = 4.0 x 10^{20} /cm^3 from Figure 7.4b, Δ E_{BM} is estimated to be around 0.15 eV, consistent with the observed shift in E_{opt}. We note that changes in structural property may also impact changes in absorbed optical gap and impact the accuracy of these estimates.

For opto-electronic applications, another important physical property of a film is work-function (ϕ). Modulation of ϕ allows improved energy alignment

necessary for either charge extraction or injection in a range of optoelectronic systems. Mobility(μ) and work-function (ϕ) measured using kelvin probe as a function of σ are shown in Figure 7.7a and 7.7b respectively. Color code is the combination of normalized XRD peak intensity and AFM surface roughness in order to provide better clarity between amorphous to poly-crystalline transition. The data shown in Figure 7.7a reinforces the conclusion that films deposition at lower pressure results in amorphous phase, and result in low to high mobility compare to crystalline c-IZTO films that have μ relatively constant between 20 cm^2/Vs to 30 cm^2/Vs with σ proportional to N. Thus, increases in conductivity in c-IZTO are mainly due to an increase in carrier generation. While in a-IZTO carrier density remains relatively constant between 0.5 $\times$ 10^{20} /cm^3 to 2 $\times 10^{20}$ /cm^3 with μ proportional to σ, indicating the increase in conductivity in a-IZTO is mainly due to the modest increase in mobility.

The mixed phase IZTO materials have σ again proportional to N, with little change in μ like c-IZTO, but ϕ increases with σ like the a-IZTO films. Both amorphous and crystalline IZTO films have some tunability in ϕ as seen in Figure 7.7b with ϕ ranging from 5.2 eV to 5.6 eV. This is consistent with the values reported in literature for other that for IZTO a trend of lower ϕ with increasing σ for c-IZTO is observed. This matches with our conclusion that increase in σ in c-IZTO is mostly due to increase in number of carriers, and which results in increase in fermi level, hence lower work function. (225) For a-IZTO increasing σ results in increase in ϕ. This difference may be due to the difference in conduction mechanism and/or band structure differences in both types of films. (181)

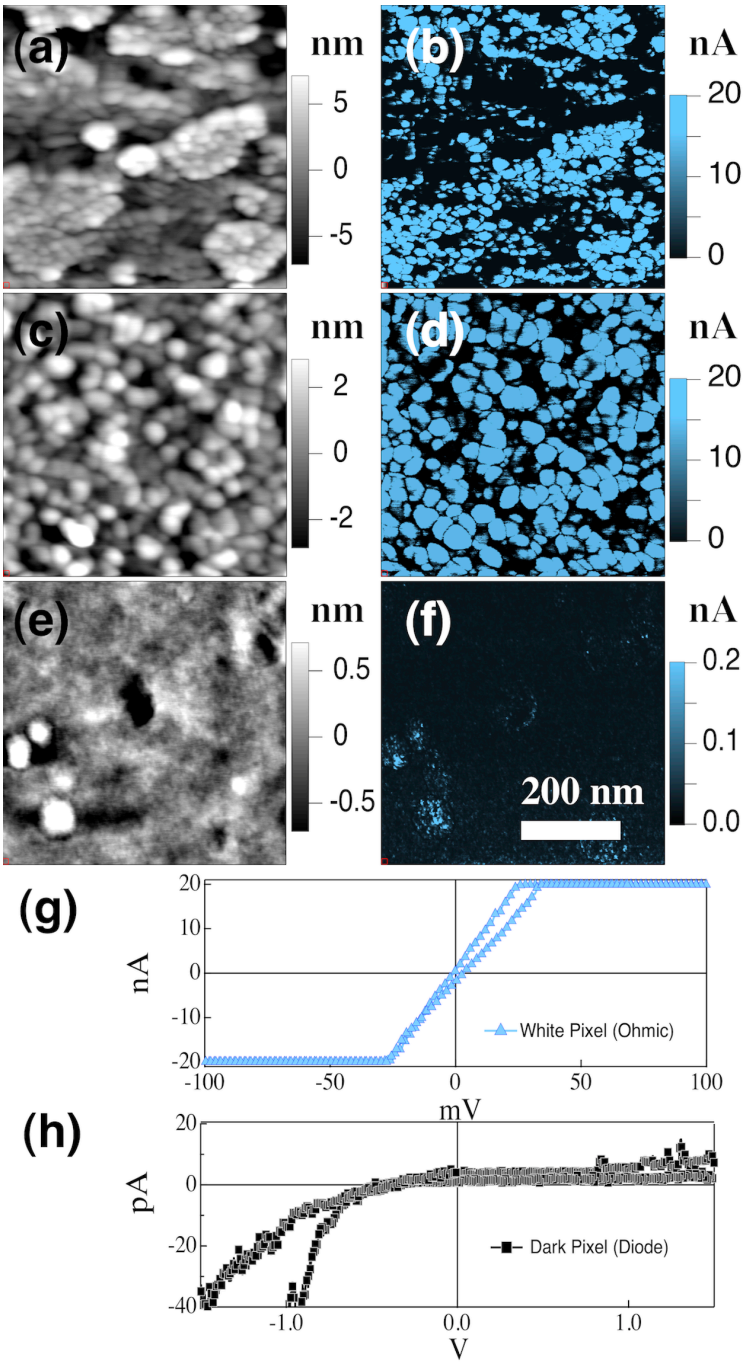

Figure 7.8: Height topography with corresponding C-AFM data of reference ITO sample(a,b), c-IZTO(c,d) and a-IZTO(e,f). Both c-IZTO and a-IZTO had similar work-function (ϕ), but very different heterogeneity in the surface. Panel (g, h) show JV data indicating the difference between white and dark pixel in the C-AFM data.

To understand this variation in ϕ, we further investigated these films using other surface sensitive conductive AFM. Surface conductivity both parallel and perpendicular to the surface of TCOs are critical in various opto-electronic devices applications. For example, a uniformly conductive and smooth contact is desired in OLED applications to ensure very thin layer of polymer ($<$100 nm) is conformal to prevent shorts. (237) Similarly, in OPV devices TCOs are typically modified by a carrier transport layer in order to make the surface electronically active and/or selective before the organic layers are deposited. (100)

The height topography images with corresponding C-AFM data of a reference ITO sample, both c-IZTO and a-IZTO with similar work-function and similar bulk σ is shown in Figure 7.8. Panel a and b are reference measurement done on colorado concept ITO. In the C-AFM setup, a Pt/Ir tip acts as a metal probe with IZTO film as a doped semi conductor to ground. If we consider the difference in ϕ between metal tip and semi-conductor IZTO as barrier height, and IZTO passivated surface defect states forming an thin insulating layer, as barrier thickness (tunneling distance), we can view this setup as metal-insulator-semiconductor (MIS) junction. In this case, we expect difference in current flowing through the junction to be controlled mainly due to difference in thickness of insulating layer, as both IZTO films have similar ϕ resulting in similar barrier height.

A small bias of 100mV was applied between sample and tip. The white and dark areas represent the ohmic contact and the diode contact as seen in Figure 7.8g and Figure 7.8h respectively. In the ohmic region, small bias voltage of $>$20 mV resulted in maximum current detection limit of 20 nA. The c-IZTO has larger

areas, in an excess of 90%, that formed ohmic contact with the tip as can be seen in Figure 7.8d similar to ITO data in Figure 7.8 b. In contrast a-IZTO formed mostly diode contact as seen in Figure 7.8f. Regions displaying diode behavior yield very low current, usually in pA regime even at high bias of $\pm$ 1.5 V. Also, in Figure 7.8e and 7.8f, we see some circular domains in height topography due to phase separated crystalline domains as seen in cross sectional TEM (not shown) that had better c-AFM response than the surrounding flat areas.

These results suggest that an amorphous IZTO film surface is more susceptible to passivation/defect states resulting in a more insulating surface layer compared to the crystalline IZTO film surface. We expect some differences in magnitude of current due to differences in tip contact area, given that the amorphous samples are flat with surface roughness $<$ 0.2 nm whereas crystalline sample have surface roughness of 1- 2 nm. However, the substantial difference in current-voltage characteristics, especially the large difference in turn on voltage in current-voltage curve seems to indicate that a-IZTO, like some other amorphous TCOs (e.g. a-IZO) we have investigated where it was observed that surface defects hinder charge transport.41 This electronic passivation of the surface could be due to presence of excessive oxygen and/or water, as IZTO films grown in excessive oxygen environment tend to be insulating in nature. (174, 231) Additional investigations of the nature of these surface defects, as well as a surface treatment method to enable change transport at these surfaces is ongoing.

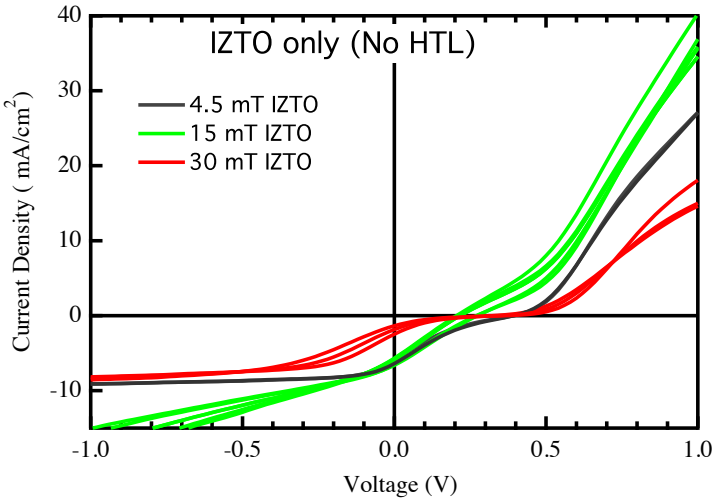

Figure 7.9: IZTO/P3HT:PCBM/Ca/Al devices on films shown in Figure 7.2

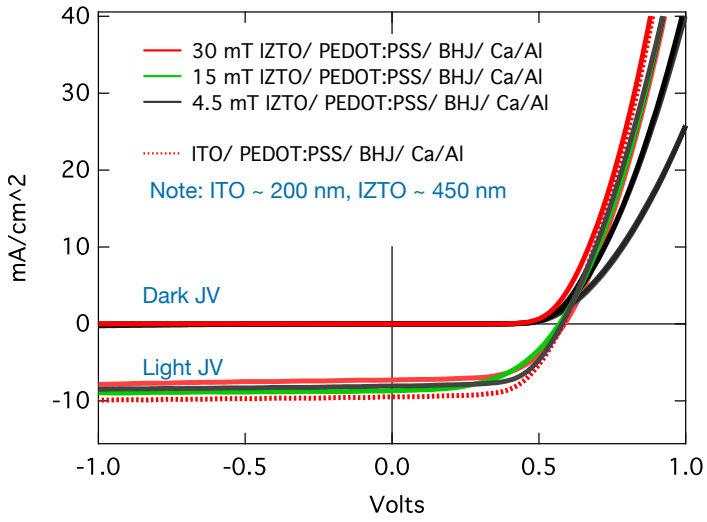

Figure 7.10: IZTO/PEDOT:PSS/P3HT:PCBM/Ag devices on films shown in Figure 7.2

7.4 OPV Device Study on Indium Zinc Tin Oxide Thin Film

To evaluate the performance of OPV devices on untreated IZTO electrodes, P3HT:PC60BM BHJ devices with an standard architecture were fabricated. (18, 26) The J-V data from the TCO/P3HT:PC60BM/Ca/Al devices are shown in Figure 7.9. We observe large differences in J-V characteristics between devices that are believed to arise from the differences in the TCO electronic, structural, and surface properties. All devices exhibit poor PV behavior with low fill factors ($< 40\%$). However as demonstrated in the Figure 7.10, the disappearance of the double diode behavior when the TCO contacts is modified by PEDOT:PSS hole transport layer organic ink suggests that surface passivation (amorphous phase) not a problem with proper device engineering.

7.5 Conclusions

Amorphous and crystalline thin films of Indium-Zinc-Tin-Oxide (a-IZTO/c-IZTO) are deposited using radio frequency magnetron sputtering using a fixed composition $In_{0.5}Zn_{0.25}Sn_{0.25}O_x$ target. The substrate temperature (T_s) in conjunction with both process gas pressure (Ps) and RF power density (ρ_{rf}) applied to target are critical for controlling crystallinity, conductivity (σ) and work function (ϕ) of thin film. As a result of these physical properties we demonstrated that a fixed composition target resulted in single composition Indium-Zinc-Tin- Oxide (IZTO) produced films relevant to traditional TCO applications but with varying

structural properties. These benefits of varying morphology coupled to tunability of the work-function are of interest for both scientific studies and the technological application.

Acknowledgements: Materials development including oxide deposition and characterization equipment was provided by the U.S. Department of Energy under Contract No. DOE-AC36-08GO28308 with the National Renewable Energy Laboratory. Support for characterization and analysis work was provided as part of the Center for Interface Science: Solar-Electric Materials (CIS:SEM), an Energy Frontier Research Center Funded by the U.S. Department of Energy, Office of Basic Sciences, under Award Number DE-SC0001084

Chapter 8

Conclusions

The main contributions of this work in the development of transparent oxide semiconductors from Earth-abundant materials for cost-effective thin film device applications, such as solar cells, light emitting diodes and various other opto-electronic applications are summarized here. In this thesis various milestones were achieved pertaining to optimizing and investigating the bulk, the surface and/or interface physical properties of oxides and understand those changes in physical properties on the device performance.

The optimization of an transparent electrode, especially the bulk opto-electronic property is typically based on improving two properties: optical transparency and electrical conductivity. In this dissertation, I have presented studies on material systems In_2O_3, SnO_2 and ZnO combinations and/or doping of these materials with elements such as Al, Ga, In in the pursuit of obtaining electrodes with optimized bulk physical properties. The improvement in bulk properties of TCOs are complicated because various physical properties are inter-dependent. For example,

various oxide materials we have investigated have the index of refraction around 1.9 around λ = 500 nm. Therefore, our ability to optimize and manipulate the transparency in these oxide systems is fairly limited. Some of the work done here involved maximizing the conductivity (σ = N$\times$ e $\times\mu$) of TCOs such that higher transparency can be obtained via employing thinner films. In this dissertation, both approaches to optimize conductivity: increase in carrier concentration (N) or increase in mobility (μ), were demonstrated on two different class of next generation TCO material systems.

A significant milestone from this thesis is the development of poly-crystalline gallium doped zinc oxide GZO (95% ZnO) from Earth abundant material, with physical properties as good as commercially available ITO (90% In_2O_3), which is the industry standard in transparent electrode application. The work related to this bulk physical property optimization of poly-crystalline TCO discussed in Chapter 3, shows the use of RF superimposed DC sputtering technique in the development of GZO with σ $>$ 4000 S/cm, T $>$ 90% using large scale sputtering. Although small scale deposition of GZO via pulse laser deposition had been previously shown to have significantly better electronic and optical properties, the contribution of this thesis is in the improvement in mobility via the improvement on the crystallographic structure, the micro-structure, and the improvement in doping efficiency in GZO using a process more directly relevant to electrodes for large area applications.

For next generation solar cells application, not only the transparency and the electrical conductivity need to be optimum, but also various other bulk properties such as robust mechanical properties and compatibility with plastic substrates

come under consideration. Also, presented in this thesis are the various studies on amorphous TCOs with robust mechanical properties that can be deposited on a flexible substrate at room temperature. In Chapter 5 and Chapter 7, both Zinc Tin Oxide and Indium Zinc Tin Oxide systems were shown to have improved carrier generations via optimizing deposition parameters, showing improvement of bulk electrical conductivity in relatively unknown amorphous TCO systems.

Implementation of oxide electrodes on opto-electronics devices such as organic light emitting diodes (OLED) and organic photovoltaic (OPV) involve using them in a layer by layer approach with surface of oxide electrodes in contact with other organic and/or inorganic semiconductors. Various studies presented in this thesis demonstrates the problem of inefficient charge collection/injection in opto-electronic devices due to poor understanding of interface properties of oxide electrodes. The detail study on the surface of GZO and IZO presented in Chapter 4, showed that surface of TCOs had different chemistry compare to the bulk due to absorbates and contaminates, yielding poor electrical heterogeneity and transport at the surface.

Similarly, the surface studies present here demonstrates that various interface or surface properties of TCOs such as the surface conductivity, the work function, can change with time due to chemical interaction with ambient or various surface treatment, which can positively or negatively impacting surface transport properties. One of the significant outcome of this thesis is in the providing insight as to the role of bulk structural properties and their influence on the surface passivation and surface charge transport in various TCOs systems. Various

studies explained here show that amorphous TCOs have greater affinity towards surface defects and passivation with relatively poor surface electrical properties, thus require more stringent/careful interface management during device fabrication.

This brings to a bigger question this thesis seeks to elucidate. If everything points towards the surface of a TCO being a problem in a particular application, can you de-couple or independently tune interface/surface properties of TCOs without changing the bulk? If so, then how do changes in these properties impact the opto-electronic device performance. The study on zinc tin oxide (ZTO) presented in Chapter 5 demonstrates that it is possible to create a hereto-structured electrode, where one can independently manage the bulk and the surface properties of a TCO. The study shows that a new electrode can be constructed that has the bulk physical properties namely good transparency and good electrical conductivity of one system (ITO and GZO) coupled with the optimum surface properties namely work function, surface roughness, chemical stability of an another system (ZTO). Using this approach, we were able to successfully demonstrate that efficient transport of charges from external circuit to the junction can be done by one electrode optimized for bulk electrical transport and transparency, while a thin interfacial layer of a material with tailored surface property provides better compatibility, and energy alignment such that it minimizes the injection barriers associated with hole injection in OLED devices. The successful application of ZTO/ITO and ZTO/GZO heterostructured electrode to obtain high efficiency blue OLEDs was a significant milestone when the study was conducted in 2009, and it paved the path for parallel approach studies on charge collections in OPV devices.

The lesson learned in optimization of oxide physical properties for charge injection in OLED studies were reexamined and implemented to understand charge collections in photovoltaic devices. Interestingly, high conductivity and deep work-functions n-type materials ZTO and IZTO both yielded poor hole collections in standard OPV devices, while fairly insulating MoOx with deeper work-function seems to work perfectly fine for the hole collections. Ideally, we would like p-type oxides to harvest the holes and the n-type oxides collects the electrons. Currently, the bulk conductivity of p-type transparent electrodes ($\sigma \sim 500$ S/cm) are orders of magnitude inferior to n-type counter part ($> 12{,}000$ S/cm), hence p-type TCOs can not function as standalone transparent electrodes to harvest holes. Some of the work completed during this thesis (although not discussed) involved development and successful use of interfacial layer of p-type oxides such as NiOx, Co-Ni-Ox, CoZnOx combined with ITO, GZO, IZO electrodes optimized for bulk properties. Similarly, ZnO and TiO_2 were previously shown to provide the energy level alignment necessary for electron collection in bulk-hetrojunction OPV devices. The results presented in Chapter 6 and 7, where various amorphous and poly-crystalline TCOs optimized for bulk properties yield efficient devices if employed with proper functional layers: ZnO (Chapter 6) or PEDOT:PSS (Chapter 7), confirming the validity of this approach of independently tuning bulk properties of one system, with surface properties of another.

During the initial phases of these studies, there were no concrete design rules or guidelines for what physical properties are necessary for good electron (or hole) selectivity in OPV devices. ZnO layers deposited via solution methods as discussed in introduction worked, but there were still outstanding issues such poor

performance with double diode behavior seemed to disappear when activated by UV light. The study presented in modulation of both bulk and surface property of oxide in this thesis are instrumental in providing insights on the device physics in the development of charge selective transport layer. The study on ZnO as electron transport layer in Chapter 6 showed that, insulating ($N<10^{16}$ /cm^3) and very conductive ($N>10^{19}$ /cm^3) ETL layers yield poor device performance. The high conductivity ZnO films are either metallic with poor optical properties and or degenerately doped with significant numbers of defects and/or carriers in the near surface regions of the oxide, of which result in an interface with poor selectivity and ultimately poor device performance. The highly resistive oxygen rich ZnO films, in contrast, have poor electrical properties, which are shown to perform poorly for election collection.

These observations of poor performance for highly resistive ZnO, or highly conductive ZnO can explain the reason why TCOs in general, and the amorphous TCOs (ZTO, IZO, IZTO) that are prone to chemical instability and surface passivation result in poor device performance when used as standalone electrodes in OPV devices. This raises a question to ponder: Will the next generation electrodes the graphenes or carbon-nano tubes with high carrier concentration provide interface with good charge collection properties in OPV without the use of these functional oxide layers? The inverse of this questions is also significantly, with some of the studies in this thesis reversing the question of much are the surface properties that are needed for electron collections (or charge transport at the interface) in OPV dictated by bulk physical properties of the same material?

List of some desirable physical property in ETL layer for BHJ OPV devices (Note: these rules are based on ZnO, 10 - 100 nm electron transport layers some of which may be applicable to thin transport layers (e.g SAMs or HTL layer)

1. High transparency
2. High electrical mobility $>$ the active layer
3. Low N with clean gap, so that defects or mid gap states do not dictate the charge collection, selectivity or recombinations
4. Chemical stability, or favorable chemistry. For example, Oxidation of Ag in inverted device yields better performing devices
5. Conformal and uniform electrical heterogeneity
6. Barrier height management or appropriate energy levels
7. Stability of various physical properties under illumination

Bibliography

[1] Albert Rose. A global view of solar energy in rational units. *Physica Status Solidi (a)*, 56(1):11–26, 1979.

[2] L. Jan Anton Koster, Sean E Shaheen, and Jan C Hummelen. Pathways to a new efficiency regime for organic solar cells. *Adv. Energy Mater.*, 2(10):12461253, October 2012.

[3] Christoph Brabec. Organic photovoltaics: technology and market. *Solar Energy Materials and Solar Cells*, 83(2):273–292, 2004.

[4] Harald Hoppe and Niyazi Serdar Sariciftci. Organic solar cells: An overview. *J Mater Res*, 19(07):1924–1945, Jul 2004.

[5] B.A Gregg. The photoconversion mechanism of excitonic solar cells. *Mrs Bull*, 30(1):20–22, 2005.

[6] R.A.J Janssen, J.C Hummelen, and N.S Sariciftci. Polymer–fullerene bulk heterojunction solar cells. *Mrs Bulletin*, 30(01):33–36, 2005.

[7] Matthew Wright and Ashraf Uddin. Organic-inorganic hybrid solar cells: A comparative review. *Solar Energy Materials and Solar Cells*, 107:87–111, 2012.

[8] David Ginley. *Handbook of Transparent Conductors*. Springer-Verlag New York, LLC, 2010.

[9] K Ellmer, A Klein, and B Rech. *Transparent Conductive ZnO: Basics and Applications in Thin Film Solar Cells*. Springer Series in Materials Science, 104, Springer-Verlag, Berlin Heidelberg, 2008.

[10] Jenny Nelson. *The Physics of Solar Cells*. Imperial College Press, London, 2003.

[11] Jun Shen, D Wang, E Langlois, and Jie Yang. Degradation mechanisms in organic light-emitting diodes. *Proc. SPIE 4105, Organic Light-Emitting Materials and Devices IV*, pages 236–242, 2001.

[12] E Fortunato, D Ginley, H Hosono, and D.C Paine. Transparent conducting oxides for photovoltaics. *Mrs Bulletin*, 32(03):242–247, 2007.

[13] Matthew T Lloyd, Dana C Olson, Ping Lu, Erica Fang, Diana L Moore, Matthew S White, Matthew O Reese, David S Ginley, and Julia W. P Hsu. Impact of contact evolution on the shelf life of organic solar cells. *J. Mater. Chem.*, 19(41):7638, Jan 2009.

[14] Daniel Abou-Ras, Thomas Kirchartz, and Uwe Rau. *Advanced Characterization Techniques for Thin Film Solar Cells*. WILEY-VCH Verlag GmbH Co. KGaA, Boschstr. 12, 69469 Weinheim, Germany, 2011.

[15] E.L Ratcliff, B Zacher, and N.R Armstrong. Selective interlayers and contacts in organic photovoltaic cells. *The Journal of Physical Chemistry Letters*, 2(11):1337–1350, 2011.

[16] H L Hartnagel. *Semiconducting transparent thin films*. Institute of Physics Pub, Philadelphia, Pa, 1995.

[17] Paul F Ndione, Andres Garcia, N. Edwin Widjonarko, Ajaya K Sigdel, K. Xerxes Steirer, Dana C Olson, Philip A Parilla, David S Ginley, Neal R Armstong, Robin E Richards, Erin L Ratcliff, and Joseph J Berry. Highly-tunable nickel cobalt oxide as a low-temperature p-type contact in organic photovoltaic devices. *Adv. Energy Mater.*, 3(4):524–531, Nov 2012.

[18] J.J Berry, N.E Widjonarko, B.A Bailey, A.K Sigdel, D.S Ginley, and D.C Olson. Surface treatment of nio hole transport layers for organic solar cells. *Selected Topics in Quantum Electronics, IEEE Journal of*, 16(6):1649–1655, 2010.

[19] N Edwin Widjonarko, Erin L Ratcliff, Craig L Perkins, Ajaya K Sigdel, Andriy Zakutayev, Paul F Ndione, Dane T Gillaspie, David S Ginley, Dana C Olson, and Joseph J Berry. Sputtered nickel oxide thin film for efficient hole transport layer in polymer–fullerene bulk-heterojunction organic solar cell. *Thin solid films*, 520(10):3813–3818, Mar 2012.

[20] A Zakutayev, J.D Perkins, P.A Parilla, N.E Widjonarko, A.K Sigdel, J.J Berry, and D.S Ginley. Zn–ni–co–o wide-band-gap p-type conductive oxides with high work functions. *MRC*, 1(01):23–26, Nov 2011.

[21] Akram A Khosroabadi, Palash Gangopadhyay, Binh Duong, Jayan Thomas, Ajaya K Sigdel, Joseph J Berry, Thomas Gennett, N Peyghambarian, and Robert A Norwood. Fabrication, electrical and optical properties of silver,

indium tin oxide (ITO) and indium ZnO (IZO) nanostructure arrays. *Physica Status Solidi (a)*, 215(5):831–838, Feb 2013.

[22] Hyeunseok Cheun, Canek Fuentes-Hernandez, Jaewon Shim, Yunnan Fang, Ye Cai, Hong Li, Ajaya K Sigdel, Jens Meyer, Julia Maibach, Amir Dindar, Yinhua Zhou, Joseph J Berry, Jean-Luc Bredas, Antoine Kahn, Kenneth H Sandhage, and Bernard Kippelen. Oriented growth of al2o3:ZnO nanolaminates for use as electron-selective electrodes in inverted polymer solar cells. *Adv. Funct. Mater.*, 22(7):1531–1538, Feb 2012.

[23] Talia S Gershon, Ajaya K Sigdel, Andrew T Marin, Maikel F A M van Hest, David S Ginley, Richard H Friend, Judith L Macmanus-Driscoll, and Joseph J Berry. Improved fill factors in solution-processed ZnO/Cu_2O photovoltaics. *Thin Solid Films*, 536:280–285, Apr 2013.

[24] Anuradha Bulusu, Sergio Paniagua, Bradley MacLeod, Ajaya Sigdel, Joseph Berry, Dana Olson, Seth Marder, and Samuel Graham. Efficient modification of metal oxide surfaces with phosphonic acids by spray coating. *Langmuir*, 29(12):3935–3942, 2013.

[25] K. Xerxes Steirer, Jordan P Chesin, N. Edwin Widjonarko, Joseph J Berry, Alex Miedaner, David S Ginley, and Dana C Olson. Solution deposited nio thin-films as hole transport layers in organic photovoltaics. *Organic Electronics*, 11(8):1414–1418, Aug 2010.

[26] Scott R Hammond, Jens Meyer, N. Edwin Widjonarko, Paul F Ndione, Ajaya K Sigdel, Andres Garcia, Alexander Miedaner, Matthew T Lloyd, Antoine Kahn, David S Ginley, Joseph J Berry, and Dana C Olson. Low-

temperature, solution-processed molybdenum oxide hole-collection layer for organic photovoltaics. *J. Mater. Chem.*, 22(7):3249, Jan 2012.

[27] M O Reese, A K Sigdel, J J Berry, D S Ginley, and S E Shaheen. A simple miniature controlled-atmosphere chamber for optoelectronic characterizations. *Solar Energy Materials and Solar Cells*, 94(7):1254–1258, Apr 2010.

[28] Matthew Gliboff, Lingzi Sang, Kristina M. Knesting, Matthew C. Schalnat, Anoma Mudalige, Erin L. Ratcliff, Hong Li, Ajaya K. Sigdel, Joseph J. Berry, Dennis Nordlund, Anthony Giordano, Gerald T. Seidler, Jean-Luc Brdas, Seth R. Marder, Jeanne E. Pemberton, and David S. Ginger. Orientation and order of phenylphosphonic acid self-assembled monolayers on a transparent conductive oxide: A combined nexafs, pm-irras and dft study. *Langmuir*, 29(7):2166–2174, Jan 2013.

[29] J Tauc, R Grigorovici, and A Vancu. Optical properties and electronic structure of amorphous germanium. *Phys. Stat. Sol. (b)*, 15(2):627–637, 1966.

[30] C Kittel. *Introduction to Solid State Physics, 7th edition*. John Wiley & Sons, New York, 1996.

[31] V I Kaydanov: Colorado School of Mines, T J Coutts, and D L Young Nrel. Bm moss shift calculations. pages 1–23, Oct 2000.

[32] V Srikant and D.R Clarke. On the optical band gap of ZnO. *Journal of Applied Physics*, 83(10):5447–5451, 1998.

[33] MD McCluskey and SJ Jokela. Defects in ZnO. *Journal of Applied Physics*, 106(7):071101–071101–13, 2009.

[34] Stephan Lany and Alex Zunger. Dopability, intrinsic conductivity, and nonstoichiometry of transparent conducting oxides. *Phys. Rev. Lett.*, 98(4):045501, Jan 2007.

[35] Anderson Janotti and Chris G Van De Walle. Fundamentals of ZnO as a semiconductor. *Rep. Prog. Phys.*, 72(12):126501, Oct 2009.

[36] V.E Henrich and P.A Cox. *The Surface Science of Metal Oxides*. Cambridge University Press, Cambridge, 1994.

[37] P Erhart and K Albe. Diffusion of zinc vacancies and interstitials in ZnO. *Applied Physics Letters*, 88(20):201918–201918–3, 2006.

[38] David Look, Donald Reynolds, JR Sizelove, RL Jones, Cole Litton, G Cantwell, and WC Harsch. Electrical properties of bulk ZnO. *Solid State Communications*, 105(6):399–401, 1998.

[39] David Ginley. *Handbook of Transparent Conductors*. Springer-Verlag New York, LLC, 2010.

[40] HJ Ko, YF Chen, SK Hong, H Wenisch, T Yao, and DC Look. Ga-doped ZnO films grown on gallium nitride templates by plasma-assisted molecular-beam epitaxy. *Applied Physics Letters*, 77(23):3761–3763, 2000.

[41] H.M Kim, J.S Ahn, K.H Lee, and K.B Lee. Optimized ferroelectric pzt films deposited on various transparent conducting oxides for ferroelectric transparent thin-film transistors. *Journal of Korean Physical Society*, 50:1740, 2007.

[42] Osamu Nakagawara, Yutaka Kishimoto, Hiroyuki Seto, Yoshihiro Koshido, Yukio Yoshino, and Takahiro Makino. Moisture-resistant ZnO transparent conductive films with ga heavy doping. *Appl. Phys. Lett.*, 89(9):091904, Jan 2006.

[43] Yutaka Kishimoto, Osamu Nakagawara, Hiroyuki Seto, Yoshihiro Koshido, and Yukio Yoshino. Improvement in moisture durability of ZnO transparent conductive films with ga heavy doping process. *Vacuum*, 83(3):544–547, Jan 2008.

[44] Zheng Xu, LiMin Chen, Guanwen Yang, ChunHao Huang, Jianhui Hou, Yue Wu, Gang Li, ChainShu Hsu, and Yang Yang. Vertical phase separation in poly (3hexylthiophene): Fullerene derivative blends and its advantage for inverted structure solar cells. *Adv. Funct. Mater.*, 19(8):1227–1234, 2009.

[45] S.R Forrest. The limits to organic photovoltaic cell efficiency. *Mrs Bulletin*, 30(1):28–32, 2005.

[46] William Shockley and Hans Queisser. Detailed balance limit of efficiency of pn junction solar cells. *Journal of Applied Physics*, 32(3):510–519, 1961.

[47] JJ Berry, DS Ginley, and P.E Burrows. Organic light emitting diodes using a ga: ZnO anode. *Applied Physics Letters*, 92(19):193304–193304–3, 2008.

[48] Christopher W Gorrie, Ajaya K Sigdel, Joseph J Berry, Brandon J Reese, Maikel F. A. M van Hest, Paul H Holloway, David S Ginley, and John D Perkins. Effect of deposition distance and temperature on electrical, optical and structural properties of radio-frequency magnetron-sputtered gallium-doped ZnO. *Thin solid films*, 519:190, Oct 2010.

[49] Dean W Matson, Charles C Bonham, James S Swensen, Liang Wang, Asanga Padmaperuma, Daniel J Gaspar, Joseph J Berry, Ajaya K Sigdel, Christopher W Gorrie, and David S Ginley. Development of large area transparent conducting oxides from a combinatorial lead for organic solid state lighting. *Proc. SPIE 7415, Organic Light Emitting Materials and Devices XIII*, pages 74150X–74150X–11, Jan 2009.

[50] E Fortunato, L Raniero, L Silva, A Goncalves, A Pimentel, P Barquinha, H Aguas, L Pereira, G Goncalves, I Ferreira, E Elangovan, and R Martins. Highly stable transparent and conducting gallium-doped ZnO thin films for photovoltaic applications. *Solar Energy Materials and Solar Cells*, 92(12):1605–1610, Jan 2008.

[51] Soo-Ghang Ihn, Kyung-Sik Shin, Mi-Jin Jin, Xavier Bulliard, Sungyoung Yun, Yeong Suk Choi, Yungi Kim, Jong-Hwan Park, Myungsun Sim, Min Kim, Kilwon Cho, Tae Sang Kim, Dukhyun Choi, Jae-Young Choi, Woong Choi, and Sang-Woo Kim. ITO-free inverted polymer solar cells using a gzo cathode modified by ZnO. *Solar Energy Materials and Solar Cells*, 95(7):1610–1614, Jan 2011.

[52] Young-Seok Park, Ho-Kyun Park, Sung-Woo Cho, Jin-A Jeong, Kwang-Hyuk Choi, Han-Ki Kim, Jae-Young Lee, Jung-Hwan Lee, Hyo-Dae Bae, and Yoon-Heong Tak. Transparent conducting azo cosputtered ITO anode films grown by a dual target dc magnetron sputtering for OLEDs. *Electrochem. Solid-State Lett.*, 11(11):J85–J88, 2008.

[53] Liang Wang, Dean W Matson, Evgueni Polikarpov, James S Swensen, Charles C Bonham, Lelia Cosimbescu, Joseph J Berry, David S Ginley,

Daniel J Gaspar, and Asanga B Padmaperuma. Highly efficient blue organic light emitting device using indium-free transparent anode ga:ZnO with scalability for large area coating. *J Appl Phys*, 107(4):043103, Jan 2010.

[54] V Verma, D Kim, H Jeon, M Jeon, and W Choi. Characteristics of low doped gallium-ZnO thin film transistors and effect of annealing under high vacuum. *Thin Solid Films*, 516(23):8736–8739, Oct 2008.

[55] Sang-Hee Ko Park, Chi-Sun Hwang, Hu Young Jeong, Hye Yong Chu, and Kyoung Ik Cho. Transparent ZnO-tft arrays fabricated by atomic layer deposition. *Electrochem Solid St*, 11(1):H10–H14, Jan 2008.

[56] XH Yu, J Ma, F Ji, YH Wang, XJ Zhang, and HL Ma. Influence of annealing on the properties of ZnO : Ga films prepared by radio frequency magnetron sputtering. *Thin Solid Films*, 483(1-2):296–300, Jan 2005.

[57] M Selmi, F Chaabouni, M Abaab, and B Rezig. Studies on the properties of sputter-deposited al-doped ZnO films. *Superlattice Microst*, 44(3):268–275, Jan 2008.

[58] V Assuncao, E Fortunato, A Marques, A Goncalves, I Ferreira, H Aguas, and R Martins. New challenges on gallium-doped ZnO films prepared by r.f. magnetron sputtering. *Thin Solid Films*, 442(1-2):102–106, Jan 2003.

[59] K Ellmer and G Vollweiler. Electrical transport parameters of heavily-doped ZnO and zinc magnesium oxide single and multilayer films heteroepitaxially grown on oxide single crystals. *Thin solid films*, 496(1):104–111, 2006.

[60] B Ahn, J Kim, H Kang, C Lee, S Oh, K Kim, G Jang, and S Lee. Thermally stable, highly conductive, and transparent ga-doped ZnO thin films. *Thin Solid Films*, 516(7):1382–1385, Feb 2008.

[61] Min-Suk Oh, Dae-Kue Hwang, Dong-Jun Seong, Hyun-Sang Hwang, Seong-Ju Park, and Eun Do Kim. Improvement of characteristics of ga-doped ZnO grown by pulsed laser deposition using plasma-enhanced oxygen radicals. *J Electrochem Soc*, 155(9):D599–D603, Jan 2008.

[62] V Khranovskyy, U Grossner, O Nilsen, V Lazorenko, G. V Lashkarev, B. G Svensson, and R Yakimova. Structural and morphological properties of ZnO : Ga thin films. *Thin Solid Films*, 515(2):472–476, Jan 2006.

[63] M. de la L Olvera, H Gomez, and A Maldonado. Doping, vacuum annealing, and thickness effect on the physical properties of ZnO films deposited by spray pyrolysis. *Solar Energy Materials and Solar Cells*, 91(15-16):1449–1453, Jan 2007.

[64] D. Y Lee, J. R Lee, D. G Kim, C. H Lee, and P. K Song. Study of ga-doped ZnO films deposited on pet substrates by dc magnetron sputtering. *J Ceram Process Res*, 9(6):638–642, Jan 2008.

[65] Naoki Yamamoto, Hisao Makino, Takahiro Yamada, Yoshinori Hirashima, Hiroaki Iwaoka, Takahiro Ito, Akira Ujihara, Hitoshi Hokari, Hidehiro Morita, and Tetsuya Yamamoto. Heat resistance of ga-doped ZnO thin films for application as transparent electrodes in liquid crystal displays. *J Electrochem Soc*, 157(2):J13–J20, Jan 2010.

[66] E Fortunato, A Goncalves, A Marques, A Viana, H Aguas, L Pereira, I Ferreira, P Vilarinho, and R Martins. New developments in gallium doped ZnO deposited on polymeric substrates by rf magnetron sputtering. *Surf Coat Tech*, 180:20–25, Jan 2004.

[67] S.M Park, T Ikegami, and K Ebihara. Effects of substrate temperature on the properties of ga-doped ZnO by pulsed laser deposition. *Thin solid films*, 513(1-2):90–94, 2006.

[68] K Ellmer and R Mientus. Carrier transport in polycrystalline transparent conductive oxides: A comparative study of ZnO and indium oxide. *Thin solid films*, 516(14):4620–4627, 2008.

[69] V Bhosle and J Narayan. Microstructure and electrical property correlations in ga : ZnO transparent conducting thin films. *J Appl Phys*, 100(9):093519, Jan 2006.

[70] M Bender, J Trube, and J Stollenwerk. Characterization of a rf/dc-magnetron discharge for the sputter deposition of transparent and highly conductive ITO films. *Applied Physics A: Materials Science & Processing*, 69(4):397–401, 1999.

[71] HC Lee. The behaviors of the carrier concentrations and mobilities in indium-tin-oxide thin films by dc and rf-superimposed dc reactive magnetron sputtering at the various process temperatures. *Appl Surf Sci*, 252(8):2647–2656, Jan 2006.

[72] S. I Kim, T. D Jung, and P. K Song. Enhanced characterization of ITO films deposited on pet by rf superimposed dc magnetron sputtering. *Thin Solid Films*, 518(11):3085–3088, Jan 2010.

[73] Jun ichi Oda, Jun ichi Nomoto, Toshihiro Miyata, and Tadatsugu Minami. Improvements of spatial resistivity distribution in transparent conducting al-doped ZnO thin films deposited by dc magnetron sputtering. *Thin solid films*, 518(11):2984–2987, Jan 2010.

[74] Ji Bong Park, Se Hun Park, and Pung Keun Song. Electrical and structural properties of in-doped ZnO films deposited by rf superimposed dc magnetron sputtering system. *J Phys Chem Solids*, 71(4):669–672, Jan 2010.

[75] Se Il Kim, Sang Hyun Cho, Sung Ryong Choi, Han Ho Yoon, and Pung Keun Song. Properties of ITO films deposited by rf superimposed dc magnetron sputtering. *Current Applied Physics*, 9:S262–S265, Jan 2009.

[76] R Cebulla, R Wendt, and K Ellmer. Al-doped ZnO films deposited by simultaneous rf and dc excitation of a magnetron plasma: Relationships between plasma parameters and structural and electrical film properties. *J Appl Phys*, 83:1087, Jan 1998.

[77] K Ellmer, R Cebulla, and R Wendt. Transparent and conducting ZnO(:al) films deposited by simultaneous rf- and dc-excitation of a magnetron. *Thin solid films*, 317:413, Apr 1998.

[78] M Stowell, J Muller, M Ruske, M Lutz, and T Linz. Rf-superimposed dc and pulsed dc sputtering for deposition of transparent conductive oxides. *Thin solid films*, 515(19):7654–7657, 2007.

[79] M Stowell, J Muller, M Ruske, M Lutz, and T Linz. Rf-superimposed dc and pulsed dc sputtering for deposition of transparent conductive oxides. *Thin solid films*, 515(19):7654–7657, 2007.

[80] Norihiro Ito, Nobuto Oka, Yasusi Sato, and Yuzo Shigesato. Effects of energetic ion bombardment on structural and electrical properties of al-doped ZnO films deposited by rf-superimposed dc magnetron sputtering. *Jpn J Appl Phys*, 49(7):071103, Jan 2010.

[81] X Bie, J. G Lu, L Gong, L Lin, B. H Zhao, and Z. Z Ye. Transparent conductive ZnO:ga films prepared by dc reactive magnetron sputtering at low temperature. *Appl Surf Sci*, 256:289, Oct 2009.

[82] M Hiramatsu, K Imaeda, N Horio, and M Nawata. Transparent conducting ZnO thin films prepared by xecl excimer laser ablation. *Journal of Vacuum Science & Technology A: Vacuum, Surfaces, and Films*, 16(2):669–673, 1998.

[83] BK Meyer, J Sann, DM Hofmann, C Neumann, and A Zeuner. Shallow donors and acceptors in ZnO. *Semiconductor science and technology*, 20(4):S62, 2005.

[84] V Bhosle, A Tiwari, and J Narayan. Electrical properties of transparent and conducting ga doped ZnO. *Journal of Applied Physics*, 100(3):033713–033713–6, 2006.

[85] Aurelien Du Pasquier, Hanhong Chen, and Yicheng Lu. Dye sensitized solar cells using well-aligned ZnO nanotip arrays. *Applied Physics Letters*, 89(25):253513–253513–3, 2006.

[86] Naoki Yamamoto, Hisao Makino, Takahiro Yamada, Yoshinori Hirashima, Hiroaki Iwaoka, Takahiro Ito, Akira Ujihara, Hitoshi Hokari, Hidehiro Morita, and Tetsuya Yamamoto. Heat resistance of ga-doped ZnO thin films for application as transparent electrodes in liquid crystal displays. *J Electrochem Soc*, 157(2):J13, Jan 2010.

[87] T Minami. Present status of transparent conducting oxide thin-film development for indium-tin-oxide (ITO) substitutes. *Thin solid films*, 516(17):5822–5828, 2008.

[88] B Du Ahn, S Hoon Oh, C Hee Lee, G Hee Kim, H Jae Kim, and S Yeol Lee. Influence of thermal annealing ambient on ga-doped ZnO thin films. *Journal of Crystal Growth*, 309(2):128–133, 2007.

[89] V Bhosle, JT Prater, F Yang, D Burk, SR Forrest, and J Narayan. Gallium-doped ZnO films as transparent electrodes for organic solar cell applications. *Journal of Applied Physics*, 102(2):023501–023501–5, 2007.

[90] Ho-Kyun Park, Jin-A Jeong, Yong-Seok Park, Han-Ki Kim, and Woon-Jo Cho. Electrical, optical, and structural properties of inznsno electrode films grown by unbalanced radio frequency magnetron sputtering. *Thin Solid Films*, 517(18):5563–5568, Jan 2009.

[91] Ho-Kyun Park, Jae-Wook Kang, Seok-In Na, Don-Yu Kim, and Han-Ki Kim. Characteristics of indium-free gzo/ag/gzo and azo/ag/azo multilayer electrode grown by dual target dc sputtering at room temperature for low-cost organic photovoltaics. *Solar Energy Materials and Solar Cells*, 93(11):1994–2002, Jan 2009.

[92] S Tanaka, AA Zakhidov, R Ovalle-Robles, Y Yoshida, I Hiromitsu, Y Fujita, and K Yoshino. Semitransparent organic photovoltaic cell with carbon nanotube-sheet anodes and ga-doped ZnO cathodes. *Synthetic Metals*, 159(21):2326–2328, 2009.

[93] Jun ichi Nomoto, Manabu Konagai, Kenji Okada, Tomoyuki Ito, Toshihiro Miyata, and Tadatsugu Minami. Comparative study of resistivity characteristics between transparent conducting azo and gzo thin films for use at high temperatures. *Thin Solid Films*, 518(11):2937–2940, Mar 2010.

[94] J.A Aranovich, D Golmayo, A.L Fahrenbruch, and R.H Bube. Photovoltaic properties of ZnO/cdte heterojunctions prepared by spray pyrolysis. *Journal of Applied Physics*, 51(8):4260–4268, 1980.

[95] K Iwata, T Sakemi, A Yamada, P Fons, K Awai, T Yamamoto, M Matsubara, H Tampo, and S Niki. Growth and electrical properties of ZnO thin films deposited by novel ion plating method. *Thin Solid Films*, 445(2):274–277, 2003.

[96] E.B Duoss, M Twardowski, and J.A Lewis. Sol-gel inks for direct-write assembly of functional oxides. *Adv. Mater.*, 19(21):3485–3489, Nov 2007.

[97] GK Paul and SK Sen. Optical properties of some sol–gel-derived gallium-doped ZnO films. *Materials Letters*, 57(4):959–963, 2002.

[98] N.D Popovich, S.S Wong, B.K.H Yen, H.Y Yeom, and D.C Paine. Influence of microstructure on the electrochemical performance of tin-doped indium oxide film electrodes. *Analytical chemistry*, 74(13):3127–3133, 2002.

[99] N. D Popovich, S.-S Wong, S Ufer, V Sakhrani, and D Paine. Electron-transfer kinetics at ITO films. *J Electrochem Soc*, 150(11):H255, Jan 2003.

[100] Michael Brumbach, P. Alex Veneman, F. Saneeha Marrikar, Thomas Schulmeyer, Adam Simmonds, Wei Xia, Paul Lee, and Neal R Armstrong. Surface composition and electrical and electrochemical properties of freshly deposited and acid-etched indium tin oxide electrodes. *Langmuir*, 23(22):11089–11099, Jan 2007.

[101] C Donley, D Dunphy, D Paine, C Carter, K Nebesny, P Lee, D Alloway, and N.R Armstrong. Characterization of indium-tin oxide interfaces using x-ray photoelectron spectroscopy and redox processes of a chemisorbed probe molecule: effect of surface pretreatment conditions. *Langmuir*, 18(2):450–457, 2002.

[102] Roland Steim, F. René Kogler, and Christoph J Brabec. Interface materials for organic solar cells. *J. Mater. Chem.*, 20(13):2499, Jan 2010.

[103] N.R Armstrong, P.A Veneman, E Ratcliff, D Placencia, and M Brumbach. Oxide contacts in organic photovoltaics: Characterization and control of near-surface composition in indium tin oxide (ITO) electrodes. *Accounts of chemical research*, 42(11):1748–1757, 2009.

[104] S Choi, W.J Potscavage, and B Kippelen. Area-scaling of organic solar cells. *Journal of Applied Physics*, 106(5):054507–054507–10, 2009.

[105] William Potscavage Jr, Asha Sharma, and Bernard Kippelen. Critical interfaces in organic solar cells and their influence on the open-circuit voltage. *Accounts of Chemical Research*, 42(11):1758–1767, 2009.

[106] Mathilde R Lilliedal, Andrew J Medford, Morten V Madsen, Kion Norrman, and Frederik C Krebs. The effect of post-processing treatments on inflection points in current–voltage curves of roll-to-roll processed polymer photovoltaics. *Solar Energy Materials and Solar Cells*, 94(12):2018–2031, Dec 2010.

[107] A Wagenpfahl, D Rauh, M Binder, C Deibel, and V Dyakonov. S-shaped current-voltage characteristics of organic solar devices. *Phys. Rev. B*, 82(11):115306, Sep 2010.

[108] M Pourbaix. *Atlas of Electrochemical Equilibria in Aqueous Solutions*. Pergamon Press, Oxford, Apr 1966.

[109] R.E.Mesmer and C.F Baes. *The Hydrolysis of Cations*. John Wiley and Sons, New York, New York, Jul 1976.

[110] Charles Baes and Robert Mesmer. The hydrolysis of cations. *American Journal of Science*, 281:935–962, Sep 1981.

[111] G Heiland and P Kunstmann. Polar surfaces of ZnO crystals. *Surface Science*, 13(1):72–84, 1969.

[112] H Moormann, D Kohl, and G Heiland. Variations of work function and surface conductivity on clean cleaved ZnO surfaces by annealing and by hydrogen adsorption. *Surface Science*, 100(2):302–314, 1980.

[113] M Nakagawa and H Mitsudo. Anomalous temperature dependence of the electrical conductivity of ZnO thin films. *Surface science*, 175(1):157–176, 1986.

[114] BJ Coppa, CC Fulton, PJ Hartlieb, RF Davis, BJ Rodriguez, BJ Shields, and RJ Nemanich. In situ cleaning and characterization of oxygen-and zinc-terminated, n-type, ZnO 0001 surfaces. *Journal of Applied Physics*, 95(10):5856–5864, 2004.

[115] W Gopel. Chemisorption and charge transfer at ionic semiconductor surfaces: implications in designing gas sensors. *Progress in surface science*, 20(1):9–103, 1985.

[116] A.K Sigdel, P.F Ndione, J.D Perkins, T Gennett, M.F.A.M van Hest, S.E Shaheen, D.S Ginley, and J.J Berry. Radio-frequency superimposed direct current magnetron sputtered ga: ZnO transparent conducting thin films. *J Appl Phys*, 111(9):093718–093718–7, 2012.

[117] A.K Sigdel, P.F Ndione, Y Ke, N.E Widjonarko, J.D Perkins, M.F.A.M van Hest, S.E Shaheen, T Gennett, D.S Ginley, and J.J Berry. Superimposed rf/dc magnetron sputtering of transparent ga: ZnO with high conductivity for photovoltaic contacts applications. *Photovoltaic Spec. Conf. (PVSC), 2010 35th IEEE*, pages 003270–003274, 2010.

[118] Zheng Yan, Humihiko Takei, and Hiroshi Kawazoe. Electrical conductivity in transparent znga2o4: Reduction and surfacelayer structure transformation. *Journal of the American Ceramic Society*, 81(1):180–186, 1998.

[119] Christopher Gorrie, Ajaya Sigdel, Joseph Berry, Brandon Reese, Maikel Van Hest, Paul Holloway, David Ginley, and John Perkins. Effect of deposition distance and temperature on electrical, optical and structural properties of

radio-frequency magnetron-sputtered gallium-doped ZnO. *Thin Solid Films*, 519(1):190–196, 2010.

[120] CJ Powell. Energy calibration of xray photoelectron spectrometers: Results of an interlaboratory comparison to evaluate a proposed calibration procedure. *Surface and interface analysis*, 23(3):121–132, 1995.

[121] G Zotti, G Schiavon, S Zecchin, A Berlin, and G Pagani. Adsorption of ferrocene compounds on indium-tin-oxide electrodes. enhancement of adsorption by decomposition of ferrocenium molecules by oxygen. *Langmuir*, 14(7):1728–1733, 1998.

[122] M Kunat, St. Gil Girol, U Burghaus, and C Wöll. The interaction of water with the oxygen-terminated, polar surface of ZnO. *The Journal of Physical Chemistry B*, 107(51):14350–14356, 2003.

[123] RG Egdell, J Rebane, TJ Walker, and DSL Law. Competition between initial- and final-state effects in valence-and core-level x-ray photoemission of sb-doped SnO_2. *Phys. Rev. B*, 59(3):1792, 1999.

[124] Y Gassenbauer, R Schafranek, A Klein, S Zafeiratos, M Hävecker, A Knop-Gericke, and R Schlögl. Surface states, surface potentials, and segregation at surfaces of tin-doped In_2O_3. *Phys. Rev. B*, 73(24):245312, Jun 2006.

[125] S Major, S Kumar, M Bhatnagar, and KL Chopra. Effect of hydrogen plasma treatment on transparent conducting oxides. *Applied Physics Letters*, 49(7):394–396, 1986.

[126] A de Souza Gonçalves, S Antonio Marques de Lima, M Rosaly Davolos, S Gutierrez Antônio, and C de Oliveira Paiva-Santos. The effects of

$ZnGa_2O_4$ formation on structural and optical properties of ZnO: Ga powders. *Journal of Solid State Chemistry*, 179(5):1330–1334, 2006.

[127] Min-Jung Lee, Jinhyong Lim, Jungsik Bang, Woong Lee, and Jae-Min Myoung. Effect of the thickness and hydrogen treatment on the properties of ga-doped ZnO transparent conductive films. *Applied Surface Science*, 255(5):3195–3200, 2008.

[128] T.E Sheridan and J Goree. Lowfrequency turbulent transport in magnetron plasmas. *Journal of Vacuum Science & Technology A: Vacuum, Surfaces, and Films*, 7(3):1014–1018, 1989.

[129] BH Choi, HB Im, JS Song, and KH Yoon. Optical and electrical properties of Ga_2O_3 doped ZnO films prepared by rf sputtering. *Thin Solid Films*, 193:712–720, 1990.

[130] K.T.R Reddy, H Gopalaswamy, PJ Reddy, and RW Miles. Effect of gallium incorporation on the physical properties of ZnO grown by spray pyrolysis. *Journal of Crystal Growth*, 210(516):520, 2000.

[131] GB Palmer and KR Poeppelmeier. Phase relations, transparency and conductivity in Ga_2O_3 - SnO_2 - ZnO. *Solid State Sciences*, 4(3):317–322, 2002.

[132] AR Phani, S Santucci, S Di Nardo, L Lozzi, M Passacantando, P Picozzi, and C Cantalini. Preparation and characterization of bulk gallium ZnO. *Journal of materials science*, 33(15):3969–3973, 1998.

[133] L Brewer. Thermodynamic properties of the oxides and their vaporization processes. *Chemical Reviews*, 52(1):1–75, 1953.

[134] R Roy, VG Hill, and EF Osborn. Polymorphism of Ga_2O_3 and the system Ga_2O_3—h2o. *Journal of the American Chemical Society*, 74(3):719–722, 1952.

[135] AW Laubengayer and HR Engle. The sesquioxide and hydroxides of gallium. *Journal of the American Chemical Society*, 61(5):1210–1214, 1939.

[136] Jean-Charles Dupin, Danielle Gonbeau, Philippe Vinatier, and Alain Levasseur. Systematic xps studies of metal oxides, hydroxides and peroxides. *Phys. Chem. Chem. Phys.*, 2(6):1319–1324, Jan 2000.

[137] Hani Khallaf, Guangyu Chai, Oleg Lupan, Helge Heinrich, Sanghoon Park, Alfons Schulte, and Lee Chow. Investigation of chemical bath deposition of ZnO thin films using six different complexing agents. *Journal of Physics D: Applied Physics*, 42(13):135304, 2009.

[138] DG Thomas. The diffusion and precipitation of indium in ZnO. *J Phys Chem Solids*, 9(1):31–42, 1959.

[139] N Roberts, R.P Wang, A.W Sleight, and W.W Warren. ^{27} al and ^{69}ga impurity nuclear magnetic resonance in ZnO: Al and ZnO: Ga. *Phys. Rev. B*, 57(10):5734, 1998.

[140] Paul Erhart, Karsten Albe, and Andreas Klein. First-principles study of intrinsic point defects in ZnO: Role of band structure, volume relaxation, and finite-size effects. *Phys. Rev. B*, 73(20):205203, May 2006.

[141] X Crispin, V Geskin, A Crispin, J Cornil, R Lazzaroni, W.R Salaneck, and J.L Bredas. Characterization of the interface dipole at organic/metal interfaces. *Journal of the American Chemical Society*, 124(27):8131–8141, 2002.

[142] A Crispin, X Crispin, M Fahlman, M Berggren, and W.R Salaneck. Transition between energy level alignment regimes at a low band gap polymer-electrode interfaces. *Applied Physics Letters*, 89(21):213503–213503–3, 2006.

[143] Slawomir Braun, William R Salaneck, and Mats Fahlman. Energy-level alignment at organic/metal and organic/organic interfaces. *Adv. Mater.*, 21(14-15):1450–1472, Apr 2009.

[144] VD Mihailetchi, PWM Blom, JC Hummelen, and MT Rispens. Cathode dependence of the open-circuit voltage of polymer: fullerene bulk heterojunction solar cells. *Journal of Applied Physics*, 94(10):6849–6854, 2003.

[145] SB Zhang, S.H Wei, and A Zunger. A phenomenological model for systematization and prediction of doping limits in ii–vi and i–iii–vi 2 compounds. *Journal of Applied Physics*, 83(6):3192–3196, 1998.

[146] W Walukiewicz. Intrinsic limitations to the doping of wide-gap semiconductors. *Physica B: Condensed Matter*, 302:123–134, 2001.

[147] Stephan Lany, Jorge Osorio-Guillén, and Alex Zunger. Origins of the doping asymmetry in oxides: Hole doping in nio versus electron doping in ZnO. *Phys. Rev. B*, 75(24):241203, Jun 2007.

[148] H Ishii, K Sugiyama, E Ito, and K Seki. Energy level alignment and interfacial electronic structures at organic/metal and organic/organic interfaces (vol 11, pg 605, 1999). *Adv. Mater.*, 11(12):972–972, 1999.

[149] WH Cheng and HH Kung. Chemical properties of anion vacancies on ZnO. *Surface Science Letters*, 102(1):L21–L28, 1981.

[150] W Göpel, RS Bauer, and G Hansson. Ultraviolet photoemission studies of chemisorption and point defect formation on ZnO nonpolar surfaces. *Surface Science*, 99(1):138–156, 1980.

[151] K Jacobi, G Zwicker, and A Gutmann. Work function, electron affinity and band bending of ZnO surfaces. *Surface science*, 141(1):109–125, 1984.

[152] I Noviandri, K.N Brown, D.S Fleming, P.T Gulyas, P.A Lay, A.F Masters, and L Phillips. The decamethylferrocenium/decamethylferrocene redox couple: A superior redox standard to the ferrocenium/ferrocene redox couple for studying solvent effects on the thermodynamics of electron transfer. *The Journal of Physical Chemistry B*, 103(32):6713–6722, 1999.

[153] R.S Nicholson. Theory and application of cyclic voltammetry for measurement of electrode reaction kinetics. *Analytical Chemistry*, 37(11):1351–1355, 1965.

[154] L Falciola, A Gennaro, A.A Isse, P.R Mussini, and M Rossi. The solvent effect in the electrocatalytic reduction of organic bromides on silver. *Journal of Electroanalytical Chemistry*, 593(1):47–56, 2006.

[155] T.J Gardner, C.D Frisbie, and M.S Wrighton. Systems for orthogonal self-assembly of electroactive monolayers on au and ITO: an approach to molecular electronics. *Journal of the American Chemical Society*, 117(26):6927–6933, 1995.

[156] E Laviron. General expression of the linear potential sweep voltammogram in the case of diffusionless electrochemical systems. *Journal of Electroanalytical Chemistry and Interfacial Electrochemistry*, 101(1):19–28, 1979.

[157] C Carter, M Brumbach, C Donley, R.D Hreha, S.R Marder, B Domercq, S.H Yoo, B Kippelen, and N.R Armstrong. Small molecule chemisorption on indium-tin oxide surfaces: enhancing probe molecule electron-transfer rates and the performance of organic light-emitting diodes. *The Journal of Physical Chemistry B*, 110(50):25191–25202, 2006.

[158] G Gonçalves, E Elangovan, P Barquinha, L Pereira, R Martins, and E Fortunato. Influence of post-annealing temperature on the properties exhibited by ITO, IZO and gzo thin films. *Thin Solid Films*, 515(24):8562–8566, 2007.

[159] Arrelaine A Dameron, David C Miller, Nathan George, Bobby To, David S Ginley, and Lin Simpson. Tensile strain and water vapor transport testing of flexible, conductive and transparent indium–zinc-oxide/silver/indium–zinc-oxide thin films. *Thin Solid Films*, 519(10):3177–3184, Mar 2011.

[160] Kian Soo Ong, Raymond Gan Ching Ruey, Eric Ou, Zhang Zheng, and Doreen Lai Mei Ying. Interfacial and mechanical studies of a composite ag–IZO–pen barrier film for effective encapsulation of organic tft. *Organic Electronics*, 11(3):463–466, 2010.

[161] Kenji Nomura, Akihiro Takagi, Toshio Kamiya, Hiromichi Ohta, Masahiro Hirano, and Hideo Hosono. Amorphous oxide semiconductors for high-performance flexible thin-film transistors. *Jpn J Appl Phys*, 45(5B):4303–4308, May 2006.

[162] Young Sung Kim, Woo Jin Hwang, Kyung Tae Eun, and Sung-Hoon Choa. Mechanical reliability of transparent conducting izto film electrodes for flexible panel displays. *Applied Surface Science*, 257(18):8134–8138, Jan 2011.

[163] H Hosono. Ionic amorphous oxide semiconductors: Material design, carrier transport, and device application. *Journal of Non-Crystalline Solids*, 352(9-20):851–858, 2006.

[164] J. D Perkins, M. F. A. M van Hest, M. P Taylor, and D. S Ginley. Conductivity and transparency in amorphous in-zn-o transparent conductors. *Int J Nanotechnol*, 6(9):850–859, Jan 2009.

[165] HQ Chiang, JF Wager, RL Hoffman, J Jeong, and D.A Keszler. High mobility transparent thin-film transistors with amorphous zinc tin oxide channel layer. *Applied Physics Letters*, 86(1):013503–013503–3, 2005.

[166] WB Jackson, GS Herman, RL Hoffman, C Taussig, S Braymen, F Jeffery, and J Hauschildt. Zinc tin oxide transistors on flexible substrates. *Journal of non-crystalline solids*, 352(9):1753–1755, 2006.

[167] Than Zaw Oo, R Devi Chandra, Natalia Yantara, Rajiv Ramanujam Prabhakar, Lydia H Wong, Nripan Mathews, and Subodh G Mhaisalkar. Zinc tin oxide (zto) electron transporting buffer layer in inverted organic solar cell. *Organic Electronics*, 13(5):870–874, May 2012.

[168] Martin Kaltenbrunner, Matthew S White, Eric D Głowacki, Tsuyoshi Sekitani, Takao Someya, Niyazi Serdar Sariciftci, and Siegfried Bauer. Ultrathin and lightweight organic solar cells with high flexibility. *Nat Comms*, 3:770, Apr 2012.

[169] W Cai, X Gong, and Y Cao. Polymer solar cells: Recent development and possible routes for improvement in the performance. *Solar Energy Materials and Solar Cells*, 94(2):114–127, 2010.

[170] M. S White, D. C Olson, S. E Shaheen, N Kopidakis, and D. S Ginley. Inverted bulk-heterojunction organic photovoltaic device using a solution-derived ZnO underlayer. *Appl. Phys. Lett.*, 89(14):143517, Jan 2006.

[171] H Cheun, J Kim, Y Zhou, Y Fang, A Dindar, J Shim, C Fuentes-Hernandez, K.H Sandhage, and B Kippelen. Inverted polymer solar cells with amorphous indium ZnO as the electron-collecting electrode. *Optics Express*, 18(104):A506–A512, 2010.

[172] T Ameri, G Dennler, C Waldauf, P Denk, K Forberich, M.C Scharber, C.J Brabec, and K Hingerl. Realization, characterization, and optical modeling of inverted bulk-heterojunction organic solar cells. *Journal of Applied Physics*, 103(8):084506–084506–6, 2008.

[173] Chunfu Zhang, Hailong You, Zhenhua Lin, and Yue Hao. Inverted organic photovoltaic cells with solution-processed ZnO as electron collecting layer. *Jpn. J. Appl. Phys.*, 50(8):082302, Aug 2011.

[174] Andrew Leenheer, John Perkins, Maikel Van Hest, Joseph Berry, Ryan O'hayre, and David Ginley. General mobility and carrier concentration relationship in transparent amorphous indium ZnO films. *Physical Review B*, 77(11):115215, Mar 2008.

[175] JM Park, JS Hong, JY Yang, JJ Kim, SH Park, HM Kim, and JS Ahn. Bending effects of indium-ZnO thin films deposited on polyethylene terephthalate substrate by radio frequency magnetron sputtering. *J Korean Phys Soc*, 48(6):1530–1533, Jan 2006.

[176] E Fortunato, P Barquinha, A Pimentel, L Pereira, G Gonçalves, and R Martins. Amorphous IZO ttfts with saturation mobilities exceeding 100 cm2/vs. *phys. stat. sol. (RRL)*, 1(1):R34–R36, Jan 2007.

[177] David C Paine, Burag Yaglioglu, Zach Beiley, and Sunghwan Lee. Amorphous IZO-based transparent thin film transistors. *Thin Solid Films*, 516(17):5894–5898, Jan 2008.

[178] K Ramamoorthy, K Kumar, R Chandramohan, and K Sankaranarayanan. Review on material properties of IZO thin films useful as epi-n-tcos in opto-electronic (sis solar cells, polymeric LEDs) devices. *Materials Science and Engineering: B*, 126(1):1–15, 2006.

[179] M Jørgensen, K Norrman, and F.C Krebs. Stability/degradation of polymer solar cells. *Solar Energy Materials and Solar Cells*, 92(7):686–714, 2008.

[180] N. Edwin Widjonarko, Erin L. Ratcliff, Craig L. Perkins, Ajaya K. Sigdel, Andriy Zakutayev, Paul F. Ndione, Dane T. Gillaspie, David S. Ginley, Dana C. Olson, and Joseph J. Berry. Sputtered nickel oxide thin film for efficient hole transport layer in polymer-fullerene bulk-heterojuntion organic solar cell. *Thin solid films*, 520(10):3813–3818, October 2011.

[181] H Hosono, M Yasukawa, and H Kawazoe. Novel oxide amorphous semiconductors: transparent conducting amorphous oxides. *Journal of Non-Crystalline Solids*, 203:334–344, 1996.

[182] R Martins, P Almeida, P Barquinha, L Pereira, A Pimentel, I Ferreira, and E Fortunato. Electron transport and optical characteristics in amorphous indium ZnO films. *Journal of non-crystalline solids*, 352(9):1471–1474, 2006.

[183] S Lee, H Park, and D.C Paine. A study of the specific contact resistance and channel resistivity of amorphous IZO thin film transistors with IZO source–drain metallization. *Journal of Applied Physics*, 109(6):063702–063702–6, 2011.

[184] Erin L Ratcliff, Ajaya K Sigdel, Mariola R Macech, Kenneth Nebesny, Paul A Lee, David S Ginley, Neal R Armstrong, and Joseph J Berry. Surface composition, work function, and electrochemical characteristics of gallium-doped ZnO. *Thin solid films*, 520(17):5652–5663, Jun 2012.

[185] Jae-Wook Kang, Won-Ik Jeong, Jang-Joo Kim, Han-Ki Kim, Do-Geun Kim, and Gun-Hwan Lee. High-performance flexible organic light-emitting diodes using amorphous indium ZnO anode. *Electrochem. Solid-State Lett.*, 10(6):J75–J78, 2007.

[186] Hsin-Hsuan Huang, Sheng-Yuan Chu, Po-Ching Kao, Yung-Chen Chen, and Ren-Chuan Chang. Improved hole-injection and power efficiency of organic light-emitting diodes using an ultrathin li-doped ZnO buffer layer. *Journal of The Electrochemical Society*, 154(3):J105–J108, 2007.

[187] ZH Huang, XT Zeng, XY Sun, ET Kang, Jerry Fuh, and L Lu. Influence of plasma treatment of ITO surface on the growth and properties of hole transport layer and the device performance of OLEDs. *Organic Electronics*, 9(1):51–62, 2008.

[188] U Betz, M Olsson, and J Marthy. On the synthesis of ultra smooth ITO thin films by conventional direct current magnetron sputtering. *Thin Solid Films*, 516(7):1334–1340, 2008.

[189] S.A Choulis, V.-E Choong, A Patwardhan, M.K Mathai, and F So. Interface modification to improve hole-injection properties in organic electronic devices. *Adv. Funct. Mater.*, 16(8):1075–1080, May 2006.

[190] M Harding, Dmitry Poplavskyy, V-E Choong, Alasdair Campbell, and Franky So. Effects of solution-processed polymer interlayers on hole injection and device performance of polymer light-emitting diodes. *Organic Electronics*, 9(2):183–190, 2008.

[191] F Marrikar, Michael Brumbach, Dennis Evans, Ariel Lebrón-Paler, Jeanne Pemberton, Ronald Wysocki, and Neal Armstrong. Modification of indium-tin oxide electrodes with thiophene copolymer thin films: Optimizing electron transfer to solution probe molecules. *Langmuir*, 23(3):1530–1542, 2007.

[192] Neetu Chopra, James Swensen, Evgueni Polikarpov, Lelia Cosimbescu, Franky So, and Asanga Padmaperuma. High efficiency and low roll-off blue phosphorescent organic light-emitting devices using mixed host architecture. *Applied Physics Letters*, 97:033304, 2010.

[193] Frederik Krebs, Thomas Tromholt, and Mikkel Jørgensen. Upscaling of polymer solar cell fabrication using full roll-to-roll processing. *Nanoscale*, 2(6):873–886, 2010.

[194] Radhouane Bel Hadj Tahar, Takayuki Ban, Yutaka Ohya, and Yasutaka Takahashi. Tin doped indium oxide thin films: Electrical properties. *Journal of Applied Physics*, 83(5):2631–2645, 1998.

[195] Myung-Gyu Kang, Myung-Su Kim, Jinsang Kim, and L. Jay Guo. Organic solar cells using nanoimprinted transparent metal electrodes. *Advanced Materials*, 20(23):4408–4413, Dec 2008.

[196] Won Hyun Shim, Sun-Young Park, Mi Yeong Park, Hyun Ook Seo, Kwang-Dae Kim, Young Tae Kim, Yang Do Kim, Jae-Wook Kang, Kyu Hwan Lee, Yongsoo Jeong, Young Dok Kim, and Dong Chan Lim. Multifunctional swcnt-ZnO nanocomposites for enhancing performance and stability of organic solar cells. *Advanced Materials*, 23(4):519–522, Nov 2010.

[197] Y Zhou, H Cheun, S Choi, W.J Potscavage, C Fuentes-Hernandez, and B Kippelen. Indium tin oxide-free and metal-free semitransparent organic solar cells. *Applied Physics Letters*, 97(15):153304–153304–3, 2010.

[198] Andrew J Leenheer, John D Perkins, Maikel F. A. M van Hest, Joseph J Berry, Ryan P O'Hayre, and David S Ginley. General mobility and carrier concentration relationship in transparent amorphous indium ZnO films. *Phys. Rev. B*, 77(11):115215, Jan 2008.

[199] Gang Li, Vishal Shrotriya, Jinsong Huang, Yan Yao, Tom Moriarty, Keith Emery, and Yang Yang. High-efficiency solution processable polymer photovoltaic cells by self-organization of polymer blends. *Nature Materials*, 4(11):864, Oct 2005.

[200] Ingo Riedel, Jürgen Parisi, Vladimir Dyakonov, Laurence Lutsen, Dirk Vanderzande, and Jan Hummelen. Effect of temperature and illumination on the electrical characteristics of polymer–fullerene bulkheterojunction solar cells. *Adv. Funct. Mater.*, 14(1):38–44, 2004.

[201] Kiyoshi Sugiyama, Hisao Ishii, Yukio Ouchi, and Kazuhiko Seki. Dependence of indium–tin–oxide work function on surface cleaning method as studied by ultraviolet and x-ray photoemission spectroscopies. *Journal of Applied Physics*, 87(1):295–298, 2000.

[202] H Cheun, C Fuentes-Hernandez, Y Zhou, W.J Potscavage Jr, S.J Kim, J Shim, A Dindar, and B Kippelen. Electrical and optical properties of ZnO processed by atomic layer deposition in inverted polymer solar cells. *The Journal of Physical Chemistry C*, 114(48):20713–20718, 2010.

[203] Hui Jin, Markus Tuomikoski, Jussi Hiltunen, Pälvi Kopola, Arto Maaninen, and Flavio Pino. Polymer electrode interfacial effect on photovoltaic performances in poly (3-hexylthiophene): Phenyl-c61-butyric acid methyl ester based solar cells. *The Journal of Physical Chemistry C*, 113(38):16807–16810, 2009.

[204] Carsten Deibel and Alexander Wagenpfahl. Comment on "interface state recombination in organic solar cells". *Physical Review B*, 82(20):207301, Nov 2010.

[205] S.K Hau, H.L Yip, K.S Chen, J Zou, and A.K.Y Jen. Solution processed inverted tandem polymer solar cells with self-assembled monolayer modified interfacial layers. *Applied Physics Letters*, 97(25):253307–253307–3, 2010.

[206] C Waldauf, M Morana, P Denk, P Schilinsky, K Coakley, SA Choulis, and CJ Brabec. Highly efficient inverted organic photovoltaics using solution based titanium oxide as electron selective contact. *Applied Physics Letters*, 89(23):233517–233517–3, 2006.

[207] Y Zhou, H Cheun, W.J Potscavage Jr, C Fuentes-Hernandez, S.J Kim, and B Kippelen. Inverted organic solar cells with ITO electrodes modified with an ultrathin al2o3 buffer layer deposited by atomic layer deposition. *J. Mater. Chem.*, 20(29):6189–6194, 2010.

[208] Roland Steim, F. René Kogler, and Christoph J Brabec. Interface materials for organic solar cells. *J. Mater. Chem.*, 20(13):2499, Jan 2010.

[209] T Krajewski, E Guziewicz, M Godlewski, L Wachnicki, IA Kowalik, A Wojcik-Glodowska, M Lukasiewicz, K Kopalko, V Osinniy, and M Guziewicz. The influence of growth temperature and precursors' doses on electrical parameters of ZnO thin films grown by atomic layer deposition technique. *Microelectronics Journal*, 40(2):293–295, 2009.

[210] K Ellmer. Resistivity of polycrystalline ZnO films: current status and physical limit. *J. Phys. D: Appl. Phys.*, 34(21):3097, 2001.

[211] Fujun Zhang, Xiaowei Xu, Weihua Tang, Jian Zhang, Zuliang Zhuo, Jian Wang, Jin Wang, Zheng Xu, and Yongsheng Wang. Recent development of the inverted configuration organic solar cells. *Solar Energy Materials and Solar Cells*, 95(7):1785–1799, Jan 2011.

[212] C.G Granqvist. Transparent conductors as solar energy materials: a panoramic review. *Solar Energy Materials and Solar Cells*, 91(17):1529–1598, 2007.

[213] T Kuwabara, Y Kawahara, T Yamaguchi, and K Takahashi. Characterization of inverted-type organic solar cells with a ZnO layer as the electron col-

lection electrode by ac impedance spectroscopy. *ACS Applied Materials & Interfaces*, 1(10):2107–2110, 2009.

[214] KJ Saji, MK Jayaraj, K Nomura, T Kamiya, and H Hosono. Optical and carrier transport properties of cosputtered zn–in–sn–o films and their applications to tfts. *J Electrochem Soc*, 155:H390, 2008.

[215] KJ Chen, FY Hung, SJ Chang, SP Chang, YC Mai, and ZS Hu. A study on crystallization, optical and electrical properties of the advanced zITO thin films using co-sputtering system. *Journal of Alloys and Compounds*, 509(8):3667–3671, 2011.

[216] HY Liu, V Avrutin, N Izyumskaya, U Ozgur, AB Yankovich, AV Kvit, PM Voyles, and H Morkoç. Electron scattering mechanisms in gzo films grown on a-sapphire substrates by plasma-enhanced molecular beam epitaxy. *Journal of Applied Physics*, 111(10):103713–103713–9, 2012.

[217] Sun-Young SOHN, Hwa-Min KIM, Seoung-Hwan PARK, and Jong-Jae KIM. Stability of sn-doped indium-zinc-oxide thin films prepared by rf-magnetron sputtering against moist heat. *J Korean Phys Soc*, 45(DEC):S732–S735, 2004.

[218] N Ito, Y Sato, P Song, A Kaijio, K Inoue, and Y Shigesato. Electrical and optical properties of amorphous indium ZnO films. *Thin solid films*, 496:99, Feb 2006.

[219] Jin-A Jeong, Han-Ki Kim, and Seok-In Na. Low resistance and high transparent amorphous izto electrode cosputtered by linear facing target sputtering for organic photovoltaics. *Electrochem Solid St*, 12(9):J80–J82, Jan 2009.

[220] T Minami. Transparent and conductive multicomponent oxide films prepared by magnetron sputtering. *J Vac Sci Technol A*, 17(4):1765–1772, Jan 1999.

[221] Diana E Proffit, Steven P Harvey, Andreas Klein, Robert Schafranek, Jonathan D Emery, D Bruce Buchholz, Robert P H Chang, Michael J Bedzyk, and Thomas O Mason. Surface studies of crystalline and amorphous zn–in–sn–o transparent conducting oxides. *Thin solid films*, 520(17):5633–5639, Jun 2012.

[222] Andreas Klein, Christoph Körber, André Wachau, Frank Säuberlich, Yvonne Gassenbauer, Steven P Harvey, Diana E Proffit, and Thomas O Mason. Transparent conducting oxides for photovoltaics: Manipulation of fermi level, work function and energy band alignment. *Materials*, 3(11):4892–4914, Nov 2010.

[223] Jung-Hyeok Bae, Jong-Min Moon, Soon Wook Jeong, Jang-Joo Kim, Jae-Wook Kang, Do-Geun Kim, Jong-Kuk Kim, Jeong-Woo Park, and Han-Ki Kim. Transparent conducting indium zinc tin oxide anode for highly efficient phosphorescent organic light emitting diodes. *J Electrochem Soc*, 155(1):J1–J6, Jan 2008.

[224] Yoon Duk Ko and Young Sung Kim. Room temperature deposition of izto transparent anode films for organic light-emitting diodes. *Materials Research Bulletin*, 47(10):2800–2803, Oct 2012.

[225] KH Choi, JA Jeong, and HK Kim. Dependence of electrical, optical, and structural properties on the thickness of izto thin films grown by linear facing

target sputtering for organic solar cells. *Solar Energy Materials and Solar Cells*, 2010.

[226] T Minami, T Yamamoto, Y Toda, and T Miyata. Transparent conducting zinc-co-doped ITO films prepared by magnetron sputtering. *Thin Solid Films*, 373(1-2):189–194, 2000.

[227] G.S Heo, Y Matsumoto, I.G Gim, H.K Lee, J.W Park, and T.W Kim. Transparent conducting amorphous zn-in-sn-o anode for flexible organic light-emitting diodes. *Solid State Communications*, 150(3-4):223–226, 2010.

[228] DY Lee, JR Lee, GH Lee, and PK Song. Study on in-zn-sn-o and in-sn-zn-o films deposited on pet substrate by magnetron co-sputtering system. *Surface and Coatings Technology*, 202(22-23):5718–5723, 2008.

[229] Dae-Hyun Kim, Woo-Jae Kim, Sang Joon Park, Hyung Wook Choi, and Kyung-Hwan Kim. Electrical and optical properties of in–zn–sn–o thin film deposited on polymer substrates through facing targets co-sputtering system. *Surface & Coatings Technology*, 205(S1):S324–S327, Jan 2010.

[230] Hee Young Lee, Joon-Hyung Lee, Jeong-Joo Kim, Daniel J Lichtenwalner, and Angus I Kingon. Zn-sn co-doping effect on crystallization and texturing characteristics of indium oxide thin films. *J Ceram Process Res*, 10:S116–S119, Jan 2009.

[231] Cleva W Ow-Yang, Hyo young Yeom, and David C Paine. Fabrication of transparent conducting amorphous zn-sn-in-o thin films by direct current magnetron sputtering. *Thin Solid Films*, 516(10):3105–3111, Jan 2008.

[232] Seung-Yeol Han, Doo-Hyoung Lee, Gregory S Herman, and Chih-Hung Chang. Inkjet-printed high mobility transparent-oxide semiconductors. *J Disp Technol*, 5(12):520–524, Jan 2009.

[233] Doo-Hyoung Lee, Seung-Yeol Han, Gregory S Herman, and Chih-Hung Chang. Inkjet printed high-mobility indium zinc tin oxide thin film transistors. *J Mater Chem*, 19(20):3135–3137, Jan 2009.

[234] Cathleen A Hoel, Thomas O Mason, Jean-Francois Gaillard, and Kenneth R Poeppelmeier. Transparent conducting oxides in the ZnO-In_2O_3-SnO_2 system. *Chem Mater*, 22(12):3569–3579, Jan 2010.

[235] Steven P Harvey, Kenneth R Poeppelmeier, and Thomas O Mason. Subsolidus phase relationships in the ZnO-In_2O_3-SnO_2 system. *Journal of the American Ceramic Society*, 91(11):3683–3689, Jan 2008.

[236] Cathleen A Hoel, Jean-François Gaillard, and Kenneth R Poeppelmeier. Probing the local structure of crystalline zITO: $In_{2-2x}sn_xzn_xo_3$ (x = 0 to 0.4). *J Solid State Chem*, 183:761, Apr 2010.

[237] GS Heo, Y Matsumoto, IG Gim, HK Lee, JW Park, and TW Kim. Transparent conducting amorphous zn-in-sn-o anode for flexible organic light-emitting diodes. *Solid State Communications*, 150(3-4):223–226, 2010.

Appendix A

Electrical Measurements

A.1 Resistivity - van der Pauw's method

The experimental method for resistivity measurement using van der Pauw's method is shown in Figure A-1.

The resistivity is then given by:

$$\rho = \frac{\pi.t}{2.ln(2)} \left[\frac{V_{43}}{I_{12}} + \frac{V_{23}}{I_{14}} \right] .F.Q \qquad \text{(A-1)}$$

where t is the thickness of the film, Q = $\frac{V_{43}I_{14}}{I_{12}V_{23}}$ or its reciprocal, whichever is greater than 1 and F is a correction factor for geometrical asymmetry. For Q $<$ 10, following approximation can be made, F = 1 - 0.34657A- 0.09236A^2, where A = $\left[\frac{Q-1}{Q+1}\right]^2$. Hall measurement done in room temperature provides μ, N, and carrier type of a semi-conductor.

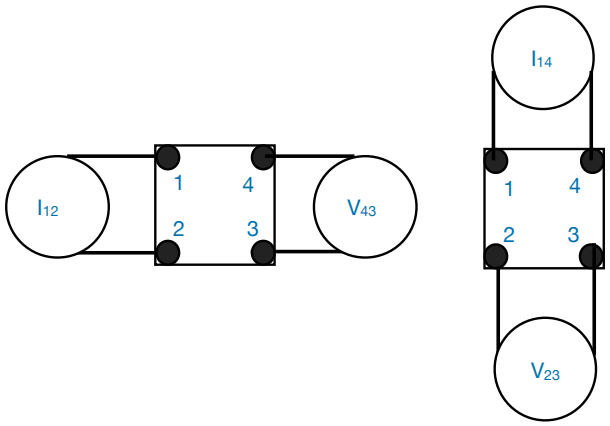

Figure A-1: Resistivity Van der Pauw configuration

A.2 Derivations for Drift Mobility

In a sample, shown in Figure A-2, where both negative and positive charge carriers present, then concentration of electron and holes are *n* and *p* respectively. Mobilities are μ_e and μ_h. For electron, the relation between the electric field and the drift velocity is

$$V_e = \mu_e E \tag{A-1}$$

where, μ_e is drift mobility, and V_e is the drift velocity.

If a single charge q (electron or hole) moves with velocity v in the presence of an electric field E and a magnetic field B, then it will experience a force

$$\mathbf{F} = q[\mathbf{E} + (\mathbf{v} \times \mathbf{B})] \tag{A-2}$$

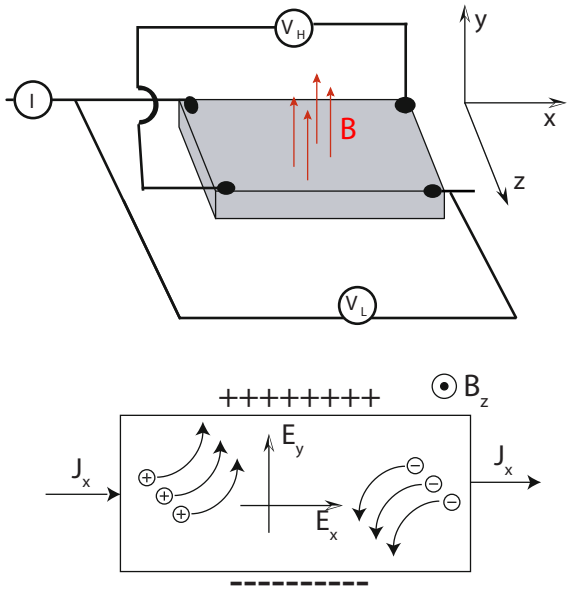

Figure A-2: Van der Pauw configuration

When both electrons and holes are present in a sample, both experience a Lorentz force in a same direction. Suppose that V_{ey} and V_{hy} are the drift velocity in -y and +y direction respectively due to the electric field. At equilibrium, net current in y-axis is zero.

$$J_y = J_n + J_h = enV_{ey} + epV_{hy} = 0 \tag{A-3}$$

$$nV_{ey} = -pV_{hy} \tag{A-4}$$

So the holes are drifting in opposite direction to E_y. The voltage associated with E_y is known as the Hall voltage V_H. Now the net force from both electrostatic and magnetic force experienced by holes and electrons is

$$\bar{F}_{hy} = eE_y - eV_{hx}B_z \tag{A-5a}$$

$$\bar{F}_{ey} = -eE_y - eV_{ex}B_z \tag{A-5b}$$

where, V_{hx} and V_{ex} are drift velocity along x-axis. Now,

$$\bar{F}_{hy} = \frac{eV_{hy}}{\mu_h} \tag{A-6a}$$

$$-\bar{F}_{ey} = \frac{eV_{ey}}{\mu_e} \tag{A-6b}$$

Plugging equation A-6b into equation A-5b, we get

$$\frac{eV_{hy}}{\mu_h} = eE_y - eV_{hx}B_z \tag{A-7a}$$

$$\frac{eV_{ey}}{\mu_e} = eE_y + eV_{ex}B_z \tag{A-7b}$$

substituting, $V_{hx} = \mu_h E_x$, $V_{ex} = \mu_e E_x$, we get

$$\frac{V_{hy}}{\mu_h} = E_y - e\mu_h E_x B_z \tag{A-8a}$$

$$\frac{V_{ey}}{\mu_e} = E_y + eV_{ex}B_z \tag{A-8b}$$

Using the relation in equation A-4, we get

$$p\mu_h[E_y - e\mu_h E_x B_z] = -n\mu_e[E_y + eV_{ex}B_z] \tag{A-9a}$$

$$E_y[p\mu_h + n\mu_e] = B_z E_x[p{\mu_h}^2 - n{\mu_e}^2] \tag{A-9b}$$

Now along x-axis,

$$J_x = epV_{hx} + enV_{ex} = eE_x[p\mu_n + n\mu_e] \tag{A-10}$$

using equation A-10 and substituting for E_x in equation A-9b, we get

$$E_y = \frac{B_z I_x[p{\mu_h}^2 - n{\mu_e}^2]}{e[p\mu_n + n\mu_e]^2} = B_z I_x R_H \tag{A-11}$$

Thus, the Hall coefficient R_H in the drift velocity approximation is

$$R_H = \frac{[p{\mu_h}^2 - n{\mu_e}^2]}{e[p\mu_n + n\mu_e]^2} \tag{A-12}$$

or

$$R_H = \frac{[p - nb^2]}{e[p + nb^2} \tag{A-13}$$

where, b = $\frac{\mu_e}{\mu_h}$. Hall coefficient depends on the drift mobility ratio and the concentrations of holes and electrons. For p $>$ nb^2, R$_H$will be positive and for p $<$ nb^2, it will be negative.

In a n-type system like ZnO, and various other TCOs, where conductivity is dominated by mobility of electrons in the conduction band. The relation simplifies to

$$R_H = -\frac{r}{ne} \tag{A-14}$$

Where, r is the scattering rate which depends on the scattering mechanism which dominates. r ($\sim$ 1.18 for acoustic phonon scattering and $\sim$ 1.93 for ionized impurities scattering) can be measured using temperature dependence mobility measurement, and usually range between 1 and 2. Note: the mobility measured by Hall is

related to drift mobility in the film by μ_H = r$\times\mu_{drift}$, where the Hall scattering r = $\frac{<\tau^2>}{<\tau>^2}$, and τ is the relaxation time of a scattering events. For most of our TCOs thin film measurements, we assumed r = 1.

Appendix B

List of symbols and acronyms

- OPV - Organic photovoltaics
- OLED - Organic Light Emitting Diode
- ITO - Indium tin oxide
- IZO - Indium zinc oxide
- ZTO - Zinc tin oxide
- IZTO - Indium zinc tin oxide
- ZnO - Zinc oxide
- GZO - Gallium doped zinc oxide
- AZO - Aluminium doped zinc oxide
- TiO2 - Titanium dioxide
- NiOx - Nickel oxide

- MoOx - Molybdenum Oxide
- NiCoO - Nickel cobalt oxide
- ZnCoO - Zinc cobalt oxide
- ZnNiCoO- Zinc nickel cobalt oxide
- Cu2O - Copper (I) oxide
- PLD - Pulsed laser deposition
- CVD - Chemical vapor deposition
- HOMO - Highest occupied molecular orbital
- LUMO - Lowest unoccupied molecular orbital
- TEM - Transmission electron microscopy
- SEM - Scanning electron microscopy
- AFM - Atomic force microscopy
- C-AFM - Conductive mode Atomic force microscopy
- UV-Vis - Ultraviolet-visible absorption spectroscopy
- J-V - Current density vs. voltage
- PL - Photoluminescence
- NEXAFS - Near Edge X-Ray Absorption Fine Structure spectroscopy

- PM-IRRAS- Polarization Modulation Infrared Reflection Adsorption Spectroscopy
- QE - Quantum efficiency
- EQE - External quantum efficiency
- V_{OC} - Open circuit potential
- J_{SC} - Short circuit current
- F.F. - Fill factor
- η - Power conversion efficiency
- ϕ - Work function
- ϵ_0 - Permittivity of free space (8.854 x 10^{-14} F/cm)
- ϵ - Permittivity of a medium, also listed as ϵ s
- q - Elementary charge (1.602 x 10^{-19} C)
- k - Boltzmann constant (8.617 x 10^{-5} eV/K)
- μ - Charge carrier mobility (cm^2/Vs)
- σ - Conductivity (S/cm)
- N - Carrier concentration
- n - electron density in the conduction band
- p - hole density in the valence band

- L - Charge carrier diffusion length
- Sun - Unit of illumination intensity corresponding to 1000 W/m^2 in the spectrum
- P3HT - poly(3-hexylthiophene)
- PCBM - phenyl-C61-butryric acid methyl ester
- PEDOT:PSS - poly(3,4-ethylenedioxythiophene):poly(styrenesulfonate)

Appendix C

List of publications

- "*Fabrication, Electrical and Optical Properties of Silver, Indium Tin Oxide (ITO) and Indium Zinc Oxide (IZO) Nanostructure Arrays.*" Akram A. Khosroabadi, Palash Gangopadhyay, Binh Duong, Jayan Thomas, **Ajaya K. Sigdel**, Joseph J. Berry, Thomas Gennett, N. Peyghambarian, Robert A. Norwood, **Cover Page Article: Phys. Status Solidi A, 2013, 210 (5), 831838**, DOI 10.1002/pssa.201329129

- "*Efficient Modification of Metal Oxide Surfaces With Phosphonic Acids, By Spray Coating.*" Bulusu, Anuradha, Paniagua, Sergio, MacLeod, Bradley, **Sigdel, Ajaya**, Berry, Joseph, Olson, Dana, Marder, Seth, Graham, Samuel, **Langmuir, 2013, 29(12), 39353942**, Web : February 19, 2013, DOI:10.1021/la303354t

- "*Correlating ZnO Layer Properties with the Performance of Solution-processed ZnO/Cu2O Photovoltaics.*" Talia S. Gershon, **Ajaya K. Sigdel**, Andrew T. Marin, Maikel van Hest, David S. Ginley, Richard H. Friend, Ju-

dith L. MacManus -Driscoll, Joseph J. Berry, **Thin Solid Films, 2013, 536, 280-285**

- "*Development of an instrument for spatially resolved Seebeck coefficient measurements and its application to Zn-Co-O and Ni-Co-O compositionally graded thin films.*" Andriy Zakutayev, Frank J. Luciano IV, **Ajaya K. Sigdel**, Paul F. Ndione, John D. Perkins, Joseph J. Berry, Philip A. Parilla, and David S. Ginley. **Rev. Sci. Instrum. 84, 053905 (2013)**

- "*Orientation and Order of Phenylphosphonic Acid Self- assembled Monolayers on Transparent Conductive Oxides: A Combined NEXAFS and PM-IRRAS study.*" Matthew Gliboff, Lingzi Sang, Kristina M. Knesting, Matthew C. Schalnat, Anoma Mudalige, Erin L. Ratcliff, Hong Li, **Ajaya K. Sigdel**, Joseph J. Berry, Dennis Nordlund, Anthony Giordano, Gerald T. Seidler, Jean-Luc Brdas, Seth R. Marder, Jeanne E. Pemberton, David S. Ginger. **Langmuir, 2013, 29 (7), pp 21662174**, DOI: 10.1021/la304594t

- "*Highly-Tunable Nickel Cobalt Oxide as a Low-Temperature P-type Contact in Organic Photovoltaic Devices.*" Paul F. Ndione, Andres Garcia, N. Edwin Widjonarko, **Ajaya K. Sigdel**, K. Xerxes Steirer, Dana C. Olson, Philip A. Parilla, David S. Ginley, Neal R. Armstrong, Robin E. Richards, Erin L. Ratcliff and Joseph J. Berry. **Adv. Energy Mater., 2013, 3(4), 524531** DOI: 10.1002/aenm.201200742

- "*Radio-Frequency Superimposed Direct Current Magnetron Sputtered Ga:ZnO Transparent Conducting Thin Films.*" **Ajaya K. Sigdel**, Paul F Ndione, John D. Perkins, Thomas Gennett, Maikel F.A.M. van Hest, Sean

E. Shaheen, David S. Ginley and Joseph J. Berry, DOI:10.1063/1.4709753, **Journal of Applied Physics, 111(9), 093718 (2012).**

- "*Surface composition, Work function and Electrochemical Characteristics of Gallium-doped Zinc Oxide (GZO) Semi-transparent Electrodes.*" Erin L. Ratcliff, **Ajaya K. Sigdel**, Mariola R. Macech, Kenneth Nebesny, Paul A. Lee, David S. Ginley, Neal R. Armstrong, Joseph J. Berry, DOI: 10.1016/j.tsf.2012.04.038, **Thin Solid Films, 520(17), 56525663 (2012)**

- "*Oriented Growth of Al2O3:ZnO Nanolaminates for use as Electron-Selective Electrodes in Inverted Polymer Solar Cells.*" Hyeunseok Cheun, Canek Fuentes-Hernandez, Jaewon Shim, Yunnan Fang, Ye Cai, Hong Li, **Ajaya K.Sigdel**, Jens Meyer, Julia Maibach, Amir Dindar, Yinhua Zhou, Joseph Berry, Jean-Luc Bredas, Antoine Kahn, Kenneth H. Sandhage, and Bernard Kippelen, **Advanced Functional Materials, Volume 22, Issue 7, pages 15311538, April 10, 2012**

- "*Low-temperature, Solution-processed Molybdenum Oxide Hole-collection layer for Organic Photovoltaics.*" Scott R. Hammond, Jens Meyer, N. Edwin Widjonarko, Paul F. Ndione, **Ajaya K. Sigdel**, Andres Garcia, Alexander Miedaner, Matthew T. Lloyd, Antoine Kahn, David S. Ginley, Joseph J. Berry and Dana C. Olson, DOI: 10.1039/C2JM14911G, **Journal of Materials Chemistry, 2012, 22, 3249-3254, Jan 9, 2012**

- "*Sputtered Nickel Oxide Thin Film for Efficient Hole Transport Layer in Polymer-Fullerene Bulk-heterojunction Organic Solar Cell.*" N. Edwin Widjonarko, Erin L. Ratcliff, Craig L. Perkins, **Ajaya K. Sigdel**, Andriy Zakutayev, Paul F. Ndione, Dane T. Gillaspie, David S. Ginley, Dana C. Olson,

Joseph J. Berry, DOI Number: 10.1016/j.tsf.2011.10.059, **Thin Solid Films, October 9, 2011**

- "*ZnNiCoO Wide-band-gap P-type Conductive Oxides with High Work Functions.*" A. Zakutayev, J.D. Perkins, P.A. Parilla, N.E. Widjonarko, **A.K. Sigdel,** J.J. Berry and D.S. Ginley, **MRS Communications, 2011, 1, 23-26.**DOI Number: 10.1557/mrc.2011.9, Publication Date (web): August 19, 2011

- "*Surface treatment of NiO hole transport layers for organic solar cells.*" Berry, J. J., Widjonarko, N. E., Bailey, B. A., **Sigdel, A. K.**, Ginley, D. S. and Olson, D. C., DOI Number: 10.1109/ JSTQE.2010.2049347, **(Invited) IEEE Journal of Selected Topics in Quantum Electronics (special issue focusing on Next-Generation Organic and Hybrid Solar Cells). December 3, 2010**

- "*Effect of deposition distance and temperature on electrical, optical and structural properties of radio-frequency magnetron-sputtered gallium-doped zinc oxide.*" Christopher Gorrie, **Ajaya K. Sigdel**, Joseph J. Berry, Brandon Reese, M. F. A. M. van Hest, Paul H. Holloway, David S. Ginley and John D. Perkins, DOI Number: 10.1016/j.tsf.2010.07.098 **Thin Solid Films, 519 (2010), p. 190. July 30, 2010**

- "*A simple miniature controlled-atmosphere chamber for optoelectronic characterizations.*" M.O. Reese, **A.K. Sigdel,** J.J. Berry, D.S. Ginley and S.E. Shaheen, DOI Number: 10.1016/j.solmat.2010.03.017, **Solar Energy Materials Solar Cells, 94 (2010) 12541258, April 18, 2010**

- "*Superimposed RF/DC magnetron sputtering of transparent Ga:ZnO with high conductivity for photovoltaic contacts applications.*" **Sigdel, A.K.**, Ndione, P.F., Yi Ke, Widjonarko, N.E., Perkins, J.D., van Hest, M.F.A.M., Shaheen, S.E., Gennett, T., Ginley, D.S. and Berry, J.J., 2010 Photovoltaic Specialists Conference (PVSC), 2010 35th IEEE

- "*Optimization of organic photovoltaic devices using tuned mixed metal oxide contact layers.*" Steirer, K.X., Widjonarko, N.E., **Sigdel, A.K.**, Lloyd, M.T., Ginley, D.S., Olson, D.C. and Berry, J.J., Photovoltaic Specialists Conference (PVSC), 2010 35th IEEE

- "*Mixed metal oxide systems for organic photovoltaics.* Berry, J.J., White, M.S., Widjonarko, N.E., Bailey, B.A., **Sigdel, A.K.**, Gorrie, C.W., Kopidakis, N., Ginley, D.S and Olson, D.C, Photovoltaic Specialists Conference (PVSC), 2009 34th IEEE page(s): 001448 - 001451, DOI:10.1109/PVSC.2009.5411320

- "*Development of large area transparent conducting oxides from a combinatorial lead for organic solid state lighting.* Dean W. Matson, Charles C. Bonham, James S. Swensen, Liang Wang, Asanga Padmaperuma, Daniel J. Gaspar, Joseph J. Berry, **Ajaya K. Sigdel**, Christopher W. Gorrie, and David S. Ginley, Proc. SPIE 7415, 74150X (2009), DOI:10.1117/12.827281